Fall 12-15-2012

Synthesis and Characterization of Ferroic and Multiferroic Nanostructures by Liquid Phase Deposition

Amin Yourdkhani
University of New Orleans, ayourdkh@uno.edu

Synthesis and Characterization of Ferroic and Multiferroic Nanostructures by Liquid Phase Deposition

A Thesis

Submitted to the Graduate faculty of the

University of New Orleans

In partial fulfillment of the

Requirements for the degree of

Doctor of Philosophy

in

Chemistry

By

Amin Yourdkhani

B. Sc. University of Semnan, Semnan, Iran, 2005

M.Sc. University of Tehran, Tehran, Iran, 2008

December 2012

Acknowledgements

I am truly fortunate to have spent almost four years at the Advanced Materials Research Institute (AMRI) and the Chemistry Department at the University of New Orleans that provided me the great opportunity to accomplish my graduate studies in a friendly but highly competitive environment. I would first like to thank my scientific advisor, Prof. Gabriel Caruntu who guided, mentored and encouraged me throughout my thesis with his knowledge, jovial disposition and patience.

I would like to acknowledge the members of the scientific committee, Prof. Charles J. O'Connor, Prof. John B. Wiley, Prof. Leonard Spinu and Prof. Branco Jursic for their useful suggestions during the preparation of this thesis.

I am indebted to a few graduate student fellows and postdoctoral researchers at AMRI who helped me during this thesis. My special thanks go to my former lab mates Dr. Cuikun Lin and Mr. Shiva Adireddy for their help in sample characterization by electron microscopy. I am also deeply grateful to Mr. Armando Perez for helping me during the wet chemistry experiments and express sincere thanks to Mr. Alaoddin Ayyad for proof-reading the introduction of my thesis. I would like to thank Mr. Rahmatalloah Eskandari, Mr. Taha Rostamzadeh and Mr. Saman Salemi Zadeh helping me with the preparation of the electronic format of this thesis. I owe my deepest gratitude to Caruntu group for their help, assistance and friendship.

Last, but not the least, I thank my parents for their love and unwavering support.

Abstract:

Magnetoelectric multiferroics have garnered an increasing interest in the past decade due to their unique properties and relevant applications in data storage, sensing and spintronics. A key requirement for the enhancement of the magnetoelectric effect at room temperature is the optimization of the interface between the constituting phases by designing nanocomposites with selectable topologies and variable chemical composition. In this research, the rational design of two-phase spinel-perovskite ceramic nanocomposites with two different geometries: coaxial nanostructures (1-D) and bilayered nanostructures (2-D), by a soft solution chemistry approach will be described. The liquid phase deposition (LPD) method is a simple and versatile route for the deposition of highly uniform spinel ferrite (MFe_2O_4) and/or titanium-based perovskite ($BaTiO_3$, $PbTiO_3$) by the controlled hydrolysis of metal fluoro-complexes at temperatures as low as 40°C. By designing a sequential deposition process, 1-D and 2-D magnetoelectric nanostructures were fabricated by filling perovskite nanotubes with the ferrite phase or depositing a ferrite layer on top of a perovskite thin film, respectively. The compositional and morphological characteristics of these highly uniform metal oxide nanostructures were investigated by X-ray diffraction (XRD), Raman spectroscopy, scanning probe microscopy (SPM) and electron microscopy (FE-SEM and TEM). The direct evidence of the stress mediated magnetoelectric coupling between the spinel and perovskite of the bilayered nanostructures was qualitatively studied by Raman spectroscopy. Additionally, the direct magnetoelectric effect in these 1-D and bilayered multiferroic nanocomposites was evaluated both quantitatively and qualitatively by using a novel magnetic field-assisted piezoelectric force microscopy (M-PFM) technique. The quantitative estimation of the magnetoelectric coupling coefficients was performed by tracking the changes in the phase and -amplitude of the piezoelectric signal signals when a in-plane *dc* magnetic field was applied parallel to the sample. Their non-resonant values typically range between 100-1200 mV/cm.Oe, thereby indicating a strong coupling between the magnetic and electrostrictive phases which can be used in different sensing and data storage applications.

Keywords: Ferroics, Multiferroics, Liquid Phase Deposition, Scanning Probe Microscopy, Magnetic Properties, Electrical Properties

Table of Contents

List of Figures

List of Tables

1. Introduction

1.1. Ferroic Materials

Ferroics are an important class of technological materials with unique properties that make them the leading candidates in many modern technologies such as electronics, data storage, sensing, communications and medicine. The word ferroics is derived from "ferrum", the Latin word for iron which is the oldest known ferroic material. At room temperature, iron displays a permanent magnetic moment which can be reversibly switched with an external magnetic field. Such a unique property is a characteristic of a class of materials known as ferromagnetics. Other examples of ferroic materials are ferroelectrics, which present a spontaneous, switchable intrinsic lattice polarization and ferroelastics, which can be reversibly deformed under the action of an external mechanical stress. A common feature shared by ferroic materials is their ability to undergo a phase transition from a non-ferroic to a ferroic state. For ferromagnetic and ferroelectric materials, this phase transition occurs at a well-defined temperature known as the Curie temperature. The symmetry of the ferroic crystal is lowered at the Curie temperature and this is accompanied by a huge variation in the ferroic property (polarization or magnetization) associated with the material. For example $BaTiO_3$, an archetypal ferroelectric material, at 120 $^{\circ}$C the crystal structure changes from cubic to tetragonal. This is due to the relative displacement of the two cationic sub-lattices which will induce the spontaneous formation of electrical dipoles and the onset of a dielectric polarization.

Ferroic properties in ferroelectric and ferromagnetic materials are associated to the presence of a polarization and magnetization, respectively. When such a material is cooled down and crosses a critical temperature, known as the Curie temperature, it undergoes a phase transition from a non-ferroic to ferroic state. These transitions are generally accompanied with a lowering of the crystal symmetry. For example bulk $BaTiO_3$ an archetypal ferroelectric presents a transition from a cubic paraelectric structure to a tetragonal ferroelectric structure around 120°C. The strong interaction between electrical and magnetic dipoles results in small regions within the material in which the ferroic property is uniform, with the dipoles arranged parallel to each other. Such regions are known as domains and are separated by domain walls, whereby the dipoles undergo a coherent rotation from the direction in one domain to that in the adjacent domain. Due to the random orientation of the magnetic and electrical dipoles of different domains in the

absence of an external stimulus, the total net polarization and magnetization is zero for ferroic materials. Ferroic properties depend on external conditions such as: magnetic field, electric field, pressure and temperature. The existence of domain structures is also responsible for the hysteretic response of the ferroic properties of the material when an external stress is applied. As a result, ferroic materials have the unique ability to store and release energy in the form of magnetic and electrical energy, an attribute which made them very attractive to different technologies[1]. Based on the above information, characteristics of ferroic materials are presented schematically in Figure 1.1 (a-c). In the following discussion, concepts of the ferroelectrics and ferro (ferri) magnetic materials will be discussed in detail

1.2. Dielectric, Piezoelectric, and Ferroelectric Materials

1.2.1. Crystal Symmetry

Crystalline materials crystallize into Bravais lattices with a finite number of unit cell symmetries. Based on the arrangement of the atoms or group of atoms, there are 14 possible Bravais lattices in three-dimensional space. By applying symmetry operations such as the center of symmetry, rotational axes (two, three, four and six fold rotational axes), inversion axes (two, three, four and six fold inversion axes) and mirror planes on microscopic unit cells 32 possible point groups arise. The combination of 14 possible Bravais lattices and 32 point groups results in 230 different ways of repeating a pattern in the three-dimensional space. Upon applying the center of symmetry operation, 11 of the point groups will be symmetric toward the center of the unit cell, while the remaining point groups will be asymmetric to the center. Centro-symmetric crystals do not exhibit polarity while non centro-symmetric crystals show polar behavior [2-3].

Crystalline substances have different electrical conductivities depending on the mobility of their electrons within the lattice. Crystalline solids are divided into three categories in terms of conductivity: conductors, semiconductors and insulators. Electrons in insulators are bonded to their molecules and are not free. Upon applying an electric field, electrons move in the opposite direction of the electric field to build electrical dipoles. An insulator is called dielectric if the variation of the polarization with the electric field is linear. Insulator solids are classified into subclasses of materials based on how the polarization varies versus the external electric field:

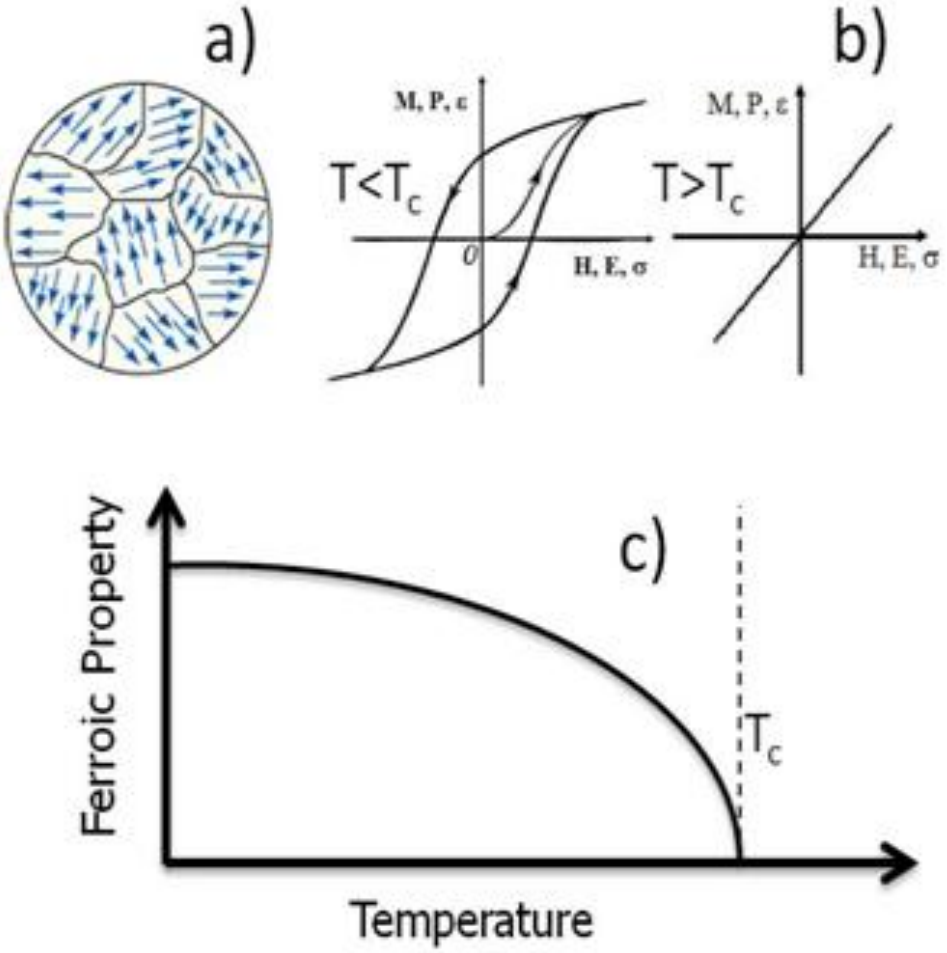

Figure 1.1. Characteristics of ferroic materials a) Ordering of physical properties, b) Hysteretic behavior and c) existence of ferroic properties below a threshold temperature

Piezoelectrics: Materials that generate a strain upon applying an electric field (converse piezoelectric effect)

Pyroelectrics: Materials that generate an electrical potential upon cooling or heating

Ferroelectrics: Materials that exhibit spontaneous polarization which is switchable by the application of an electrical field

As it was discussed earlier, if one considers the inversion operation, only 11 out of thirty two point groups are centro-symmetric. These twenty non centro-symmetric crystals are piezoelectrics and carry spontaneous polarization. Groups with a spontaneous polarization are then divided into two subgroups containing 10 point groups each: one group with a unique polarization axis and the other without. Spontaneous polarization means the existence of polarization without the application of an external electrical field. The non centro-symmetric crystals which present a spontaneous polarization and a unique polarization axis are pyroelectrics. Among the pyroelectric crystals, those which possess a spontaneous polarization which is reversibly switchable by an electric field are known as ferroelectrics. Figure 1.2 presents the relationship between the ferroelectric, pyroelectric and piezoelectric materials.

1.2.2. Dielectric Materials

Dielectrics are insulator materials which are polarized (P_i, C/m^2) linearly upon application of an electric field (E_i, V/m):

(1.1)

is the dielectric permittivity of the vacuum and κ_{ij} is the second rank tensor for the relative dielectric permittivity of the material (also known as the dielectric constant of the material). When an external electric field is applied, the microscopic polarization can originate in a medium by three different mechanisms: electronic, ionic and orientation polarization (Figure 1.3 (a-c)). The electronic polarization effect is due to the influence of the electric field on the electronic cloud on the positive nuclei. The ionic polarization results from the displacement of electrical charges in the presence of an electric field, whereas the rotation of the polar molecules in the direction of the electric field results in the orientational or rotational alignment of the permanent dipoles.

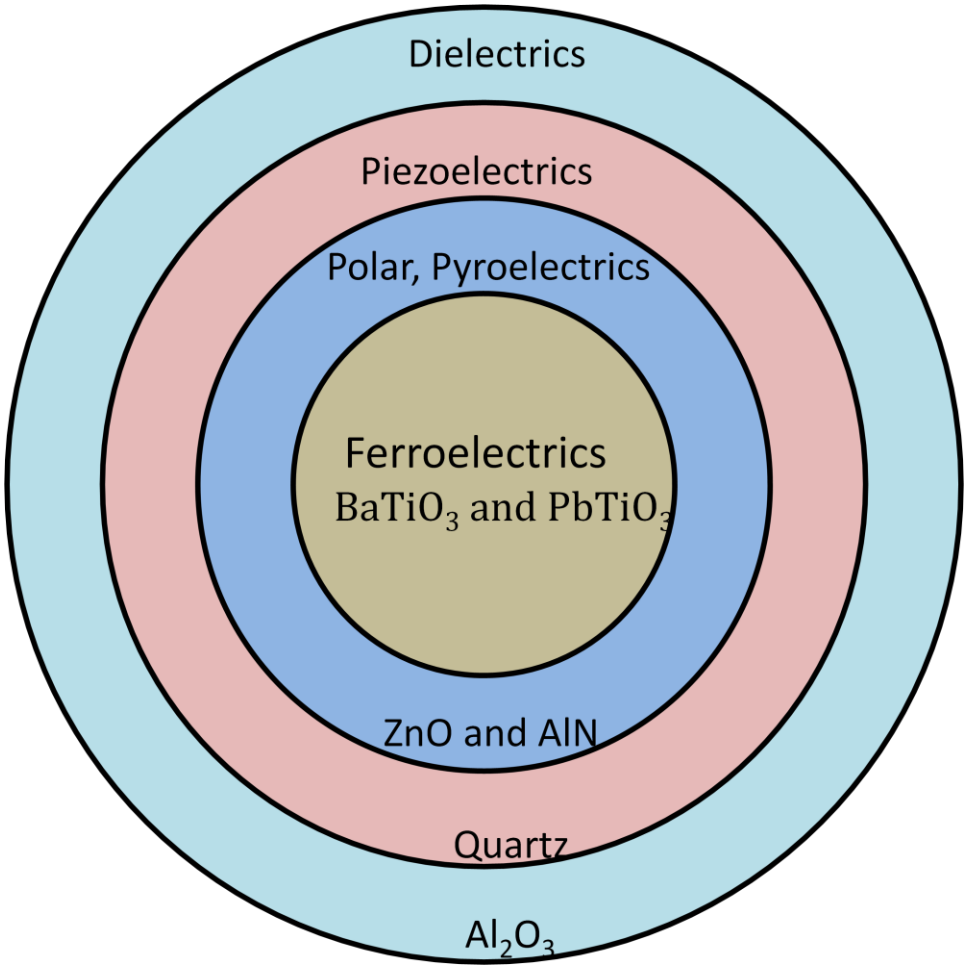

Figure 1.2. Schematic representation of ferroelectric, pyroelectric and piezoelectric materials

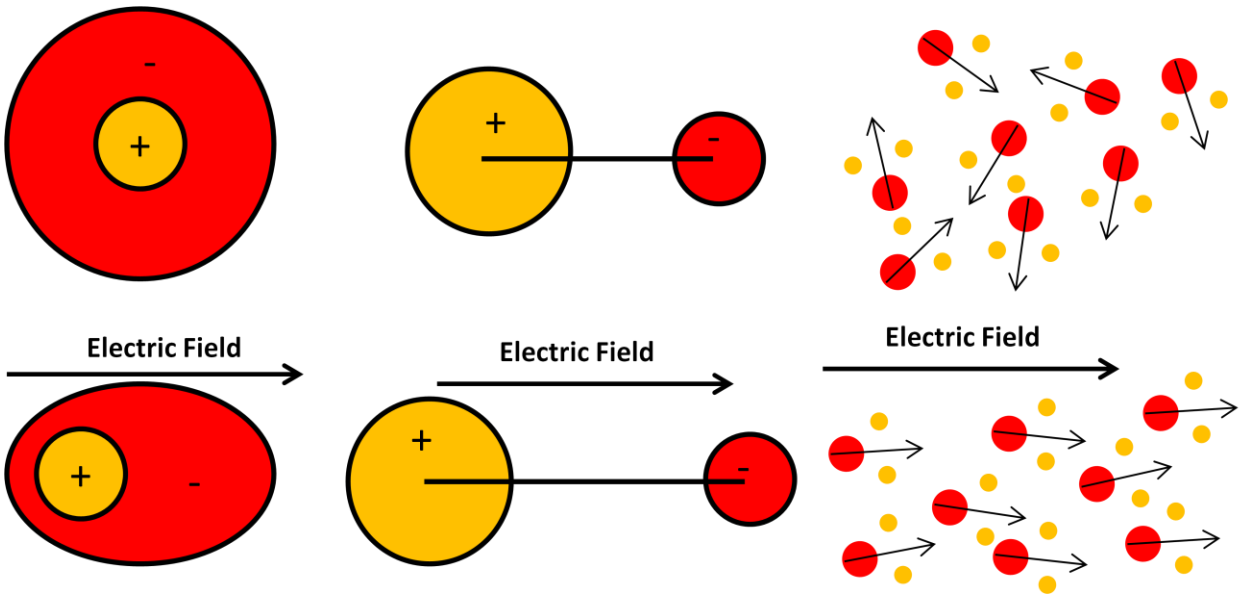

Figure 1.3. Possible mechanisms of polarization in dielectrics a) Electronic polarization, shift of electron cloud relative to the nucleus, b) Ionic polarization, change of ionic distance, c) Orientational or rotational alignment of the permanent dipoles

The dielectric displacement is defined as the total surface charge density (D_i) induced by application of an electric field and it is the sum of induced polarizations (P_i) inside the material and in vacuum ($\varepsilon_0 E_i$):

(1.2)

where $\varepsilon_0 E_i$ is the contribution of the vacuum in the dielectric displacement caused by an external electric field. By combining (1.1) and (1.2), it results that:

(1.3)

$\varepsilon_{r,ij}$ is the second rank tensor of the dielectric constant of the material. Since $\varepsilon_{r,ij}$ is a symmetrical tensor ($\varepsilon_{r,ij=}\ \varepsilon_{r,ji}$), its components reduce to six components. The number of independent components of the dielectric constant tensor may reduce upon further consideration of the symmetry of the crystal. Ceramic materials usually have a dielectric constant in the range of 5-10, but ferroelectric ceramics such as $BaTiO_3$ have a dielectric constant in the order of thousands in the vicinity of the Curie temperature. In addition, the dielectric constant varies with the frequency of the applied electric field[4].

1.2.3. Piezoelectric Materials

Materials which are polarized when a mechanical stress is applied are known as piezoelectrics (direct piezoelectric effect). The word "Piezo" is derived from the Greek word "Piezein" which means to squeeze or press. The piezoelectric effect was discovered in 1880 by Pierre Curie. They discovered that a quartz crystal changes its dimension under the application of an electric field and it generates an electrical difference potential when pressing on it. The generated surface charge density (D_i) has a linear relationship with the applied stress as a result of the direct piezoelectric effect:

(1.4)

d_{ijk} is the third rank tensor of piezoelectric coefficients and the corresponding unit is $-$.

The inverse piezoelectric effect is the creation of a mechanical strain in the material when it is subjected to an externally applied electric field:

(1.5)

The superscript "*t*" represents the sign for the transposed matrix. The unit for the converse piezoelectric coefficient is $-$. By using the conventional thermodynamic formalism, it results that the direct and converse piezoelectric coefficients are identical ($d_{direct}=d_{converse}$).

The third rank tensor of the piezoelectric coefficient has 27 components. In the direct piezoelectric effect, the input is the second rank stress tensor ( ) and the output is the first rank surface charge density tensor ( ). The input in the converse piezoelectric effect is the first rank electric field tensor ( ) and the output is the second rank strain tensor ( ). Since the second rank tensors for both stress and strain are symmetrical, the third rank piezoelectric coefficient tensor is symmetrical as well; therefore, the components of the piezoelectric tensor will be reduced from 27 to 18. The number of independent components of the piezoelectric constant tensor may reduce upon considering the symmetry of the crystal. The subscript of the components in the third rank piezoelectric coefficient tensor can be simplified by assigning 11 to 1, 22 to 2, 33 to 3, 23 or 32 to 4, 13 or 31 to 5 and 12 or 21 to 6. The converse piezoelectric effect can be re-written in a matrix form by reducing the components of the third rank piezoelectric coefficient tensor:

(1.6)

The piezoelectric coefficients are measured through the converse piezoelectric effect. When the piezoelectric coefficient is measured along the applied electric field, it is called a longitudinal piezoelectric coefficient whereas the component measured perpendicular to the electric field is known as the transverse piezoelectric coefficient. Other piezoelectric coefficients are called shear coefficients[5].

1.2.4. Ferroelectric Materials

Ferroelectrics are materials that possess a spontaneous polarization which can be switched at least between two equilibrium orientations by applying a suitable electric field. Ferroelectricity

was discovered in 1921 by Valasek in the Rochelle salt. When cooled, ferroelectrics typically undergo a phase transition from a high symmetry paraelectric state into a lower symmetry ferroelectric state. This temperature is known as the Curie temperature (T_c). Upon heating, the dielectric permittivity of the ferroelectric phase presents an irregular variation; that is it decreases slowly and abruptly around the Curie temperature to decrease again at temperatures above the transition point. The decrease of the dielectric permittivity above the Curie temperature is conventionally described by the Curie-Weiss' law:

$$\frac{C}{T - T_0} \tag{1.7}$$

C is the Curie constant and T_0 is the Curie-Weiss temperature ($T_0 < T$).

Phase transition phenomena are always associated with changes in the thermodynamic state of the system. Ferroelectrics are no exception and, therefore, thermodynamics is used to explain the phase transition in these types of materials.

The change of the Gibbs free energy of a ferroelectric material at a constant pressure can be written as following:

(1.8)

where S, T, σ, ε, E and P stand for the entropy, temperature, stress, strain, electric field and polarization, respectively. From Equation (8), one may obtain:

(1.9)

Phase transitions can be generally classified in two broad categories: first order and second order. First order phase transitions involve with a latent heat and macroscopic variables, such as the entropy, volume, polarization and the structure of a crystal present a discontinuous variation with respect to the temperature. Unlike first order transitions, second order phase transitions present a continuous variation of these parameters with respect to the temperature whereas their first order derivatives with respect to the temperature are discontinuous at the transition point.

At temperatures close to the phase transition, the Gibbs free energy of a ferroelectric can be written as a function of spontaneous polarization (P). G is an even function with respect to the

spontaneous polarization because of the symmetry of the crystal. Therefore, the odd-powers of P are eliminated from the expression of the free energy and expanding it in a Taylor series and neglecting the powers higher than six, the following Equation is obtained:

– – – (10)

where G_0 is the Gibbs free energy when *P is* annulled. The coefficients, c_2, c_4 and c_6 depend on the temperature, but c_4 and c_6 are simply independent of temperature for first and second order phase transitions. Moreover, around the Curie-Weiss temperature, the c_2 coefficient (T_0) can be approximated as:

(1.11)

The solutions for the Equation — =0 when the free energy G reaches a minimum (Equation 10), determines the values of stable spontaneous polarizations:

— (1.12)

— — (1.13)

Equation (1.12) can be solved for P=0 which represents the existence of the paraelectric phase when By combining Equation (1.11) and Equation (1.13), we obtain the Curie-Weiss' law for the electrical susceptibility (χ) when the material is paraelectric (P=0):

—— (1.14)

For first order phase transition, metastable phases form due to the existence of kinetic barriers (the nucleation of new phase in the old phase matrix) When the ferroelectric material is cooled.

Solving the Equation — determines polarization states of a ferroelectric material close to the phase transition point:

(1.15)

For $g_4<0$ and $g_6>0$, the solutions of Equation (12) are P=0 or:

(1.16)

The solutions of Equation (12) depend on how far or how close the temperature is from the phase transition point. It should be noticed that the Curie-Weiss temperature (T_0) is not equal to the phase transition temperature (T_C). The following temperature values are considered to evaluate the solutions of Equation (1.12) (See Figure 1.4 (a)):

- When $T>>T_C$, the only root is P=0 and the stable phase is the paraelectric phase
- If $T>T_C$, the stable phase is the paraelectric phase (P=0), and the metastable phase is the ferroelectric phase
- At $T=T_C$, both stable ferroelectric and paraelectric phases coexist
- When $T_0<T<T_C$, the stable phase is the ferroelectric and the metastable phase is the paraelectric
- If $T<T_0$, the stable phase is the ferroelectric phase

Unlike the first order, the second order phase transition associates with a continuous change in the physical properties of the material when the temperature crosses the phase transition point. By considering the Gibbs free energy of the ferroelectric material only up to the fourth order, the derivative of Equation (1.10) becomes:

(1.17)

The roots of Equation (1.17) are P=0 and:

(1.18)

Spontaneous polarization can exist if and only if the temperature is lower than T_0. Therefore, the phase transition and Curie-Weiss temperatures appear to be the same in the second order phase transition (Figure 1.4 (b)). By combining the Equations (1.18) and (1.13),

the electrical susceptibility of the ferroelectric material obtained below the Curie temperature is as follows:

——— (1.19)

In Figure 1.4 (a) and (b), the Gibbs free energy is shown as a function of polarization for ferroelectrics undergoing first order and second order phase transitions, respectively[6].

1.2.5. Ferroelectric Domains

In ferroelectrics, the spontaneous polarization is not aligned throughout the entire crystal. A bulk single crystal or a polycrystalline ferroelectric material contains small regions called domains. Within a domain, the electrical dipoles are parallel to each other and point to the same direction but their orientation changes coherently from a domain to another. Domains are separated by small regions whereby the dielectric polarization undergoes a coherent rotation from the orientation adopted by one domain to that of the next domain called domain walls. Domain structures form spontaneously in bulk ferroelectrics below the Curie temperature due to the tendency of the system to minimize its energy. Ferroelectric domains are associated with the minimum of the total energy which corresponds to the electrostatic and elastic energy (mechanical boundary). Perovskite titanates are one of the most important classes of ferroelectric crystals. They have the general formula of $ATiO_3$ (A=Ba, Pb) in which the cations in the A site are divalent and the titanium cations have four positive charges. . $PbTiO_3$ undergoes a phase transition from a cubic paraelectric to a tetragonal ferroelectric state at the Curie temperature of 480°C. In Figure 1.5, the unit cells of the perovskite $PbTiO_3$ are shown in both tetragonal ferroelectric and cubic paraelectric states. The Ti^{+4} is surrounded by six O^{-2} in an octahedral geometry. In a cubic crystal structure of $PbTiO_3$, the ionic distances of Ti^{+4} and the O^{-2} are the same and the electrostatic environment around the titanium ions is symmetrical. In such conditions, the cubic crystal structure does not possess a spontaneous polarization whereas the Ti^{+4} in the unit cell of the tetragonal phase of the $PbTiO_3$ present an off-center shift which leads to the formation of a possesses spontaneous polarization parallel to (001) direction.

When a cubic paraelectric phase undergoes a phase transition into a tetragonal ferroelectric phase, the off-center shift of the Ti^{+4} ions can occur with the same probability along

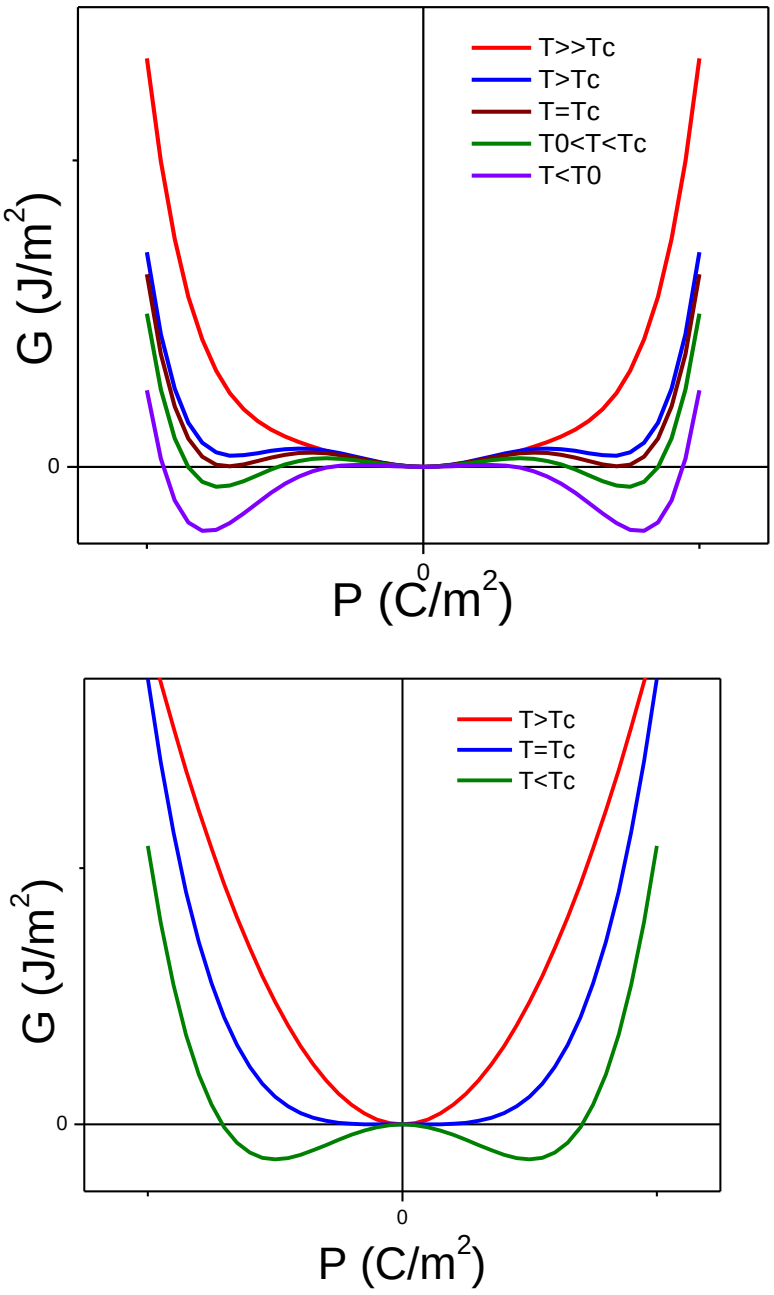

Figure 1.4. Gibbs free energy as a function of polarization for ferroelectrics undergoing a) first order transition and b) second order phase transition

six possible directions.. The dielectric and ferroelectric properties of nanoscale perovskites are strongly dependent on the electrical and mechanical boundary conditions of the sample.

Let's suppose a ferroelectric material exists naturally in a single domain state (without electrical polling). In these conditions, the complete alignment of the electrical dipoles will lead to the formation of opposite electrical charges on the surface of the ferroelectric material. These surface charges will produce an electric field, known as the depolarization field which is pointing to a direction opposite to that of the polarization vector. The single ferroelectric domain is associated with a strong depolarization field corresponding to a large electrostatic energy which makes the assumed single domain state thermodynamically unstable. In order to minimize the electrostatic energy, it is thermodynamically favorable that the single ferroelectric domain divides into domains with opposite orientations (Figure 1.6). These domains are known as 180° domains and the walls separating them are called 180° domain walls. The splitting of a domain can also occur as a result of the mechanical boundary conditions in order to minimize the total energy. To illustrate this, let's consider that above the Curie temperature a portion of a $PbTiO_3$ crystal is subjected to a mechanical stress in the direction of [100] of the cubic crystal. The stress will create an elastic energy as a result of the elastic deformation of the crystal. When the crystal is cooled down below the Curie temperature, a spontaneous polarization appears along the axis perpendicular to the direction of the applied stress. This type of domain is known as a 90° domain. In other parts of the crystal not subjected to a stress, the 180° domains will develop along the axis of stress. 90° domains exhibit both ferroelectric and ferroelastic properties simultaneously since the direction of the spontaneous polarization and the spontaneous strain vectors do not coincide. Therefore, the domain structure of a ferroelectric material is defined as the result of both the electrical and mechanical boundary conditions and the domain configuration will be a complex combination of 180° and 90° domains. Figure 1.6 illustrates the formation of ferroelectric domains under electrical and mechanical boundary conditions.

In a ferroelectric crystal with a non-tetragonal crystal structure, domain walls other than 180° and 90° may also develop. For example $BiFeO_3$ has a rhombohedral crystal structure and the spontaneous polarization lies in the eight possible directions of <111>. These eight possible orientations give rise to three kinds of domain walls which are 180°, 71° and 109°. Usually, the widths of the ferroelectric domain walls are on the order of several nanometers. In the absence of

an electric field, ferroelectrics have a zero macroscopic polarization due to random orientations of the ferroelectric domains. The most important characteristic of ferroelectrics is their unique ability to switch their polarization when subjected to an external electric field.

Ferroelectrics exhibit a non-linear and hysteretic behavior with respect to an applied electric field. The hysteretic behavior of ferroelectrics results from the reversible alignment of ferroelectric domains with the external field. Figure 1.7 shows the typical hysteresis loop of a ferroelectric material. Bulk ferroelectrics possess poly-domain structures with many domain walls. In the presence of a sufficiently strong electric field, the domains whose polarization is parallel or quasi-parallel to the direction of the field will grow at the expense of the domains whose polarization is oriented in other directions, which will eventually disappear. When saturation is reached, the polarization of the sample will remain constant regardless of the strength of the external field because all dipoles in the material are already aligned with the electric field. The shape of the hysteresis loop depends on other factors, such as the sample's thermal and electrical history, temperature, humidity and crystalline texture[7].

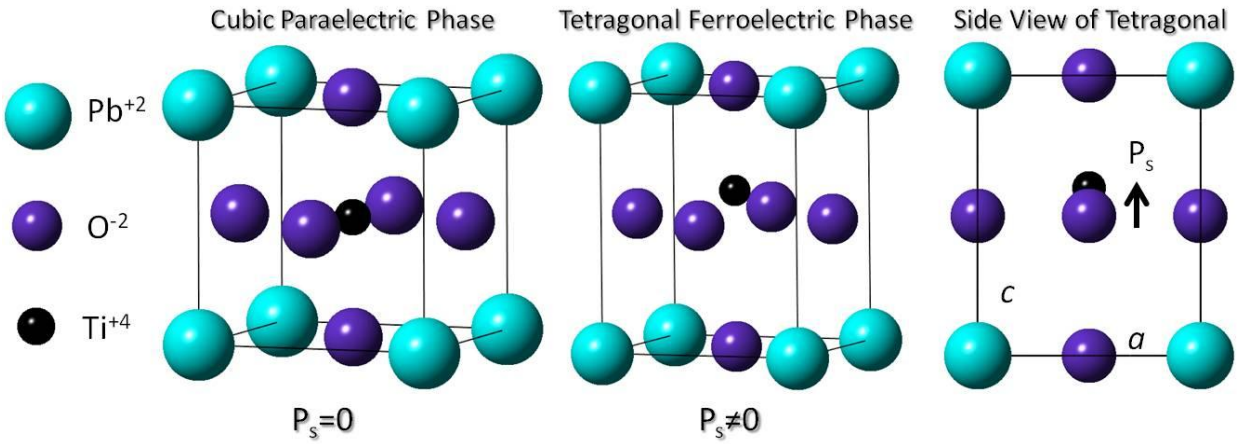

Figure 1.5. The unit cell of $PbTiO_3$ a) Cubic paraelectric, b) Tetragonal ferroelectric and c) side view of the tetragonal unit cell (note displacement of Ti^{+4} at the center)

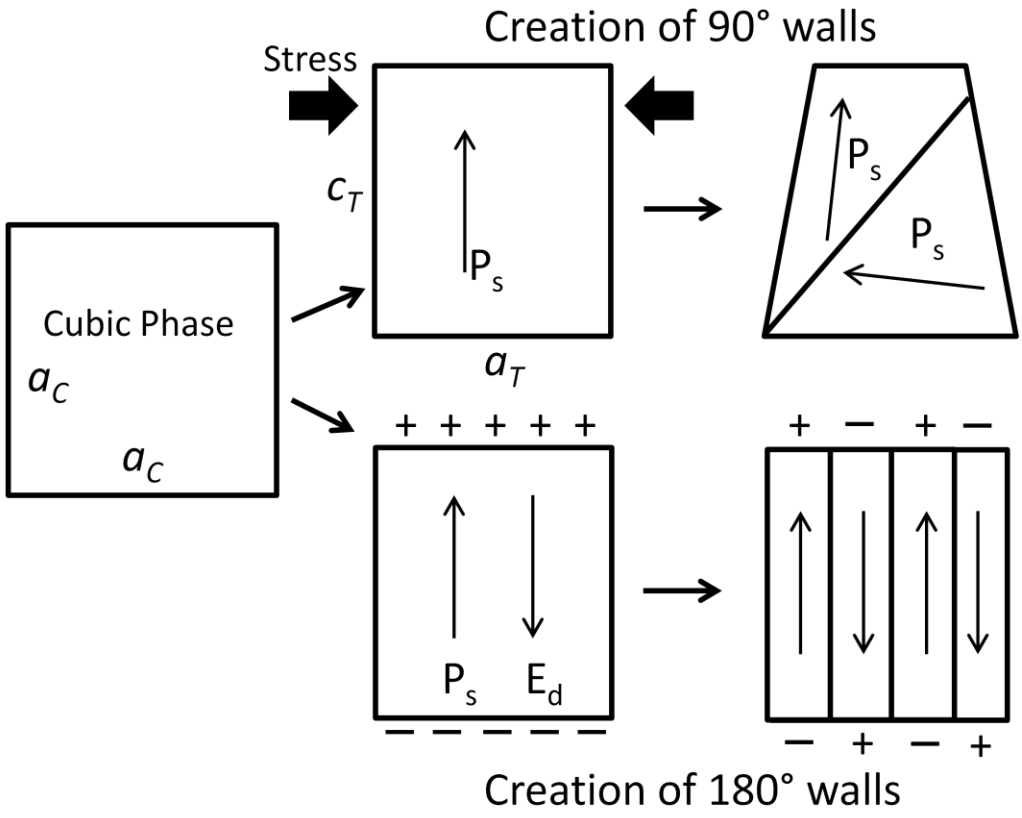

Figure 1.6. Formation of 90° and 180° ferroelectric domain walls in a tetragonal perovskite ferroelectric

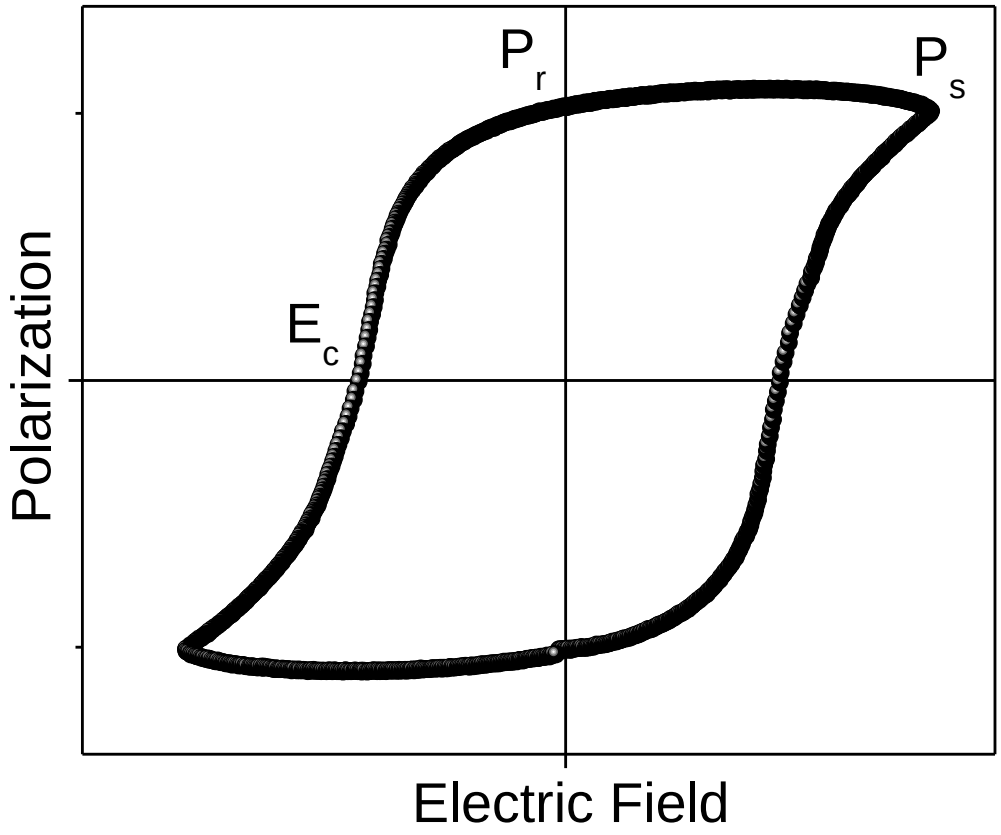

Figure 1.7 Typical hysteresis loop of a ferroelectric material

1.3. Ferromagnetic and Ferrimagnetic Materials

1.3.1. Origin of Magnetism

Magnetism originates from the rotational movement of electrons around the nucleus as well as the spinning motion of electrons around their axes. Therefore, the orbital and spin magnetic moments of electrons are responsible for the net magnetic moment of atoms or ions. The orbital magnetic moment of electrons can be considered similar to the circulation of an electrical current in a loop. The magnetic moment ( ) associated with the orbital motion of the electron lies in the same direction of the angular momentum ( ):

(1.20)

where γ_0 is a constant known as the gyromagnetic ratio which is equal to — . The orbital angular momentum, ( ), is quantized for the value of —. From the Equation (20), the magnetic moment can be expressed as

— (1.21)

μ_B is known as the Bohr magneton, which is used to express the atomic magnetic unit.

Similarly, the spinning motion of the electrons causes an intrinsic angular momentum. The spin of the electron is a quantized value which determines the intrinsic angular momentum. There are two possible values for the quantized spin, — and —. Similar to Equation (1.21), the intrinsic angular momentum can be expressed in terms of quantized values of spin as follows:

— (1.22)

where *S* is the spin quantum number. Therefore, both the orbital and spin angular momenta contribute to the total magnetic moment with different relative weights. The net magnetic moment of an atom or an ion is the total sum of the magnetic moments of each electron[8-9].

1.3.2. Exchange Interaction

The Magnetic properties of matter are the result of the interactions of the magnetic moments of atoms to each other. Based upon the interaction of the atomic magnetic moments, materials

can be divided into two categories. The first category represented by systems whereby the individual atomic magnetic moments do not interact with each other. Typical examples of such materials are paramagnetic and diamagnetic materials. The second group is represented by systems which present interactions between the magnetic moments of individual atoms or ions with formation of magnetically ordered states, interaction which is generally known as exchange coupling interaction.. The coupling interaction is explained by quantum mechanics by the overlap of atomic orbital and Pauli's exclusion principle. The exchange interaction of the atomic spins is explained by the Heisenberg spin Hamiltonian:

(1.23)

where J_{ij} is the exchange integral which explains the magnitude of the coupling between the spins of S_i and S_j. The positive sign of J_{ij} determines whether neighboring atoms have parallel magnetic moments as in ferromagnetic systems or antiparallel magnetic moments as in antiferromagnets and ferrimagnets (Negative sign of J_{ij}). According to Bethe and Slater, a negative sign of the exchange integral corresponds to , the antiparallel alignment of magnetic moments while the positive value results in parallel alignments of the spins.

The distance between the neighboring atoms determines the magnitude of the coupling of their magnetic moments. When atoms are close enough, their orbital wavefunctions (spin and orbital wavefunctions) can overlap and, the electrons will spend most of their time in the interatomic space to minimize the coulomb interactions. According to Pauli's exclusion principle, the magnetic spins must have opposite signs. This interaction leads to the occurrence of an antiparallel ordering of the magnetic moments which corresponds to a negative sign of the exchange energy known as antiferromagntic ordering., if the atomic distance is large enough, electrons will spend their time far away from each other in order to decrease the energy associated with the electron-electron repulsion which will result in positive value of the magnetic exchange energy. This will lead to a parallel alignment of the magnetic spins known as ferromagnetic ordering.

Because the exchange integral (J_{ij}) is temperature dependent, below a critical temperature (the Curie temperature (T_c)), the magnetic moments of neighboring atoms will be aligned parallel to each other via long range interactions. In such conditions, below the Curie temperature, a

ferromagnetic material possesses a spontaneous magnetization. When the temperature is increased, the spontaneous magnetization is progressively reduced to reach a zero value in the vicinity of the Curie temperature. In such conditions, the material is no longer ferromagnetic. Instead, the material becomes paramagnetic and its magnetic behavior is then explained by the Curie-Weiss' law If the exchange integral (J_{ij}) has a negative value, the magnetic moments are aligned antiparallel to each other and the material is antiferromagnetic below a critical temperature known as the Neel temperature (T_N). The spontaneous magnetization in antiferromagnetic materials is zero due to antiparallel alignment of the magnetic moments. Ferromagnetism usually occurs in compounds including more than one chemical species which include different magnetic moments occupying crystallography sites. To exemplify this, we will consider a compound with two magnetic species in two different crystallography sites of A and B. Similar magnetic species interact each other and their interaction is described by a positive value of the positive exchange integral, whereas dissimilar species , such as A and B present a negative value of their exchange integral. Since two different magnetic species have different magnetic moments, a net spontaneous magnetization is obtained.

Spinel ferrites are typical examples of ferrimagnetic materials. The term "spinel" comes from the name of the naturally occurring mineral $MgAl_2O_4$. The general chemical formula of spinel ferrites is MFe_2O_4 (where M is a divalent transition metal) and their crystal structure can be described as a closed-packed arrangement of the voluminous oxygen ions with the cations distributed over the 64 tetrahedral and 32 octahedral sites. When the oxygen ions arrange in a faced centered closed pack structure thereby defining two types of interstitial sites: tetrahedral and octahedral, respectively. There are 32 octahedral sites and 64 tetrahedral sites, respectively, When 1/8 of the tetrahedral sites are occupied with the smaller Fe^{3+} cations and ½ of the octahedral interstices are occupied by the M^{2+} ions, the structure of the ferrite is called normal (Figure 1.8). When the divalent ions swap up with half of the trivalent Fe^{3+} species the structure is called an inverse spinel. Three types of exchange interactions between A sites, B sites, and A and B sites can occur in the spinel ferrite structure: interactions between the cation occupying the A sites, interactions between the cation occupying the B sites and interactions between cations occupying the A and B sites, respectively. The interactions between the cations in the A and B sites are ferromagnetic, as the magnetic moments of these ions occupying the same sites are parallel, but the interactions between cations in the A and B sites are antiferromagnetic, since

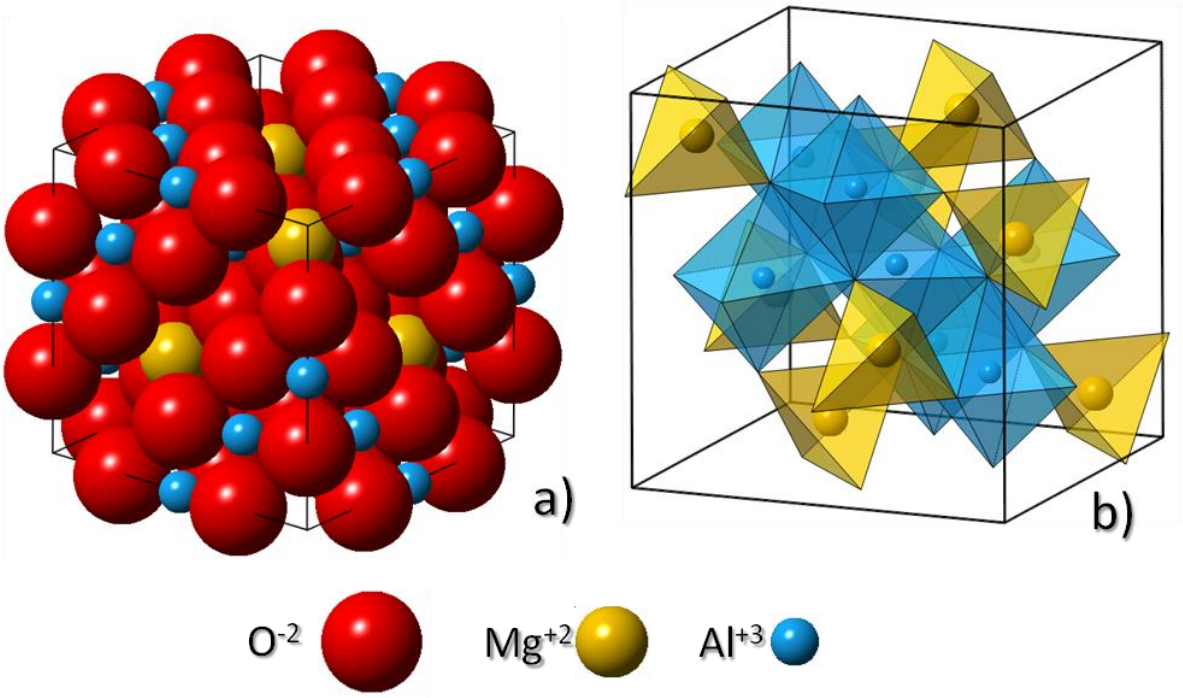

Figure 1.8. a) The crystal structure of normal spinel and b) Octahedral and tetrahedral sites in normal spinel (the oxygen ions are not represented)

their moments are oriented in opposite directions. For most of transition metal ferrites, the magnetic moments are oriented parallel to the <111> direction of the crystal; however there are some exceptions, including CoFe2O4, for which the magnetic moments are oriented parallel to the <100> direction. In Table 1 is shown how the net magnetic moment can be calculated for nickel ferrite and zinc ferrite structures, which are inverse and normal spinel ferrites, respectively[8].

1.3.3. Magnetic Domains

Similar to ferroelectric materials, the spatial regions in bulk magnetic materials in which the spins are aligned parallel to each other are known as magnetic domains. The existence of the magnetic domains was predicted theoretically by Weiss. The spontaneous onset of multi-domain structures is a consequence of the material to minimize its total energy, including the magnetostatic energy and the domain wall energy. Within a magnetic domain the spins are aligned parallel each other and point to the same direction but the orientation of the magnetization changes from one to another. Therefore, the magnetization of a magnetic domain in the material is compensated by those of the other domains, leaving the value of the magnetization close to zero in the absence of a magnetic field. Similarly, magnetic domain structures can develop in antiferromagnetic and ferrimagnetic materials in which the magnetic moments are aligned in opposite directions.

Magnetic domains are separated by domain or Bloch walls. Domain walls can be classified depending on the orientations of the magnetic moments in the neighboring domains. If the neighboring domains have antiparallel magnetization vectors, the domain wall is called a 180° domain wall. Conversely, if the neighboring domains have perpendicular magnetization vectors, the domain walls are known as 90° domain walls. Across a domain wall the orientation of the magnetic moment changes gradually towards the direction of the magnetic moment in the neighboring domain. Figure 1.9 (a) depicts the formation of 90° and 180° domains in a closure domain structure whereas in Figure 1.9 (b) is represented the 180° rotation of the magnetic moments across the domain wall. The typical width of the magnetic domain walls ranges from one to one-hundred nanometers depending on the values of the magnetic exchange energy and magnetic anisotropy. These two parameters have an opposite effect on the width of a magnetic wall. Whereas larger magnetic exchange energy results in wider magnetic domain walls, a high

magnetic anisotropy will lead to the formation of narrower walls. The width of the magnetic domain wall can be expressed as follows:

$$\delta = \pi \sqrt{\frac{A}{K}} \tag{1.24}$$

where A is the magnetic exchange energy and K is the magnetic anisotropy constant.

Similar to other ferroics ferromagnetic and ferrimagnetic materials exhibit a hysteretic behavior of their magnetization versus the applied magnetic field. The change in the magnetization is related to the response of the magnetic domains to an external magnetic field.. In the absence of the magnetic field, the net magnetization of a ferromagnetic material is zero due to the mutual compensation of the magnetization vectors of different magnetic domains in the ferromagnetic material.

When a magnetic body is subjected to the action of a magnetic field, the magnetization process occurs in via two different mechanisms depending on the relative strength of the magnetic field. At relatively low magnetic fields, the magnetic domains whose magnetization is parallel or quasi-parallel to the direction of the applied magnetic field will expand through the movement of the domain walls. This process is accompanied by a sharp change of the macroscopic magnetization. At relatively high magnetic fields, changes in the direction of the magnetization are slower than in the previous case because now domains which orientations other than that of the external magnetic field will be involved. Figure 1.10 presents the variation of the initial magnetization of a ferromagnetic or a ferrimagnetic material with the magnetic field. When all the magnetic moments are oriented in the direction of the applied field, the magnetization of the system reaches saturation (M_s). A further decrease followed by an increase of the applied magnetic field in the opposite direction results in a hysteretic variation of the magnetization with the magnetic field. The magnetization of the sample corresponding to a zero magnetic field is called remanent magnetization (M_r). The magnetic field which is required to cancel out the magnetization of the sample is known as a coercive field (H_c). Figure 1.11 shows a typical magnetic hysteresis loop[8].

Table 1.1. Cationic distribution and net magnetic moment per molecule of two typical ferrites[8]

Substance	structure	Tetrahedral A sites	Octahedral B Sites	Net Magnetic Moment (μ_B)
$NiFe_2O_4$	Inverse	Fe^{3+}	Fe^{3+} , Ni^{2+}	2
$ZnFe_2O_4$	Normal	Zn^{2+} 0	Fe^{3+} , Fe^{3+}	0

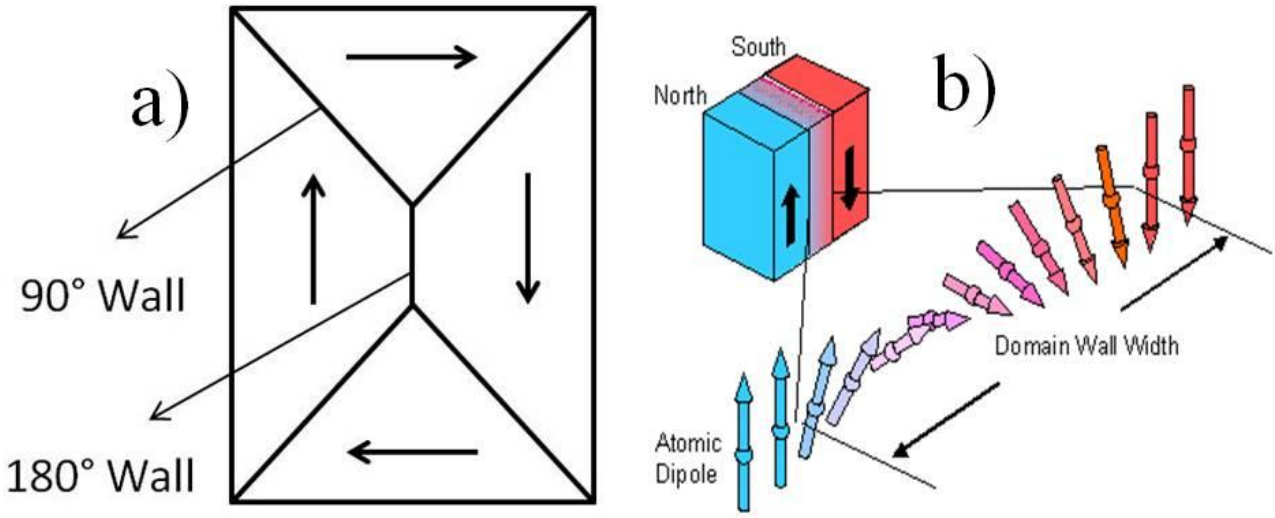

Figure 1.9. a) Formation of a closure magnetic domain structure including 90° and 180° domain walls and b) Rotation of the magnetic moments through the 180° domain wall

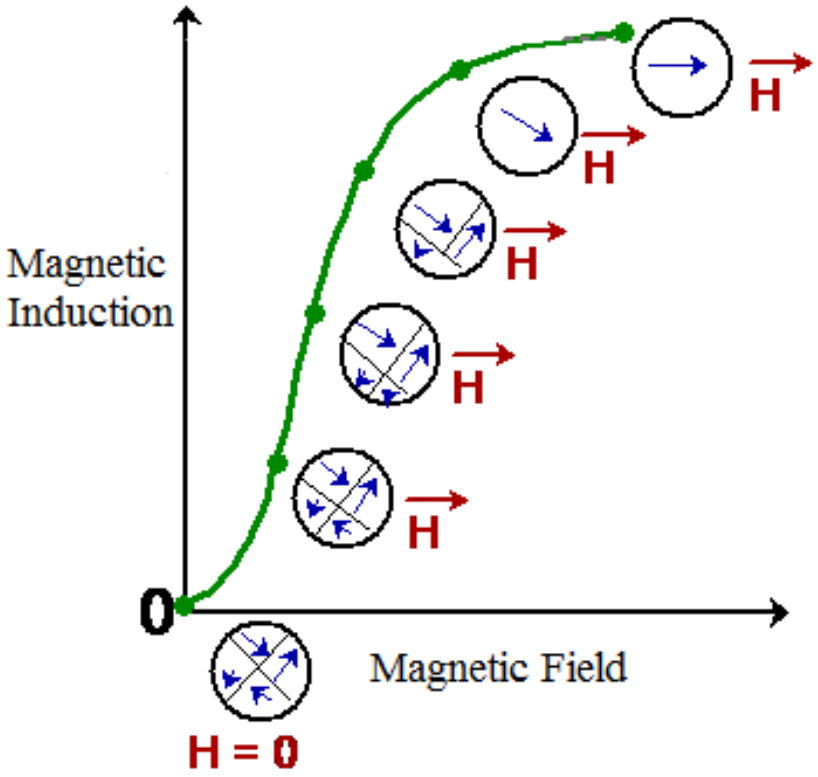

Figure 1.10. Initial magnetization of a ferromagnetic or ferrimagnetic material versus the magnetic field

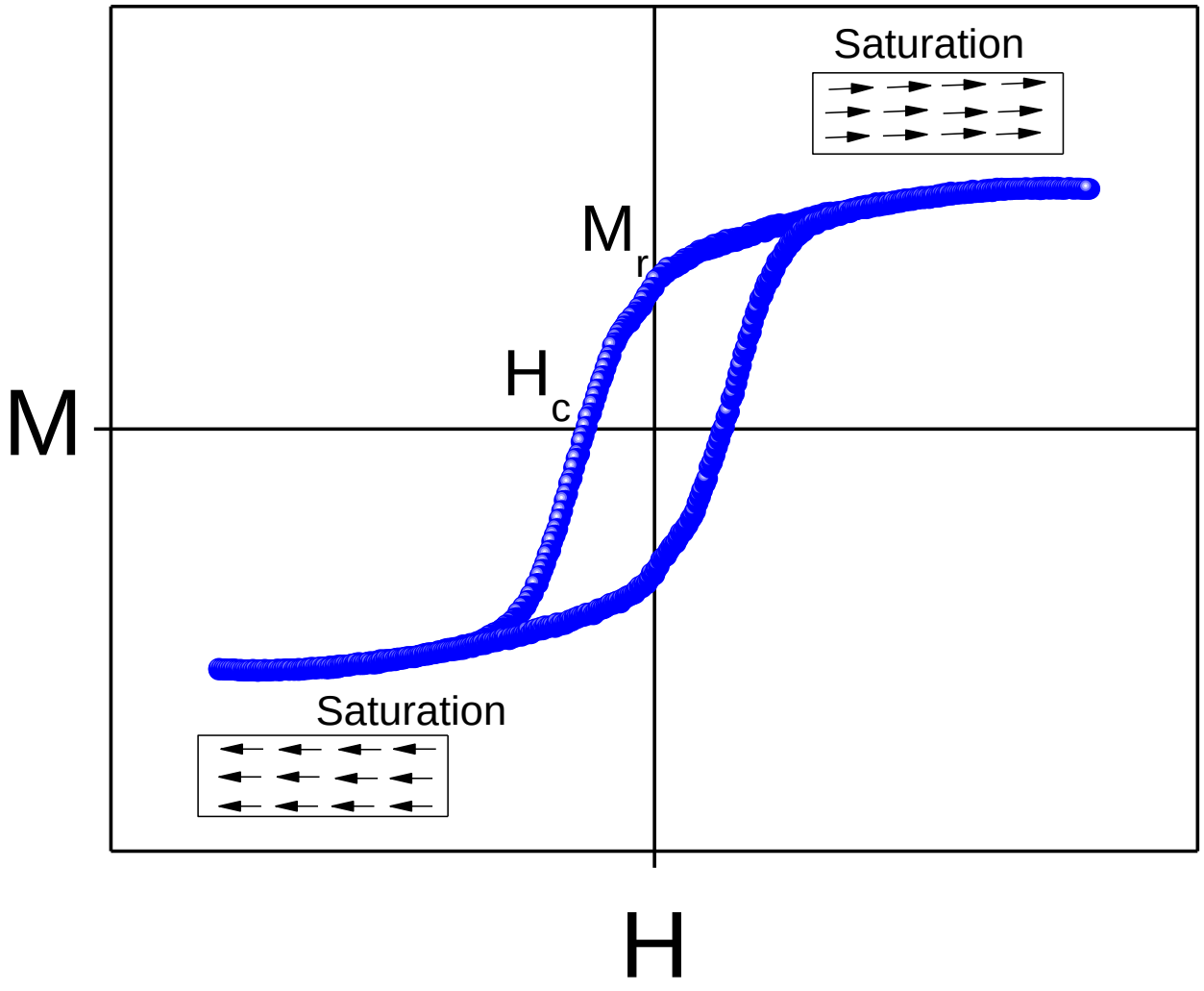

Figure 1.11. Typical magnetic hysteresis loop

1.3.4. Magnetic Anisotropy

For a magnetic material, the shape of the magnetic hysteresis loop is quite different when the magnetic field is applied parallel to different particular directions. Magnetic materials can be magnetized easier along a particular crystallographic direction as a result of the magnetic anisotropy[8]. There are several types of magnetic anisotropy:

1.3.5. Magnetocrystalline Anisotropy

Magnetocrystalline anisotropy is the only type of intrinsic magnetic anisotropy. For example, if one considers a single crystal with a cubic crystal structure which has been grown along a particular crystallographic direction, the values of the magnetization along different directions in the crystal will be different. . Figure 1.12 shows the initial magnetization curve for a body centered cubic iron single crystal. The magnetization along <100> reaches saturation at relatively lower fields compared to that along the <110> and <111> directions. Such substantial differences in the magnetization originate from the spin-orbital coupling associated with a particular crystal structure. In fact, the orbital wavefunction is the reflectance of the crystal symmetry and the spin is affected by the spin-orbital coupling which induces the anisotropy[8].

1.3.6. Shape Anisotropy

As the name says it, the shape anisotropy, also known as the magnetostatic anisotropy, differs from magnetocrystalline anisotropy, the anisotropy of a magnetic object induced by its shape. Spheroidal magnetic objects, their shape will lead to a magnetization process which is inherently uniform in all directions. Similarly, non-spherical magnetic objects magnetize easier along the long axis than along a short one. This is due to the fact that the demagnetization field along the long axis is weaker than along the short axis which will favor the magnetization processes occurring along the long axis. In bulk materials, the magnetic anisotropy is the total sum of magnetocrystalline and shape anisotropies. For materials with different types of boundary conditions, such as thin films and nanostructures, other types of anisotropies, including surface, stress and dipolar anisotropy will contribute to the total anisotropy. In many cases, in magnetic thin film structures the shape anisotropy is dominant since thin films have a high shape anisotropy in the plane of the film[8].

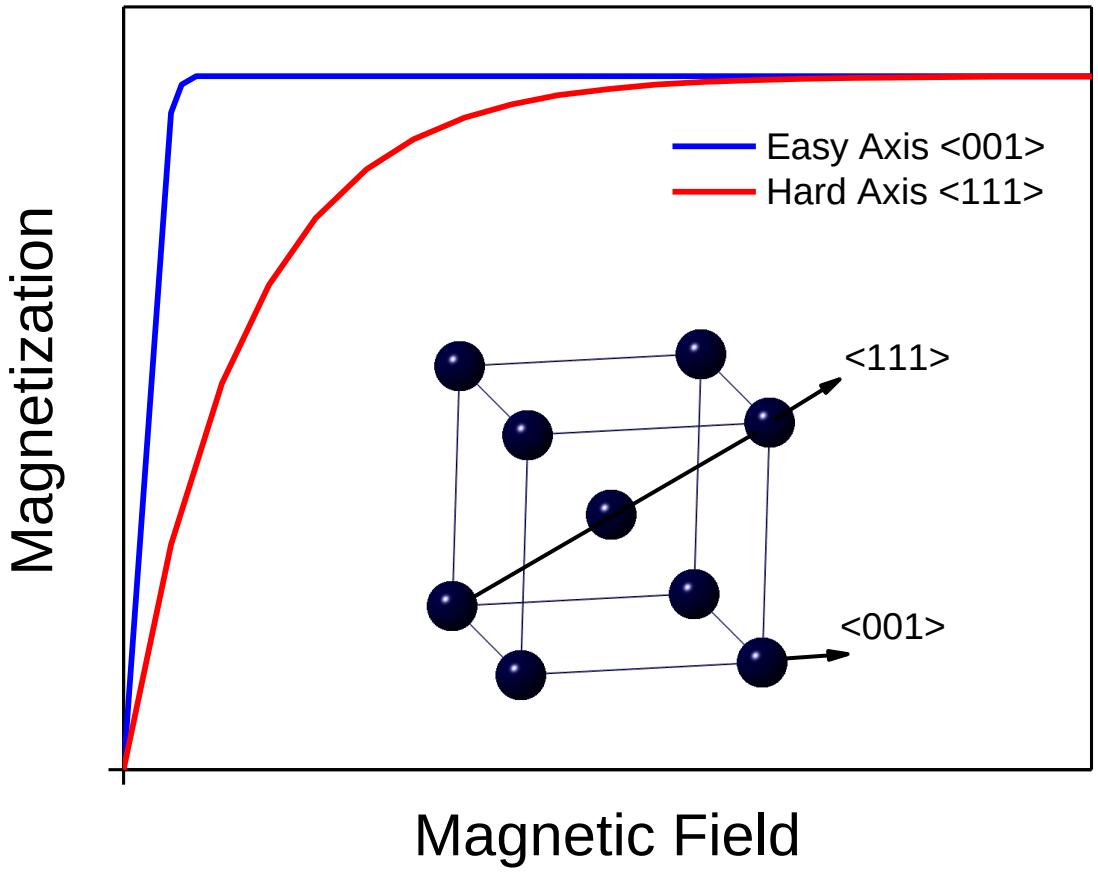

Figure 1.12. Initial Magnetization curves for easy and hard axes of the α-Fe (bcc), The Inset image depicts the easy and hard axes in a unit cell of a-Fe with bcc crystal structure

1.3.7. Surface Anisotropy

The surface to volume ratio for thin films and nanostructured objects is much higher than in the case of their bulk counterparts. In such cases, the coordination environment of the atoms on the surfaces is drastically lowered compared to regions situated in the bulk volume of the material. These anomalies occurring on the surface of low dimensional magnetic materials lead to a new type of anisotropy, known as surface anisotropy. The surface anisotropy increases with the surface to volume ratio, whereas species adsorbed species on the surface of nanoscale magnetic structures will alter the surface anisotropy[8].

1.3.8. Stress Anisotropy

The stress anisotropy originates from the magnetostriction effect. Upon application of a tensile or a compressive stress the interatomic distances will change as a result of the elastic deformation of the crystal. This will affect the spin-orbit coupling as the crystal symmetry changes. . The occurrence of an easy axis in the presence of a stress depends on the signs of the magnetostriction coefficient and the applied stress. For example, if the material possesses a negative magnetostriction coefficient, upon applying a compressive stress an easy axis appears in the crystal and vice versa[8].

1.3.9. Magnetostrictive Materials

Similar to electrostriction observed in ferroelectric materials, ferro/ferri magnetic materials have the property to change their physical dimensions when subjected to a magnetic field, property which is known as magnetostriction. The change in the physical dimensions of a rod shaped material by an applied stress can be expressed as a strain:

— (1.25)

In strong magnetic materials, the magnetostrictive effect is very small and λ at for magnetic fields reaching saturation is on the order of 10^{-5}. By transferring the induced strain to the stress using the Hooke's law, the produced stress is on the order of several 0.1 kg/mm^2. Based upon the strength of the magnetic field and the resultant magnetization, magnetostriction coefficient can have values which vary from positive to negative. At a certain magnetic field, the magnetostriction can also reach a zero value.

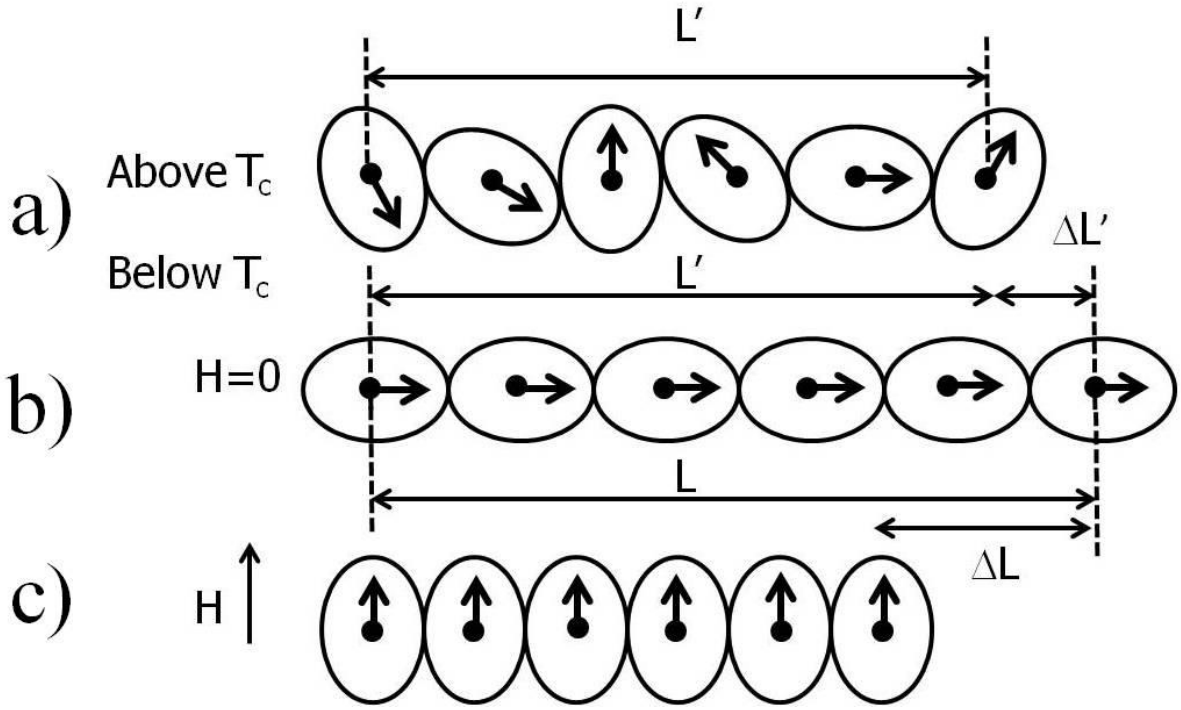

Figure 1.13. a) Paramagnetic states of the materials above the Curie temperature, b) Ferromagnetic state below the Curie temperature in the absence of the magnetic field and c) Ferromagnetic state below the Curie temperature in the magnetic field

The magnetostriction effect originates from the spin-orbit coupling. A simple model of atoms in a row in a crystal can be used to explain the origin of magnetostriction (Figure 1.13). The black dots represent the nuclei of the atoms whereas the arrows represent the net magnetic moment of each atom. The ellipses represent the probability of finding the electrons whose orbital motion around the nuclei is non-spherical trajectories (electron clouds). Figure 1.13 (a) indicates the paramagnetic state of a magnetic substance above its Curie temperature. Below the Curie temperature (Figure 13. (b)), the spins of the atoms and consequently the electron clouds lie on the easy axis. At the same time, the nuclei of the atoms are forced to be relocated which causes the spontaneous strain (spontaneous strain, —). Upon application of a strong magnetic field perpendicular to the spontaneous magnetization, the spins and the electron clouds rotate 90°. The part of the crystal which belongs to these atoms experiences a strain of — induced by the external magnetic field[8].

1.4. Magnetoelectric Multiferroics

The coexistence and coupling of at least two ferromagnetic, ferroelectric and ferroelastic material properties is a characteristic feature of an important class of advanced materials, known as magnetoelectric multiferroics. In such materials, an electric current can be induced upon application of an external magnetic field (the direct magnetoelectric effect) and vice-versa (the converse magnetoelectric effect). Figure 1.14 schematically illustrates the direct and converse magnetoelectric effects. Pierre Curie anticipated the existence of the magnetoelectric effect in 1894 and it also predicted for Cr_2O_3 by Dzyaloshinskii in 1959. A magnetically induced polarization was first reported for Cr_2O_3 by Astrov in 1960. One year later, Rado and Folen observed the converse magnetoelectric effect for Cr_2O_3[10-11]. In the following section, a simple thermodynamic model is used to correlate the direct and converse magnetoelectric effects of a multiferroic material in the presence of external stimuli.

The Gibbs free energy of a multiferroic system is dependent on temperature, pressure, the electric field and the magnetic field, as described by Equation (1.26)[12].

(1.26)

where V is the volume, p is the pressure, S is the entropy, P is the polarization, E is the electric field, M is the magnetization and H is the magnetic field. At a constant pressure and temperature, the Equation (1.26) can be simplified to Equation (1.27) as follows:

(1.27)

By using the equality of cross derivatives, it results that:

$$\left(\frac{\partial P}{\partial H}\right)_E = \left(\frac{\partial M}{\partial E}\right)_H \tag{1.28}$$

In general, the above term is known as the direct magnetoelectric coefficient ($\alpha_{direct} = \left(\frac{\partial P}{\partial H}\right)_E$ In a similar fashion, we can define the indirect magnetoelectric coefficient ($\alpha_{indirect} = \left(\frac{\partial M}{\partial E}\right)_H$).In terms of the material constituents, multiferroics are generally divided into two categories; that is single phase multiferroics and composites:

1.4.1. Single Phase Multiferroics

In general, the magnetoelectric coupling in single phase multiferroics is very weak since it involves the relativistic spin-orbit coupling and occurs at temperatures well below room temperature (for example in R_2CuO_4, R: Rare earth element it occurs at 6°K). Meanwhile, strong magnetic fields (>20 T for $BiFeO_3$) are required for a sizeable magnetoelectric effect. As such, these disadvantages drastically limit the use of single phase multiferroics in practical applications[10].

1.4.2. Magnetoelectric Composites

Composites consist of at least two ferroic materials in which neither of the pristine ferroics shows magnetoelectric properties. The coupling between the magnetostriction in the magnetic phase (Magnetomechanical coupling) and the piezoelectricity in the electrostrictive phase (Electromechanical coupling) induces the magnetoelectric properties. Since it is a product property, the response in composite materials can be described expressed by:

——— ——— (1.29) and ——— ——— (1.30)

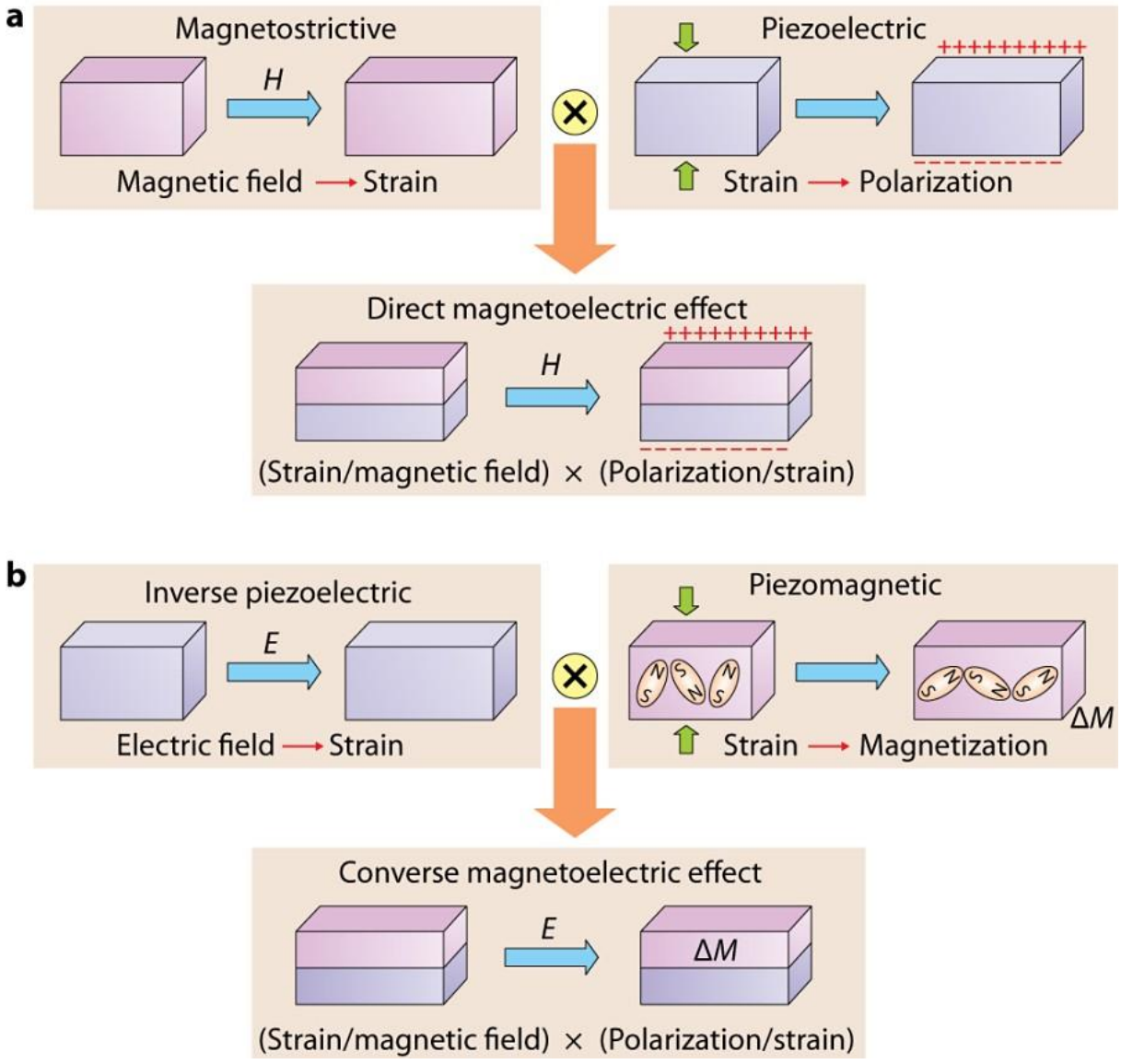

Figure 1.14. Schematic representation of the direct (a) and converse (b) Magnetoelectric effects[13]

When a magnetoelectric composite material is subjected to the action of a magnetic/electric field, the ferroelectric/ferromagnetic phase, which has electrostrictive/magnetostrictive properties, will respond to the external stimulus by changing its physical dimensions. Such a change in the physical dimensions of one of these phases induces a stress which is subsequently transferred to the other phase across the shared interface, eventually leading to a change of its ferroic properties. As the interface between ferroic phases plays a key role in the magnetoelectric coupling, there is an increasing technological interest in designing magnetoelectric composites with high interfacial contact between the two dissimilar phases which, in turn will lead to an enhancement of the magnetoelectric coupling. . One practical way to increase the surface contact area between the constituting phases in a magnetoelectric composite material is nanostructuring. This will result in a reduction of the interface losses compared to the conventional magnetoelectric composites obtained by co-sintering or adhesive bonding. In addition, epitaxial and superlattice structures of magnetoelectric nanocomposite films can be grown by properly selecting the ferroic phases based on their crystal structures and values of the lattice parameters. magnetoelectric nanocomposite architectures consisting of a ferromagnetic and a ferroelectric phase can be generally designed in three types of selectable topologies: particulate nanocomposite films with magnetic particles embedded in a ferroelectric film matrix (also referred to as 0-3 composites), nanopillars of one phase embedded into a matrix formed by the other phase (1-3) and horizontal heterostructures consisting of alternating ferroelectric and magnetic layers (2-2)[14-16].

1.4.2. Magnetoelectric Nanocomposites

Spinel ferrite-perovskite nanocomposites received a great deal of interest in design and fabrication of magnetoelectrics since they exhibit a robust magnetoelectric effect room temperature which can be potentially used in various applications in data storage, spintronics and sensing [17-19]. The strong magnetoelectric coupling in nanocomposites is due to higher interphase area between the ferroics in compare to the bulk composites. As the technological performance of these materials is expressed by the amount of the energy converted, which, in turn, is proportional to the coupling between the two phases, a significant effort was directed to the design of magnetoelectric nanocomposites with a maximum surface area by varying (1) the local architecture of the magnetoelectric nanocomposite and (2) the connectivity scheme between the ferroelectric and magnetic phases. Thermodynamic calculations show that among the possible

geometries, vertical heterostructures with magnetic phase nanopillars embedded in a ferroelectric matrix provide the maximum interphase surface area and this can lead to a substantial enhancement of the magnetoelectric coupling [20]. Such an assumption was experimentally proven by Zheng and coworkers who designed thin film structures whereby $CoFe_2O_4$ nanopillars are embedded epitaxially into a $BaTiO_3$ matrix [19].

Several methods have been proposed for the fabrication of two-phase magnetoelectric nanocomposites consisting of magnetostrictive spinel ferrites and ferroelectric perovskite titanates. They include solid state sintering of magnetic nanoparticles embedded into a ferroelectric matrix[21], successive sol-gel processing steps using anodic aluminum oxide (AAO) membranes to confine the magnetic oxide core within the ferroelectric oxide shell[22], electrodeposition of ferromagnetic transition metals into the free space of ferroelectric oxide nanotubes embedded into the AAO membrane[23]and electrospinnig in combination with a sol-gel method[24].

1.4.3. Magnetoelectric Characterization of Nanocomposites

As the conventional measurement set-up (for bulk magnetoelectric composite) fails to determine the magnetoelectric properties of the nanostructures due to difficulties in the separation of the magnetoelectric signal and noise, Raman spectroscopy and scanning probe microscope (SPM) have been recently introduced for the magnetoelectric characterization of bilayered nanocomposites[25-26]. The direct strain-mediated magnetoelectric effect has been demonstrated for bilayered nanocomposites by tracking the changes in the wavenumbers of the lattice dynamic vibrations corresponding to the ferroelectric phase in the presence of a magnetic field[27-28]. Unfortunately, magnetic field assisted Raman spectroscopy is not enabled for the nanoscale ME characterization of nanocomposites such as core-shell nanotubes and nanocables due to the diffraction limit of the visible light. To overcome this obstacle, piezoresponse force microscopy, was used to image the ferroelectric domains and measure the local piezoelectric properties[29-32]. Recently, a novel technique based on the piezoresponse force microscopy has been developed to evaluate the stress-mediated magnetoelectric properties of the multiferroic nanocomposites[33]. The ability of the piezoresponse force microscopy to probe nanoscale objects due to the nanometer size and the geometry of the conductive tip enables us to measure the piezoelectric properties of isolated 1-D multiferroic nanocomposites by applying an in-plane *dc*

magnetic field in conjunction with an electric field applied perpendicular to the plane of the sample.

1.5. The Liquid Phase Deposition (LPD) Method

The liquid phase deposition (LPD) is a soft solution technique based on the slow hydrolysis of metal-fluoro complex species at temperatures below 60°C. The hydrolysis occurs via an equilibrium reaction m whereby the fluoride ions from the inner coordination sphere of the metal are gradually replaced by OH^- ions and/or water molecules thereby yielding mixtures of metal hydroxydes/oxyhydroxides. These reaction intermediates can be converted into the desired oxides upon a heat treatment at temperatures typically ranging between 400 and 800 ^oC. The liquid phase deposition is simple, easily scalable, allows the deposition of oxide films on substrates with complex morphologies and does not require expensive vacuum equipment as in the case of most physical deposition techniques. Moreover, these reactions can be performed at low temperatures and are environmentally friendly.. In the absence of a fluorine scavenger, the hydrolysis reaction is slow when performed room temperature and the equilibrium is reached. (Reaction 1.1). Adding boric acid to the treatment solution will lead to the consumption of the fluoride ions with the formation of a complex of $[BF_4]^-$ ion which is stable water soluble and allows the elimination of the F_ ions from the resulting oxide (reaction 1.2).

$$MF_n^{(n-2m)-} + mH_2O \rightleftharpoons 1\,MO_m + nF^- + 2mH^+ \quad (1.1)$$

$$H_3BO_3 + 4HF \rightleftharpoons BF_4^- + H_3O^+ + 2H_2O \quad (1.2)$$

The liquid phase deposition was first introduced by Deki et al. for silica thin films and has been subsequently extended to other simple oxides such as TiO_2[34], SiO_2[35], ZrO_2[36], SnO_2[37], Fe_2O_3[38] and NiO[39]. This method was recently used for the deposition of for complex metal oxides of spinel ferrites, AFe_2O_4 (A=Co, Ni and Zn)[40-41], perovsikites such as ABO_3 (A= Ba, Sr and Pb, B=Ti and Zr)[42-43], magnetoplumbite hexagonal ferrite and bilayered perovskite/spinel ferrites [27]. Due to the ability of the liquid phase deposition technique to coat surfaces with complex spatial geometry, this method was also proposed for the fabrication of patterned nano-objects and 1-D nanostructures. Deki and coworkers fabricated vertically aligned iron oxide nanopillars using the liquid phase deposition technique[44]. Vertically aligned $PbTiO_3$ nanotubes on the substrates were fabricated by LPD using ZnO nanorods as the sacrificial templates. Also,

highly ordered spinel ferrite $M_xFe_{3-x}O_4$ (M=Ni, Co, Zn)[45] and ABO_3 (A=Ba and Sr)[46] nanotube arrays were synthesized in AAO templates with a pore size of 200 nm by a template-assisted LPD route.

1.6. References

(1) Wadhawan, V. *Introduction to Ferroic Materials*; Taylor & Francis, 2000.

(2) Burfoot, J. C. *Ferroelectrics: an introduction to the physical principles*; Van Nostrand, 1967.

(3) Sands, D. E. *Introduction to Crystallography*; Dover Publications, 1994.

(4) Von Hippel, A. R. *Dielectric materials and applications*; Artech House, 1954.

(5) Nelson, W. G. *Piezoelectric Materials: Structure, Properties and Applications*; Nova Science Pub Incorporated, 2010.

(6) Rabe, K. M.; Ahn, C. H.; Triscone, J. M. *Physics of Ferroelectrics: A Modern Perspective*; Springer, 2007.

(7) Damjanovic, D. *Reports on Progress in Physics* **1998**, *61*, 1267.

(8) Cullity, B. D.; Graham, C. D. *Introduction to Magnetic Materials*; Wiley, 2011.

(9) Buschow, K. H. J.; de Boer, F. R. *Physics of Magnetism and Magnetic Materials*; Springer, 2003.

(10) Nan, C.-W.; Bichurin, M. I.; Dong, S.; Viehland, D.; Srinivasan, G. *Journal of Applied Physics* **2008**, *103*, 031101.

(11) Wang, Y.; Hu, J.; Lin, Y.; Nan, C.-W. *NPG Asia Mater* **2010**, *2*, 61.

(12) Vopsaroiu, M.; Stewart, M.; Hegarty, T.; Muniz-Piniella, A.; McCartney, N.; Cain, M.; Srinivasan, G. *Measurement Science & Technology* **2008**, *19*.

(13) Wang, Y.; Hu, J. M.; Lin, Y. H.; Nan, C. W. *Npg Asia Materials* **2010**, *2*, 61.

(14) Nan, C. W.; Bichurin, M. I.; Dong, S. X.; Viehland, D.; Srinivasan, G. *Journal of Applied Physics* **2008**, *103*.

(15) Srinivasan, G. In *Annual Review of Materials Research, Vol 40* 2010; Vol. 40, p 153.

(16) Martin, L. W.; Chu, Y. H.; Ramesh, R. *Materials Science & Engineering R-Reports* **2010**, *68*, III.

(17) Gao, X. S.; Rodriguez, B. J.; Liu, L. F.; Birajdar, B.; Pantel, D.; Ziese, M.; Alexe, M.; Hesse, D. *Acs Nano* **2010**, *4*, 1099.

(18) Yan, L.; Yang, Y. D.; Wang, Z. G.; Xing, Z. P.; Li, J. F.; Viehland, D. *Journal of Materials Science* **2009**, *44*, 5080.

(19) Zheng, H.; Wang, J.; Lofland, S. E.; Ma, Z.; Mohaddes-Ardabili, L.; Zhao, T.; Salamanca-Riba, L.; Shinde, S. R.; Ogale, S. B.; Bai, F.; Viehland, D.; Jia, Y.; Schlom, D. G.; Wuttig, M.; Roytburd, A.; Ramesh, R. *Science* **2004**, *303*, 661.

(20) Liu, G.; Nan, C. W.; Xu, Z. K.; Chen, H. D. *Journal of Physics D-Applied Physics* **2005**, *38*, 2321.

(21) Babu, S. N.; Srinivas, K.; Suryanarayana, S. V.; Bhimasankaram, T. *Journal of Physics D-Applied Physics* **2008**, *41*.

(22) Raidongia, K.; Nag, A.; Sundaresan, A.; Rao, C. N. R. *Multiferroic and magnetoelectric properties of core-shell CoFe2O4@BaTiO3 nanocomposites*; AIP, 2010; Vol. 97.

(23) Liu, M.; Li, X.; Imrane, H.; Chen, Y.; Goodrich, T.; Cai, Z.; Ziemer, K. S.; Huang, J. Y.; Sun, N. X. *Synthesis of ordered arrays of multiferroic NiFe2O4-Pb(Zr0.52Ti0.48)O3 core-shell nanowires*; AIP, 2007; Vol. 90.

(24) Xie, S.; Ma, F.; Liu, Y.; Li, J. *Nanoscale* **2011**, *3*, 3152.

(25) Zavaliche, F.; Zheng, H.; Mohaddes-Ardabili, L.; Yang, S. Y.; Zhan, Q.; Shafer, P.; Reilly, E.; Chopdekar, R.; Jia, Y.; Wright, P.; Schlom, D. G.; Suzuki, Y.; Ramesh, R. *Nano Letters* **2005**, *5*, 1793.

(26) Yan, L.; Xing, Z. P.; Wang, Z. G.; Wang, T.; Lei, G. Y.; Li, J. F.; Viehland, D. *Applied Physics Letters* **2009**, *94*.

(27) Yourdkhani, A.; Perez, A. K.; Lin, C. K.; Caruntu, G. *Chemistry of Materials* **2010**, *22*, 6075.

(28) Li, Z.; Wang, Y.; Lin, Y. H.; Nan, C. *Physical Review B* **2009**, *79*.

(29) Kim, Y.; Han, H.; Lee, W.; Baik, S.; Hesse, D.; Alexe, M. *Nano Letters* **2010**, *10*, 1266.

(30) Kalinin, S. V.; Morozovska, A. N.; Chen, L. Q.; Rodriguez, B. J. *Reports on Progress in Physics* **2010**, *73*.

(31) Morozovska, A. N.; Eliseev, E. A.; Kalinin, S. V. *Journal of Applied Physics* **2007**, *102*.

(32) Anbusathaiah, V.; Jesse, S.; Arredondo, M. A.; Kartawidjaja, F. C.; Ovchinnikov, O. S.; Wang, J.; Kalinin, S. V.; Nagarajan, V. *Acta Mater* **2010**, *58*, 5316.

(33) Yourdkhani, A.; Garza, E.; Zaldivar, L.; Spinu, L.; Caruntu, G. *Magnetics, IEEE Transactions on* **2011**, *47*, 3939.

(34) Deki, S.; Aoi, Y.; Hiroi, O.; Kajinami, A. *Chemistry Letters* **1996**, 433.

(35) Deki, S.; Ko, H. Y. Y.; Fujita, T.; Akamatsu, K.; Mizuhata, M.; Kajinami, A. *European Physical Journal D* **2001**, *16*, 325.

(36) Kuratani, K.; Uemura, M.; Mizuhata, M.; Kajinami, A.; Deki, S. *Journal of the American Ceramic Society* **2005**, *88*, 2923.

(37) Saito, Y.; Sekiguchi, Y.; Mizuhata, M.; Deki, S. *Journal of the Ceramic Society of Japan* **2007**, *115*, 856.

(38) Deki, S.; Aoi, Y.; Okibe, J.; Yanagimoto, H.; Kajinami, A.; Mizuhata, M. *Journal of Materials Chemistry* **1997**, *7*, 1769.

(39) Lee, M.-K.; Fan, C.-H. *Journal of The Electrochemical Society* **2009**, *156*, D395.

(40) Caruntu, G.; Newell, A.; Caruntu, D.; O'Connor, C. J. *Journal of Alloys and Compounds* **2007**, *434*, 637.

(41) Caruntu, G.; Bush, G. G.; O'Connor, C. J. *Journal of Materials Chemistry* **2004**, *14*, 2753.

(42) Hsu, M.-C.; Sun, Y.-M.; Leu, I.-C.; Hon, M.-H. *Applied Surface Science* **2007**, *253*, 7639.

(43) Lee, M. K.; Liao, H. C.; Tung, K. W.; Shih, C. M.; Shih, T. H. *Journal of Physics D-Applied Physics* **2002**, *35*, 61.

(44) Deki, S.; Iizuka, S.; Horie, A.; Mizuhata, M.; Kajinami, A. *Journal of Materials Chemistry* **2004**, *14*, 3127.

(45) Yourdkhani, A.; Caruntu, G. *Journal of Materials Chemistry* **2011**, *21*, 7145.

(46) Chen, Y.-Y.; Yu, B.-Y.; Wang, J.-H.; Cochran, R. E.; Shyue, J.-J. *Inorganic Chemistry* **2008**, *48*, 681.

2. Analytical Techniques and Instrumentation Used in This Work

2.1. X-Ray Diffractometer

Crystal structure and lattice parameters of the synthesized nanostructures were determined by X-ray diffraction technique. A Philips-X'PERT Diffractometer operated at 40 kV and 40 mA with a wavelength of 1.5406Å (CuK_α) was used. Experiments were performed in grazing incidence mode (2^o) with a curved graphite single-crystal monochromator.

2.2. Scanning Probe Microscopy

The most versatile tool to study the surface properties of the thin films and nanostructures is the scanning probe microscopes. Upon changing the scanning probes and modes, various forces between surface and probe such as atomic, electrostatic, piezoelectric and magnetic forces are recorded during the raster scan of the surface. Recorded forces are processed to obtain the images which provide information about the surface morphology, surfaces charges, ferroelectric and magnetic domains, respectively.

The working operation of the scanning probe microscope is schemed in Figure 1. A spring-like cantilever with a sharp tip at the end is brought close to the top surface to detect the various forces between tip and surface depending on the tip properties and the scanning modes. The cantilever from another end is mounted on a piezoelectric tube which detects the applied forces on the tip by direct piezoelectric effect. The piezoelectric tube has another two sets which are normal to each other. Upon applying voltages to the piezoelectric tubes, the end of the tubes bends in x and y axes due to the converse piezoelectric effect. After careful calibration of the applied voltages, the position of the tip is able to be read accurately and the surface is raster scanned by tip in a zigzag track.

A laser beam is focused on the back side of the cantilever which is reflected to a position sensitive photodetector. When the reflected laser is in the middle of the photodetector, the voltage output from the photodetector is 0V. If the tip raster scans a very smooth surface the reflected laser is in the center of the photodetector. When the reflected laser is on the upper and lower portion of the photodetector, the output voltage of the detector is positive and negative, respectively. If the tip raster scans a small bump or pit, the end of the cantilever will bend up or down, consequently the reflected laser on the photodetector will move up or down in the

photodetector. By combination of the position (x,y) and the height (z) of the tip, a map of the surface can be obtained.

In addition to height, the information related to the phase is important, too. The cantilever oscillates at the resonance frequency. In this case, if the surface of the sample is flat and smooth, the variation of the frequency during the raster scanning is constant. If tip experiences uphill gradient or a surface with high stiffness, the vibration period of the tip decreases. If the tip raster scans the downhill gradient or a soft material, the vibration period of the tip increases. In fact, phase is given by the shift of the vibration period of the tip during the raster scanning.

Basically, the tip raster scans the surface in three different modes: contact, tapping and lift. In contact mode, a direct current is applied to the piezoelectric tube and therefore, a certain force is applied to the surface while the tip is brought in contact to the surface. Contact mode also is known as DC mode. In this mode, the tip wears out quickly and the surface is scratched during the raster scan. Piezoelectric force microscopy (PFM) works in the contact mode in which the conductive tip is positively biased while the sample is ground. In tapping mode, the tip tapes close to the surface at the resonance frequency. In this mode, the tip wears out slowly and the chance for scratching the surface is also reduced. Tapping mode is the most common mode for studying the surface topography of the thin films. In the lift mode, the tip raster scans the surface while it is lifted about 10 to 300 nm off the surface without touching the surface. The tip does not wear out while the resolution of the collected image decreases due to the lift height of the tip. This mode also is known as nape mode. Tips coated by the ferromagnetic materials are used in this mode to map the magnetic domain configuration of the thin films which is called magnetic force microscopy (MFM).

PFM measurements are based on tracking the mechanical response of the surface upon applying an electrical voltage through the conductive tip. In fact, PFM works in capacitor geometry in which the top electrode is the conductive tip which is positively biased and bottom electrode is grounded. By applying an AC or DC electric field to the conductive tip, the tip responds to both height and piezo-response signals. These two generated signals are at two different frequencies and by using two internal lock-in amplifiers working at two different frequencies, the height and piezo-response signals is measured separately.

Magnetic force microscopy works in two successive modes, tapping and lifts modes. First, tip raster scans the surface in tapping mode to map the topography and then, the tip raster scans the same surface in the lift mode. In the lift mode, vibration frequency of the tip is altered due to the magnetic force between tip and sample. The changes in the phase of the tip in lifting mode provide a map of the magnetic domain configuration of the surface.

2.3. Transmission electron microscope

Transmission electron microscope (TEM) was used for studying the morphology of the nanostructures and their crystal structure. TEM is one the most powerful tools to image the nanostructure materials down to atomic resolution to correlate their chemical and physical properties. A fine electron beam is focused on a thin enough sample allowing the electrons to pass through. An enlarged image of the nanostructures is recorded on a fluorescent screen. The smaller the diameter of focused beam results in higher resolution of the obtained image. The spot size and convergence of the electron beam are tuned using condenser lenses and condenser apertures. Depending on the detection the transmitted electrons and scattered electrons, bright filed and dark field images are recorded. In this thesis, microstructural studies of the nanostructures were performed by a transmission electron microscopy (TEM) with a JEOL 3010 microscope with an accelerating voltage of 300 kV.

2.4. Scanning Electron Microscope

Scanning electron microscope (SEM) was used to study the morphology and chemical composition of fabricated nanostructures in this thesis. In SEM, a fine beam of high energy electrons is produced by an electron gun. The electron beam is controlled by condenser lenses and condenser apertures. The electron beam passes through the scanning coil located in objective lens that deflect the beam to raster scan the surface over rectangle areas. When the election beam incidents the surface, the electrons are scattered by inelastically by atoms. Electrons will diffuse to the bulk volume of the sample in a teardrop –shape. The length of this interaction volume varies from 100 to 5000 nm depending on the energy of the electron beam and properties of the material. Due to inelastic interaction of the electrons with atoms, emissions of secondary electrons, back scattered electrons, Auger electrons and characteristic X-ray occur. The emitted electrons are detected for SEM imaging and characteristic X-ray is used for chemical elemental analysis. In this research, secondary electrons and energy dispersive X-ray were used for SEM

imaging and elemental analysis respectively by using a LEO 1530VP field emission scanning electron microscope (FE-SEM) operating in low vacuum mode at an accelerating voltage of 200 kV and equipped with an energy dispersive (EDS) detector.

2.5. Inductively Couple Plasma spectrometer

Chemical composition of fabricated nanostructure was determined by inductive coupled plasma (ICP) spectroscopy, model Varian FT220S flame absorption spectrometer. In ICP, plasma is produced by ionization of a noble gas (Argon) as the source of energy. The temperature of the produced plasma is about 5500 to 8000°K. These temperatures are high enough to ionize and excite the elements. Excited electrons decay to the ground state and light is emitted and detected. As excited ion emits a characteristic light of certain wavelength, a line spectrum of the emitted light of different excited ions is produced. The spectrum is used to quantitatively determine the elements of the sample.

2.6. Raman Spectroscopy

Raman spectroscopy is a technique to study vibrational, rotational and low frequency modes of the matter. Raman spectroscopy is based on the inelastic scattering of the monochromatic light with the phonons of the crystalline lattice. Energy of the scattered light shift up or down which provides information about the vibrational modes in the system. Room-temperature Raman scattering studies were performed on both thin films and powdered samples with a Thermo-Fisher DXR dispersive Raman spectrometer in a conventional backward geometry. A 532-nm line of a laser with a spectral resolution of 3 cm_1 was used as the excitation source. The output power of the laser source was 6 mW to avoid the film restructuring and/or damage resulting from the overheating created by the laser source. The scattered light was analyzed with a triple monochromator coupled with an optical microscope, which allows the incident light to be focused on the sample as a circular spot of about 2 μm in diameter.

2.7. Vibrating Sample Magnetometer

Room temperature magnetic hysteresis loops of the thin films were measured by vibrating sample magnetometer (VSM). The sample is placed between the poles of an electromagnet with a uniform magnetic field. The sample experiences a mechanical vibration which induces a change in the magnetic flux. The magnetic flux change induces a voltage in the pickup coils. After carefully calibration of the VSM with standard sample, the magnetic moment

of the sample is measured. The amount of the electrical signal in the picked up coil is proportional to the frequency and amplitude of the vibration of the sample, and the magnetic moment of the sample at the applied magnetic field. The frequency and amplitude of the vibration of the sample is maintained constant by the reference capacitor. After carefully calibration of the VSM with standard sample, the magnetic moment of the sample is measured. A VSM from Princeton Measurement Corporation model 3900 was employed to collect the room temperature magnetic hysteresis loops of the thin films by applying a maximum magnetic field of 2 T in both geometries of in-plane and out-plane in respect to the plane of the film.

2.8. Superconducting Quantum Interference Device

Temperature dependent measurements of the magnetization and magnetic hysteresis loops of the magnetic nanostructures were performed by a Superconducting quantum interface device (SQUID), model Quantum Design MPMS-7XL, in the range from 5 to 300K by applying a static magnetic field up to 6T. Working principle of the SQUID is based on the superconducting loops containing Josephson junctions to detect the magnetization of the sample.

3. Highly Ordered Transition Metal Ferrite Nanotube Arrays Synthesized by Template-Assisted Liquid Phase Deposition

3.1. Introduction

Nanotubular architectures of metal oxides have attracted a growing interest due to their unique size and shape-dependent properties which find potential applications in highly efficient selective catalysis[1-3], chemical and biological sensing[4-6], photonics[7], pollutants decomposition [8-9], generation of hydrogen fuel[10-11], energy conversion and storage[12-14] and biotechnology[15-16]. In particular, one-dimensional magnetic nanostructures are very promising for the design of ultrahigh density magnetic storage media since they exhibit a structural anisotropy resulting from the nanoscale confinement in two-dimensions[17]. With the increasing trend towards miniaturization in computing and data storage, the natural tendency to achieve high areal densities in magnetic storage media consists of reducing the bit size and increasing the number of magnetic grains. However, down scaling the individual magnetic grains is limited by the disappearance of the magnetic order in 0-D magnetic structures below a critical size. This phenomenon, known as the superparamagnetic limit is the result of the thermal fluctuations which become comparable to the energy associated with the magnetic phase transition as the size of the nanoparticles is decreased below a threshold value characteristic to each magnetic material[18-19]. This thermally activated magnetization reversal can be alleviated by replacing the 0-D nanostructures (nanodots and spherical nanoparticles) with regular arrays of 1-D nanostructures (nanowires, nanotubes, nanorods or nanobelts) which are magnetic due to their enhanced magnetic anisotropy, thereby extending the storage densities beyond the superparamagnetic limit.

Among the metal oxides, spinel ferrites MFe_2O_4 have a particular technological relevance due to their relatively easy and low cost synthesis, high chemical stability and mechanical hardness coupled with the wide range of tunable magnetic properties by simply changing the ratio and the chemical identity of the metal ions[20-24]. In addition, nanotubular iron oxide nanostructures are biocompatible, have porosity and can float in fluids along with large, distinct inner and outer surfaces which enable the capture, concentration and encapsulation of different chemical and biological species being attractive as magnetic vectors in cell targeting and drug delivery [15,25-27], molecular and bio-separation[28-29] and contrast agents in magnetic resonance imaging. Despite their unique physical and morphological properties and the wide range of

potential technological applications, the synthesis of high quality transition metal ferrite nanotubular structures still remains a sparsely investigated area. Spinel ferrite nanotubes are conventionally prepared by template-assisted methods in which hollow 1-D structures are formed in the space confined within the pores of a template by electrodeposition of the metals followed by oxidation[30-31], sol-gel[32-33], thermal decomposition[34] or chemical vapor deposition[35]. Anodic aluminum oxide (AAO) or carbon nanotubes[36] have been used as templates and since the resulting nanotubes are usually amorphous a post-synthesis heat treatment step is needed in order to ensure the crystallization of the desired oxide. Upon the subsequent removal of the template the nanotubes can be liberated; however in most cases are not free standing, due to their high aspect ratio which reproduces the thickness and the pore diameter of the template.

A simple, environmentally benign and easily scalable method for the chemical deposition of thin film structures is the so-called liquid phase deposition (LPD). This approach is based on slow hydrolysis of supersaturated solutions of metal fluoro-complexes at low temperature whereby the fluoride ions in the inner coordination sphere of the metal are progressively replaced by OH^- ions and/or water molecules:

$$MF_n^{(n-2m)-} + mH_2O \rightleftharpoons MO_m + nF^- + 2mH^+ \quad (1)$$

$$H_3BO_3 + 4HF \rightleftharpoons BF_4^- + H_3O^+ + 2H_2O \quad (2)$$

Since the hydrolysis occurs via an equilibrium reaction, the formation of the metal oxide can be accelerated by adding a fluoride scavenger such as H_3BO_3 which captures the F^- ions forming water soluble complexes which can be easily removed from the solution. This method was initially developed for the deposition of thin films of binary oxides being extended to the preparation of nanotubes of binary oxides and core-shell nanotubular architectures such as TiO_2[37-38] and CdS@TiO_2[39]. Recently, Hsu and coworkers extended this approach to the synthesis of multicomponent oxide nanotubes, such as perovskite titanates ABO_3 (A=Ba, and Pb)[40-41], whereas our research group developed a LPD-based synthetic methodology for the fabrication of highly uniform transition metal ferrite films[42-43], as well as magnetoelectric bilayered structures, respectively[44].

In this work we describe the first synthesis of transition metal ferrite $M_xFe_{3-x}O4$ (M=Co, Ni, Zn) tubular nanostructures with controlled diameter and wall thickness by using a template-assisted liquid phase deposition (LPD) method. The ferrite nanotubes were obtained under nearly

ambient conditions using anodic aluminum oxide (AAO) membranes with a pore of 200 nm as templates. These nanotubes can, be used as templates for the design of tubular core-shell spinel-perovskite nanocomposites which can potentially exhibit an enhanced magnetoelectric effect as a result of the high interfacial coupling between the two constituent phases.

3.2. Experimental Procedure

The synthesis of spinel ferrite nanotubular structures was performed in open atmosphere by using a magnetic hotplate (IKA Works, Inc.) equipped with a temperature controller and a pH electrode. Ordered arrays of ferrite nanotubes were fabricated from treatment solutions obtained by mixing a solution containing 0.25 g FeOOH dissolved in 50 ml of a 1M $NH_4{\cdot}HF$ solution with a homogeneous 2.22 M solution of a transition metal nitrate $M(NO_3)_2$ (M=Co, Ni, Zn) and 40 ml of 0.5 M boric acid solution used as a fluoride scavenger[42]. The treatment solutions were prepared by dissolving reagent grade purity chemicals (Alfa Aesar) in deionized water (18 MΩ) obtained from a Barnstead Nanopure water purification system. These initial solutions were clear and retained the color of the transition metal nitrate salt without the formation of precipitates at room temperature. Prior to each experiment, Whatman Anodisc anodized aluminum oxide (AAO) templates with a thickness of 60 μm and a pore diameter of 200 nm were immersed vertically in the solution and maintained at 45°C for different time periods. During deposition the color of the AAO templates changed progressively from white to color to brown. At the end of the deposition process the templates were removed from the solution, rinsed carefully with deionized water and dried at room temperature for 3 hours. Samples were subsequently annealed at temperatures 750 °C for 6 hours to promote the dehydroxylation and dehydration reactions and yield the corresponding crystalline spinel ferrite nanotubes. After the formation of the metal oxide nanotubes, the superficial metal oxide layer formed templates each side of the template was mechanically polished followed by the removal of the membrane upon immersion in a 6 M sodium hydroxide solution for 30 min, followed by washing and centrifugation in water. The resulting spinel ferrite nanotube powders were dried under vacuum for 8 h at room temperature then stored and subjected to structural characterization and the measurement of the magnetic properties.

3.3. Characterization of the Spinel Ferrite Nanotube Arrays

The identification of the crystalline phases was performed by X-ray diffraction using a Philips X'Pert system equipped with a curved graphite single-crystal monochromator (CuKα radiation; λ=0.1541778 nm at 40 mA and 40 kV). Chemical composition of fabricated nanotubes was determined by inductive coupled plasma (ICP) spectroscopy, model Varian FT220S flame absorption spectrometer. Field-emission scanning electron microscopy experiments (FE-SEM) were performed with a LEO 1530VP instrument with an accelerating voltage of 200 kV for the study of the structure, surface topology and the morphological characteristics of metal oxide nanotubes. Temperature dependent measurements of the magnetization of the nanotubes immobilized within the pores of the AAO templates was performed with a superconducting quantum interference device (SQUID), model Quantum Design MPMS-7XL, in the range from 5 to 300 K by applying a static magnetic field up to 6 Tesla.

3.4. Results and Discussion

3.4.1. Mechanism of formation of the Spinel Ferrite Nanotubular Structures

Similar to the methodology that we developed previously for the deposition of mirror-like ferrite thin films[42-43], nanotubular structures were synthesized method at temperatures as low as 45 ^{o}C. The pH of the initial solutions ranged between 4.8 and 5.5 and progressively decreased to values between 3.9 and 4.4 at the end of the deposition process. It is worth mentioning that the formation of spinel ferrite nanotubes by the proposed template-assisted route occurs much faster than that conventional liquid phase deposition of thin film structures. Specifically, during the deposition of thin film structures turbidity is observed in the treatment solution maintained at 45 ^{o}C only after 3.5-4 h and the deposition of the films is complete after 1-2 more additional hours after the solution turned cloudy. Unlike the thin film structures, under similar conditions a change in color of the AAO template is observed after 15-30 min after its immersion in the treatment solution indicating the formation of spinel ferrite nanotubes which can increase the thickness of their walls while maintained in solution up to 4-5 h, eventually leading to the formation of nanowires, depending on the concentration of the metal precursors in solution. Generally, the deposition of metal oxide nanostructures by the LPD method is considered to take place by a two-step mechanism. While in the first step the metal fluoro-complexes formed in solution undergo a slow hydrolysis process generating metal oxides, hydroxides and

oxyhydroxides, in the second step these intermediates are heat-treated at temperatures typically above 450 ^{o}C thereby yielding the desired metal oxide nanostructures.

Chen and coworkers suggested that during the deposition of perovskite-type $ATiO_3$ nanotubes (A=Ba, Sr) by a template-assisted LPD route the metal clusters, which are negatively charged attach onto the walls of the positively charged pores of the alumina template[40]. This assumption was based on the value of the isoelectric point of alumina, according to which the surface of alumina has no electrical charges at pH values between 8 and 9 whereas in acidic solutions, which are conventionally used in the deposition of metal oxides by the liquid phase deposition method[45-47] the alumina surface is positively charged. To confirm the validity of this hypothesis, a control experiment was performed by immersing an AAO membrane, a microscope slide and a 1 cm^2 piece of (100) silicon into a solution containing stoichiometric amounts of Fe^{3+} and Co^{2+} ions, $NH_4F{\cdot}HF$ and boric acid. The treatment solution was subsequently heated to 45 ^{o}C. After 30 min at this temperature the membrane gradually changed its color from white to light brown, whereas no deposition of thin films was noticed onto the glass and silicon substrates. As the hydrolysis reaction progressed, the color of the membrane darkened and the formation of a thin film structure was noticed on the planar substrates. These observations confirm that the fast deposition of the spinel ferrite nanotubular structures in the presence of AAO templates is the result of the electrostatic attractions between the positive charges induced on the surface of the alumina and the negatively charged complex ions generated in the treatment solution. A schematic of the deposition process is shown in Figure 3.1.

When the treatment solution penetrates the pores of the membrane, the negatively charged species from the solution are attracted by the positively charged surfaces of the membrane. As the concentration of the negative charge metal fluoro-complex within the pores of the membrane increases, they accumulate along the inner walls whereby they undergo a slow hydrolysis leading to the preferential growth of metal oxide/hydroxide or oxyhydroxide species along the pore wall, thereby producing nanotubular structures.

3.4.2. Structural and Morphological Characteristics of the Transition Metal Ferrite Nanotubes

The room temperature crystal structure of the transition metal ferrite nanotubes was investigated by powder X-ray diffraction (PXRD). As seen in Figure 3.2, the ferrite nanotubes obtained after the heat treatment at 750 ^{o}C are crystalline and free of impurities phases such as Fe_2O_3 or MO (M=Co, Ni, Zn) oxides. All the reflection peaks in the XRD pattern of the ferrite

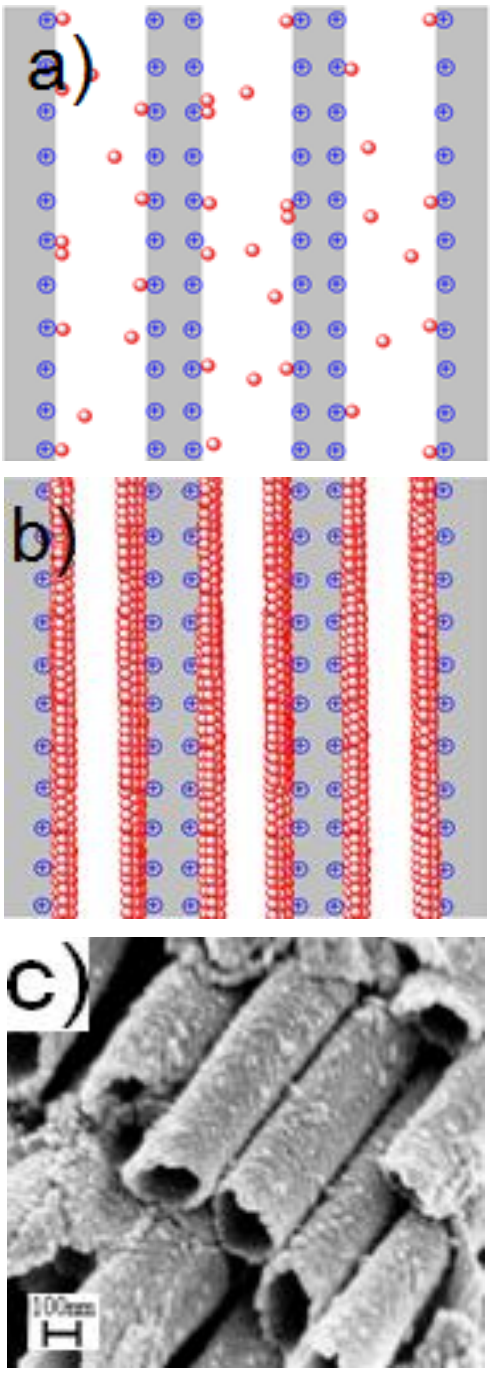

Figure 3.1. Schematic of the mechanism of formation of spinel ferrite nanotubular architectures by the attachment and immobilization of the negatively charged metal clusters onto the inner walls of the positively charged AAO membranes (a-b); c) a typical FE-SEM image of nanoparticulate nanotubes

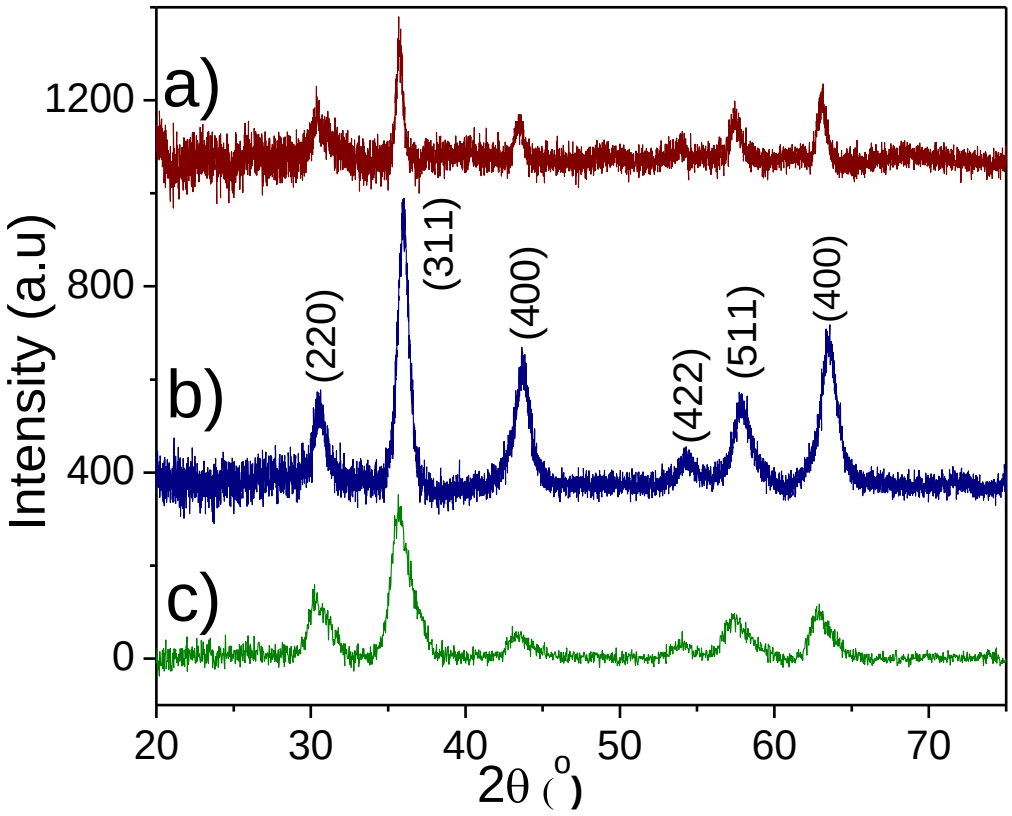

Figure 3.2. XRD patterns of Co (a); Ni (b) and Zn (c) ferrite nanotubes annealed at 750 ^{o}C for 6 h

nanotubes can be readily indexed into a cubic unit cell (space group Fd3m) and the refined lattice constants of 8.33(1) Å, 8.274(2) Å and 8.32(7) Å for the Co-ferrite, nickel ferrite and the Zn-ferrite, respectively.

The intensity of the reflections of the nanotube powdered samples is lower than that corresponding to the bulk phase whereas the peaks are broadened due to the small size of the crystalline domains diffracting coherently the X-Ray radiation. For the cobalt ferrite nanotubes samples the average grain size calculated by using the Scherer's formula[48] was 11 nm for the nanotubes obtained after 1 h and increased to 17 and 24 nm for ferrite nanotubes obtained after 2 h and 4 h, respectively. The apparent asymmetry and broadening of the peaks in the XRD pattern of the zinc ferrite nanotubes is presumably due to the lower crystallinity of the sample associated with a smaller size of the crystallites as compared to those of the other ferrite nanotubes (7.8 nm) .

The composition of the ferrite nanotubes separated from the AAO membranes was determined by ICP combined with EDX analysis. The values of the M/Fe molar ratios determined by ICP analysis were 0.32/2.68; 0.66/2.34 and 1.5/1.5 for the $MFe_{3-x}O_4$ (M= Co, Ni and Zn), respectively. Although in this paper we describe the synthesis of transition metal ferrite nanotubes with the particular chemical compositions indicated above, as it has been documented in the case of ferrite films obtained by the LPD method, the composition of the nanostructured spinel ferrites can be varied in a wide range by simply adjusting the molar ratio between the metal and the Fe^{3+} in the treatment solution, which also allows for a fine control of their magnetic properties[42]. The FE-SEM micrographs of the ferrite nanotubular architectures after the heat treatment at 750 ^{o}C are presented in Figures 3(a)-(i). Except for Figure 3(h), which shows Zn-ferrite nanotubes immobilized within the pores of the AAO membrane, all the other figures show free standing ferrite nanotubes obtained after the removal of the AAO templates in a 6 M NaOH solution followed by the washing and drying of the nanopowders. Prior to the removal of the membranes, their surfaces were cleaned by mechanical polishing in order to eliminate the superficial metal oxide layer formed during the deposition. All nanotubes are open-ended; they have smooth and uniform surfaces and free of defects, such as cracks or holes. The observed filling rate is 100% indicating that the ferrite nanotubular structures form via a homogeneous growth mechanism. The length of the nanotubes is 60 μm whereas the average outer diameter is

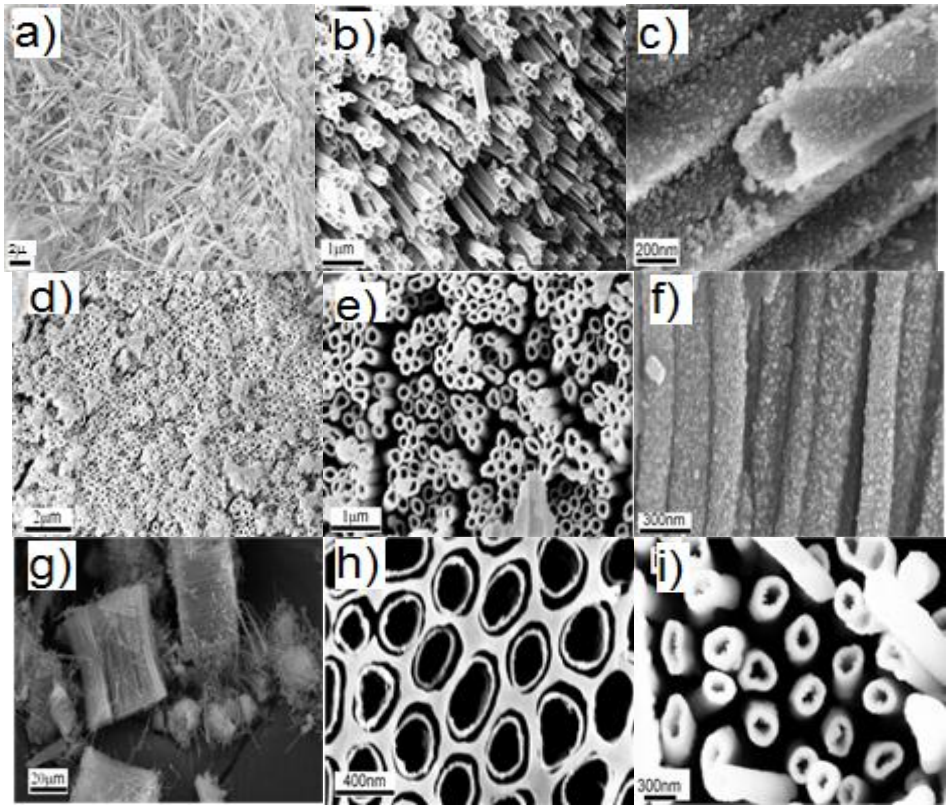

Figure 3.3 Top and side view FE-SEM micrographs of Co-ferrite (a-c); Ni-ferrite (d-f) and Zn-ferrite (g)-(i) nanotubes with a diameter of 200 nm

200 nm, values which are comparable to the physical dimensions of the AAO templates. One of the main advantages of the LPD method as compared by the other chemical methods used in the template-assisted synthesis of ferrite tubular nanostructures is that the hydrolysis reactions are performed in solutions with a pH typically higher than 3.5 which prevents the etching of the AAO templates or increase the pore sizes as it was reported previously in the case of other template-assisted solution-mediated methods for the synthesis of tubular nanostructures[39]. The FE-SEM micrographs also reveal the influence of the sonication process on the orientation of the nanotubes: while the Co-ferrite nanotubes obtained by sonicating the sample during the removal of the AAO template are oriented in random directions (Figure 3.3a), in the case when no sonication was used to remove the template highly aligned nanotube arrays were obtained.

In Figure 3.4 is presented the mass loss profile of a sample collected by scratching the film formed after the deposition of the $Co_{0.32}Fe_{2.68}O_4$ nanotubes and then subjected to a thermal treatment in the temperature range from 25 to 700 ^oC under flowing N_2. The TGA curve exhibits a very well defined decrease in the mass of the sample with two inflection points. While the first inflection point appears at 88 ^oC and corresponds to the elimination of the hydrated water molecules (~ 17.08 % mass loss), the second appears at 241 ^oC and is associated with the elimination of lattice water molecules in tandem with dehydroxylation and condensation reactions of the metal hydroxydes and oxyhydroxides (~30.16 % mass loss) eventually yielding the corresponding spinel ferrite. These thermal events are also observed in the DSC curve which exhibits five well defined endothermic peaks at 43, 68, 189, 272 and 692 ^oC which are indicative of the transition from the metal hydroxide precursors to the spinel ferrite structure. In general, in conventional template-assisted sol-gel approaches metal oxide nanotubes form by the wetting the inner pores of the template with a sol and its subsequent subsequently conversion into a gel followed by a heat treatment at high temperature which makes virtually impossible the variation of the wall thickness of the nanotubes[49-52].

Unlike the sol-gel routes, in the liquid phase deposition method metal oxides with different dimensionality (1-D or 2-D) form by the attachment of fine particles initially formed in solution[42]. Based on the foregoing arguments, it is reasonable to assume that nanotubes initially form near the inner walls of the template and then extend towards the inner volume of the nanopores by the attachment of fine particles initially precipitated in solution[44]. Therefore, when the deposition is performed at a particular temperature, the wall thickness of the metal oxide

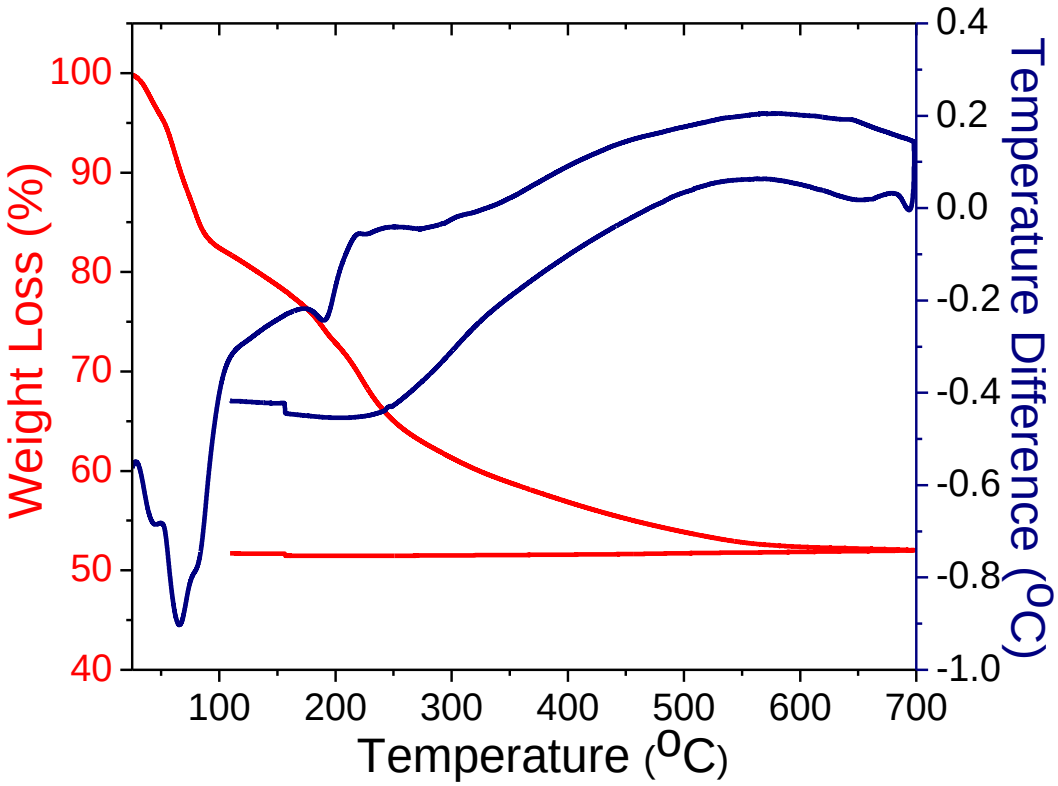

Figure 3.4. TGA and DSC profiles of as-prepared powder obtained during the synthesis of the $Co_{0.32}Fe_{2.68}O_4$

nanotubes can be controlled by varying the deposition time. In Figures 3.5(a)-(c) are presented the TEM images of the individual $Co_{0.32}Fe_{2.68}O_4$ nanotubes with a diameter of 200 nm obtained by soaking the AAO membranes into the treatment solution for different periods of time; that is 1, 2 and 4 hours, respectively. Examination of the TEM micrographs of the Co-ferrite nanotubes presented in Figures 5(a)-(c) clearly shows that the wall thickness increases from 10 to 16 and 21 nm with increasing the deposition time from 1 to 2 and 4 h, respectively. Moreover, the ferrite nanotubes are uniform being composed by small, spheroidal particles with an average diameter of 4-5 nm; they possess a straight shape without holes or other defects which are oftentimes observed in oxide nanotubes obtained by sol-gel approaches which form as a result of the so-called Raleigh instabilities [52].

Figure 3.5(d) represents the SAED image of the individual nanotube presented in Figure 5(c) which exhibits a series of strong, concentric rings with a spotted appearance, which overlap perfectly the diffraction peaks in the XRD pattern thereby substantiating that the individual ferrite nanotubes are highly crystalline. The zone axis for the SAED image is the {001} crystalline direction. The high crystallinity of the nanotubes was also proved by the HRTEM analysis which suggests that the ferrite nanotubes obtained by this method are smooth and dense. The lattice fringes appearing in Figure 3.5(e) correspond to an interplanar distance of 2.93 Å, ascribed to the (222) family of planes of the $CoFe_2O_4$ structure (Figure 3.5 (e)).

3.4.3. Magnetic Properties of Transition Metal Ferrite Nanotubes

In Figures 3.6(a)-(b) are shown the hysteresis loops of the $Zn_{1.5}Fe_{1.5}O_4$ nanotube arrays measured at room temperature with the magnetic field applied parallel and perpendicular to the long axis of the nanotubes.

The $Zn_{1.5}Fe_{1.5}O_4$ nanotube arrays are saturated at H= 4 kOe and present coercivity and squarness ($SQ=M_r/M_s$) values which vary from $H_{c\parallel}$=51 Oe and $SQ_\parallel$=0.047 to $H_{c\perp}$=56 Oe and $SQ_\perp$=0.051 by changing the orientation with respect to the magnetic field. The absence of a noticeable difference in the coercivity values of the sample when its orientation changes from parallel to perpendicular to the magnetic field suggests that the Zn-ferrite nanotubes do not present perpendicular anisotropy and the shape anisotropy contribution is not significant to the total anisotropy of the samples. This may be due to the polycrystalline nature of the nanotubes as well as the small size and random orientation of the constituting grains. This will lead to an irregular

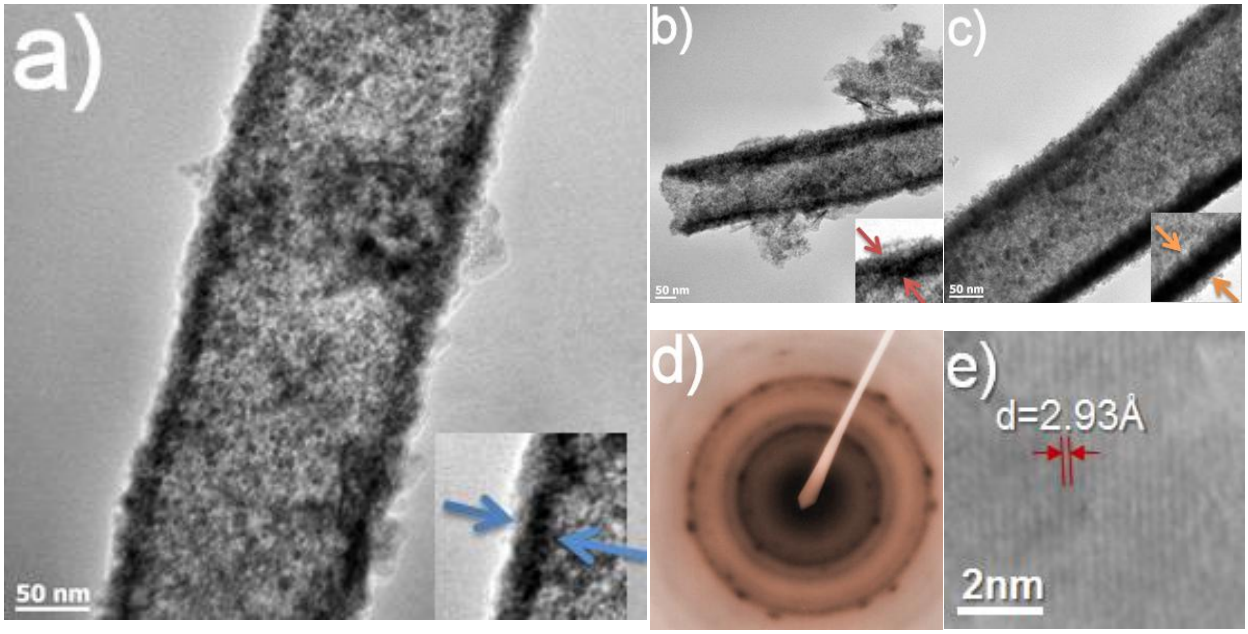

Figure 3.5. TEM images of $Co_{0.32}Fe_{2.68}O_4$ nanotubes with different wall thicknesses fabricated via LPD by maintaining the template in the treatment solution for 1h (a); 2 h (b) and 4 h (c), respectively. (d) and (e) SAED and HRTEM patterns of a single nanotube

distribution of the magnetic spins and was experimentally observed in the case of other ferrite nanotubular structures obtained by solution-based routes such as γ-Fe_2O_3[33,53-54], Co-ferrite[33] or Ni-ferrite nanotubes[54], respectively. To gain a better insight into the magnetic properties of the Zn-ferrite nanotubes the magnetization of the sample was measured as a function of the temperature in both zero-field-cooling (ZFC) and field-cooling (FC) modes. During these measurements a magnetic field of H=100 Oe was applied parallel to the long axis of the nanotube arrays and the magnetization of the sample was measured in the temperature range from 5 to 300 K.

As seen in Figure 3.6(d), Zn-ferrite nanotubes are superparamagnetic at room temperature and present a maximum in the ZFC curve at T=97 K, which corresponds to the blocking temperature T_B. When the sample reaches this temperature the magnetic energy of the Zn-ferrite nanotubes becomes equal to the thermal energy and the orientation of the magnetic spins is randomized by the thermal disorder. This behavior was furthermore confirmed by the measurement of the hysteresis loops at 5 K (Figure 3.6(c)), which clearly indicate a ferrimagnetic behavior of the $Zn_{1.5}Fe_{1.5}O_4$ nanotubes with values of the coercivity of $Hc_{\parallel}$= 1.36 kOe and $Hc_{\perp}$=1.17 kOe, whereas the remanent squarness was $SQ_{\parallel}$=0.29 and $SQ_{\perp}$=0.26, respectively. These results are in agreement with those obtained in the case of spinel ferrite thin film structures obtained by liquid phase deposition which are also constructed by small particles and present a blocking temperature of 108 K[42-44]. Similar to the Zn-ferrite nanotube arrays, the Ni-ferrite nanotubes are superparamagnetic at room temperature, with a blocking temperature of 256 K (ZFC/FC data not shown). The hysteresis loops of the $Ni_{0.66}Fe_{2.34}O_4$ nanotubes measured at room temperature and 5 K with the magnetic field applied parallel to the long axis of the nanotubes are presented in Figures 3.7 (a) and (b). The values of the coercivity and squarness increased from $Hc_{\parallel}$= 73 Oe and $SQ_{\parallel}$=0.065 at 300 K to $Hc_{\parallel}$= 1520 Oe and $SQ_{\parallel}$=0.38 at 5 K, indicating that the $Ni_{0.66}Fe_{2.34}O_4$ nanotubular structures present a magnetic behavior similar to that observed in the case of the Zn-ferrite nanotubes.

In Figure 3.8 are shown the magnetization curves of the $Co_{0.32}Fe_{2.68}O_4$ nanotubes with different wall thicknesses deposited by LPD at 45 ^oC. After the synthesis, the ferrite nanotubes were subjected to a heat treatment at 750 ^oC for 6 h under a static atmosphere and the measurement of the magnetic properties was performed with non-interacting nanotubes confined within the channels of the AAO membrane. As seen in Figures 3.8 and 3.9, a high magnetic field

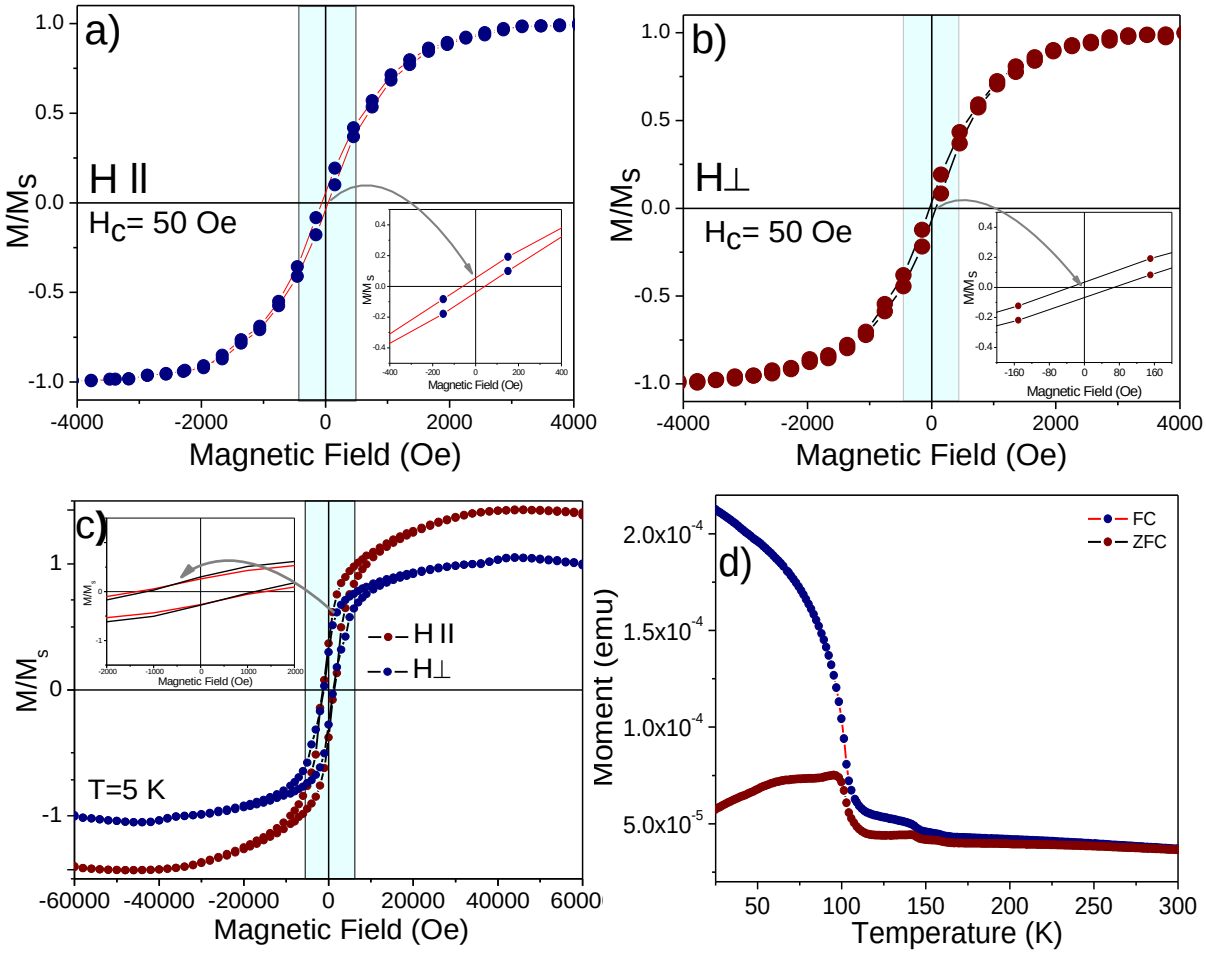

Figure 3.6. Representative room temperature hysteresis loops (a-c) and magnetization vs. temperature curves for $Zn_{1.5}Fe_{1.5}O_4$ nanotubes (d) with a diameter of 200 nm immobilized within the pores of the AAO membrane. The insets represent an enlarged view of the M vs. H curves in the low field region

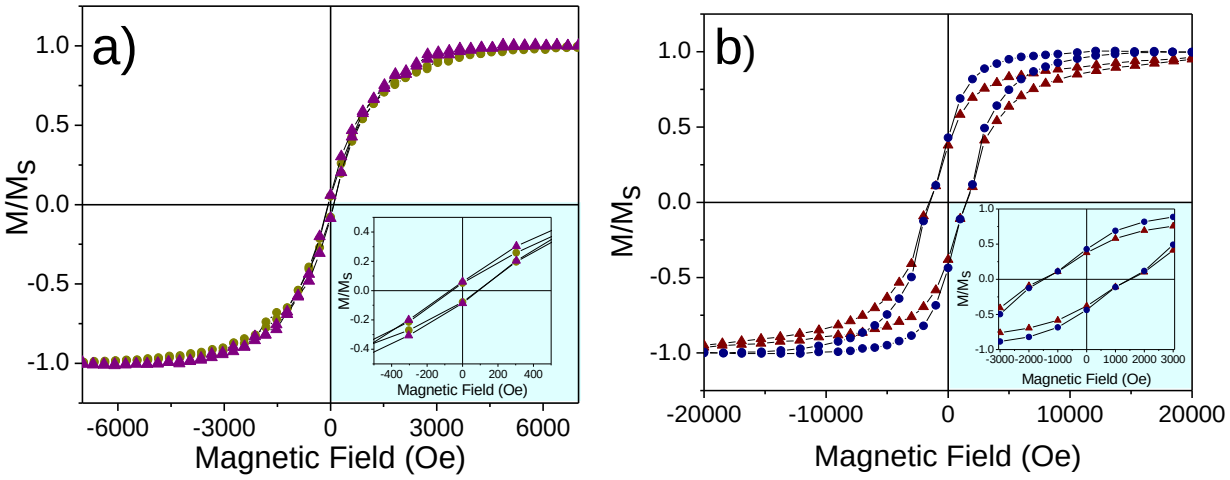

Figure 3.7. M. vs. H curves at 300 K (a) and 5 K (b) of the $Ni_{0.66}Fe_{2.34}O_4$ nanotubes. Insets represent close-ups of the hysteresis loops to indicate their coercivity. The insets represent an enlarged view of the M vs. H curves in the low field region

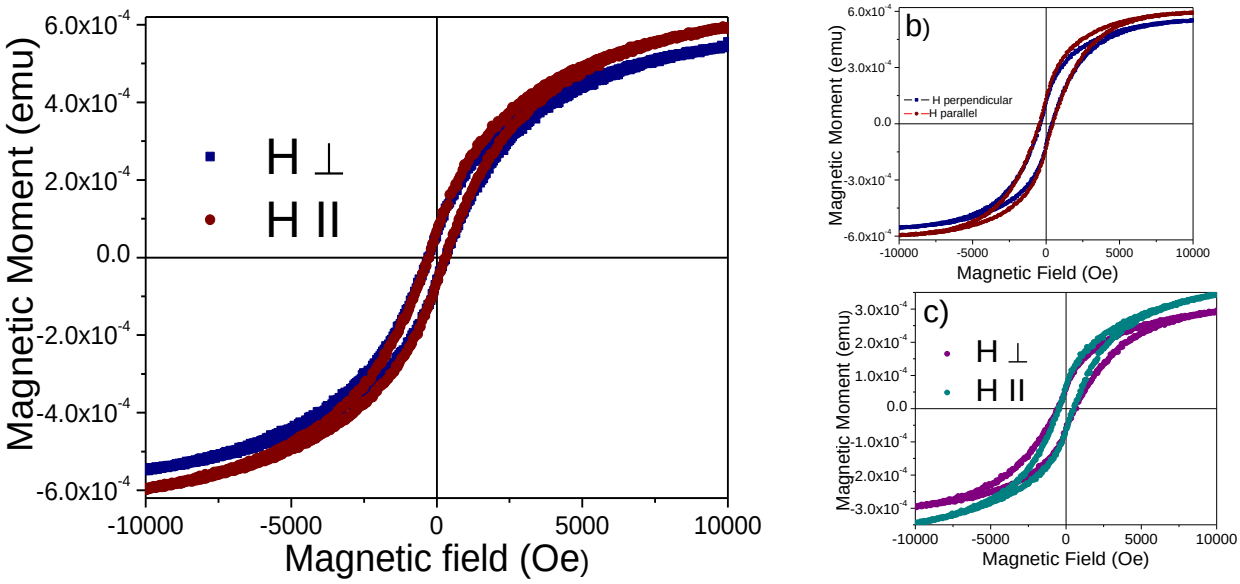

Figure 3.8. Room temperature hysteresis loops of the $Co_{0.32}Fe_{2.68}O_4$ nanotubes with different wall thicknesses (10 (a), 16 (b) and 21 nm (c), respectively. The nanotubular structures were deposited by the LPD method and heat treated at 750°C for 6 h in air.

does not saturate the magnetization of the nanotube samples; this situation is similar to that reported previously in the case of iron oxide[55] and spinel ferrite[33,54] and can be presumably ascribed to the surface disorder of the magnetic spins in these nanotubular structures. The values of the coercivity and squarness for the $Co_{0.32}Fe_{2.68}O_4$ nanotubes with different wall thickness are presented in Table 3.1. The hysteresis loops become broader with increasing the wall thickness of the Co-ferrite nanotubes which corresponds to a monotonous increase of the coercive field. The remanent squarness of the nanotubes follows a similar pattern, although its variation is not as uniform as that observed for coercivity. Moreover, the values of the remanent squarness were consistently found to be slightly higher in the parallel direction of the nanotubes as compared to those observed for a perpendicular direction, which suggests that the easy axis of the Co-ferrite nanotubes is parallel to the long axis of the nanotubes.

In order to study the influence of the annealing temperature on their magnetic properties, a second series of Co-ferrite nanotube arrays was annealed at 850 ^oC in air for 6 h. As seen in Figure 3.9, the Co-ferrite nanotubes are ferrimagnetic at room temperature and the values of the coercivity are almost three times higher than those of the samples annealed at 750 ^oC. For example, $H_{c\parallel}$= 288 Oe for the nanotubes with a wall thickness of 10 nm annealed at 750 OC increases to $H_{c\parallel}$= 958 Oe after annealing at 850 ^oC, whereas for the nanotubes with a wall thickness of 21 nm, $Hc_{\parallel}$ increased from 517 Oe to 1450 Oe, respectively. This variation of the coercive field with the annealing temperature in nanotubular structures can be ascribed to the increase of the coercivity of the individual nanoparticles constructing the nanotubes, as a result of the densification and coalescence of the individual grains which eventually lead to an increase of their average diameter.

A detailed characterization of the Co-ferrite nanotubes with different diameters and wall thickness in order to elucidate the mechanism of magnetization reversal is currently underway and will be reported in a forthcoming paper. In summary, we have developed a novel, simple and highly reliable synthetic procedure for the fabrication of transition metal ferrite nanotubular structures that combines a template-assisted route with the liquid phase deposition (LPD) method. Uniform $M_xFe_{3-x}O_4$ (M=Co, Ni, Zn) nanotube arrays with an average diameter of 200 nm were deposited within the pores of AAO templates by the controlled hydrolysis of metal fluoro-complexes at temperatures as low as 45 ^oC. A subsequent heat treatment at temperatures between 750 and 850 ^oC in air lead to the formation of the spinel structure from the

Table 3.1. The values of the coercivity and remanent squarness of the $Co_{0.32}Fe_{2.68}O_4$ nanotubes with different wall thickness obtained at 750 and 850 °C, respectively.

Wall Thickness (nm)	H_c (Oe)		$SQ=M_r/M_s$	
Annealed at 750 °C	∥	⊥	∥	⊥
10	288	308	0.11	0.09
16	388	451	0.22	0.20
21	517	615	0.19	0.20
Annealed at 850 °C				
10	958	990	0.47	0.45
16	1332	1228	0.56	0.52
21	1450	1148	0.54	0.45

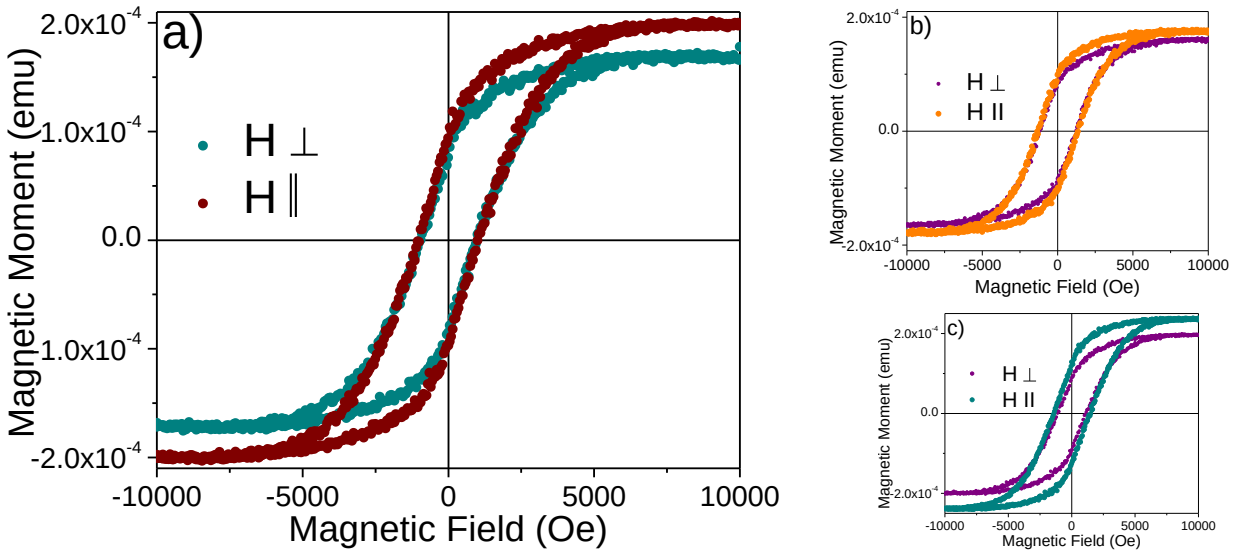

Figure 3.9. Room temperature hysteresis loops of the $Co_{0.32}Fe_{2.68}O_4$ nanotubes with different wall thicknesses (10 (a), 16 (b) and 21 nm (c), respectively). The nanotubular structures were deposited by the LPD method and heat treated at 850 °C for 6 h in air.

stoichiometric mixtures of metal hydroxide intermediates. These structures can be obtained as free-standing nanotubes by the selective dissolution of the AAO membrane template. The wall thickness of the metal oxide nanotubes can be controlled from 10 to 21 nm by varying the deposition time. Small differences in the coercivity of the ferrite nanotubes were observed when changing their orientation from parallel to perpendicular to the magnetic field, indicating that the magnetocrystalline anisotropy is dominant and the shape anisotropy and the shape anisotropy has a little influence on the magnetic anisotropy. Therefore, unlike the Ni and Zn-ferrite nanotubes, which exhibit a superparamagnetic behavior at room temperature, the Co-ferrite nanotubes are ferrimagnetic and their coercivity increases with increasing the wall thickness and the annealing temperature.

3.5. Conclusions

This new process opens up opportunities for the controlled synthesis of ferrite materials with nanotubular geometry, high surface area, controllable morphology and distinct magnetic properties which can be potentially used in different biomedical applications, as well as building blocks for the design of core–shell nanotubular architectures in magnetic data storage and energy conversion applications.

3.6. References

(1) Tian, Z. R. R.; Voigt, J. A.; Liu, J.; McKenzie, B.; McDermott, M. J.; Rodriguez, M. A.; Konishi, H.; Xu, H. F. Nature Materials **2003**, 2, 821.

(2) Kolmakov, A.; Moskovits, M. Annual Review of Materials Research **2004**, 34, 151.

(3) Bavykin, D. V.; Friedrich, J. M.; Walsh, F. C. Advanced Materials **2006**, 18, 2807.

(4) Sljukic, B.; Banks, C. E.; Compton, R. G. Nano Letters **2006**, 6, 1556.

(5) Rao, C. N. R.; Nath, M. Dalton Trans. **2003**, 1.

(6) Ding, Y. S.; Shen, X. F.; Gomez, S.; Luo, H.; Aindow, M.; Suib, S. L. Advanced Functional Materials **2006**, 16, 549.

(7) Varghese, O. K.; Paulose, M.; Grimes, C. A. Nat Nano **2009**, 4, 592.

(8) Quan, X.; Yang, S.; Ruan, X.; Zhao, H. Environmental Science & Technology **2005**, 39, 3770.

(9) Agarwal, P.; Paramasivam, I.; Shrestha, N. K.; Schmuki, P. Chemistry – An Asian Journal **2010**, 5, 66.

(10) Park, J. H.; Kim, S.; Bard, A. J. Nano Letters **2005**, 6, 24.

(11) Mor, G. K.; Shankar, K.; Paulose, M.; Varghese, O. K.; Grimes, C. A. Nano Letters **2004**, 5, 191.

(12) Zhu, K.; Neale, N. R.; Miedaner, A.; Frank, A. J. Nano Letters **2006**, 7, 69.

(13) Sauvage, F.; Di Fonzo, F.; Li Bassi, A.; Casari, C. S.; Russo, V.; Divitini, G.; Ducati, C.; Bottani, C. E.; Comte, P.; Graetzel, M. Nano Letters **2010**, 10, 2562.

(14) Zhu, K.; Vinzant, T. B.; Neale, N. R.; Frank, A. J. Nano Letters **2007**, 7, 3739.

(15) Hillebrenner, H.; Buyukserin, F.; Stewart, J. D.; Martin, C. R. Nanomedicine **2006**, 1, 39.

(16) Bjursten, L. M.; Rasmusson, L.; Oh, S.; Smith, G. C.; Brammer, K. S.; Jin, S. Journal of Biomedical Materials Research Part A **2010**, 92A, 1218.

(17) Escrig, J.; Landeros, P.; Altbir, D.; Vogel, E. E.; Vargas, P. Journal of Magnetism and Magnetic Materials **2007**, 308, 233.

(18) Weller, D.; Moser, A. Ieee Transactions on Magnetics **1999**, 35, 4423.

(19) Thompson, D. A.; Best, J. S. Ibm Journal of Research and Development **2000**, 44, 311.

(20) Sun, S.; Zeng, H.; Robinson, D. B.; Raoux, S.; Rice, P. M.; Wang, S. X.; Li, G. Journal of the American Chemical Society **2003**, 126, 273.

(21) Adireddy, S.; Lin, C. K.; Palshin, V.; Dong, Y. M.; Cole, R.; Caruntu, G. Journal of Physical Chemistry C **2009**, 113, 20800.

(22) Caruntu, D.; Remond, Y.; Chou, N. H.; Jun, M. J.; Caruntu, G.; He, J. B.; Goloverda, G.; O'Connor, C.; Kolesnichenko, V. Inorganic Chemistry **2002**, 41, 6137.

(23) Deng, H.; Li, X.; Peng, Q.; Wang, X.; Chen, J.; Li, Y. Angewandte Chemie International Edition **2005**, 44, 2782.

(24) Chong, Y. T.; Yau, E. M. Y.; Nielsch, K.; Bachmann, J. Chemistry of Materials **2010**, 22, 6506.

(25) Martin, C. R.; Kohli, P. Nat Rev Drug Discov **2003**, 2, 29.

(26) Hillebrenner, H.; Buyukserin, F.; Stewart, J. D.; Martin, C. R. Journal of Nanoscience and Nanotechnology **2007**, 7, 2211.

(27) Son, S. J.; Reichel, J.; He, B.; Schuchman, M.; Lee, S. B. Journal of the American Chemical Society **2005**, 127, 7316.

(28) Lee, S. B.; Mitchell, D. T.; Trofin, L.; Nevanen, T. K.; Soderlund, H.; Martin, C. R. Science **2002**, 296, 2198.

(29) Lee, M.; Kim, T.; Bae, C.; Shin, H.; Kim, J. JOM Journal of the Minerals, Metals and Materials Society **2010**, 62, 44.

(30) Hua, Z. H.; Chen, R. S.; Li, C. L.; Yang, S. G.; Lu, M.; Gu, B. X.; Du, Y. W. Journal of Alloys and Compounds **2007**, 427, 199.

(31) Gao, D. Q.; Shi, Z. H.; Xu, Y.; Zhang, J.; Yang, G. J.; Zhang, J. L.; Wang, X. H.; Xue, D. S. Nanoscale Research Letters **2010**, 5, 1289.

(32) Xu, Y.; Wei, H.; Yao, J.; Fu, J.; Xue, D. Materials Letters **2008**, 62, 1403.

(33) Ji, G. B.; Su, H. L.; Tang, S. L.; Du, Y. W.; Xu, B. L. Chemistry Letters **2005**, 34, 86.

(34) Liu, S.; Yue, B.; Jiao, K.; Zhou, Y.; He, H. Materials Letters **2006**, 60, 154.

(35) Kohli, S.; McCurdy, P. R.; Johnson, D. C.; Das, J.; Prieto, A. L.; Rithner, C. D.; Fisher, E. R. The Journal of Physical Chemistry C **2010**, null.

(36) Pham-Huu, C.; Keller, N.; Estournes, C.; Ehret, G.; Greneche, J. M.; Ledoux, M. J. Physical Chemistry Chemical Physics **2003**, 5, 3716.

(37) Wang, J.; Cui, Y.; Li, H.; Wang, Z.; Huang, K.; Sun, G. Research on Chemical Intermediates **2010**, 36, 17.

(38) Zhang, Y.; Chen, J.; Li, X. Catalysis Letters **2010**, 139, 129.

(39) Hsu, M. C.; Leu, I. C.; Sun, Y. M.; Hon, M. H. Journal of Crystal Growth **2005**, 285, 642.

(40) Chen, Y.-Y.; Yu, B.-Y.; Wang, J.-H.; Cochran, R. E.; Shyue, J.-J. Inorganic Chemistry **2008**, 48, 681.

(41) Hsu, M. C.; Sun, Y. M.; Leu, I. C.; Hon, M. H. Journal of the Electrochemical Society **2006**, 153, F260.

(42) Caruntu, G.; Bush, G. G.; O'Connor, C. J. Journal of Materials Chemistry **2004**, 14, 2753.

(43) Caruntu, G.; Newell, A.; Caruntu, D.; O'Connor, C. J. Journal of Alloys and Compounds **2007**, 434, 637.

(44) Yourdkhani, A.; Perez, A. K.; Lin, C.; Caruntu, G. Chemistry of Materials **2010**, 22, 6075.

(45) Lewis, J. A. Journal of the American Ceramic Society **2000**, 83, 2341.

(46) Yang, D.; Krasowska, M.; Sedev, R.; Ralston, J. Physical Chemistry Chemical Physics **2010**, 12, 13724.

(47) Pettersson, A.; Marino, G.; Pursiheimo, A.; Rosenholm, J. B. Journal of Colloid and Interface Science **2000**, 228, 73.

(48) Patterson, A. L. Physical Review **1939**, 56, 978.

(49) Cheng, F.; Tao, Z.; Liang, J.; Chen, J. Chemistry of Materials **2008**, 20, 667.

(50) Hernandez, B. A.; Chang, K. S.; Fisher, E. R.; Dorhout, P. K. Chemistry of Materials **2002**, 14, 480.

(51) Kim, J.; Yang, S. A.; Choi, Y. C.; Han, J. K.; Jeong, K. O.; Yun, Y. J.; Kim, D. J.; Yang, S. M.; Yoon, D.; Cheong, H.; Chang, K. S.; Noh, T. W.; Bu, S. D. Nano Letters **2008**, 8, 1813.

(52) Kuang, Q.; Lin, Z. W.; Lian, W.; Jiang, Z. Y.; Xie, Z. X.; Huang, R. B.; Zheng, L. S. Journal of Solid State Chemistry **2007**, 180, 1236.

(53) Wang, J. H.; Ma, Y. W.; Watanabe, K. Chemistry of Materials **2008**, 20, 20.

(54) Li, F. S.; Song, L. J.; Zhou, D.; Wang, T.; Wang, Y.; Wang, H. B. Journal of Materials Science **2007**, 42, 7214.

(55) Wang, T.; Wang, Y.; Li, F. S.; Xu, C. T.; Zhou, D. Journal of Physics-Condensed Matter **2006**, 18, 10545.

4. Synthesis and Characterization of One Dimensional Ferroic Nanostructures by Liquid Phase Deposition

4.1. Introduction

The coexistence of at least two ferromagnetic, ferroelectric and ferroelastic material properties is a characteristic feature of an important class of advanced materials, known as magnetoelectric (ME) multiferroics. In such materials an electric current can be induced upon application of an external magnetic field (the direct ME effect) and vice-versa (the converse ME effect). In terms of the material constituents, multiferroics are generally divided into two categories: single phase and composites. Unfortunately, the ME coupling in single phase multiferroics is not as strong as that ME composites. Moreover, this generally occurs at temperatures well below the room temperature, which drastically limits the use of single phase multiferroics in practical applications. When a ME composite material is subjected to the action of a magnetic/electric field, the ferroelectric/ferromagnetic phase, which has electrostrictive/magnetostrictive properties will respond to the external stimulus by changing its physical dimensions. Such a change in the physical dimensions of one of these phases will induce a stress which is transferred to the other phase across the shared interface, eventually leading to a change of its ferroic properties. As the interphase boundary between ferroic phases plays a key role in the ME coupling, there is an increasing technological interest in designing ME nanocomposites with a high interfacial contact between the constituent magnetic and electrostrictive phases. ME hybrid nanocomposites consisting of a ferromagnetic and a ferroelectric phase can be designed generally in three different geometries: particulate nanocomposite films with magnetic particles embedded in a ferroelectric matrix (also referred to 0-3 nanocomposites), vertical heterostructures with one-phase nanopillars (1-3), horizontal heterostructures with alternating ferroelectric and magnetic layers (2-2) and one dimensional (1D) core-shell structures (nanotubes and nanocables) having the magnetic and ferroelectric materials as core and shell, respectively, (1-1)[1-3]. It has been predicted that 1D ME core-shell nanocomposites exhibit a stronger ME coupling compared to the other types of nanocomposites as a result of the higher interfacial contact area between the constituting phases and the absence of the clamping effect exerted by the substrate as commonly observed in bilayered ME nanostructures[4]. From this point of view, 1D ME core-shell nanocomposites are promising materials for the miniaturization of ME devices such as ME self-sensing cantilever actuators[5].

Several methods were proposed to fabricate 1D ME core-shell nanocomposites consisting of magnetostrictive spinel ferrites and ferroelectric perovskite titanates. These are successive sol-gel processing steps using anodic aluminum oxide (AAO) membranes to confine the magnetic oxide core within the ferroelectric oxide shell[6], electrodeposition of ferromagnetic transition metals into the free space of ferroelectric oxide nanotubes embedded in the AAO membrane[7], and electrospinnig in combination with a sol-gel method[8].

Liquid phase deposition (LPD) is a soft chemical technique based on the slow hydrolysis of metal-fluoro complex species at temperatures below 60°C. The hydrolysis occurs with an equilibrium whereby the fluoride ions from the inner coordination sphere of the metal are gradually replaced by OH^- ions and/or water molecules yielding mixtures of metal hydroxydes/oxyhydroxides. These reaction intermediates can be converted into the desired oxides upon a heat treatment at temperatures typically between 400 and 800 ^oC. LPD is simple and does not require expensive vacuum equipment. Also, these reactions can be performed at low temperatures and are environmentally friendly. Surfaces with complex spatial geometries can be coated by the LPD process, which make it attractive for the deposition of the high quality thin films of the functional ceramic oxides. In the absence of a fluorine scavenger, the hydrolysis reaction of supersaturated solutions of metal fluoro-complexes is slow at room temperature and reaches equilibrium (reaction 1). Adding boric acid to the treatment solution will induce the consumption of the fluoride ions with formation of a stable water soluble complex of $[BF_4]^-$ ion (reaction 2).

$$MF_n^{(n-2m)-} + mH_2O \rightleftharpoons 1\,MO_m + nF^- + 2mH^+ \quad (1)$$

$$H_3BO_3 + 4HF \rightleftharpoons BF_4^- + H_3O^+ + 2H_2O \quad (2)$$

LPD was proposed by Deki et al for silica thin films which subsequently was developed for other ceramic oxides such as TiO_2[9], SiO_2[10], ZrO_2[11], SnO_2[12], Fe_2O_3[13]and NiO[14]. LPD also has been extended for complex ceramic metal oxides of spinel ferrites, AFe_2O_4 (A=Co, Ni and Zn)[15-16], perovsikites such as ABO_3 (A= Ba, Sr and Pb, B=Ti and Zr)[17-18], magnetoplumbite hexagonal ferrite and bilayered of perovskite/spinel ferrites [19]. Due to the ability of the LPD technique to coat surfaces with complex spatial geometry, this method also has been extended to fabricate patterned nano-objects and 1D nanostructures. Deki et al based on replica lithography fabricated highly ordered vertically aligned iron oxide nanopillars using the LPD technique[20]. Vertically

aligned $PbTiO_3$ nanotubes on the substrates were fabricated by LPD using ZnO nanorods as the sacrificial templates. Highly ordered spinel ferrite $M_xFe_{3-x}O_4$ (M=Ni, Co, Zn)[21] and ABO_3 (A=Ba and Sr)[22] nanotube arrays were synthesized in AAO templates with the pore size of 200 nm by the LPD route combined with the template-assisted approach. As the conventional measurement set-up (for bulk ME composite) fails to determine the ME properties of the nanostructures due to the difficulties in the separation of the ME signal and noise, recently, Raman spectroscopy and scanning probe microscope (SPM) have been introduced to ME characterization of bilayered nanocomposites[23-24]. The Direct strain mediated ME effect has been demonstrated for bilayered nanocomposites by tracking the changes in the wavenumbers of the lattice dynamic vibrations corresponding to the ferroelectric phase in the presence of a magnetic field[19,25]. Unfortunately the magnetic field assisted Raman spectroscopy is not enabled for nanoscale ME characterizations of nanocomposites such as core-shell nanotubes and nanocables due to the diffraction limit of the visible light. However, piezoelectric force microscope (PFM) has been introduced as a robust tool to characterize the ferroelectric and piezoelectric materials at the nanoscale to image the ferroelectric domains and to measure the local piezoelectric properties[26-29]. Recently, a novel technique based on the PFM has been developed in our research group to evaluate the ME properties of the multiferroic nanocomposites[30]. The ability of the PFM to probe the nanoscale objects due to the nanometer size and the geometry of the conductive tip enabled us to measure the piezoelectric properties of a single 1D multiferroic nanocomposite in the presence of an in-plane *dc* magnetic field which allows us to measure the direct ME coefficient.

In this chapter, the synthesis and characterizations of the 1D ferroelectric phase and the multiferroic nanocomposites by template assisted LPD obtained at the ambient conditions will be presented. Due to the assembled nature of such structures, such a work will inherently consist of several successive steps: the synthesis of pristine spinel and ferrite nanotubular structures, filling the nanotubes of one phase with the second one, the complete characterization (local and bulk) of the ferroic phases, as well as of the study of the strain-mediated ME coupling effect in ceramic hybrid 1-D nanostructures.

4.2. Experimental Procedure

4.2.1. Synthesis of Ferroic Metal Oxide Nanotube arrays

All experiments were carried out in open atmosphere by using a magnetic hotplate (IKA Works, Inc.) while simultaneously the temperature and the pH of the solution were monitored.

LPD treatment solutions were prepared by dissolving the chemicals with high purity in deionized water (DI-water) (18 MΩ). Commercial anodized aluminum oxide (AAO) templates with 200 nm pore diameter and 60 μm thickness (Whatman) were immersed vertically in the treatment solution to grow the nanotube arrays of ferroic oxides for different time intervals. At the end of the deposition process the templates were removed from the solution, rinsed carefully with deionized water (DI-water) and dried at room temperature for 3 hours. As as-synthesized nanotubes are amorphous and subsequent heat treatment is required around 750°C to ensure the crystallization of the nanotubes. After the formation of the metal oxide nanotubes, the deposited superficial films on the sides of the AAO template were removed by mechanical polishing to expose the confined nanotubes inside the AAO templates. Nanotubes were characterized depending on the characterization techniques either free standing or confined inside the AAO templates. Free standing nanotubes were released by dissolving the AAO template in the 6 M sodium hydroxide solution for 30 min to release the nanotubes, followed by washing and centrifuging. Free standing nanotubes were collected and dried at 100°C for 6 hours then stored and subjected to different structural and physical characterizations.

4.2.2. Synthesis of ferroelectric perovskite nanotube arrays

Three different aqueous solutions of $(NH_4)_2TiF_6$ (0.025M), H_3BO_3 (0.075M) and $Ba(NO_3)_2$ (0.025M) were mixed together to obtain a treatment solution. AAO templates were immersed vertically in the treatment solution heated to 40°C for different of periods of time.

4.2.3. Synthesis of ferrimagnetic transition metal ferrite nanotube arrays

Transition metal ferrite nanotubes were fabricated from the LPD treatment solution prepared by mixing a solution containing 0.25 g of FeOOH dissolved in 50 ml of a 1M NH_4.HF solution with a homogeneous 2.22 M solution of a transition metal nitrate $M(NO_3)_2$ (M=Co, Ni, Zn) and 40 ml of 0.5 M boric acid solution used as a fluoride scavenger. AAO templates were immersed in the treatment solution at 45°C for different periods of time. During the deposition the color of the AAO templates changed progressively from white to brown.

4.2.4. Synthesis of 1D multiferroic nanocomposites

1D multiferroic nanocomposites were synthesized in two successive LPD processes for ferroelectric perovskite and ferrimagnetic spinel ferrites as explained above. First, ferroelectric perovskite nanotubes were synthesized and then the centric empty spaces of ferroelectric

nanotubes were partially (double shell nanotubes) and completely (core-shell nanocables) filled to obtain the 1D multiferroic arrays (See the schematic in Figure 4.1).

4.3. Results and Discussions

4.3.1. Structural, Morphological and Piezoelectric Characteristics of the Perovskite Nanotubes

$BaTiO_3$ nanotubes were synthesized by template assisted LPD in the ambient atmosphere and temperatures as low as 40°C. In the following, these nanotubes have been used as templates for the fabrication of the multiferroic nanocomposites consisting spinel ferrite and perovskite. The powder X-ray diffraction technique was performed for the phase identification of the fabricated nanotubes. As seen in Figure 4.2 (a), fabricated nanotubes are crystalline and free of impurities after annealing at 750°C. The reflected peaks in the XRD pattern are indexed to $BaTiO_3$ with a cubic crystal structure (Space group Pm3m and the cubic lattice constant refined to 4.029 Å) in the absences of multiplicities for the reflected peaks of {002}, {102} and {112} corresponding to the tetragonal crystal structure.

These absences could originate from the broadening of the reflected peaks due to the small size of the crystallites coherently diffracting the X-Ray radiation. Further investigation of the crystal structure of the $BaTiO_3$ nanotubes were carried out by the Raman vibrational spectroscopy technique. Figure 4.2 (b) shows Raman spectrum of the fabricated nanotubes with the appearances of the Raman modes corresponding to the tetragonal crystal structure which have located the position of the individual peaks in the Raman spectrum. The cubic crystal structure of $BaTiO_3$ has the O_h symmetry within an octahedron in which Ti^{+4} has been surrounded with eight O^{-2} in which electrical dipoles generated in the octahedron of each unit cell cancel out each other. A slight shift in the position of Ti^{+4} in the lattice unit cell of $BaTiO_3$ (Lattice distortion) lead to the breaking down of the symmetry to the non-centrosymmetric of C_{4V} having a net polarization vector in the unit cell of $BaTiO_3$ with the tetragonal crystal structure [31]. Therefore, $BaTiO_3$ with the cubic crystal structure is Raman inactive while distorted tetragonality in the $BaTiO_3$ lead to a splitting of the four, degenerate $3F_{1u}+F_{2u}$ modes into eight Raman active transverse (TO) and longitudinal (LO) phonons that are responsible for the tetragonal crystal structure of $BaTiO_3$. FE-SEM images of the $BaTiO_3$ nanotubular architectures are indicated in Figure 4a-c after heat treatment at 750°C. Figure 4.3 (a) presents the confinement of $BaTiO_3$

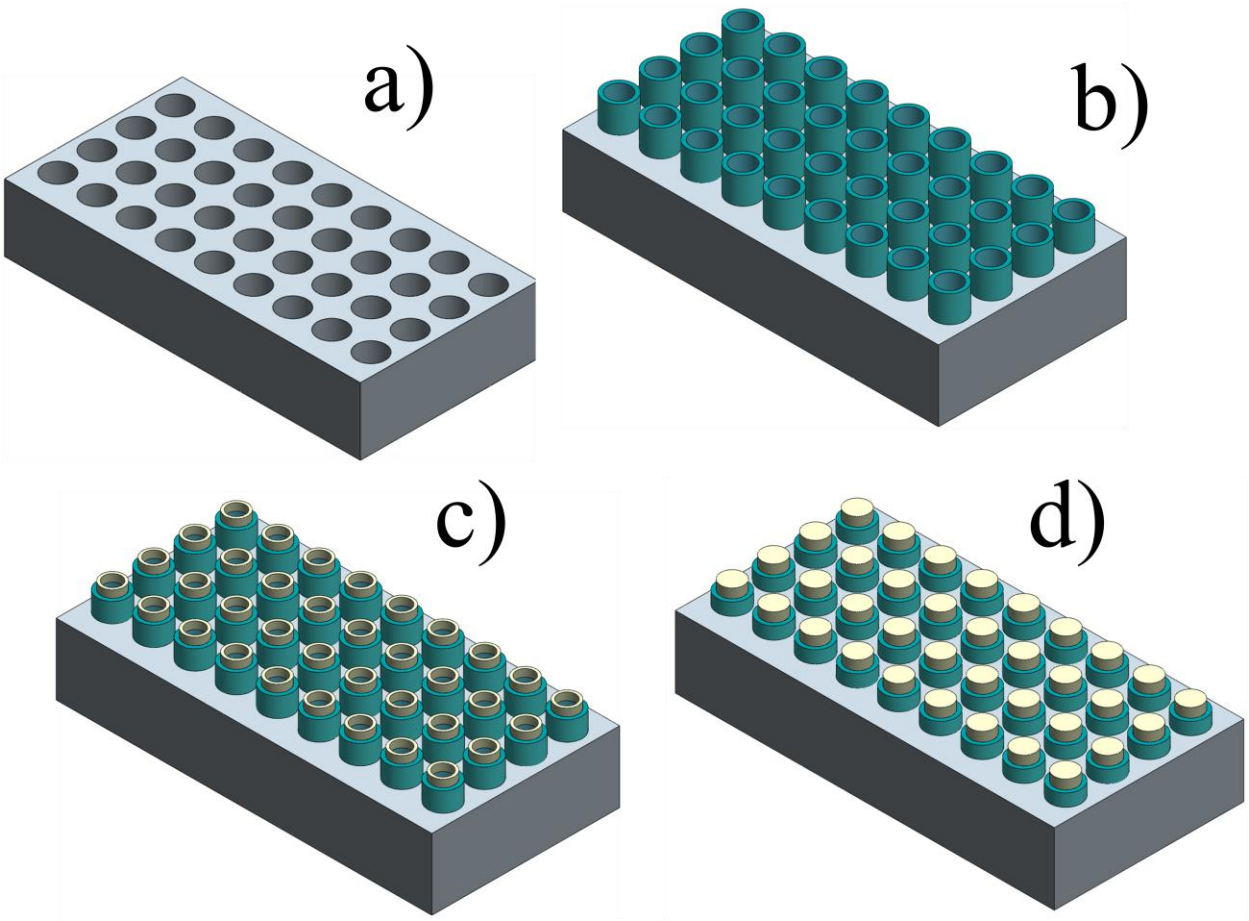

Figure 4.1. Schematic views of a) AAO template, b) Naonotube arrays confined in AAO template, c) partially and d) completely filled the perovskite nanotubes by transition metal ferrites

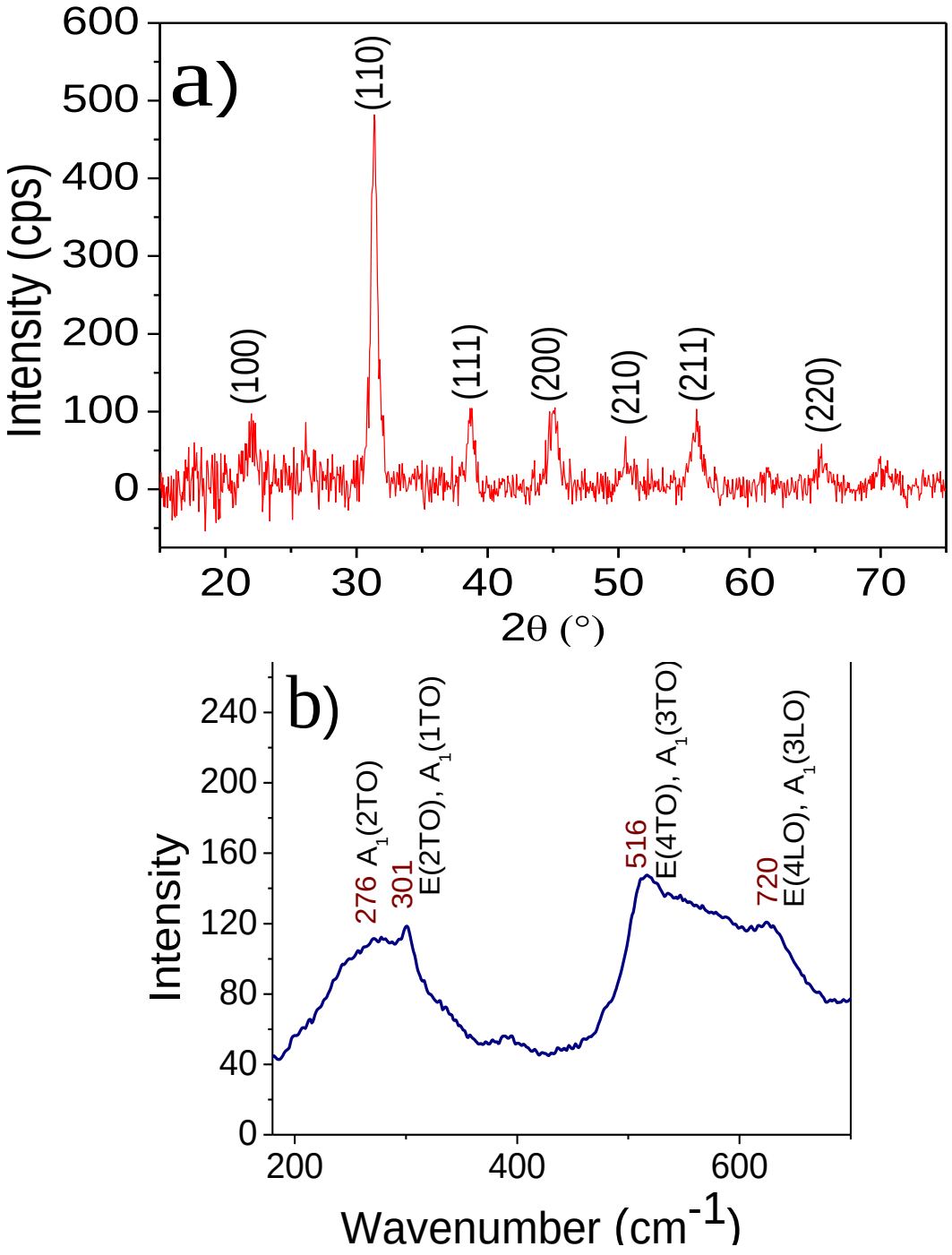

Figure 4.2. a) X-ray diffraction pattern and b) Raman spectrum of BaTiO3 nanotubes

nanotubes inside the AAO template with 200 nm diameters and shows the superficial layer has been removed from the sides of template by mechanical polishing.

It must be noticed that the pH of the LPD treatment solution changes from 3.9 to 4.5 during the deposition process which cannot etch off the AAO template to increase the pore size as previously reported [32]. Figure 4b shows $BaTiO_3$ nanotubes which have been partially released by etching the AAO template using 5wt% phosphoric acid for 15 min. Figure 4c shows high quality free standing $BaTiO_3$ nanotubes with open ends, smooth surfaces and are free of defects such as cracks and holes. These characteristics make template assisted LPD unique from other template assisted techniques such as conventional sol-gel which suffers from forming cracks and holes on nanotubes caused by the Rayleigh-Taylor instabilities during the wetting process of the pore walls and pyrolysis of the sol during the heat treatment.

$BaTiO_3$ nanotubes were dispersed in DI-water and then drop casted on highly doped Si (100). Individual nanotubes lied on the Si substrate were raster scanned by the piezoelectric force microscope. Figure 4.4 (a) shows topography of two $BaTiO_3$ nanotubes attached together while Figures 4.4 (b) and (c) correspond to the piezo-phase image. The marked areas in the piezo-phase images were electrically polled by 22 V DC-applied voltage transversal to the axis of the nanotubes by placing the conductive tip in contact with the surface. The polled areas appeared with different contrast in the images. The cross sectional values of the drawn line in Figure 4.4 (b) have been plotted versus the line distance.

The difference in the piezo-phase values for the un-poled and polled areas is about 180° this difference is the evidence that electrical dipoles on the surface of the nanotube were oriented downward (Dark areas) upon applying an electric field greater than the local coercive field. Switching spectroscopy piezoelectric force microscope (SSPFM) was used to evaluate the piezoelectric behavior of the individual nanotube using a conductive tip as a top electrode in capacitor geometry while the highly doped Si substrate acted as a bottom electrode. Piezo-phase and piezo-amplitude signals were collected locally by applying a square-triangular voltage with amplitude of 22 V and a frequency of 400 mHz through the conductive tip. Piezo-phase and piezo-amplitude signals of the individual nanotubes are shown in Figure 4.4 (d). Piezo-phase

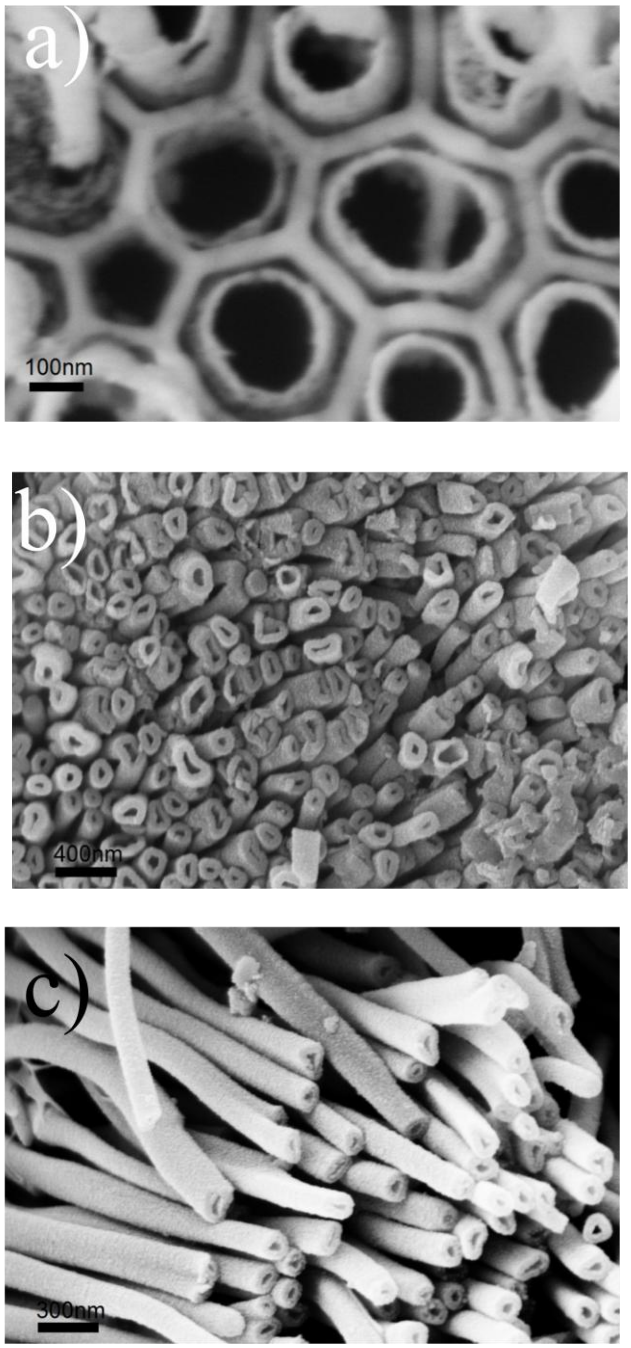

Figure 4.3. FE-SEM images of the BaTiO3 nanotubular architectures a) confined in the AAO template, b) partially exposed and c) free standing

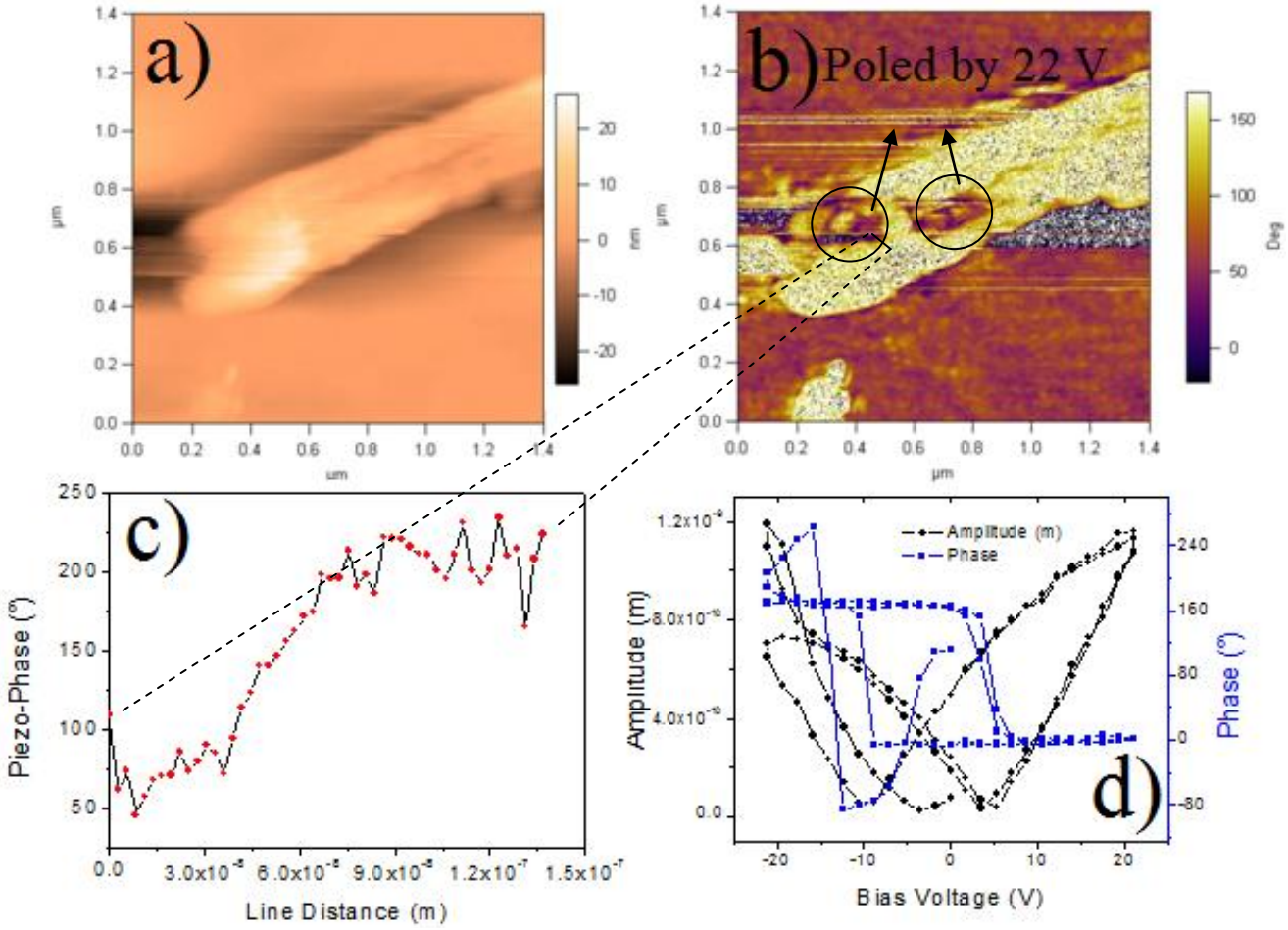

Figure 4.4. a) AFM topography of BaTiO3 nanotubes, b) Piezo-phase image c) line scan of the piezo-phase image on the drawn line on the piezo-phase image and d) piezo-amplitude and piezo-phase hysteresis loops versus applied voltage

versus applied voltage shows hysteretic behavior with a 180° change in the value of the piezo-phase when the applied voltage was switched from 22 to -22 V indicating a ferroelectric characteristic of $BaTiO_3$ the nanotubes. Corresponding coercive filed to change the orientation of polarization dipoles was measured about 6.8 V. The amplitude signal versus applied dc-voltage shown in Figure 4.4 (d) displays a butterfly shaped loop. The shift of the butterfly loop toward the positive applied voltage could be attributed to the surface charges between the conductive tip and the surface.

In the conventional AAO template assisted sol-gel of the metal oxides, the filling degree of the pores could not be controlled to tune the wall thickness and subsequently their physical properties. Unlike the sol-gel method, in the liquid phase deposition method metal oxides with different dimensionality (1-D or 2-D) form by the attachment of the fine particles initially formed in solution. Based on the presented mechanism for the formation of the metal oxide nanotubes, nanotubes form on the surface of the pores and progressive deposition of the metal oxide continues toward the inner volume of the holes. Therefore, when the deposition is carried out at the particular temperature, the wall thickness of the nanotubes can be controlled by varying the deposition time. Figure 4.5 (a-c) presents the transmission electron microscopy (TEM) images of the $BaTiO_3$ nanotubes synthesized by soaking the AAO templates inside the treatment solution for the different periods of time. Examination of the TEM micrographs of the $BaTiO_3$ nanotubes presented in Figures 4.5 (a-c) clearly shows that the wall thickness increases from 9, 20 and 32 nm with increasing the deposition time from 0.5 to 3 and 5 h, respectively.

The piezoelectric responses of the nanotubes with three different thicknesses were measured by SSPFM. Piezo-amplitude butterfly loops of the nanotubes with wall thicknesses of 9, 20 and 32 nm are shown in Figure 4.6. The corresponding piezoelectric response strongly depends on the wall thickness of the nanotubes through effects of surface tension and near-surface eigenstrain relaxation. In fact, surface tension induces radial and shear stress in the cylindrical geometry of the nanotubes which enhances the polarization values and ferroelectric phase transition temperature of the nanotubes. However, the piezoelectric coefficient (d_{33}) of the ferroelectric nanotubes is directly proportional to the polarization values. The measured d33 values are 5.2, 11.4 and 22.2 pm/v for nanotubes having wall thicknesses of 9, 20 and 32 nm, respectively.

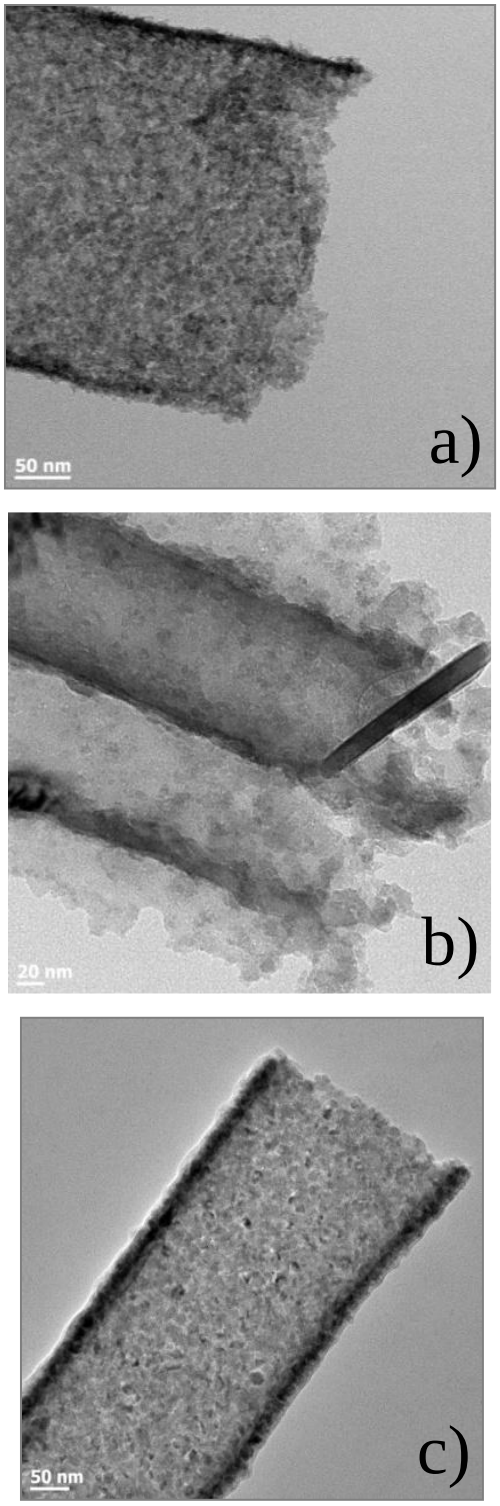

Figure 4.5. TEM images of BaTiO3 nanotubes having wall thicknesses of a) 9 nm, b) 20 nm and c) 32 nm with increasing the deposition time from 0.5 to 3 and 5 h, respectively

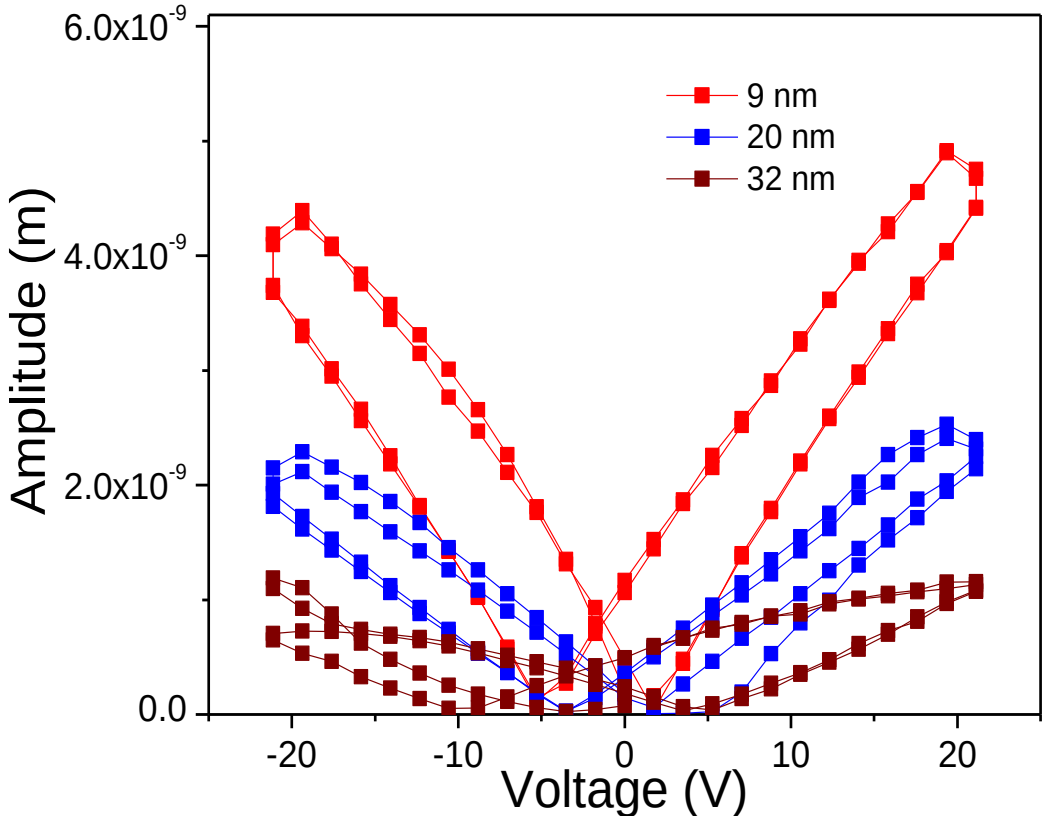

Figure 4.6. Piezo-amplitude butterfly loops of nanotubes having wall thicknesses of 9, 20 and 32 nm

4.3.2. Fabrication and characterizations of 1D multiferroic (Perovskite/Spinel ferrite) nanocomposite

1D multiferroic (Perovskite/Spinel ferrite) nanocomposites were fabricated by two successive LPD processing steps. In the first step, $BaTiO_3$ nanotubes were prepared by AAO template assisted LPD and then $BaTiO_3$ nanotubes (first ferroic phase) confined inside the AAO membranes were used as a template to deposit the second ferroic phase, spinel ferrite, to obtain the nanocomposites. Figure 4.7 (a) and (b) present FE-SEM images of the multiferroic nanocomposites consisting of ferroic phases of $BaTiO_3$/Zn-ferrite.

The magnetic hysteresis loop of the $BaTiO_3$/Zn-ferrite nanocomposites is shown in Figure 4.8 (a). By comparing the magnetic properties of the fabricated Zn-ferrite nanotubes presented with the magnetic properties of the $BaTiO_3$/Zn-ferrite nanocomposite, there is a change in the magnetization process from superparamagnetic to ferrimagnetic which could be attributed to the increments in the total magnetic anisotropy of the Zn-ferrite in the composite geometry in contact with $BaTiO_3$. The coercive magnetic field and magnetization saturation for the $BaTiO_3$/Zn-ferrite nanocomposites were measured 118 Oe and 0.21 emu/g, respectively. Magnetic force microscopy was employed to image the magnetic domain configuration of the $BaTiO_3$/Zn-ferrite nanocomposites (Figure 4.8 (b)). The strip like domains with light and dark contrasts in the MFM image represent domains with the magnetization up (repulsive interaction) and magnetization down (attractive interaction), respectively. Due to the cylindrical geometry of the 1D nanocomposite, some artifacts appeared at the edges where the magnetic tip cannot raster scan the surface properly. The changes in the magnetic phase for the line cross section drawn in Figure 4.8 (b) have been plotted versus the line distance (Figure 4.8 (c)). The magnetic phase changes on the line when passes across the magnetic domains having different magnetic domain configurations for the magnetic phase.

Recently, a novel technique based on the piezoelectric force microscopy technique has been developed in our research group which allows us to evaluate the ME properties of multiferroic nanocomposites. 1D nanocomposites of $BaTiO_3$/Zn-ferrite were dispersed in DI-water and then drop casted on a piece of Si substrate (001). Piezoelectric properties of the sample were measured in the present of a uniform in-plane *dc* magnetic field produced during the PFM measurements by using a variable field module (VFM). Figure 4.9 shows the piezo-hysteresis

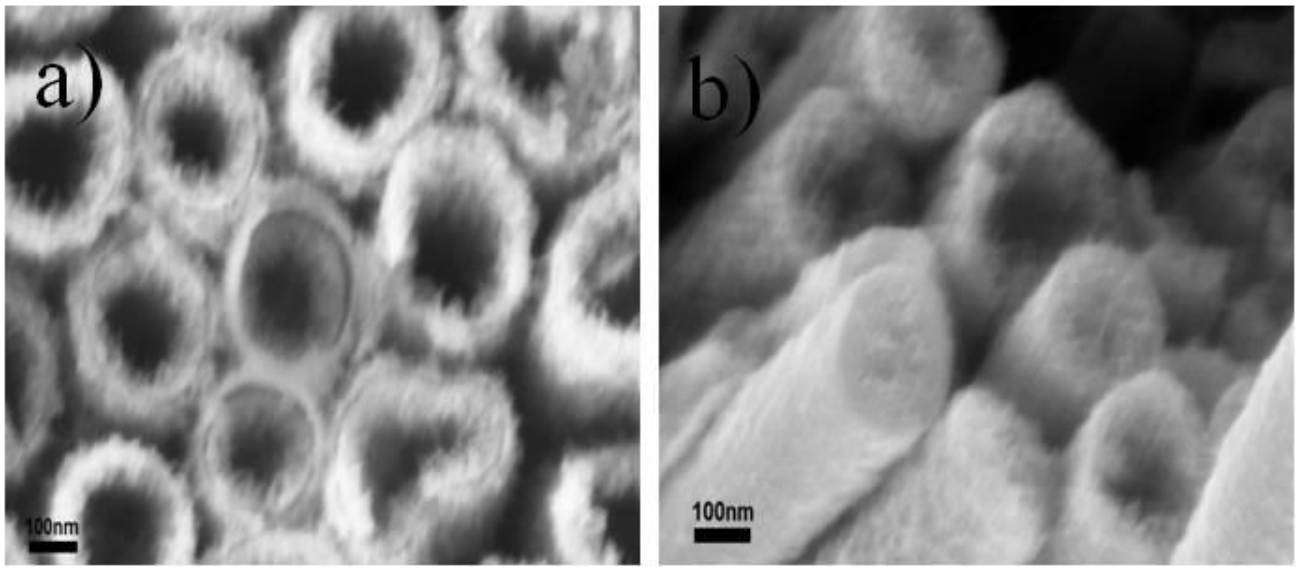

Figure 4.7. a) and b) FE-SEM images of 1D multiferroic nanocomposites consisting of ferroic phases of BaTiO3 and Zn-ferrite

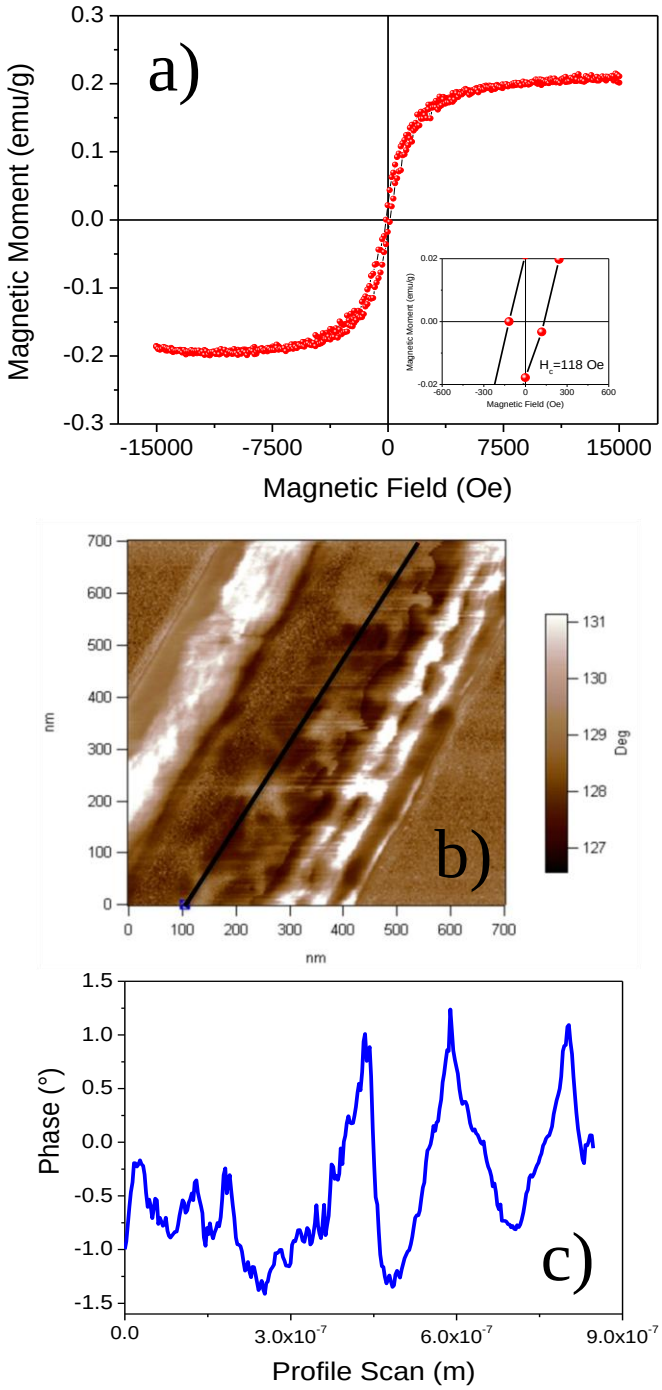

Figure 4.8. a) Magnetic hysteresis loop, b) MFM image of the 1D multiferroic nanocomposites of BaTiO3/Zn-ferrite and c) Cross section profile of the magnetic phase for the line drawn on MFM image

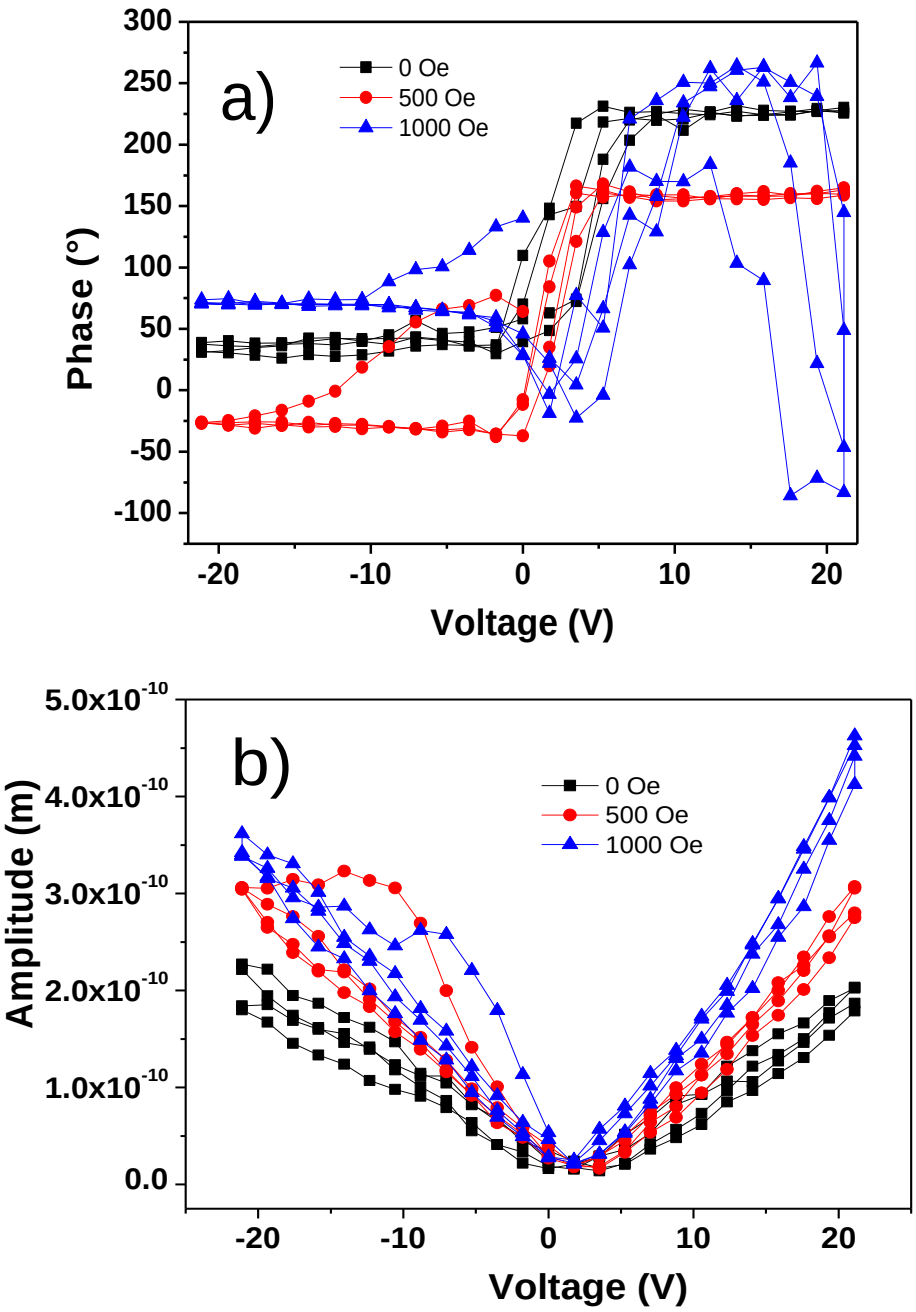

Figure 4.9. The piezo- hysteresis loops of a) phase and b) amplitude versus voltage for the 1D multiferroics nanocomposite of BaTiO3/Zn-ferrite in the applied magnetic field

loops of the phase and the amplitude versus voltage for the 1D multiferroics nanocomposite of $BaTiO_3$/Zn-ferrite in the applied magnetic field. The difference in the maximum and minimum of the piezo-phase when the applied voltage was swept from -22 to +22 V is about 180° indicates the existence of 180° ferroelectric domains in the $BaTiO_3$. The piezo-amplitude versus voltage loops exhibit the well-known "butterfly-type" behavior which is the characteristic of the ferroelectric materials. As indicated in Figure 12b, the slope of the piezo-amplitude signal increased when the magnetic field increased from 0 to 500 and 1000 Oe. The piezoelectric coefficients (d_{33}) were obtained by fitting the linear portion of the butterfly loops 27.54, 47.04 and 81.72 pm/V at applied magnetic fields of 0, 500 and 1000 Oe, respectively. This systematic variation in the piezoelectric coefficient of the sample originates from the ME coupling between the ferroic phases which is the strain mediated ME coupling.

4.3.3. Calculation of the direct magnetoelectric coefficient

The Gibbs free energy for a multiferroic system as a function of temperature, pressure, electric field and magnetic field is expressed by equation (1)[33].

(1)

Where V is the volume, p is the pressure, S is the entropy, P is the polarization, E is the electric field, M is the magnetization and H is the magnetic field. At a constant pressure and temperature the equation (1) simplifies to equation (2) as follow:

(2)

By using the equality of cross derivatives, it is followed by equation (2).

$$\left(\frac{\partial P}{\partial H}\right)_E = \left(\frac{\partial M}{\partial E}\right)_H \qquad (3)$$

The term above is known as magnetoelectric (ME) coefficient in which measuring the change in polarization by varying the magnetic field is the direct magnetoelectric coefficient ($\alpha_{direct} = \left(\frac{\partial P}{\partial H}\right)_E$) while measuring the change in magnetization by variation of the electric field is the indirect ME coefficient ($\alpha_{direct} = \left(\frac{\partial M}{\partial E}\right)_H$). From the thermodynamics of ferroelectrics, piezoelectric coefficient and polarization are related by following equation[34]:

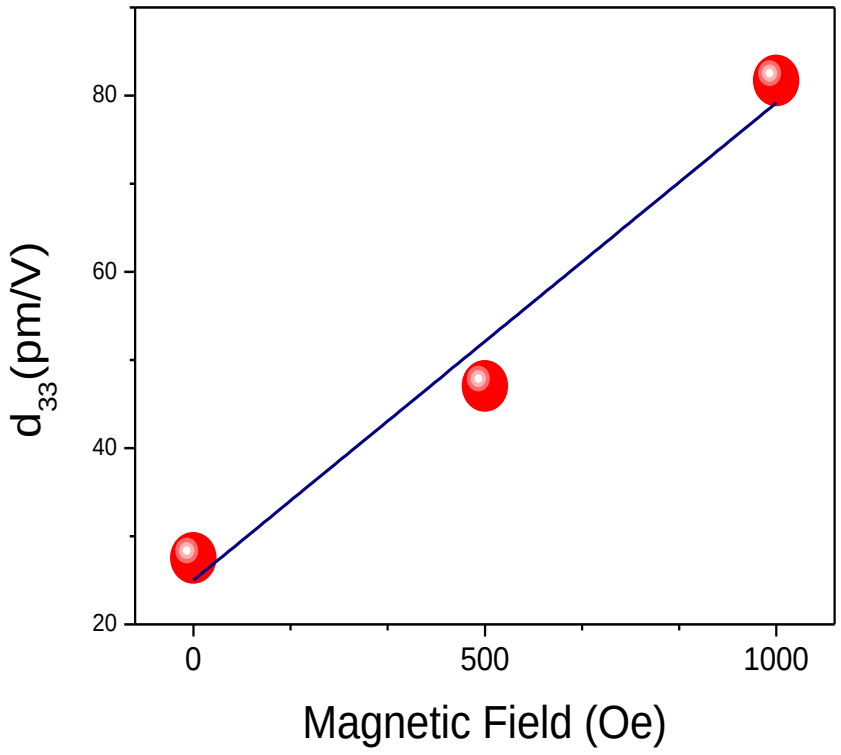

Figure 4.10. Magnetic field-dependence of the d_{33} coefficient for the multiferroics nanocomposite of BaTiO3/Zn-ferrite

(4)

where Q is electrostrictive coefficient and is out of plane component of dielectric permittivity tensor. By replacing the —— in the direct ME coefficient equation, the following equation is obtained:

$$\alpha_{direct} = \left(\frac{\partial P}{\partial H}\right)_E = \frac{1}{2Q\varepsilon_{33}}\left(\frac{\partial d_{33}}{\partial H}\right)_E \quad (5)$$

By combining the — (6) and — (7) with (5) where is the piezoelectric coefficient [33]:

$$\alpha_{direct} = -\sigma\left(\frac{\partial d_{33}}{\partial H}\right)_E \quad (8)$$

The direct ME coefficient in equation (8) is proportional to the mechanical stress ( ). In the case of the $BaTiO_3$/Zn-ferrite nanocomposites, mechanical stress is compressive (negative term) while the $\left(\frac{\partial d_{33}}{\partial H}\right)_E$ term is positive. The variation of d_{33} coefficient with the magnetic field for the $BaTiO_3$/Zn-ferrite nanocomposites has been shown in Figure 4.10 and the direct ME coefficient was calculated using equation (5) about 1.08 V/cm.Oe.

The same behavior also was observed in the thin films of bilayered nanocomposites in which the magnetic layers possessed both negative and positive magnetostriction coefficients and variations of the piezoelectric coefficients are positive and negative, respectively. It is emphasized here that positive/negative variation of the piezoelectric coefficient of the multiferroic nanocomposite in the presence of the magnetic field corresponds to negative/positive sign of the magnetostriction coefficients.

4.4. Conclusion

Metal oxide ferroelectric nanotubes with different wall thicknesses were successfully synthesized by a template assisted liquid phase deposition technique. The $BaTiO_3$ nanotubes showed a strong ferroelectric response at room temperature as indicated by both piezo-amplitude and piezo-phase components of the piezoelectric signal. Piezoelectric coefficients of the $BaTiO_3$ nanotubes decreased with increasing the wall thickness. Investigations on the direct ME effect of the 1D multiferroics nanocomposite consisting ferroic phases by MA-PFM revealed the strain mediated

ME coupling with ME coefficient of 1.08 V/cm.Oe. Due to magnetostriction of the ferrite phase, when the magnetic field is applied the produced stress is transferred through the interface to the perovskite phase changing the piezoelectric coefficients.

4.5. References

(1) Nan, C. W.; Bichurin, M. I.; Dong, S. X.; Viehland, D.; Srinivasan, G. *Journal of Applied Physics* **2008**, *103*.

(2) Srinivasan, G. In *Annual Review of Materials Research, Vol 40*; Clarke, D. R., Ruhle, M., Zok, F., Eds. 2010; Vol. 40, p 153.

(3) Martin, L. W.; Chu, Y. H.; Ramesh, R. *Materials Science & Engineering R-Reports* **2010**, *68*, III.

(4) Liu, G.; Nan, C. W.; Xu, Z. K.; Chen, H. D. *Journal of Physics D-Applied Physics* **2005**, *38*, 2321.

(5) Prashanthi, K.; Mandal, M.; Duttagupta, S. P.; Pinto, R.; Palkar, V. R. *Sensors and Actuators a-Physical* **2011**, *166*, 83.

(6) Raidongia, K.; Nag, A.; Sundaresan, A.; Rao, C. N. R. *Multiferroic and magnetoelectric properties of core-shell $CoFe_2O_4$@$BaTiO_3$ nanocomposites*; AIP, 2010; Vol. 97.

(7) Liu, M.; Li, X.; Imrane, H.; Chen, Y.; Goodrich, T.; Cai, Z.; Ziemer, K. S.; Huang, J. Y.; Sun, N. X. *Synthesis of ordered arrays of multiferroic NiFe2O4-Pb(Zr0.52Ti0.48)O3 core-shell nanowires*; AIP, 2007; Vol. 90.

(8) Xie, S.; Ma, F.; Liu, Y.; Li, J. *Nanoscale* **2011**, *3*, 3152.

(9) Deki, S.; Aoi, Y.; Hiroi, O.; Kajinami, A. *Chemistry Letters* **1996**, 433.

(10) Deki, S.; Ko, H. Y. Y.; Fujita, T.; Akamatsu, K.; Mizuhata, M.; Kajinami, A. *European Physical Journal D* **2001**, *16*, 325.

(11) Kuratani, K.; Uemura, M.; Mizuhata, M.; Kajinami, A.; Deki, S. *Journal of the American Ceramic Society* **2005**, *88*, 2923.

(12) Saito, Y.; Sekiguchi, Y.; Mizuhata, M.; Deki, S. *Journal of the Ceramic Society of Japan* **2007**, *115*, 856.

(13) Deki, S.; Aoi, Y.; Okibe, J.; Yanagimoto, H.; Kajinami, A.; Mizuhata, M. *Journal of Materials Chemistry* **1997**, *7*, 1769.

(14) Lee, M.-K.; Fan, C.-H. *Journal of The Electrochemical Society* **2009**, *156*, D395.

(15) Caruntu, G.; Newell, A.; Caruntu, D.; O'Connor, C. J. *Journal of Alloys and Compounds* **2007**, *434*, 637.

(16) Caruntu, G.; Bush, G. G.; O'Connor, C. J. *Journal of Materials Chemistry* **2004**, *14*, 2753.

(17) Hsu, M.-C.; Sun, Y.-M.; Leu, I.-C.; Hon, M.-H. *Applied Surface Science* **2007**, *253*, 7639.

(18) Lee, M. K.; Liao, H. C.; Tung, K. W.; Shih, C. M.; Shih, T. H. *Journal of Physics D-Applied Physics* **2002**, *35*, 61.

(19) Yourdkhani, A.; Perez, A. K.; Lin, C. K.; Caruntu, G. *Chemistry of Materials* **2010**, *22*, 6075.

(20) Deki, S.; Iizuka, S.; Horie, A.; Mizuhata, M.; Kajinami, A. *Journal of Materials Chemistry* **2004**, *14*, 3127.

(21) Yourdkhani, A.; Caruntu, G. *Journal of Materials Chemistry* **2011**, *21*, 7145.

(22) Chen, Y.-Y.; Yu, B.-Y.; Wang, J.-H.; Cochran, R. E.; Shyue, J.-J. *Inorganic Chemistry* **2008**, *48*, 681.

(23) Zavaliche, F.; Zheng, H.; Mohaddes-Ardabili, L.; Yang, S. Y.; Zhan, Q.; Shafer, P.; Reilly, E.; Chopdekar, R.; Jia, Y.; Wright, P.; Schlom, D. G.; Suzuki, Y.; Ramesh, R. *Nano Letters* **2005**, *5*, 1793.

(24) Yan, L.; Xing, Z. P.; Wang, Z. G.; Wang, T.; Lei, G. Y.; Li, J. F.; Viehland, D. *Applied Physics Letters* **2009**, *94*.

(25) Li, Z.; Wang, Y.; Lin, Y. H.; Nan, C. *Physical Review B* **2009**, *79*.

(26) Kim, Y.; Han, H.; Lee, W.; Baik, S.; Hesse, D.; Alexe, M. *Nano Letters* **2010**, *10*, 1266.

(27) Kalinin, S. V.; Morozovska, A. N.; Chen, L. Q.; Rodriguez, B. J. *Reports on Progress in Physics* **2010**, *73*.

(28) Morozovska, A. N.; Eliseev, E. A.; Kalinin, S. V. *Journal of Applied Physics* **2007**, *102*.

(29) Anbusathaiah, V.; Jesse, S.; Arredondo, M. A.; Kartawidjaja, F. C.; Ovchinnikov, O. S.; Wang, J.; Kalinin, S. V.; Nagarajan, V. *Acta Mater* **2010**, *58*, 5316.

(30) Yourdkhani, A.; Garza, E.; Zaldivar, L.; Spinu, L.; Caruntu, G. *Magnetics, IEEE Transactions on* **2011**, *47*, 3939.

(31) Adireddy, S.; Lin, C. K.; Cao, B. B.; Zhou, W. L.; Caruntu, G. *Chemistry of Materials* **2010**, *22*, 1946.

(32) Hsu, M. C.; Leu, I. C.; Sun, Y. M.; Hon, M. H. *Journal of Crystal Growth* **2005**, *285*, 642.

(33) Vopsaroiu, M.; Stewart, M.; Hegarty, T.; Muniz-Piniella, A.; McCartney, N.; Cain, M.; Srinivasan, G. *Measurement Science & Technology* **2008**, *19*.

(34) Damjanovic, D. *Reports on Progress in Physics* **1998**, *61*, 1267.

5. Microstructural Characterization and Ferroelectric Properties of $PbTiO_3$ Thin Films Synthesized by Liquid Phase Deposition

5.1. Introduction

Low dimensional ferroelectric perovskites have attracted an increased interest in the past decade due to their wide range of potential applications in integrated piezoelectric devices[1-2], microsensors[3-4], infrared detectors[5], optical wave p-guiding devices[6], electro-optic modulators[7-8], actuators, ultra-high density storage media[9] and micro-electromechanical devices[4,10]. As the temperature stability of the electrical properties and the critical size at which ferroelectricity is suppressed are key requirements for device applications, $PbTiO_3$, with its chemical stability, high Curie temperature (T_c=490 ^oC), large spontaneous polarization, small dielectric constant, small coercivity and low permittivity is one of the most technologically relevant member of the Ti-containing perovskite family. It has been proposed that the design of a device consisting of a thin ferroelectric film deposited onto bulk semiconductor substrates exhibits stability greater than that of a similar device using the reverse configuration; that is a semiconductor thin film deposited onto a ferroelectric substrate. Therefore, much effort has been directed towards the controlled synthesis of $PbTiO_3$ thin film structures due to their compatibility with the existing silicon integrated circuit technology.

A series of chemical methods have been proposed for the synthesis of $PbTiO_3$ thin films; they include hydrothermal[11-13], chemical solution deposition[14-17], sol-gel[18-20], microemulsion-assisted sol-gel[21] and metal organic chemical vapor deposition (MOCVD)[22-24]. In general, the preparation of single phase, highly uniform $PbTiO_3$ thin film structures, in particular polycrystalline films, is difficult due to two main obstacles related to their chemical processing by using solution-based chemistry. First, the different values of the thermal expansion coefficients of the film and the substrate along with the thermal expansion anisotropy and large spontaneous strain (~6 %) of $PbTiO_3$ oftentimes result into the mechanical fracture of the thin film structures as they are cooled down after the heat treatment process. A second problem is related to the formation of pyrochlore-type secondary phases, such as $Pb_2Ti_2O_{6+x}$ which reduce significantly the value of the relative permittivity and, therefore, should be avoided as much as possible[25-32]. It is well known that tetragonal $PbTiO_3$ results from a phase transformation of the intermediate $Pb_2Ti_2O_6$ metastable phase; the activation energy of this phase transformation as estimated to be close to E_a=0.45 eV[33] and this process usually requires temperatures above 650 $^\circ C$. Wang and coworkers

have recently shown that single crystalline $PbTiO_3$ nanorods can be obtained by the phase transformation of $PbTi_2O_6$ nanorods prepared under solvothermal conditions at 200 $^{\circ}C$[34]. These results clearly suggest that that the preparation of single phase $PbTiO_3$ is not trivial and the stabilization of the pure perovskite phase oftentimes requires a fine control over the reaction parameters, such as the pH of the solution[27], temperature[35] and reaction time[34,36], respectively.

Recently, the so-called liquid phase deposition (LPD) method has been proposed as a very versatile route for the chemical deposition of mirror-like perovskite thin film structures[37-42]. This approach is simple, low cost and environmentally friendly and allows the coating of large areas with complex morphologies by defect-free, uniform metal oxide layers. Mechanistically, the LPD method consists of the direct precipitation of homogenous metal oxide films from supersaturated solutions by the controlled hydrolysis of transition metal-fluoro complexes in presence of aluminum or boric acid (1).

$$MF_n^{(n-2m)-} + mH_2O \rightleftharpoons MO_m + nF^- + 2mH^+ \quad (1)$$

$$H_3BO_3 + 4HF \rightleftharpoons BF_4^- + H_3O^+ + 2H_2O \quad (2)$$

In general, the chemical precipitation of metal oxide films in aqueous solutions requires a very slow hydrolysis process in order to prevent the spontaneous bulk precipitation of the solution Boric acid has been conventionally used as a scavenger for the fluoride ions due to its ability to form a stable complex $[BF_4]^-$ ion, which causes the equilibrium reaction (1) to proceed to the right side with formation of the metal oxide. Moreover, the $[BF_4]^-$ ion is water soluble, which allows its easy elimination from the film surface upon rinsing the resulting metal oxide/hydroxide coatings, thereby preventing the contamination of the metal oxide thin film structures with F^-, which can be otherwise detrimental to the stoichiometry of the films and, therefore their physical and chemical properties[43].

Despite the fact that a significant effort was put on the preparation of perovskite thin film structures by the liquid phase deposition, little is known about the correlation between the influence microstructure and the ferroelectric properties of the films. It is well known that thin film structures possess a residual stress generated by the clamping of the grains when the films are cooled down and the paraelectric to ferroelectric region is crossed. Both experimental and theoretical studies have evidenced that the residual stress affects significantly the microstructure of the films and therefore will affect the optical, mechanical and electrical properties of the films

by influencing the domain structure formation and the dielectric constant. For example, by using the Devonshire thermodynamic formalism, it has been demonstrated that the two-dimensional stress plays a key role in modifying the Curie temperature in ferroelectric perovskite thin film structures[44].

In this paper we report on the structural and ferroelectric properties of polycrystalline $PbTiO_3$ thin film structures with different thicknesses obtained by liquid phase deposition at temperatures as low as 45 ^{o} C. The stress in these thin film structures was investigated by using Raman spectroscopy and the experimental results were correlated with the ferroelectric properties of the thin films measured by piezoelectric force microscopy (PFM) at room temperature.

5.2. Experimental

5.2.1. Chemical Deposition of Metal Oxide Thin Films

All experiments were performed in open atmosphere by using a magnetic hotplate (IKA Works, Inc.) equipped with a temperature controller and a pH electrode. $PbTiO_3$ thin films were deposited from treatment solutions prepared by dissolving reagent grade purity chemicals (Alfa Aesar) in deionized water (18 MΩ) obtained from a Barnstead Nanopure water purification system. Perovskite films were deposited on commercial single side polished (100) Si wafers with a resistivity of 0.05 Ωcm. Since the glass melts at temperatures above 600 ^{o}C only the perovskite films deposited on silicon were annealed at 750 ^{o}C. Prior to deposition, the substrates were cleaned with a mixture of acetone and ethanol (50:50% wt.) and blow-dried with compressed argon. A 200 nm $LaNiO_3$ bottom electrode was spin coated on the Si substrates by using a 0.4 M solution of $La(NO_3)_3$ and $Ni(ac)_2$ dissolved in ethanol according to a procedure similar to that proposed by Meng and cowokers [45]. The precursor solution was spin coated at 3500 rpm for 30 s and the resulting films were dried at 150 ^{o}C for 2 h to allow the removal of the solvent and subsequently at 700 ^{o}C for 2 h in open atmosphere. In addition to serving as a bottom electrode, the $LaNiO_3$ buffer layer can substantially minimize the clamping effect exerted by the substrate ultimately leading to the enhancement of magnetoelectric effect.[46] The deposition of perovskite films was performed by adapting the experimental procedure proposed by Hsu and coworkers[35,47]. In a typical experiment three individual solutions containing 1 mmoL $Ba(NO_3)_2$ or $Pb(NO_3)_2$, 1 mmoL $(NH_4)_2TiF_6$ and 3 mmoL of H_3BO_3 were mixed together and water was added to a final volume of 100 mL The deposition of the $PbTiO_3$ (PTO) thin films was performed in treatment solutions whose initial pH varied between 5.2 and 5.6, depending on the

pH of the deionized water and decreased slowly to 4.1-4.7 after the deposition of the films. High quality nanoparticle-based perovskite thin films with variable thicknesses were obtained by soaking the substrates in the treatment solution at 45 ^{o}C for a period of time, typically varying between 1 and 4 h. After the deposition, the substrates were removed, rinsed and cleaned ultrasonically with distilled water, dried with a N_2 flow and heat treated at 750 ^{o}C in open atmosphere for 3 h followed by natural cooling to room temperature.

5.2.2. Characterization of the Perovskite Films

The surface morphology, chemical composition and the microstructure of the films were investigated with a LEO 1530VP field emission scanning electron microscope (FE-SEM) operating in low vacuum mode at an accelerating voltage of 200 kV and equipped with an energy dispersive (EDS) detector. The phase purity and the crystal structure of the PTO films were investigated by X-Ray diffraction in grazing incidence mode (2^{o}) with a Philips X'Pert System equipped with a curved graphite single-crystal monochromator (CuK_{α} radiation). Patterns were recorded in a step scanning mode in the 15-60^{o} 2θ range with a step of 0.02^{o} and a counting time of 10 s. The angular range was restricted to 15-60^{o} due to a very strong reflection of the Si substrate which appears around 68^{o} in 2θ and obscures the peaks of the metal oxide films. The chemical composition of the layered structures was determined by energy dispersion X-Ray (EDX) analysis system attached to the FE-SEM instrument, whereas the thickness of the films was examined by a spectral reflectance method with a F20 film thickness measurement system from Filmetrics.

AFM images of the PTO films were collected at room temperature with an Asylum Research MFP-3D atomic force microscope working in tapping mode and using commercial Si_3N_4 cantilevers with a force constant of 0.7 $N{\cdot}m^{-1}$.The piezoelectric properties of the perovskite films were measured with the same instrument by using a silicon tip coated with a 20 nm Pt/Ir layer. The piezoelectric signal of the samples was measured with the high voltage PFM module of the MFP-3D AFM by using an AC240TM cantilever made of a tetrahedral silicon tip coated with platinum/titanium. For the fabrication of the layered capacitors, Au top electrodes with areas of 5 mm^2 and a thickness of 50 nm and were sputtered on the film samples followed by a standard lithography process. The measurement of the piezoelectric properties of the thin film samples was performed in different areas of the sample and experiments were repeated 5 times to reduce the experimental error and ensure a high reproducibility of the results. Room temperature Raman

scattering studies were performed on both thin films and powdered samples with a Thermo-Fisher DXR dispersive Raman spectrometer in a conventional backward geometry. A 532-nm line of a laser was used as the excitation source with a spectral resolution of 3 cm^{-1} and an output power of 6 mW in order to avoid the film restructuring and/or damage resulting from the overheating created by the laser source. The scattered light was analyzed with a triple monochromator coupled with an optical microscope, which allows the incident light to be focused on the sample as a circular spot of about 2 μm in diameter.

5.3. Results and Discussion

In Figure 5.1 (a) is shown the FE-SEM images of a $PbTiO_3$ thin film deposited onto a (001) Si substrate covered by a native SiO_2 layer. The image clearly indicates that the thin film has a granular morphology being formed by quasi-spherical particles with an average diameter of 80 nm which are densely packed forming a continuous layer onto the substrate. The thickness of this film, obtained after a 3 h deposition at 45 ^oC was 180 nm.

In order to obtain information about the mechanism of formation of the $PbTiO_3$ thin films by the LPD method, a control experiment was performed by maintaining the (100) Si substrates into the treatment solution for different periods of time; that is 30, 60 and 90 min, respectively. After the deposition the films were rinsed with water, dried with N_2 and then their morphology was investigated by FE-SEM. The micrographs of the samples, along with that of the bare silicon film are presented in Figures 5.1(b-e). As seen in the FE-SEM images, after 30 min the surface of the Si substrate is partially covered by two types of particles: quasi-spherical, with an avergage diameter of 30 nm and irregularly-shaped particles with a size of about 5-7 nm (Figure 5.1 (c)). With increasing the deposition time the morphology of these particles does not change siggnificantly, but the space between the islands decreases as more and more particles attach to the substrae (Figure 5.1 (d)). As seeen in Figure 1 (e), after 120 min the substrate is uniformly covered by a thin layer resulting from the percolation and coalescence of the isolated islands, similar to liquid droplets with a finite contact angle, thereby indicating that the resulting polycrystalline films form via a Volmer-Weber mechanism[48-51].

X-Ray diffraction analysis of the as-prepared films evidenced that the as-prepared films are amorphous in nature presumably consisting of a mixture of metal oxides/hydroxides, similar to the results reported by Hsu and coworkers for $PbTiO_3$ thin films deposited at 30 ^oC onto $LaNiO_3$-buferred Si substrates[37-38]. The thickness of the films measured by spectral reflectance

lead to values of 112, 240 and 394 nm for the thin film structures obtained by soaking the substrates in the treatment solution for 1, 2 and 4 h, respectively. In Figure 5.2 is shown the X-Ray diffraction (XRD) pattern of a $PbTiO_3$ thin film with a thickness of 180 nm obtained by annealing the as-deposited film at 750 ^oC for 6 h in air.

Although the most intense peaks of the $PbTiO_3$ structure overlap with those of the underlying $LaNiO_3$ layer, the XRD pattern shows that the film is single phase without impurities, such as pyrochlore $Pb_2Ti_2O_{6+x}$ or fluorite $Pb_{2+x}Ti_{2-x}O_{7-y}$, commonly encountered in the preparation of $PbTiO_3$ powders[52-54]. The aspect of the XRD pattern suggests that the film is polycrystalline and exhibits peaks which match to those of the tetragonal bulk $PbTiO_3$ (Macedonite), JCPDS File No.6-452), indicating that the resulting ferroelectric film is chemically pure and highly crystalline Interestingly, the absence of a particular spatial orientation, either crystallographic or morphological of the $PbTiO_3$ supports the existence of a homogeneous nucleation mechanism involved in the growth of the perovskite-like films by liquid phase deposition. The refined lattice parameters are a=3.907(4) Å and c=4.123(5) $Å^3$ (c/a=1.055), values which are very close to those reported in the literature for $PbTiO_3$ thin film structures prepared by other chemical methods[55-57]. Moreover, the calculated unit cell volume V=62.93 $Å^3$ is slightly smaller than the value reported in the literature for bulk PTO (V=63.135 $Å^3$). Again, this finding is in very good agreement with those reported by other authors for thin film structures deposited onto (100) Si, and strongly suggests that the PTO films obtained by the LPD method are under a compressive stress[57-58].

In polycrystalline films residual stress plays a key role on their macroscopic properties being typically considered as a sum of elementary stresses, intrinsic, extrinsic, and thermal. These include the misfit strain with the substrate, stress resulting from grain boundaries, the constrained shrinkage during the drying, pyrolysis and crystallization, as well as the thermal expansion mismatch between the film and substrate during the cooling process. Raman spectroscopy is a powerful and versatile tool to investigate the microstructure and the lattice dynamics in crystalline solids and, in particular, to study the magnitude and types of residual stress in thin films. The high temperature cubic $PbTiO_3$ presents 12 optical modes at the Γ point in the Brillouin zone which transform as the $3T_{1u}+T_{2u}$ irreducible representation of the point group Oh.[59] While the triply degenerate T_{1u} mode is only infrared active, the T_{2u} mode is neither Raman nor infrared active, being called “the silent mode”. Below the Curie temperature $PbTiO_3$

adopts a tetragonal structure and the T_{1u} optical lattice modes split into the A_1+E modes, whereas the T_{2u} will split into B_1+E modes, respectively.[59-60] The degeneracy of the lattice vibrations at long wavelengths is furthermore lifted due to the long_range electrostatic interactions into a doubly degenerate transverse mode (TO) and a single longitudinal optical (LO) mode. The E(1TO) and A_1(1TO)modes originating from the T1u mode are known as "soft modes" because they tend to zero frequency when the sample is heated to the Curie temperature.[61]

In parts (a) and (b) of Figure 5.3 are represented the room-temperature Raman spectra of the 143-, 215-, 302-, and 388-nm-thick $PbTiO_3$ films and that of the powdered sample collected from the same experiment. The Raman spectra of the $LaNiO_3$ buffer layer were collected in a separate experiment and compared to those of the $PbTiO_3$ films deposited onto LaNiO3-buferred (100) Si substrates (data not presented). The Raman bands are similar to those reported by Chaban et al.[62] for $LaNiO_3$ films deposited onto (100) Si substrates by MOCVD, but their intensity are very low as compared to that of the Raman peaks of PbTiO3 and can be assimilated with the background. For example, the most intense Raman band in LaNiO3 centered around 400 cm^{-1} appears as a very small bump in the Raman spectrum of the PbTiO3 (Figure 5.3 (b)). On the basis of the foregoing, we can ascribe the vibrational bands in the Raman spectra exclusively to the $PbTiO_3$ film. The Raman spectra of the film samples closely resemble those of the single crystal and polycrystalline bulk PTO and exhibit all phonon modes allowed in the tetragonal phase, that is, E(1TO), A_1(1TO), E(2TO), B1+E, A_1(2TO), and E(2LO)+A_1(2LO), respectively. Unlike the spectra of the thin film structures, the Raman spectrum of the PTO powder collected from the same experiment (Figure 5.3 (b)) exhibits welldefined intense bands that also can be ascribed to those of tetragonal $PbTiO_3$. Two salient characteristics can be observed upon examination of the Raman spectra presented in Figure 5.3 (a). First, the intensity of the peaks increases as the films get thicker due to the increase of the scattering volume. Second, an up-shift of the Raman modes is observed with increasing the thickness of the corresponding films. The variation of the frequency modes for the E(1TO), E(1LO), E(2TO), B1+E, and A1(2TO) soft mode with the thickness of the films is shown in Figure 5.4 (a). All modes, except for the silent mode B1+E, which remains practically unchanged, undergo a hardening process; that is, they are shifted to higher wave numbers with increasing the film thickness.

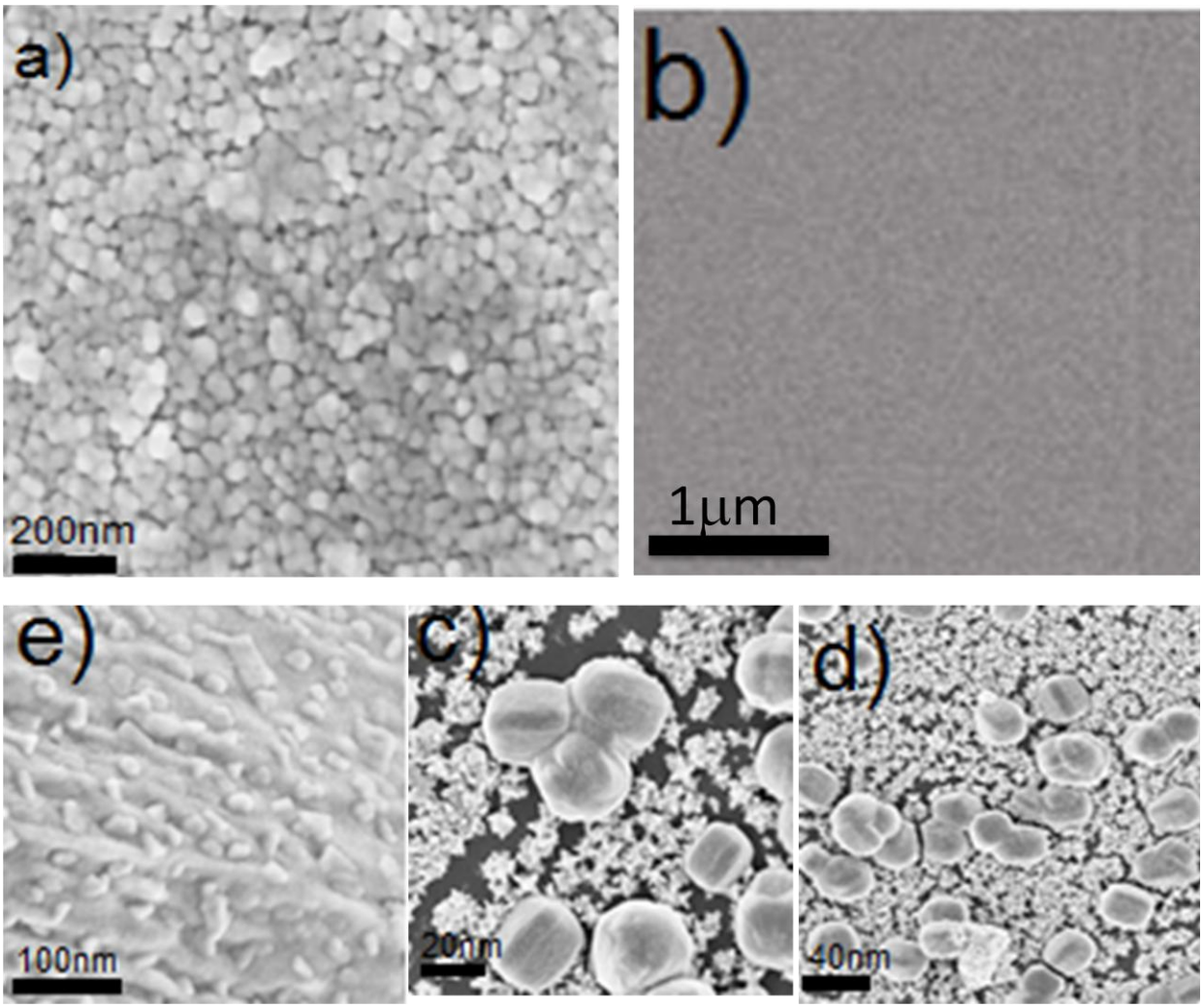

Figure 5.1. Low magnification (a) and high magnification (b) top view FE-SEM images of the 374 nm-thick $PbTiO_3$ thin films

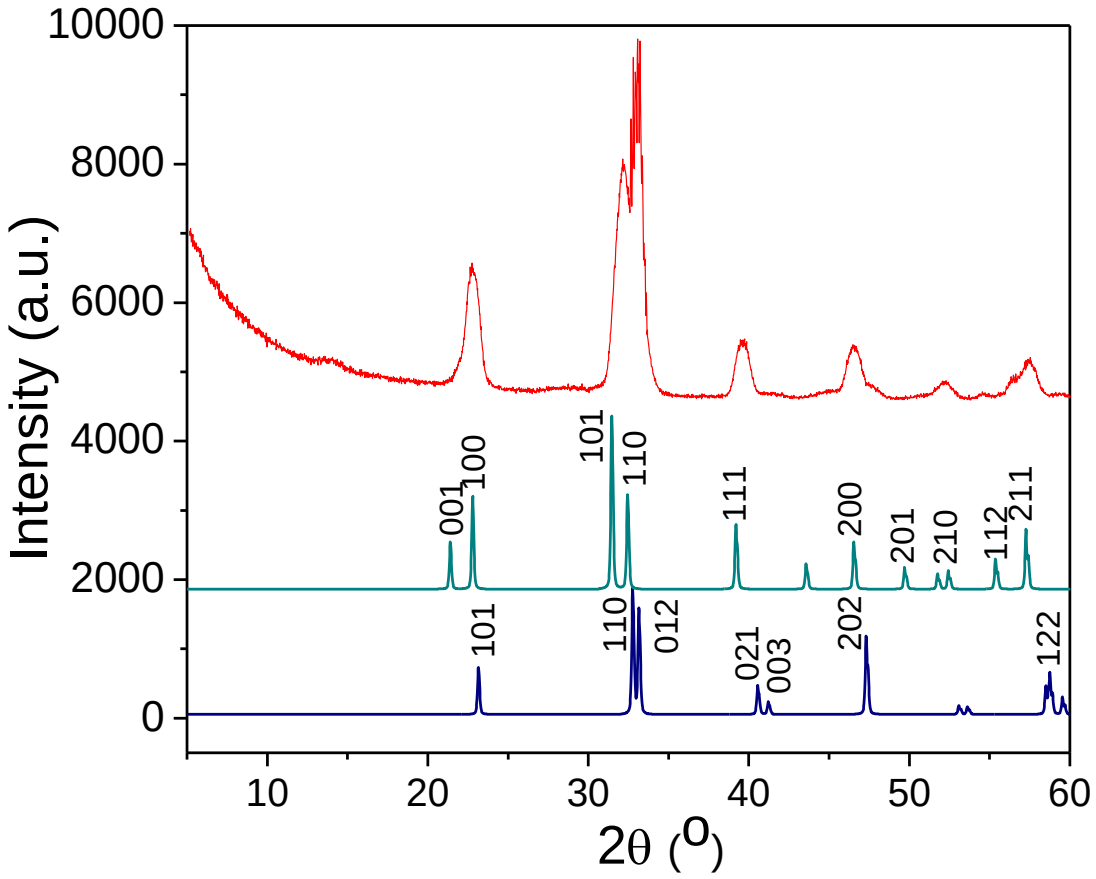

Figure 5.2. θ–2θ X-Ray diffraction pattern of a 240 nm-thick PbTiO3 thin film deposited onto a LaNiO3-buferred (001) Si substrate

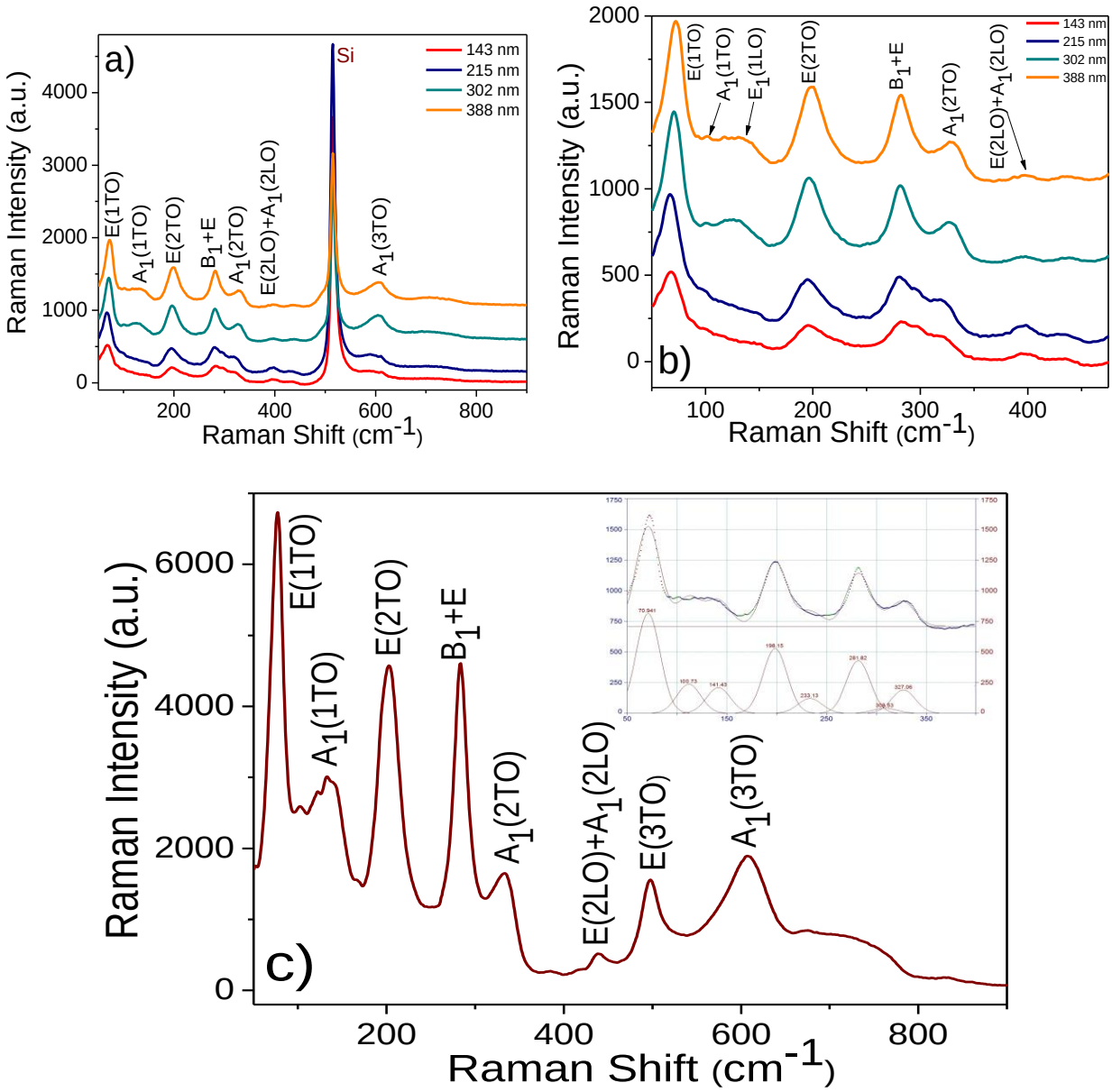

Figure 5.3. (a) Raman spectra of the 143-, 215-, 302-, and 388-nm-thick PbTiO3 thin films deposited onto a LaNiO3-buferred (100) Si substrate; (b) a close-up of Figure 3 (a) without the intense Si peak; (c) Raman spectrum of the PTO powder collected from the same experiment. The inset shows the Raman bands fitted with the Peak Fit software to precisely locate the position of the individual peaks.

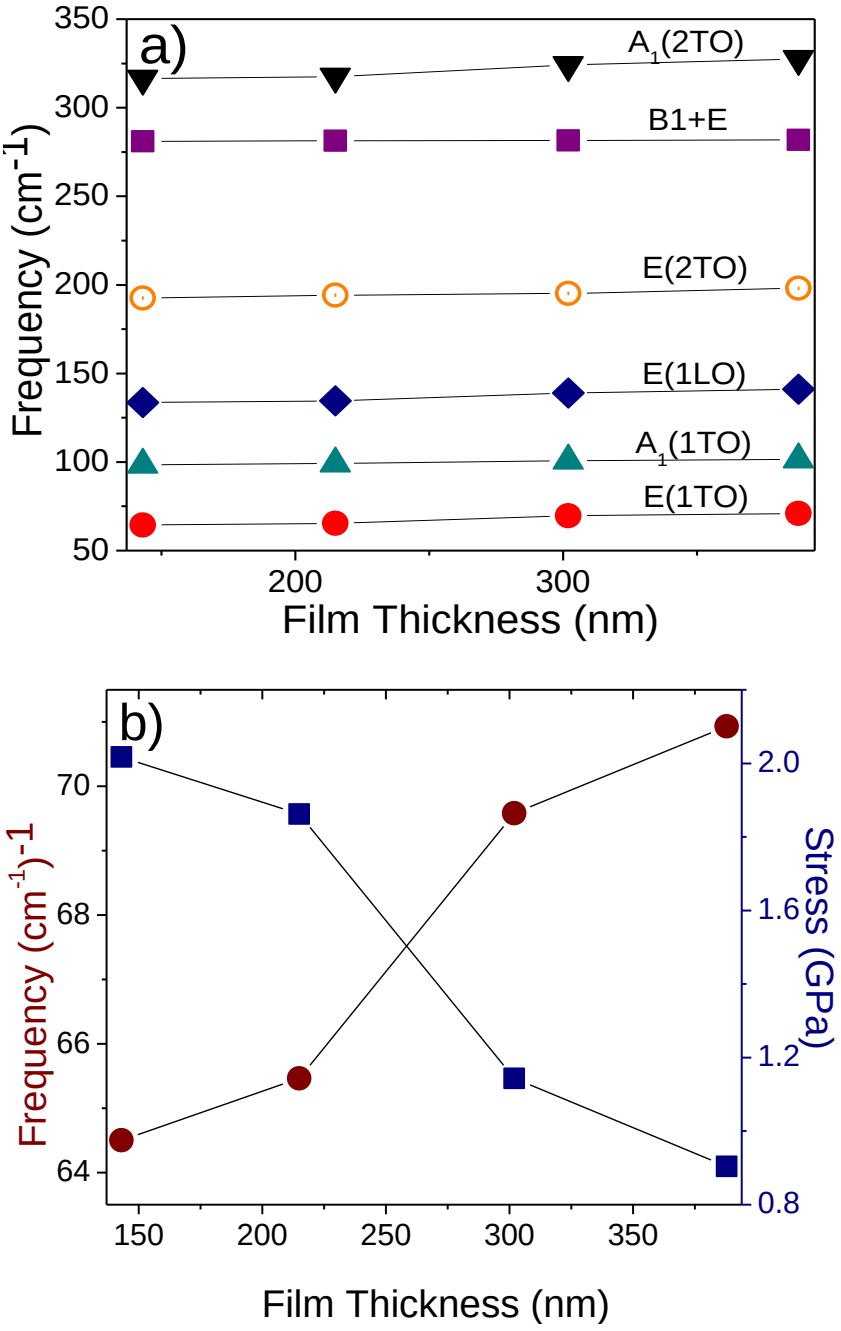

Figure 5.4. (a) Variation of the mode frequency with the thickness of the PTO thin films. (b) Dependence of the E(1TO) soft mode phonon frequency (red circles; left ordinate) and the residual stress (blue squares, right ordinate) on the thickness of the films

For the estimation of the residual stress, we considered the E(TO) modes in the Raman spectrum, since it is well-known that they are very sensitive to the hydrostatic pressure,[61,63,64] the temperature,[65] and the chemical substitution of the cations with other elements.[66-68] Quantitatively, the variation of the (E1TO) soft mode can be modeled by the following equation: $\omega(\sigma) = \omega(0) - (\partial\omega)/(\partial\sigma)\sigma$ (eq 1),[61] where $\omega(\sigma)$ represents the angular mode frequency under a stress and the $\omega(0)$ is the free phonon mode frequency, respectively. For a very accurate estimation of the peak positions in the spectrum, a deconvolution algorithm with a linear baseline was used and the experimental data was smoothed with a four-order polynomial function (Savitsky- Golay). The fitting process was performed with the PeakFit 4.12 software using a Gaussian function, and the reliability factors for each refinement procedure were higher than 98%.

These results were obtained by using 76.2 and 204.5 cm^{-1} for the Raman frequencies of these two modes in the powdered sample, measured experimentally, and the value of -5.8 cm^{-1}/GPa[61] for the $(\partial\omega)/(\partial\sigma)$ term, respectively. As seen in Table 1, the values of the internal stress deduced from the E(1TO) and E(2TO) Raman modes are very close, also in an excellent agreement with those reported by others for PTO films deposited via both physical and chemical methods.[69, 60, 64,70,71] The negative sign of σ indicates that the polycrystalline PTO films obtained by the LPD method are under a compressive stress; results that are in good agreement with those obtained from the estimation of the lattice volume by using XRD data. Sun and co-workers reported the existence of an in-plane compressive stress in $PbTiO_3$ grown epitaxially by MOCVD onto (110) $NdGaO_3$ substrates.[63] The residual compressive stress has been ascribed to the interaction between the substrate and the film. Likewise, the granular $PbTiO_3$ films prepared by the liquid phase deposition have a compressive stress due to the mismatch between the films and the LaNiO3 buffer layer. $LaNiO_3$ crystallizes in a rhombohedral lattice with a cell parameter a = 0.382 nm, which is slightly smaller than that of $PbTiO_3$ (a = 0.3907 nm) and therefore can induce a compressive stress. Furthermore, as illustrated in Figure 5.4 (b), the compressive stress in the PTO thin films decreases significantly with increasing the thickness of the films.

The AFM image of the 143-, 215-, 302-, and 388-nm-thick PbTiO3 films (parts a, d, g, and j of Figure 5.5) show that the films are uniform over the scanned surface (10 μm X 10 μm) and are

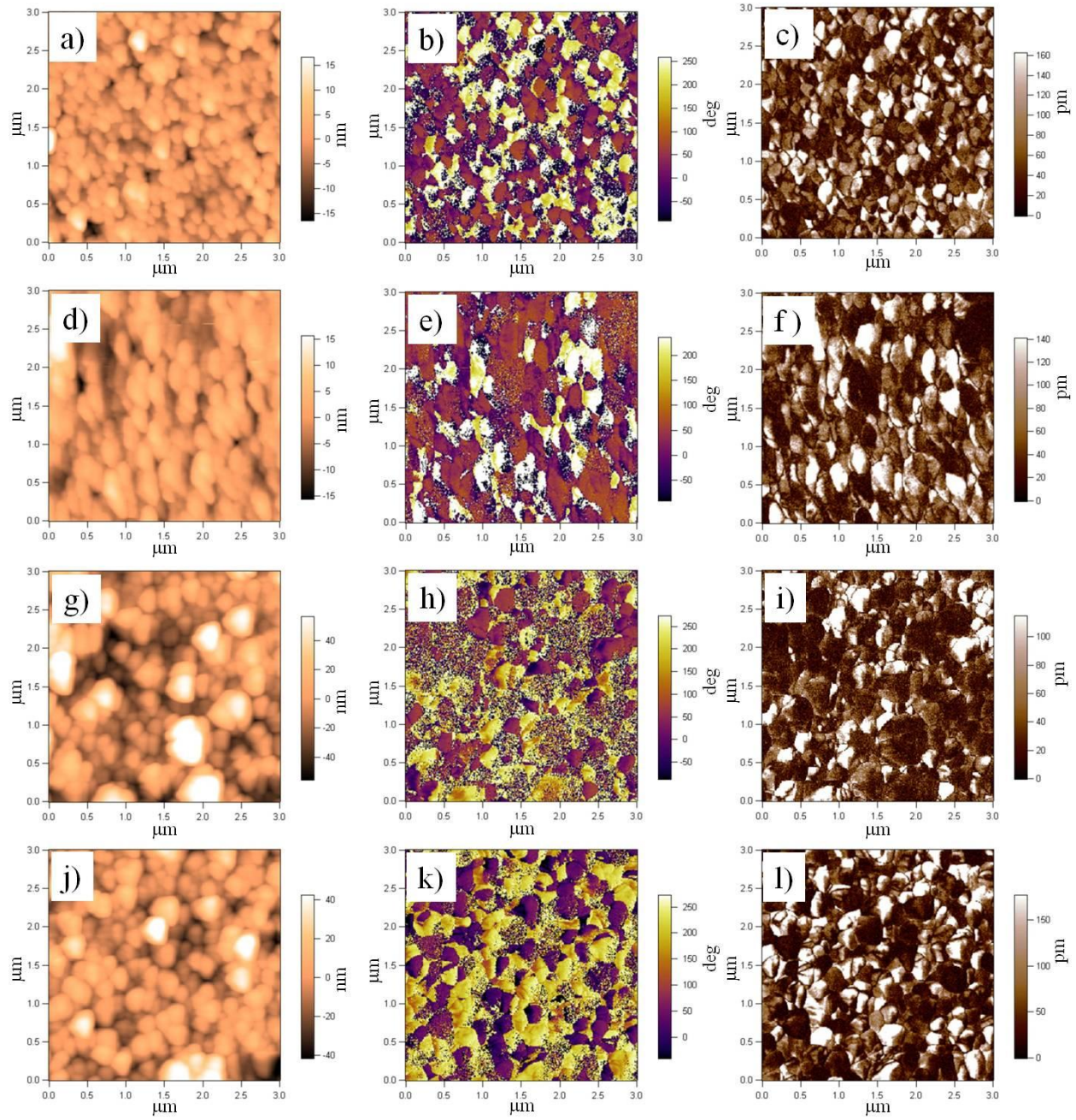

Figure 5.5. Topography AFM (a, d, g, and j), phase contrast (b, e, h, and k) and amplitude (c, f, i, and l) images of the of the 143-, 215-, 302-, and 388-nmthick PTO films.

free of defects. These films are constructed by densely packed spheroidal grains with an average size of 240 nm, and the root mean-square (rms) roughness is about 11.3 nm. Parts b, e, h, k, c, f, i, and l of Figure 5.5 show the phase and amplitude contrast images of the same films without poling the samples. The amplitude and phase images feature randomly distributed bright and dark areas distributed randomly over the surface of the films. While the bright areas correspond to negative domains with the polarization vector perpendicular to the surface of the film and oriented downward, the dark spots corresponding to positive domains having the polarization oriented upward, respectively.

The high quality of the films is confirmed by PFM bit-mapped lithography experiments (Figure 5.6 (c)) that shows that domain arrays and complex patterns can be "written" on the film without changing the topography of the surface. In PFM measurements and PFM lithography, an alternating current electric field is applied in a direction perpendicular to the film between a bottom electrode and a conductive tip, which acts as the top electrode having the sample designed in capacitor geometry. The word "amri" (abbreviation for the "Advanced Materials Research Institute") was written onto the 215 nm-thick $PbTiO_3$ film by using PFM bit-mapped lithography. In the first step of the writing process all the electrical dipoles in the film were oriented upward (bright areas) by applying a direct current electric field higher than the local coercive field. The tip was subsequently removed from the surface of the film and the electric field passing through the tip was reversed followed by writing the pattern by raster scanning the tip over specific areas. This process induced the reversal of the polarization in these areas, corresponding to discernible dark regions in Figure 5.6 (c). The written polarization was subsequently read by electrostatic force microscopy. The piezoelectric signal is detected by applying a periodic bias voltage $V = V_{dc} + V_{ac} \cos(\omega t)$ to the tip which brought in contact with the film surface and measuring the first harmonic component of the tip deflection $A = A_0 + A_{1\omega} \cos(\omega t+j)$.The variation of the phase and amplitude of the local piezoelectric response of $PbTiO_3$ films with different thicknesses are presented in Figure 5.7. The amplitude of the piezoelectric signal is related to the local electromechanical interaction, whereas the phase of the piezoelectric signal provides information about the polarization direction below the tip.[72] The hysteretic behavior of the phase and amplitude signal reveals the existence of a switchable intrinsic lattice polarization in the PTO films. The polarization can be reversed at voltages below 5 V, and the saturation can be reached at bias voltages typically below 10 V. The values of the coercive bias

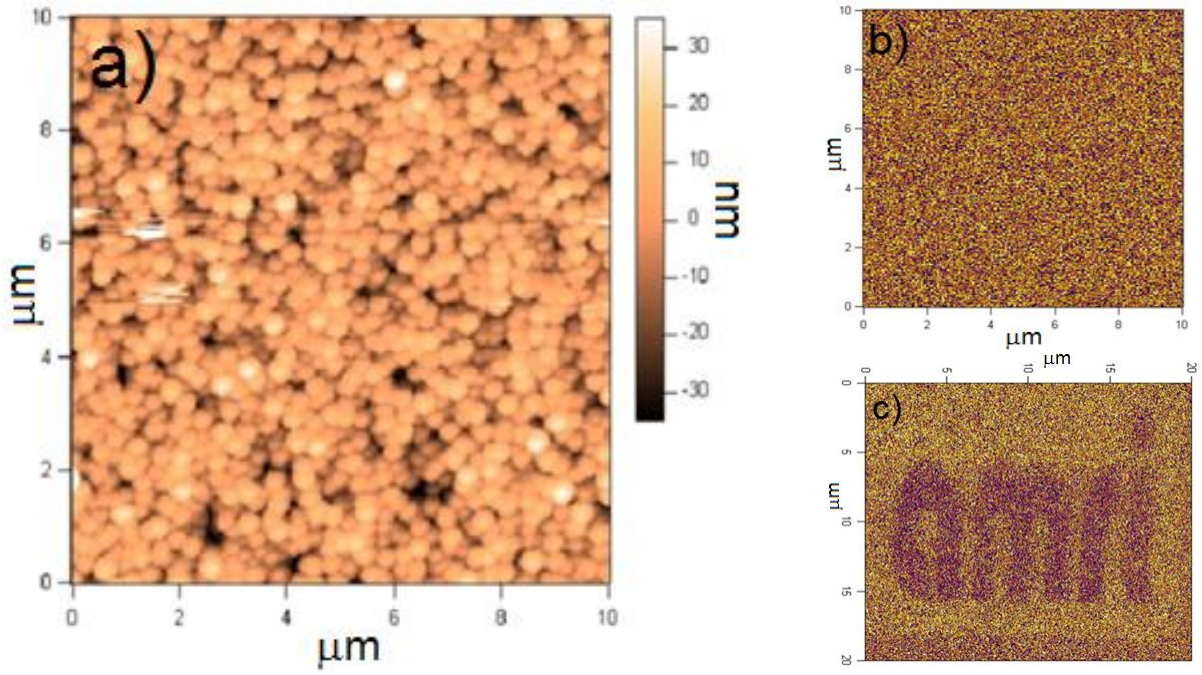

Figure 5.6 (a) Topography AFM image of the 240 nm-thick PbTiO3 film; (b) of the PTO thin films; (b) Variation of the E(1TO) phonon frequency and the residual stress values with the thickness of the films

of the PTO films for local switching were 4.1, 4.9, and 5.2 V, respectively. The change in the phase signal for all the films when the bias voltage is swept from 20 to +20 V is 179, which is associated with the existence of 180 domain structures. The dominance of 180 domain structures of the dielectric dipoles in the out-of plane direction is also suggested by the linearity of the amplitude loops of the piezoelectric signal measured by a lock-in technique.

As seen in Figure 5.7 (b), a linear response of the amplitude component of the piezoelectric response of the films was measured by varying the bias voltage with a maximum displacement of 0.168, 0.163, and 0.194 nm at a driving voltage of E = +19.4 V. The effective values of the zero-field piezoelectric coefficient (d_{33}) of the films were calculated by fitting the linear portion of the amplitude plot, since it is well-known that the amplitude of the displacement of the tip (A) is directly proportional with the ac bias voltage (V_{ac}): $A = d_{33}V_{ac}Q$, where Q stands for a proportionality factor that can vary between 10 and 100 and accounts for the amplitude enhancement at the tip sample resonance. By considering the value of the proportionality factor in the lower end of this range, the magnitude of the piezoelectric coefficient (d_{33}) of the143-, 215-, 302-, and 388-nm-thick PTO films are 12.1, 27.6, 36.1, and 99.3 pm/V, which are in good agreement with those reported in the literature for layered PbTiO3.[71,73] Morita et al. have found a value of the effective piezoelectric constant of 97 pm/V in PbTiO3 epitaxial thin films deposited hydrothermally onto (100) $SrTiO_3$ single crystals and speculated that the high value of d_{33} may originate from the a-domain structure which is included into the dominant c domains.[74] In our films, however, the variation of the piezoelectric coefficient with the film thickness is similar to that reported for other Pb-based perovskite thin films structures obtained by both physical[75] and chemical[76] methods. This is the result of the reduction of the stress and the substrate-induced clamping effect which will substantially ease the domain movement and will improve the electrical properties of the films. However, other authors suggested an opposite trend, whereby the variation of the piezoelectric coefficient with the thickness of perovskite films this being ascribed to the influence of other factors, such as the tetragonality of the films, which decreases linearly with increasing the film thickness seemingly playing an important role in decreasing the value of the piezoelectric coefficient.[71,77]

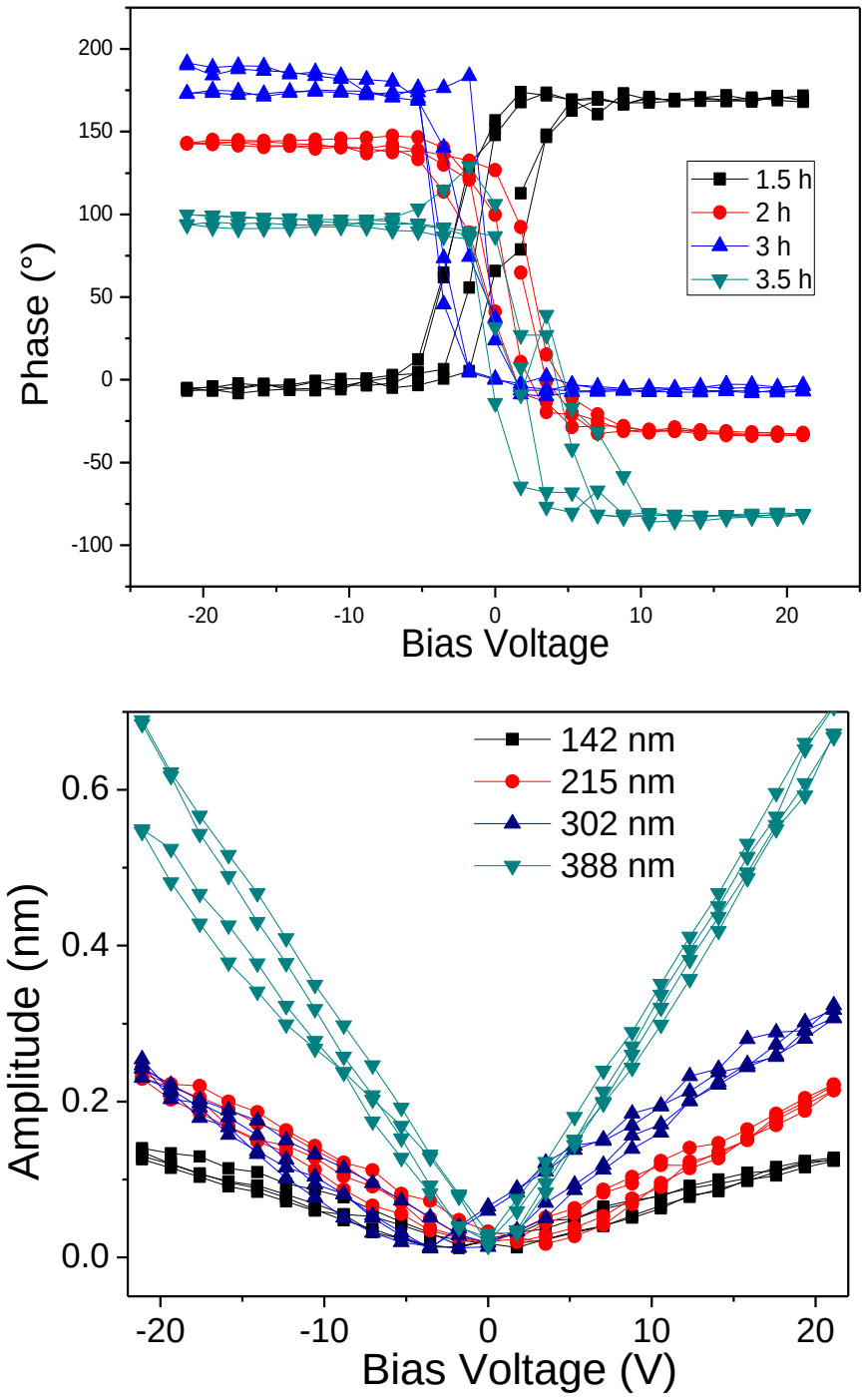

Figure.5.7. Phase (a) and amplitude (b) local hysteresis loops of the piezoelectric signal of the PTO thin films with different thicknesses

5.4. Conclusions

In summary, the morphological and piezoelectric properties of highly uniform PTO films obtained by the liquid-phase deposition were studied by Raman and PFM. Granular, polycrystalline PTO films with an excellent adhesion to LaNiO3-buffered (100) Si substrates are constructed by densely packed spheroidal particles with an average size of 30 nm and grow via a Volmer-Weber mechanism. The residual stress estimated from the E(2TO) band in the Raman spectrum is compressive and decreases from 2.03 to 1.09 GPa, whereas the static piezoelectric coefficient d33 varied from 12.1 to 99.3 pm/V with increasing the film thickness. These PbTiO3 thin film structures may be promising candidates for the design of future optoelectronic and piezoelectric sensors, as well as can serve in the design of multilayered magnetoelectric structures in combination with magnetostrictive materials, both metallic alloys or oxides.

5.5. References

(1) Huang, H.; Yao, X.; Wu, X.; Wang, M.; Zhang, L. *Microelectronic Engineering* **2003**, *66*, 688.

(2) Cho, C. R.; Jang, M. S.; Jeong, S. Y. *Crystal Research and Technology* **1995**, *30*, 873.

(3) Ye, C.; Tamagawa, T.; Schiller, P.; Polla, D. L. *Sensors and Actuators A: Physical* **1992**, *35*, 77.

(4) Wong, C. W.; Jeon, Y.; Barbastathis, G.; Kim, S.-G. *Appl. Opt.* **2003**, *42*, 621.

(5) Chopra, S.; Sharma, S.; Goel, T. C.; Mendiratta, R. G. *Journal of Electroceramics* **2004**, *13*, 155.

(6) Dogheche, E.; Jaber, B.; Rémiens, D. *Appl. Opt.* **1998**, *37*, 4245.

(7) Okuyama, M.; Hamakawa, Y. *International Journal of Engineering Science* **1991**, *29*, 391.

(8) Wang, Z.; Hu, T.; Tang, L.; Ma, N.; Song, C.; Han, G.; Weng, W.; Du, P. *Applied Physics Letters* **2008**, *93*, 222901.

(9) Morita, T.; Cho, Y. *Integrated Ferroelectrics* **2004**, *64*, 247.

(10) Polta, D. L. *Microelectronic Engineering* **1995**, *29*, 51.

(11) Chien, A. T.; Sachleben, J.; Kim, J. H.; Speck, J. S.; Lange, F. F. *J. Mater. Res.* **1999**, *14*, 3303.

(12) Xu, W. P.; Zheng, L. R.; Lin, C. L.; Okuyama, M. *Philosophical Magazine B-Physics of Condensed Matter Statistical Mechanics Electronic Optical and Magnetic Properties* **1998**, *77*, 177.

(13) Cho, W. S.; Yoshimura, M. *J. Mater. Res.* **1997**, *12*, 833.

(14) Dippel, A. C.; Schneller, T.; Waser, R. *Integrated Ferroelectrics* **2008**, *98*, 3.

(15) Wu, G. H.; Zhou, H.; Zhou, X. Y.; Qin, N.; Bao, D. H. *Journal of the American Ceramic Society* **2010**, *93*, 925.

(16) He, G.; Iijima, T.; Funakubo, H. *J. Mater. Res.* **2002**, *17*, 2217.

(17) De Dobbelaere, C.; Hardy, A.; D'Haen, J.; Van den Rul, H.; Van Bael, M. K.; Mullens, J. *Journal of the European Ceramic Society* **2009**, *29*, 1703.

(18) Fernandez, R.; Holgado, S.; Huang, Z. R.; Calzada, M. L.; Ricote, J. *Journal of Materials Research* **2010**, *25*, 890.

(19) Nagarajan, V.; Stanishevsky, A.; Ramesh, R. *Nanotechnology* **2006**, *17*, 338.

(20) Wang, D. G.; Chen, C. Z.; Ma, J.; Liu, T. H. *Applied Surface Science* **2008**, *255*, 1637.

(21) Calzada, M. L.; Torres, M.; Fuentes-Cobas, L. E.; Mehta, A.; Ricote, J.; Pardo, L. *Nanotechnology* **2007**, *18*.

(22) Negi, N. S.; Sharma, D. R.; Rastogi, A. C. *Journal of Physics and Chemistry of Solids* **2008**, *69*, 41.

(23) Yamazaki, H.; Shimura, T.; Sakamoto, W.; Yogo, T. *Journal of the Ceramic Society of Japan* **2010**, *118*, 631.

(24) Byun, C.; Jang, J. W.; Cho, Y. J.; Lee, K. J.; Lee, B. W. *Thin Solid Films* **1998**, *324*, 94.

(25) Papiernik, R.; Hubert-Pfalzgraf, L. G.; Chaput, F. *Journal of Non-Crystalline Solids* **1992**, *147-148*, 36.

(26) Krupanidhi, S. B.; Hu, H.; Kumar, V. *Journal of Applied Physics* **1992**, *71*, 376.

(27) Ju, J.; Wang, D.; Lin, J.; Li, G.; Chen, J.; You, L.; Liao, F.; Wu, N.; Huang, H.; Yao, G. *Chemistry of Materials* **2003**, *15*, 3530.

(28) Klee, M.; Eusemann, R.; Waser, R.; Brand, W.; van Hal, H. *Journal of Applied Physics* **1992**, *72*, 1566.

(29) Moon, J.; Li, T.; Randall, C. A.; Adair, J. H. *Journal of Materials Research* **1997**, *12*, 189.

(30) Cheng, H. M.; Ma, J. M.; Zhao, Z. G. *Chemistry of Materials* **1994**, *6*, 1033.

(31) Palkar, V. R.; Malik, S. K. *Solid State Communications* **2005**, *134*, 783.

(32) Liu, X. D.; Funakubo, H.; Noda, S.; Komiyama, H. *Chemical Vapor Deposition* **2001**, *7*, 253.

(33) Stankus, V.; Dudonis, J.; Pranevicius, L.; Pranevicius, L. L.; Milcius, D.; Templier, C.; Riviere, J. P. *Thin Solid Films* **2003**, *426*, 78.

(34) Wang, Y. G.; Xu, G.; Yang, L. L.; Ren, Z. H.; Wei, X.; Weng, W. J.; Du, P. Y.; Shen, G.; Han, G. R. *Journal of Alloys and Compounds* **2009**, *481*, L27.

(35) Hsu, M. C.; Leu, I. C.; Sun, Y. M.; Hon, M. H. *Journal of Solid State Chemistry* **2006**, *179*, 1421.

(36) Modeshia, D. R.; Walton, R. I. *Chemical Society Reviews* **2010**, *39*, 4303.

(37) Hsu, M. C.; Sun, Y. M.; Leu, I. C.; Hon, M. H. *Applied Surface Science* **2007**, *253*, 7639.

(38) Hsu, M. C.; Sun, Y. M.; Leu, I. C.; Hon, M. H. *Journal of the Electrochemical Society* **2006**, *153*, F260.

(39) Yourdkhani, A.; Perez, A. K.; Lin, C.; Caruntu, G. *Chemistry of Materials* **2010**, *22*, 6075.

(40) Gao, Y. F.; Masuda, Y.; Yonezawa, T.; Koumoto, K. *Materials Science and Engineering B-Solid State Materials for Advanced Technology* **2003**, *99*, 290.

(41) Gao, Y. F.; Masuda, Y.; Koumoto, K. *Chemistry of Materials* **2003**, *15*, 2399.

(42) Lee, M. K.; Liao, H. C.; Tung, K. W.; Shih, C. M.; Shih, T. H. *Journal of Physics D-Applied Physics* **2002**, *35*, 61.

(43) Gutierrez-Tauste, D.; Domenech, X.; Hernandez-Fenollosa, M. A.; Ayllon, J. A. *Journal of Materials Chemistry* **2006**, *16*, 2249.

(44) Rossetti, G. A.; Cross, L. E.; Kushida, K. *Applied Physics Letters* **1991**, *59*, 2524.

(45) Meng, X. J.; Sun, J. L.; Yu, J.; Ye, H. J.; Guo, S. L.; Chu, J. H. *Appl. Surf. Sci.* **2001**, *171*, 68.

(46) He, H. C.; Ma, J.; Lin, Y. H.; Nan, C. W. *Journal of Physics D-Applied Physics* **2009**, *42*.

(47) Vopsaroiu, M.; Blackburn, J.; Cain, M. G. *Journal of Physics D-Applied Physics* **2007**, *40*, 5027.

(48) Jesser, W. A.; Matthews, J. W. *Philosophical Magazine* **1968**, *17*, 461

(49) Koch, R. *Journal of Physics-Condensed Matter* **1994**, *6*, 9519.

(50) Yu, X.; Duxbury, P. M.; Jeffers, G.; Dubson, M. A. *Physical Review B* **1991**, *44*, 13163.

(51) Abermann, R.; Koch, R.; Martinz, H. P. *Vacuum* **1983**, *33*, 871.

(52) Li, A. D.; Wu, D.; Ge, C. Z.; Lu, P.; Ma, W. H.; Zhang, M. S.; Xu, C. Y.; Zuo, J.; Ming, N. B. *Journal of Applied Physics* **1999**, *85*, 2146.

(53) Seifert, A.; Lange, F. F.; Speck, J. S. *Journal of Materials Research* **1995**, *10*, 680.

(54) Seifert, A.; Vojta, A.; Speck, J. S.; Lange, F. F. *Journal of Materials Research* **1996**, *11*, 1470.

(55) Maeda, M.; Ishida, H.; Soe, K. K. K.; Suzuki, I. *Japanese Journal of Applied Physics Part 1-Regular Papers Short Notes & Review Papers* **1993**, *32*, 4136.

(56) Liu, W. G.; Kong, L. B.; Zhang, L. Y.; Yao, X. *Solid State Communications* **1995**, *93*, 653.

(57) Valim, D.; Souza, A. G.; Freire, P. T. C.; Mendes, J.; Guarany, C. A.; Reis, R. N.; Araujo, E. B. *Journal of Physics D-Applied Physics* **2004**, *37*, 744.

(58) Bartasyte, A.; Chaix-Pluchery, O.; Kreisel, J.; Santiso, J.; Margueron, S.; Boudard, M.; Jimenez, C.; Abrutis, A.; Weiss, F. O. *Ieee Transactions on Ultrasonics Ferroelectrics and Frequency Control* **2007**, *54*, 2623.

(59) Pignolet, A.; Schmid, P. E.; Wang, L.; Levy, F. *Journal of Physics D: Applied Physics* **1991**, *24*, 619.

(60) Taguchi, I.; Pignolet, A.; Wang, L.; Proctor, M.; Levy, F.; Schmid, P. E. *Journal of Applied Physics* **1993**, *73*, 394.

(61) Sanjurjo, J. A.; López-Cruz, E.; Burns, G. *Physical Review B* **1983**, *28*, 7260.

(62) Chaban, N.; Weber, M.; Pignard, S.; Kreisel, J. *Applied Physics Letters* **2010**, *97*, 031915.

(63) Sun, L.; Chen, Y.-F.; He, L.; Ge, C.-Z.; Ding, D.-S.; Yu, T.; Zhang, M.-S.; Ming, N.-B. *Physical Review B* **1997**, *55*, 12218.

(64) Fu, D.; Ogawa, T.; Suzuki, H.; Ishikawa, K. *Applied Physics Letters* **2000**, *77*, 1532.

(65) Burns, G.; Scott, B. A. *Physical Review B* **1973**, *7*, 3088.

(66) Shen, B.-g.; Cheng, Z.-h.; Gong, H.-y.; Liang, B.; Yan, Q.-w.; Zhan, W.-s. *Solid State Communications* **1995**, *95*, 813.

(67) Burns, G.; Scott, B. A. *Solid State Communications* **1973**, *13*, 417.

(68) Frantti, J.; Lantto, V. *Physical Review B* **1996**, *54*, 12139.

(69) Valim, D.; Filho, A. G. S.; Freire, P. T. C.; Filho, J. M.; Guarany, C. A.; Reis, R. N.; Araújo, E. B. *Journal of Physics D: Applied Physics* **2004**, *37*, 744.

(70) Ching-Prado, E.; Reynes-Figueroa, A.; Katiyar, R. S.; Majumder, S. B.; Agrawal, D. C. *Journal of Applied Physics* **1995**, *78*, 1920.

(71) Kim, Y. K.; Kim, S. S.; Shin, H.; Baik, S. *Applied Physics Letters* **2004**, *84*, 5085.

(72) Rodriguez, B. J.; Jesse, S.; Alexe, M.; Kalinin, S. V. *Advanced Materials* **2008**, *20*, 109.

(73) Kighelman, Z.; Damjanovic, D.; Cantoni, M.; Setter, N. *Journal of Applied Physics* **2002**, *91*, 1495.

(74) Morita, T.; Cho, Y. *Applied Physics Letters* **2006**, *88*, 112908.

(75) Kim, D. M.; Eom, C. B.; Nagarajan, V.; Ouyang, J.; Ramesh, R.; Vaithyanathan, V.; Schlom, D. G. *Applied Physics Letters* **2006**, *88*, 142904.

(76) Li, J.-F.; Zhu, Z.-X.; Lai, F.-P. *The Journal of Physical Chemistry C* **2010**, *114*, 17796.

(77) Roytburd, A. L.; Alpay, S. P.; Nagarajan, V.; Ganpule, C. S.; Aggarwal, S.; Williams, E. D.; Ramesh, R. *Physical Review Letters* **2000**, *85*, 190.

6. Magnetoelectric Perovskite-Spinel Bilayered Nanocomposites Synthesized by Liquid Phase Deposition

6.1. Introduction

Recent advances in miniaturization in electronics and computing generated a surge of interest in magnetoelectric ceramic nanocomposites as they exhibit a strong room temperature magnetoelectric effect (ME) which can be potentially used in various applications in magnetic data storage, spintronics and sensing.[1-3] Magnetoelectric nanocomposites are hybrid architectures consisting of a ferromagnetic and a ferroelectric phase coupled together via a strain. Upon application of an electric field, the ferroelectric phase, which has electrostrictive properties, will respond to the external stimulus by changing its physical dimensions. Therefore, the induced stress is transmitted to the magnetostrictive phase through the shared interface eventually leading to a change of its magnetization. Among the most studied magnetoelectric nanocomposites are those obtained by combining a ferro/ferrimagnetic spinel (MFe_2O_4) with a ferroelectric perovskite (ABO_3). This is because both spinels and perovskites have high chemical, thermal and mechanical stabilities and form a limited number of secondary phases when mixed together. One of the possible geometries in which these phases can be assembled is a horizontal multilayered structure consisting of alternate layers of a spinel and a perovskite material. When the oxide phases are single crystalline, their growth during the formation of hybrid architectures takes place epitaxially as a result of the commensurability of their lattice (lattice mismatch <5%) thereby leading to strong interfacial coupling between the spinel and perovskite phases. Last, but not least, interfacing a ferroelectric with a ferromagnetic material in a planar geometry will greatly simplify the chip-integration required for miniaturization of electronics and will minimize the leakage currents due to the high resistivity of the ferrites preventing the composites from electric breakdown during the poling process. Thus, perovskite-spinel nanocomposite layered structures are very attractive for the design of many functional devices including controlled phase shifters, transducers, reading/writing devices in magnetic data storage, spin transistors, broadband magnetic field sensors, magnetoelectric memory cells and magnetically controlled electro-optic or piezoelectric devices.[4-11] Multilayered MFe_2O_4-ABO_3 nanostructures have been fabricated almost exclusively by physical methods including pulse laser deposition (PLD)[12-14], laser molecular beam epitaxy (LMBE)[15-16] or radio-frequency (rf) sputtering[17]. Although these techniques yield highly uniform, epitaxial films they are restricted to surfaces

with simple morphologies and require highly pure targets and expensive equipment. Fontcuberta *et al*. grown nanocomposite films with the nominal composition $0.35CoFe_2O_4$-$0.65BaTiO_3$ onto (001) Nb-doped $SrTiO_3$ single crystals by radio–frequency (rf) sputtering. They observed a decrease of the dielectric losses as the thickness of the films decrease and with increasing the synthesis temperature from 750 to 850 ^oC.[18] Srinivasan and coworkers have fabricated laminate structures by the so-called tape casting technique[19] whereas Hao *et al.* prepared 40, 60, 80 and 100 nm-thick $CoFe_2O_4$ films deposited onto 100 nm-thick $BaTiO_3$ by molecular beam epitaxy.[20]

Solution-based approaches are very attractive for the design of perovskite-spinel magnetoelectric nanocomposites. This is because they allow the mixing of the precursors at the atomic scale which can potentially enhance the coupling between the two phases. Also, they use relatively low processing temperatures which can significantly reduce the diffusion pathways of the molecular species, thereby preventing the formation of unwanted, secondary phases. Despite these advantages, chemical methods have been rarely used in the fabrication of magnetoelectric multilayers. Recently, Jia and coworkers prepared self-assembled epitaxial $BaTiO_3$-$NiFe_2O_4$ thin film nanocomposites by a spin coating process using solutions of the metal precursors mixed with etylenediaminetetraacetic acid (EDTA) and polyethyleneimine followed by a heat treatment at 950 ^oC.[21] A simple, environmentally benign, highly efficient and easily scalable chemical deposition method yielding highly uniform metal oxide thin films is the so-called liquid phase deposition (LPD). This approach exploits the slow hydrolysis of supersaturated solutions of metal fluoro-complexes at low temperature whereby the fluoride ions in the inner coordination sphere of the metal are progressively replaced by OH^- ions and/or water molecules.

$$MF_n^{(n-2m)-} + mH_2O \rightleftharpoons 1MO_m + nF^- + 2mH^+ \quad (1)$$

$$H_3BO_3 + 4HF \rightleftharpoons BF_4^- + H_3O^+ + 2H_2O \quad (2)$$

The hydrolysis reaction can be shifted to the right side upon addition of a fluoride scavenger such as H_3BO_3 which forms water soluble complexes with the F^- ions. Initially developed for the deposition of binary oxides, such as TiO_2[22], SiO_2[23], ZrO_2[24], SnO_2[25], Fe_2O_3[26] and NiO[27] the LPD method was rapidly extended to the deposition of complex oxides, such as perovskite titanates ABO_3 (A=Ba, Sr and Pb)[28-29]. Recently, our group has successfully used this methodology for the deposition of highly uniform transition metal ferrite films with tunable chemical composition and controllable magnetic properties.[30-31] In this work we describe an alternative soft-solution route

for the fabrication of layered magnetoelectric nanostructures using the liquid phase deposition method. The synthesis and characterization of two types of bilayered structures consisting of $PbTiO_3$ as the ferroelectric phase and a hard (cobalt ferrite)/soft (nickel ferrite) transition metal ferrite as the magnetostrictive materials are presented to exemplify the generality of this approach. However, due to its simplicity, this method can be virtually used for the design of any combination of perovskite-type titanate and transition metal ferrite in a layered geometry whereby the number of layers and their thickness can be easily controlled upon properly adjusting the number of deposition steps and the deposition time, respectively.

6.2. Experimental

6.2.1. Chemical Deposition of Metal Oxide Thin Films

All experiments were performed in open atmosphere by using a magnetic hotplate (IKA Works, Inc.) equipped with a temperature controller and a pH electrode. $PbTiO_3$ and MFe_2O_4 (M=Co, Ni) thin films were deposited from treatment solutions prepared by dissolving reagent grade purity chemicals (Alfa Aesar) in deionized water (18 MΩ) obtained from a Barnstead Nanopure water purification system. Both perovskite and spinel thin films were deposited on highly doped (100) silicon wafers with a resistivity of 0.05 Ωcm and commercial non-alkali glass plates (Corning no. 7059). Since the glass melts at temperatures above 600 ^oC only the perovskite films deposited on silicon were annealed at 750 ^oC. Prior to deposition, the substrates were cleaned with a mixture of acetone and ethanol (50:50% wt.) and blow-dried with compressed argon. A 200 nm $LaNiO_3$ bottom electrode was spin coated on the Si substrates by using a 0.4 M solution of $La(NO_3)_3$ and $Ni(ac)_2$ dissolved in ethanol according to a procedure similar to that proposed by Meng and cowokers.[32] The precursor solution was spin coated at 3500 rpm for 30 s and the resulting films were dried at 150 ^oC for 2 h to allow the removal of the solvent and subsequently at 700 ^oC for 2 h in open atmosphere. In addition to serving as a bottom electrode, the $LaNiO_3$ buffer layer can substantially minimize the clamping effect exerted by the substrate ultimately leading to the enhancement of magnetoelectric effect.[33]

a) *Deposition of $PbTiO_3$ thin films*

The deposition of perovskite films was performed by adapting the experimental procedure proposed by Hsu and coworkers.[34-35] In a typical experiment three individual solutions containing 1 mmol $Ba(NO_3)_2$ or $Pb(NO_3)_2$, 1 mmol $(NH_4)_2TiF_6$ and 3 mmol of H_3BO_3 were

mixed together and water was added to a final volume of 100 mL. The deposition of the $PbTiO_3$ (PTO) thin films was performed in treatment solutions whose initial pH varied between 5.2 and 5.6, depending on the pH of the deionized water and decreased slowly to 4.1-4.7 after the deposition of the films. High quality nanoparticle-based perovskite thin films with variable thicknesses were obtained by soaking the substrates in the treatment solution at 45 ^{o}C for a period of time, typically varying between 1 and 4 h. After the deposition, the substrates were removed, rinsed and cleaned ultrasonically with distilled water, dried with a N_2 flow and heat treated at 750 ^{o}C in open atmosphere for 3 h followed by natural cooling to room temperature.

b) *Deposition of MFe_2O_4 (M=Co, Ni) thin films*

The iron source used in the deposition of the MFe_2O_4 thin films was a solution obtained by dissolving 0.25 g of FeO(OH) in 50 ml of 1M $NH_4F{\cdot}HF$ aqueous solution. FeOOH was obtained by precipitating an aqueous solution of $Fe(NO_3)_3{\cdot}7H_2O$ with a diluted solution of ammonia. The solid product was subsequently filtered, washed and dried at room temperature in open atmosphere to ensure the oxidation of the Fe^{2+} ions. A volume of 10 mL of the Fe-containing solution was mixed with 40 mL of 0.5 M H_3BO_3 and 3 mL of 2.2 M $Co(NO_3)_2$ or $Ni(NO_3)_2$ with formation of the treatment solution. Substrates were suspended vertically and kept in the treatment solution at 45 ^{o}C for 4 h for the $CoFe_2O_4$ (CFO) films and 6 h for the $NiFe_2O_4$ (NFO) films, respectively. The initial pH of the solutions typically ranged between 5.5 and 5.9 to decrease slowly over the course of the deposition to values between 3.9 and 4.4. After their removal from the reaction solution, the films were carefully rinsed, cleaned ultrasonically with distilled water and dried under flow of nitrogen. To ensure the conversion of the metal hydroxides/oxyhydroxides into the spinel structure and the complete crystallization of the films, the thin film samples were annealed in open air at a temperature of 600 ^{o}C followed by a natural cooling to room temperature. Although in this work we report only on the design of bilayered perovskite-spinel structures, by sequential dipping the substrates into treatment solutions with containing different types of metal salt precursors one can design multilayered ceramic composites on a film-on-substrate geometry. The advantage of this method consists of its simplicity, high reliability and flexibility in varying the number of layers, their thickness, order of succession and chemical composition, respectively.

6.2.2. Characterization of the Metal Oxide Thin Films

The surface morphology, chemical composition and the microstructure of the films were investigated with a LEO 1530VP field emission scanning electron microscope (FE-SEM) operating in low vacuum mode at an accelerating voltage of 200 kV and equipped with an energy dispersive (EDS) detector. X-Ray diffraction experiments were performed in grazing incidence mode (2^o) with a Philips X'Pert System equipped with a curved graphite single-crystal monochromator (CuK_α radiation). Patterns were recorded in a step scanning mode in the 15-60^o 2θ range with a step of 0.02^o and a counting time of 10 s. The angular range was restricted to 15-60^o due to a very strong reflection of the Si substrate which appears around 68^o in 2θ and obscures the peaks of the metal oxide films. The chemical composition of the layered structures was determined by energy dispersion X-Ray (EDX) analysis and inductive coupled plasma (ICP) spectroscopy with a Varian FT220s flame absorption spectrometer. The correlation coefficient used to calibrate the instrument was 0.99915 and the calibration error did not exceed 5%. The corresponding solutions were prepared by dissolving the films in 18%HCl and then diluting them to the required concentrations. The thickness of the films was examined by a spectral reflectance method with a F20 film thickness measurement system from Filmetrics. AFM images of the thin films were collected at room temperature with an Asylum Research MFP-3D atomic force microscope working in tapping mode and using commercial Si_3N_4 cantilevers with a force constant of 0.7 Nm^{-1}.The piezoelectric properties of the perovskite films were measured with the same instrument by using a silicon tip coated with a 20 nm Pt/Ir layer. The piezoelectric signal of the samples was measured with the high voltage PFM module of the MFP-3D AFM by using an AC240TM cantilever made of tetrahedral silicon tip coated with platinum/titanium. For the fabrication of layered capacitors, Au top electrodes with areas of 5 mm^2 and a thickness of 50 nm and were sputtered on the film samples followed by the standard lithography process. Investigation of the magnetic properties of the ferrite films and ferrite/perovskite multilayered nanocomposites was performed with a Quantum Design MPMS-5S SQUID magnetometer working in the temperature range from 2 to 300 K and generating a magnetic field up to 6 T. Room temperature magnetic-field assisted Raman scattering studies were performed with a Thermo-Fisher DXR dispersive Raman spectrometer in a conventional backward geometry by using the λ=532 nm line. The spectral resolution was 3 cm^{-1}. The scattered light was analyzed with a triple monochromator coupled with an optical microscope, which allows the incident light

to be focused on the sample as a circular spot of about 2 μm in diameter. The power of the incident laser beam was relatively low (6 mW) in order to avoid film restructuring due to overheating from the laser source. Prior to collecting each Raman spectrum, samples were subjected to the action of a uniform, in-plane magnetic field with a maximum strength up to 2 kOe by using a variable-field magnetometer (VFM) provided by Asylum Research, Inc.

6.3. Results and Discussions

As previously described elsewhere[30-31], the liquid phase deposition process is based on the slow hydrolysis of metal oxyfluoro-complexes which are converted into the corresponding hydroxides and/or oxyhydroxides which form the as-deposited films. These stoichiometric mixtures of hydroxides/oxyhydroxides are usually amorphous and transform into the corresponding oxides upon heat treatment at temperatures above 500 ^{o}C. During our preliminary experiments we have systematically observed that a high concentration of the precursors in the treatment solution the addition of $Pb(NO_3)_2$ induces the instant precipitation of the hydroxyl-containing metal species and no films are deposited onto the substrates. Other authors suggested that the premature precipitation of the hydroxides can be prevented by adding few drops of diluted HNO_3 until the pH of the treatment solution is below 2.8.[2,35] However, when the pH of the treatment solution was brought below pH=3 no deposition was observed even when the substrates were soaked in solution for 24 h at 45^{o}C. Upon optimizing the reaction conditions mirror-like films could be obtained within 1-6 hours without adjusting the pH and maintaining the concentration of the precursors in the treatment solution below 10^{-2} M. Such as, the starting solution was clear at room temperature and visible precipitation was observed only 10-20 min after the solution reached the temperature of 45 ^{o}C. The treatment solution becomes turbid during the deposition due to the generation of fine particles as a result of a homogeneous nucleation process. To minimize their high surface energy, these particles have the tendency to attach to all available surfaces, thereby leading to the formation of highly uniform, scratch resistant nanoparticle-based films through a Volmer-Weber-type deposition mechanism.[36] All films have shown interference, rainbow-like color when exposed to the light, as a result of the different values of the refractive index of the substrate and the film. In Figure 6.1 are presented the top view (Figure 6.1 (a and inset)) and cross section (Figure 6.1 (b)) field emission scanning

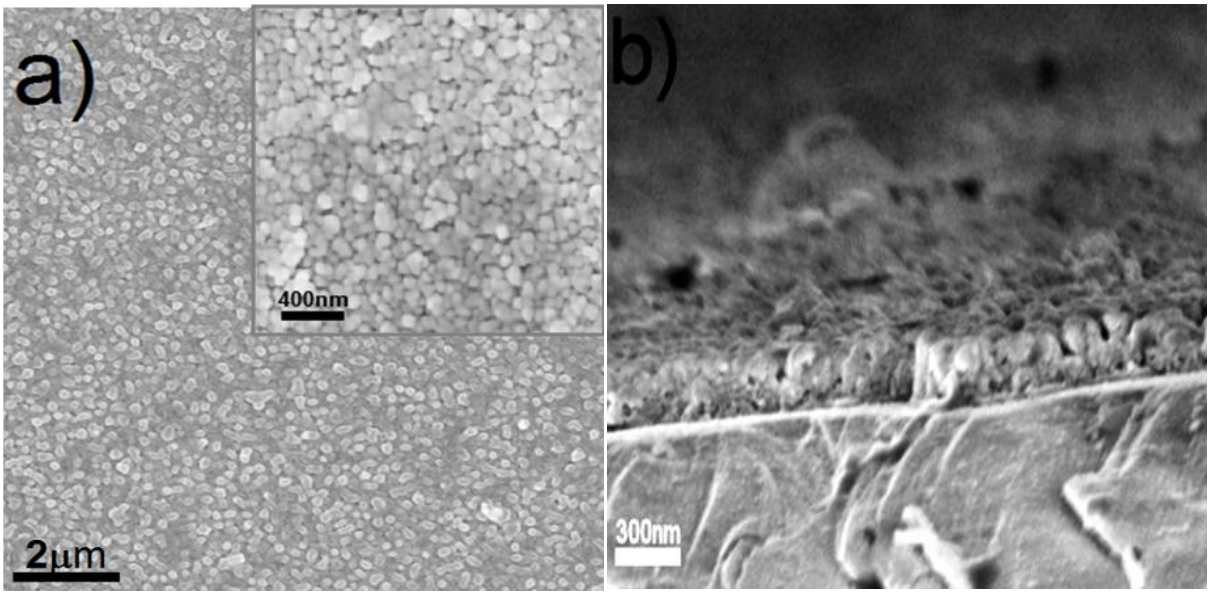

Figure 6.1. Top view (a) and cross-sectional (b) FE-SEM) images of a ~180 nm-thick $PbTiO_3$ layer obtained by liquid phase deposition.

electron microscopy (FE-SEM) images of a $PbTiO_3$ film deposited at 45 ^oC for 4 h followed by a heat treatment at 750 ^oC for 6 h in air. The $PbTiO_3$ film is continuous, being constructed by densely-packed grains with an average diameter of 77 nm. From the cross-section FE-SEM image, we can observe that the $PbTiO_3$ film is uniform and has a thickness of about 180 nm. The EDX analysis of several randomly selected areas of the $PbTiO_3$ films indicated the presence of both Pb and Ti. The Pb/Ti molar ratio obtained from inductive plasma coupled spectrometry was 0.978:1, which indicates that the films are compositionally homogeneous and nearly stoichiometric. Our results relative to the chemical composition of the perovskite films are consistent with those of Hsu and coworkers, who suggested that the Ti^{4+} and Pb^{2+} ions are incorporated into a complex ion during hydrolysis and there is no loss of lead during the heat treatment.[35]

Figure 6.2 (a) shows that the X-Ray diffraction pattern of the $PbTiO_3$ film heat treated in air at 750 ^oC for 3 h exhibits well defined peaks which can be classified into two categories. The first series matches well with those of $LaNiO_3$, whereas the second series of peaks belong to the tetragonal bulk $PbTiO_3$ (Macedonite, JCPDS File No.6-452), indicating that the resulting ferroelectric film is chemically pure and highly crystalline. The similarity of the XRD patterns of the $LaNiO_3$ and $PbTiO_3$ layers along with the strong (002) peak at 34^o in 2θ originating from the Si substrate and the peak broadening due to the nanostructured nature of the $PbTiO_3$ film made virtually impossible the estimation of the crystallite size. Unlike the film, the $PbTiO_3$ powder collected after the deposition and subjected to the same heat treatment presents a XRD pattern with distinct peaks with no preferential orientation (Figure 6.2 (b)) which confirms that the product of the deposition at 45 ^oC is tetragonal $PbTiO_3$. No impurities, such as pyrochlore $Pb_2Ti_2O_{7-y}$ or fluorite $Pb_{2+x}Ti_{2-x}O_{7-y}$, commonly encountered in the preparation of $PbTiO_3$ powders were observed in the XRD pattern. The absence of a particular spatial orientation, either crystallographic or morphological of the $PbTiO_3$ supports the existence of a homogeneous nucleation mechanism involved in the growth of the perovskite-like films by liquid phase deposition.

On the basis of XRD analysis, Hsu and coworkers suggested that the as-deposited hydroxide intermediate can be converted into a perovskite phase upon annealing for 30 min at temperatures as low as 550 ^oC. They observed that the product presented a small amount (5% wt.) of pyrochlore ($Pb_2Ti_2O_6$) impurity was eliminated by increasing the annealing temperature to 600

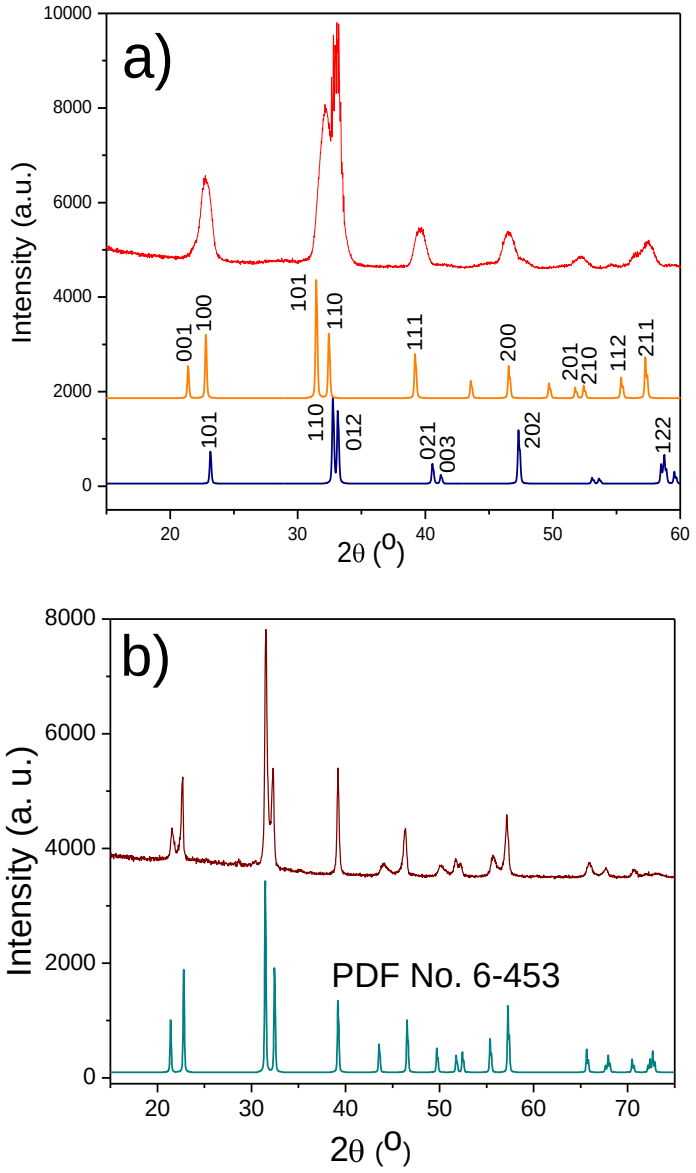

Figure 6.2. (a) X-Ray diffraction profiles of the $PbTiO_3$ film crystallized at 750°C. The red curve represents the experimental pattern of the $PbTiO_3$ film, whereas the orange and blue curves represent the simulated curves of bulk $PbTiO_3$ (PDF. No. 6-452) and $LaNiO_3$ (PDF No. 10-341), respectively. (b) Experimental XRD pattern of the $PbTiO_3$ powdered sample collected from the same experiment (red curve) and the simulated curves of bulk PbTiO3 (blue curve).

^{o}C. It is worth mentioning that all samples annealed at temperatures below 750 ^{o}C contained an important amount (~40% wt.) of pyrochlore impurity. This phase is not ferroelectric and alters the piezoelectric properties of the samples. However, upon annealing the as-deposited films at 750 ^{o}C for three hours in air the pyrochlore phase can be completely converted into $PbTiO_3$. The lattice constants of the perovskite film crystallized onto the $LaNiO_3$ buffer layer were refined within a tetragonal cell by using the TREOR program. [37] These refined values of a=3.908(7) Å and c=4.123(1) Å. are in very good agreement with those of the bulk material (a=3.899(3) Å and c=4.153(2) Å), furthermore confirming the high quality of the films.

The piezoresponse hysteresis loops of the 180 nm-thick $PbTiO_3$ film are presented in Figure 6. 3. Both the phase and amplitude curves confirm the existence of a switchable intrinsic lattice polarization in the PTO layer at room temperature. The film exhibits the well-known "butterfly-type" behavior for the variation of the amplitude versus the voltage with a maximum displacement of 1.2 nm at a driving voltage E= +17.55 V. The effective value of the zero field piezoelectric coefficient (d_{33}) of the $PbTiO_3$ film was calculated by fitting of the linear portion of the butterfly loop. It is well known that the amplitude of the displacement of the tip (A) is proportional to the ac bias voltage (V_{ac}): $A=d_{33}V_{ac}Q$, where Q is a proportionality factor which varies from 10 to 100 and accounts for the amplitude enhancement at the tip-sample resonance. By considering the value of the proportionality factor in the lower end of this range, the magnitude of the piezoelectric coefficient of the PTO layer is d_{33}=14.1 pm/V, value which is good agreement with those reported in the literature for layered $PbTiO_3$ nanostructures.[38-39]

The 2-D images of the 180 nm-thick $PbTiO_3$ film presented in Figure 6.4(a) and the inset of Figure 6.4 (a) show that the perovskite film is free of cracks and has a uniform morphology over its whole surface (scanned area was 10x10 μm) being constructed by densely-packed spherical grains. The root mean square roughness (rms) of the film was found to 9.7 nm. The piezoelectric force microscopy (PFM) contrast image of the same film without poling reveals a random distribution of bright and dark areas all across the film surface (Figure 6.4 (b)). The bright regions correspond to positive domains with the normal component of the polarization pointing toward the film surface, whereas the dark spots indicate areas where the polarization is oriented in the opposite direction, respectively.

To design perovskite-spinel bilayered nanocomposites, a cobalt ferrite (CFO) layer was subsequently deposited onto the 180 nm-thick $PbTiO_3$ film by the same procedure. Similar to the

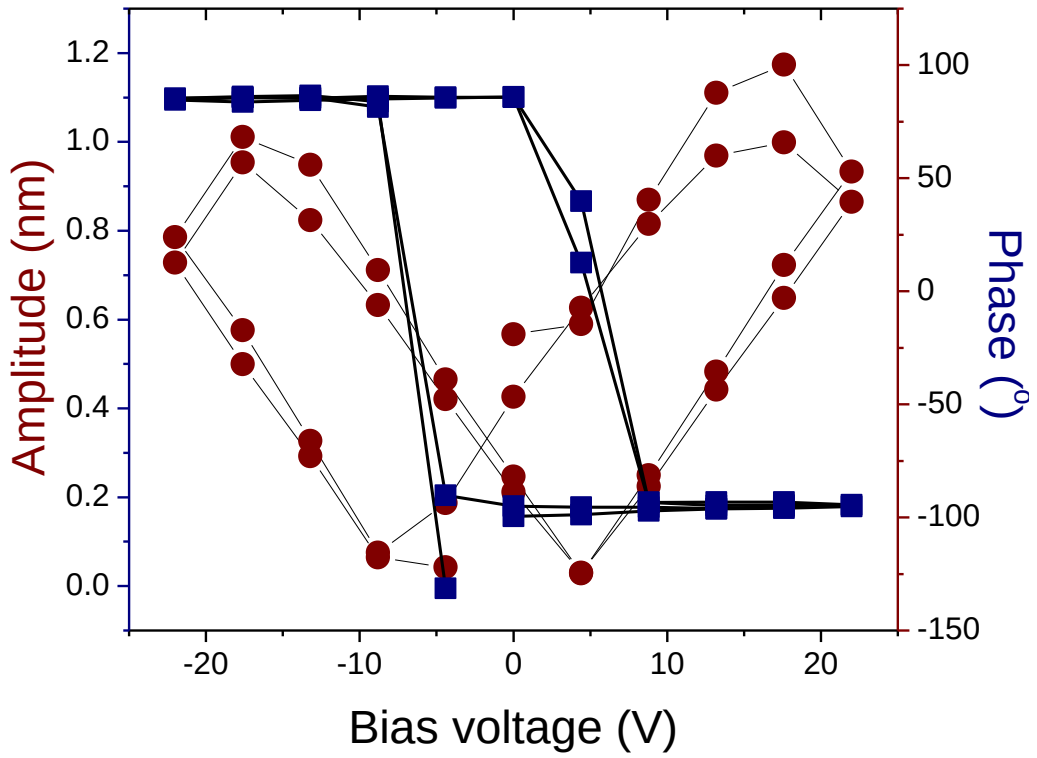

Figure.6.3. Local hysteresis loops of the phase (red curve) and amplitude (blue curve) of the piezoelectric signal of the ~180 nm-thick PbTiO3 film.

case of the perovskite films, the spinel films were obtained upon a heat treatment at 600 ^{o}C in air of the as-deposited films followed by the natural cooling to room temperature. Inductive coupled plasma (ICP) spectroscopy measurements of the solutions obtained by dissolving the film in a 10% HCl solution have indicated that for the particular concentration of the $Co(NO_3)_2$ precursor in the treatment solution the chemical composition of the ferrite film is $Co_{0.32}Fe_{2.68}O_4$, whereas their thickness, measured by the spectral reflectance technique was 193 nm. As seen in Figure 6.5, the top view FE-SEM images of the PTO/CFO nanocomposite shows that the surface of the CFO top layer is smooth and free of defects. Furthermore, the ferrite layer is constructed by densely-packed spherically-shaped grains with an average diameter of 90 nm (Figure 6.5 (b)).

The X-ray diffraction pattern of the PTO-CFO double-layered structure is dominated by the strong reflection around 32^{o} in 2θ corresponding to the $LaNiO_3$ buffer layer (Figure 6.6 (a)). However, relatively strong peaks ascribed to the $PbTiO_3$ film as well as a small peak at 35.8^{o} in 2θ, corresponding to the most intense reflection of the bulk $CoFe_2O_4$ spinel structure (PDF No. 1-1121) can be easily observed, confirming the formation of a perovskite-spinel bilayered structure. Since the relatively intense peaks corresponding to the silicon substrate and the perovskite phases obscure those of the spinel phase, to assess that the ferrite film was is single phase we investigated the XRD pattern of a $CoFe_2O_4$ thin film deposited onto a glass substrate under the same experimental conditions. As seen in Figure 6.6 (b), the XRD pattern suggests that the CFO film is polycrystalline, with no preferential orientation and is chemically pure. The refined unit cell parameter of the film annealed at 600 ^{o}C was a=8.39(1) Å, which is close to the value of the bulk standard $CoFe_2O_4$.

Figure 6.7 (a) displays the surface morphology of the CFO film forming the top layer of the PTO-CFO perovskite-spinel heteroepitaxial bilayered structure obtained by atomic force microscopy. The film has a smooth surface and consists of a continuous array of small and uniform grains with an average diameter of 98 nm, which is in excellent agreement with the results obtained from electron microscopy. The root mean square roughness (Rms) for the whole measured area was 34 nm. The magnetic force microscopy (MFM) image of the film (Figure 6. 7 (b)) exhibits several regions with a bright-dark contrast which indicates the existence of the magnetic domains with upward and downward orientations of the magnetization. The magnetic properties of the PTO-CFO bilayered structure were measured by SQUID magnetometry. Hysteresis loops presented in Figure 6.8 indicate that the samples present a strong magnetic

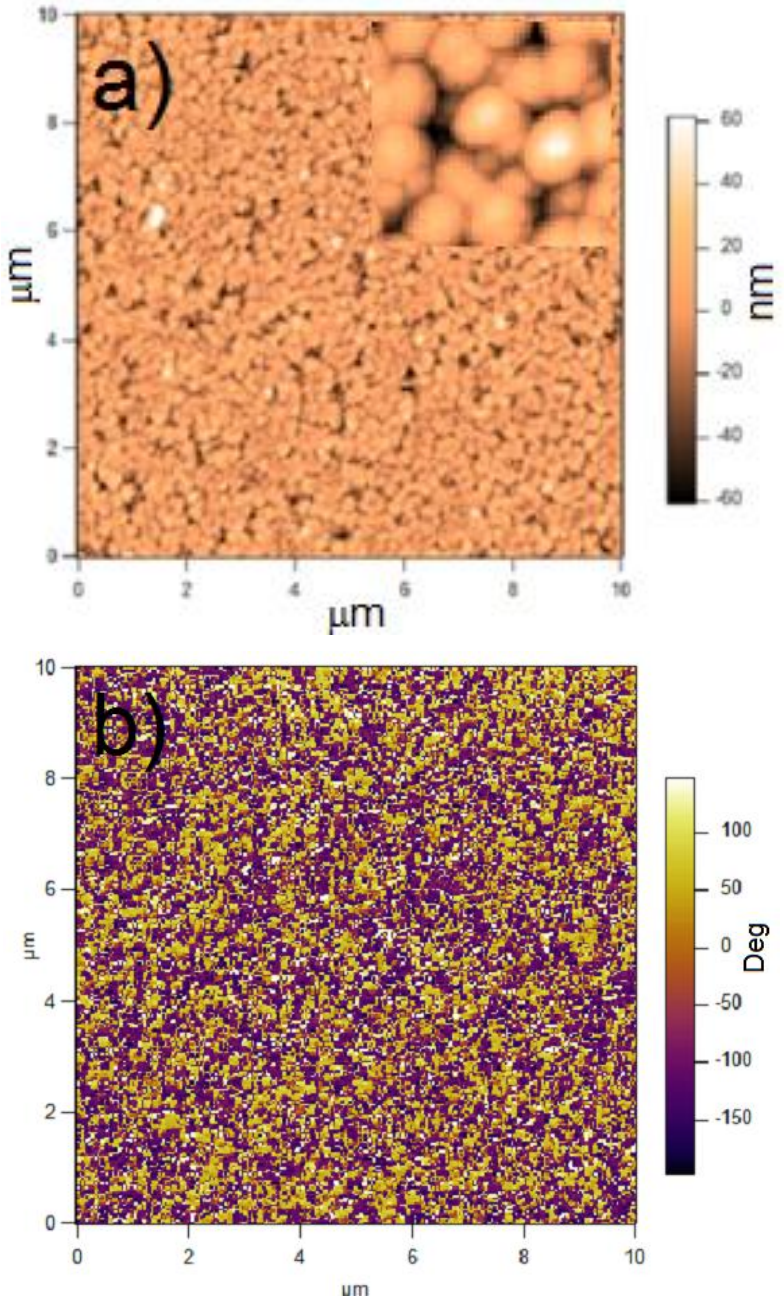

Figure.6.4. (a) AFM image of the ~180 nm-thick $PbTiO_3$ film deposited at 45°C. The inset is a close-up of the same image showing the size of the spherical particles constructing the film; (b) 10x10 μm phase contrast PFM image of the same film.

signal at room temperature and neither the PTO-CFO nanocomposite nor the pure CFO films reach saturation at a magnetic field of 8 kGauss. A negligible variation of the coercivity was noticed when the samples were measured with the magnetic field oriented parallel (in-plane) and perpendicular (out-of-plane) to the film surface suggesting that they possesses a randomly oriented magnetic anisotropy. The coercivity increases from 1.82 kOe to 13.39 kOe was found when the temperature of the in-plane measurement was decreased from 300 to 5 K. The room temperature coercivity of the PTO-CFO bilayered nanocomposite is smaller than that of pure CFO film (H_c =2.071 KOe), which can be presumably ascribed to the coupling between the $Co_{0.32}Fe_{2.68}O_4$ and the $PbTiO_3$ phases at the shared interfaces. The saturation magnetization calculated after dissolving the film in diluted HCl solution followed by weighing the sample and the glass substrate is 234.4 emu/cm^3, which is lower than the value of ~400 emu/cm^3 reported for the bulk $CoFe_2O_4$.[40]

To further demonstrate the feasibility of this method, a second series of bilayered structures, consisting of a 200 nm-thick nickel ferrite (NFO) film deposited onto the initial PTO film was fabricated by the same experimental procedure. Similar with the CFO film, the 2θ scans XRD scans (not shown) indicated that both the PTO and NFO layers are single phase and are polycrystalline with the absence of any preferential orientation. Inductive coupling plasma (ICP) measurements of samples collected by dissolving randomly selected areas of the film (by masking it with scotch tape and immersing it in a diluted HCl solution) indicated that the NFO layer is compositionally uniform and corresponds to the composition $Ni_{0.66}Fe_{2.34}O_4$. The FE-SEM micrograph of the PTO-NFO nanocomposite film (Figure 6.9) shows that unlike the $CoFe_2O_4$ film, the NFO top layer is constructed by rod-like nanoparticles with an average length of 200 nm and an average diameter of 15 nm.

As seen in the top view FE-SEM image, the constituent nanoparticles of the NFO layer seem to have their long axes oriented out of the film plane. They are also densely packed and form a very uniform film which covers completely the PTO layer. The cross section FE-SEM image of the PTO-NFO bilayered nanocomposite shows the $LaNiO_3$, PTO and NFO layers. In general, ceramic thin films grow in solution via two mechanisms: homogeneous nucleation and attachment of the nanoparticles and heterogeneous nucleation, respectively. While homogeneous nucleation usually results in the formation of films constructed by spherically-shaped nanoparticles, heterogeneous nucleation occurs through a surface-directed growth leading to a

preferential growth of the nucleated solid leading to the formation of columnar structures.[41] Regardless of the chemical composition of the ferrite films, in all experiments the treatment solution turned progressively cloudy during the course of the hydrolysis process and turned back clear at the end of the deposition. However, because the morphology of the particles constructing the ferrite film changes from spherical to rod-like, it results that, depending on their composition the spinel films grow thorough both a homogeneous nucleation and a surface-directed heterogeneous nucleation mechanism.

The room temperature magnetization curves of the pure NFO film and the bilayered PTO-NFO nanocomposite are shown in Figure 6.10 (a). Similar to the PTO-CFO nanocomposite films, no significant change in the coercivity and the orientation of the loops was noticed for measurements performed with the substrate oriented parallel and perpendicular to the magnetic field indicating the existence of randomly oriented anisotropy axes. The saturation magnetization of the bilayered structure was 223.2 emu/g, value smaller than both that of the pure $Ni_{0.66}Fe_{2.34}O_4$ film (M_s=241.5 emu/g) and that of the bulk $NiFe_2O_4$ (M_s=302.4 emu/g).[42] As in the case of the $CoFe_2O_4$ films, the decrease of the saturation magnetization of the $NiFe_2O_4$ layered structure can be ascribed to the existence of a non-colinear ferromagnetic spin structure in the vicinity of the surface of the individual nanoparticles constructing the film.[43] Unlike the PTO-CFO nanocomposite, the coercivity of the PTO-NFO layered nanocomposites is slightly higher (H_c=108 Oe) than that of the pristine ferrite film (H_c=90 Oe). These results were reproduced independently for three series of different samples and are in good agreement with those reported by Luo and coworkers for a $BaTiO_3$-$NiFe_2O_4$ epitaxial nanocomposite thin film obtained by a polymer assisted deposition whereby the coercivity decreased from 150 to 140 Oe, respectively.[21]

Raman spectroscopy has been proven as being a very versatile tool for the investigation of both the lattice dynamics in crystalline solids and the magnitude and types of residual stresses in ferroelectric thin film structures. The high temperature cubic $PbTiO_3$ presents 12 optical modes which transform as the $3T_{1u}+T_{2u}$ irreducible representation of the point group O_h.[44] The triply degenerate T_{1u} mode is only infrared active, whereas the T_{1u} mode is neither Raman nor infrared active, being called “the silent mode”. At room temperature $PbTiO_3$ adopts a tetragonal structure and the T_{1u} optical lattice modes split into A_1+E, whereas the T_{2u} will split into B_1+E, respectively.[44-45] Due to long–range electrostatic interactions the degeneracy of the lattice

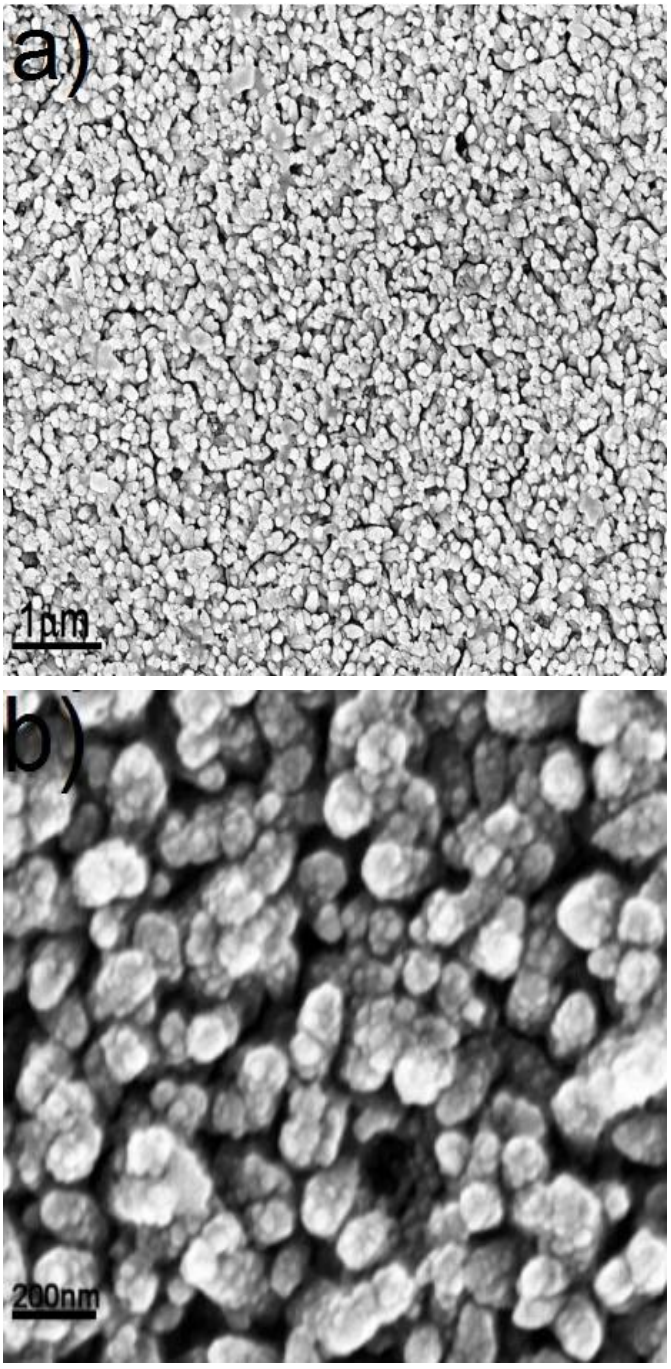

Figure.6.5. (a-b) FE-SEM images showing the typical morphology of the $CoFe_2O_4$ top layer of the PTO-CFO heteroepitaxial bilayered structure.

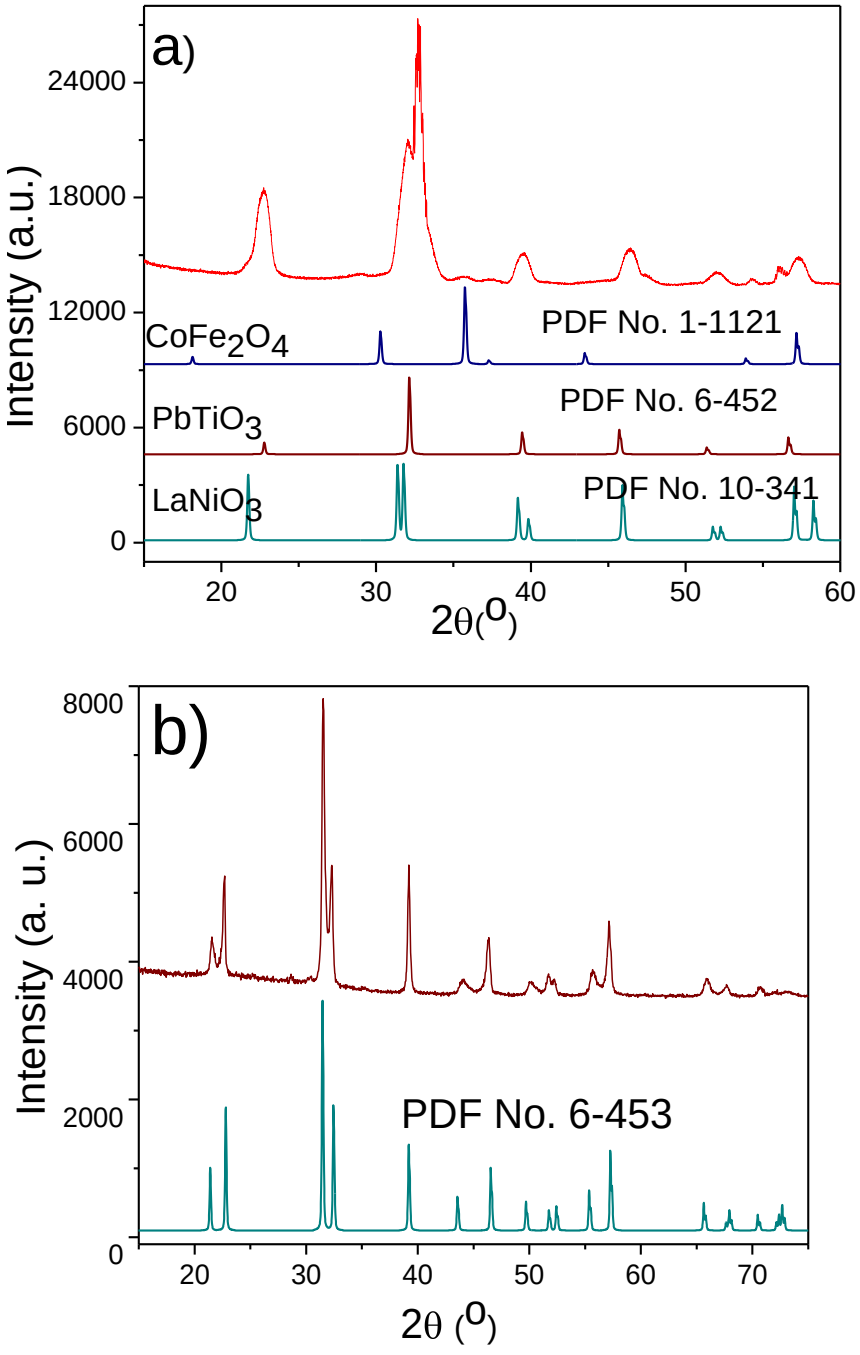

Figure.6.6. XRD profiles of the PTO-CFO bilayered structure deposited on $LaNiO_3$-buffered Si (a) and the pure $Co_{0.32}Fe_{2.68}O_4$ film deposited onto a glass substrate.

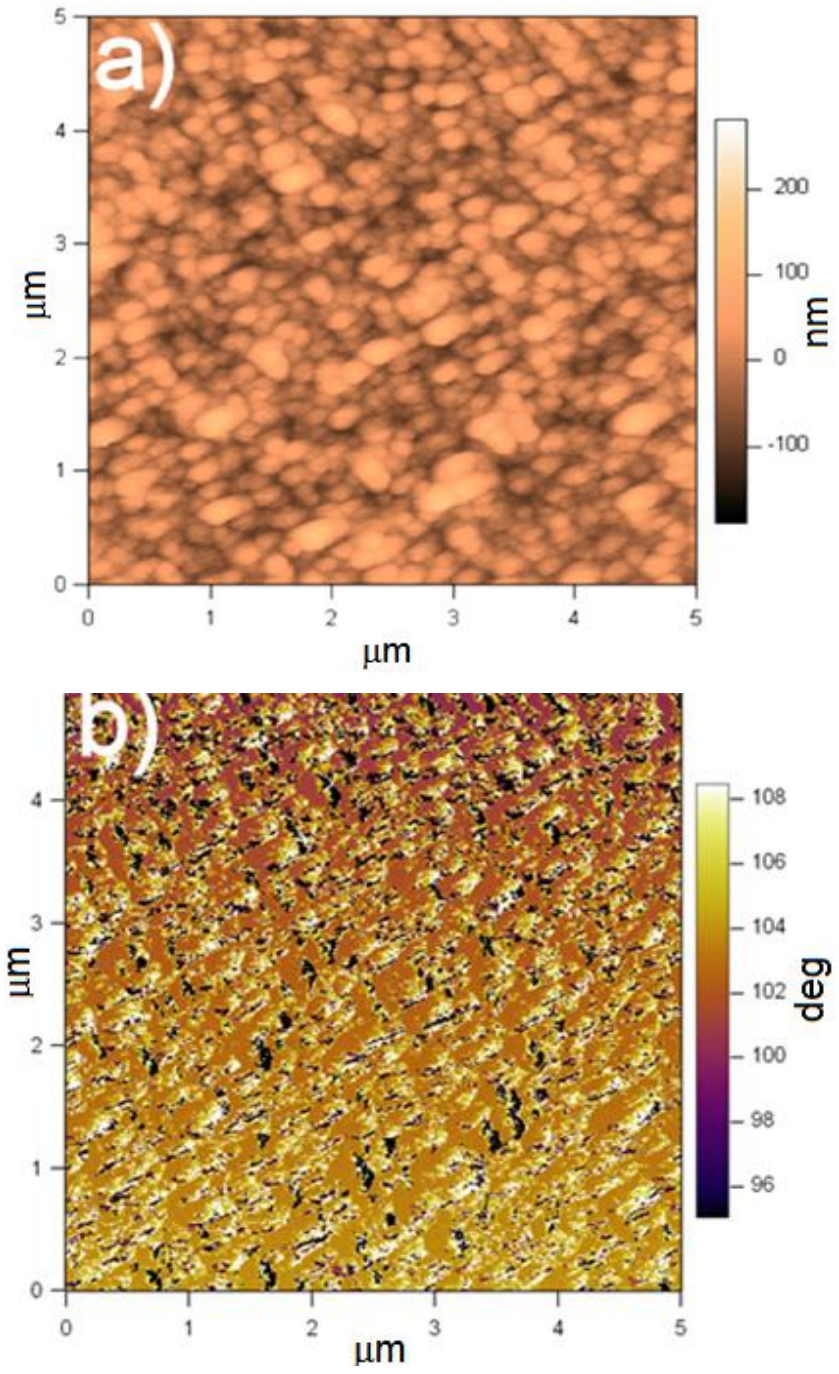

Figure 6.7. (a) Representative tapping-mode AFM and (b) MFM image of the ~180 nm-thick $Co_{0.32}Fe_{2.68}O_4$ top layer of the PTO/CFO bilayered structure.

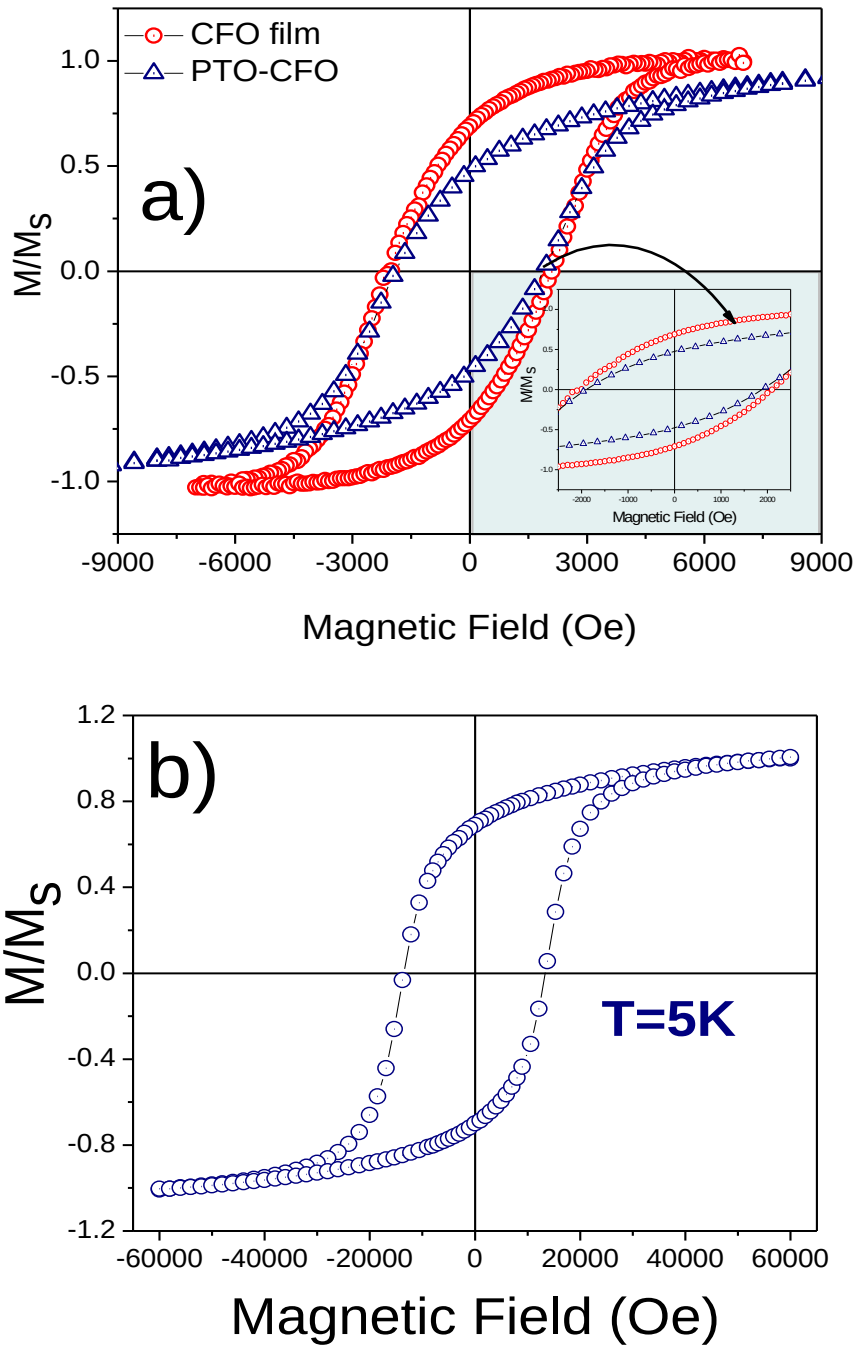

Figure.6.8. (a) Magnetization vs. field curves at 300 K for the pure CFO film and the PTO-CFO bilayered structure; (b) Hysteresis loop of the PTO-CFO layered nanocomposite at 5 K (b). Magnetization values have been normalized to the value of the saturation magnetization.

vibrations at long wavelength is furthermore lifted into a doubly degenerate transverse mode (TO), corresponding to an orientation of the polarization perpendicular to the wave vector **k** and a single longitudinal optical (LO) mode with polarization parallel to **k**. Likewise, the signature bands in ferrites Raman spectra are T_{2g} modes, corresponding to lattice vibrations in the MO_4 tetrahedra and the A_{1g} modes, associated to vibrations of the octahedral sites of the cubic lattice.[46-48]

In Figure 6.11 are represented the room temperature Raman spectra of the PTO-CFO bilayered film with and without a magnetic field. To locate precisely the Raman bands the spectra were deconvoluted with the PeakFit 4.12 software by using a linear baseline. The experimental data was smoothed with a four-order polynomial function (Savitsky-Golay) and the fitting process was performed with a Gaussian function. The reliability factors of each refinement procedure were higher than 90%. As seen in Figure 6.11, three different types of peaks can be distinguished in each Raman spectrum: three bands around 222, 290 and 609 cm^{-1} ascribed to the E(2TO), B_1+E and A_1(3TO) vibrational modes of tetragonal $PbTiO_3$ (point group C_{4v}), a sharp, strong line around 520 cm^1 characteristic to the silicon substrate and two broad bands around 472 and 687 cm^{-1} corresponding to the T_{2g} and A_{1g} modes of the cubic spinel structure. T_{2g} and A_{1g} modes of the spinel layer and the E(2TO) and A_1(3TO) modes of the perovskite layer at different values of the in-plane magnetic field and room temperature, whereas the wave numbers at which these bands are located are represented in Table 6.1.

Upon increasing of the magnetic field, the Raman modes of both the spinel and the perovskite layers shift slightly towards higher frequency, whereas the position of the B_1+E band remains almost unchanged, suggesting that the silent mode is almost insensitive to the action of the magnetic field. Such a behavior is similar to that observed by Li and coworkers for a Pb(Zr, Ti)O_3-$CoFe_2O_4$ bilayered structure obtained by a sol-gel method.[49] As the shift of the Raman bands in thin film structures is generally due residual stresses[50-51], the upward frequency shift in the Raman modes of both perovskite and spinel layers clearly indicates the existence of a stress-mediated magnetoelectric coupling in the PTO-CFO bilayered structure. Such a shift to higher frequencies of the ferrite Raman modes are ascribed to the convergent effect of changes in the lattice along and reorientation of the magnetic domains.[49] Under the action of an in-plane magnetic field, the ferrite layer, with a negative magnetostriction coefficient[52] will shrink along

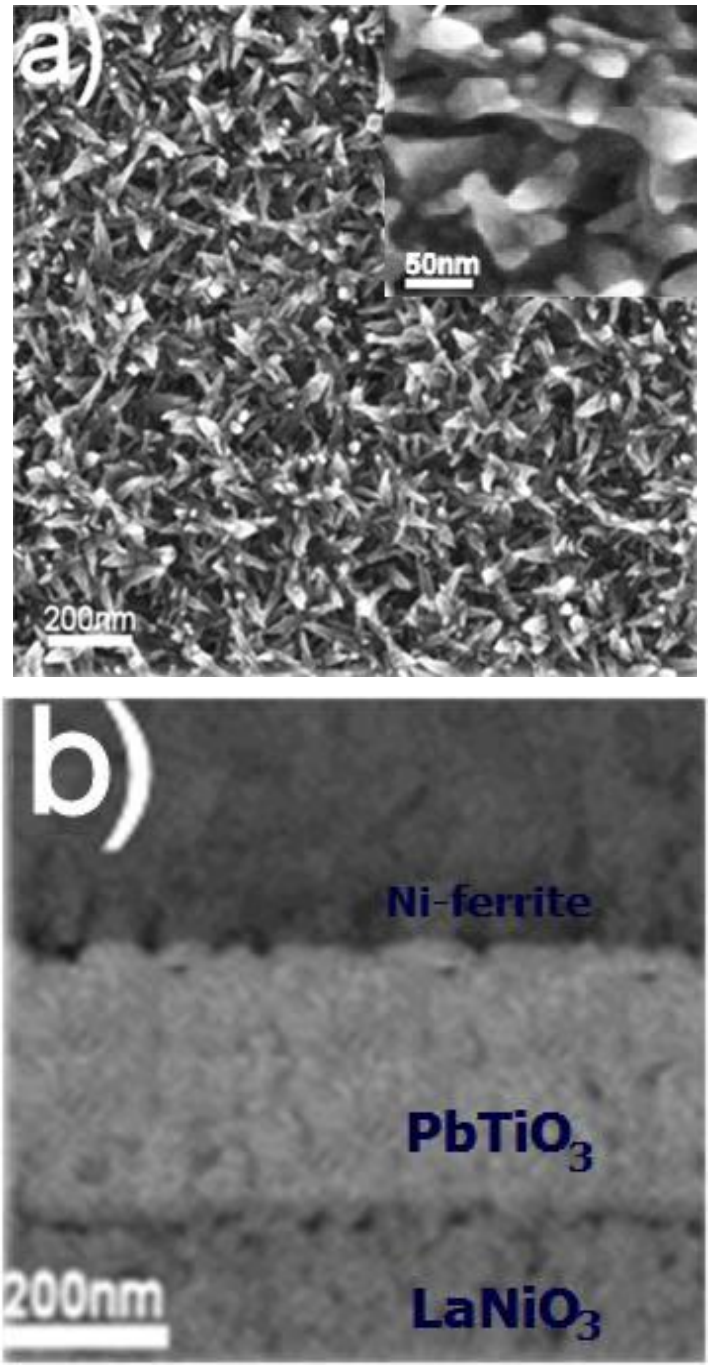

Figure.6.9. (a) Top view FE-SEM images of the NFO thin film forming the top layer of the PTO-NFO multilayered structure; (b) Cross section FE-SEM image of the PTO-NFO layered nanocomposite.

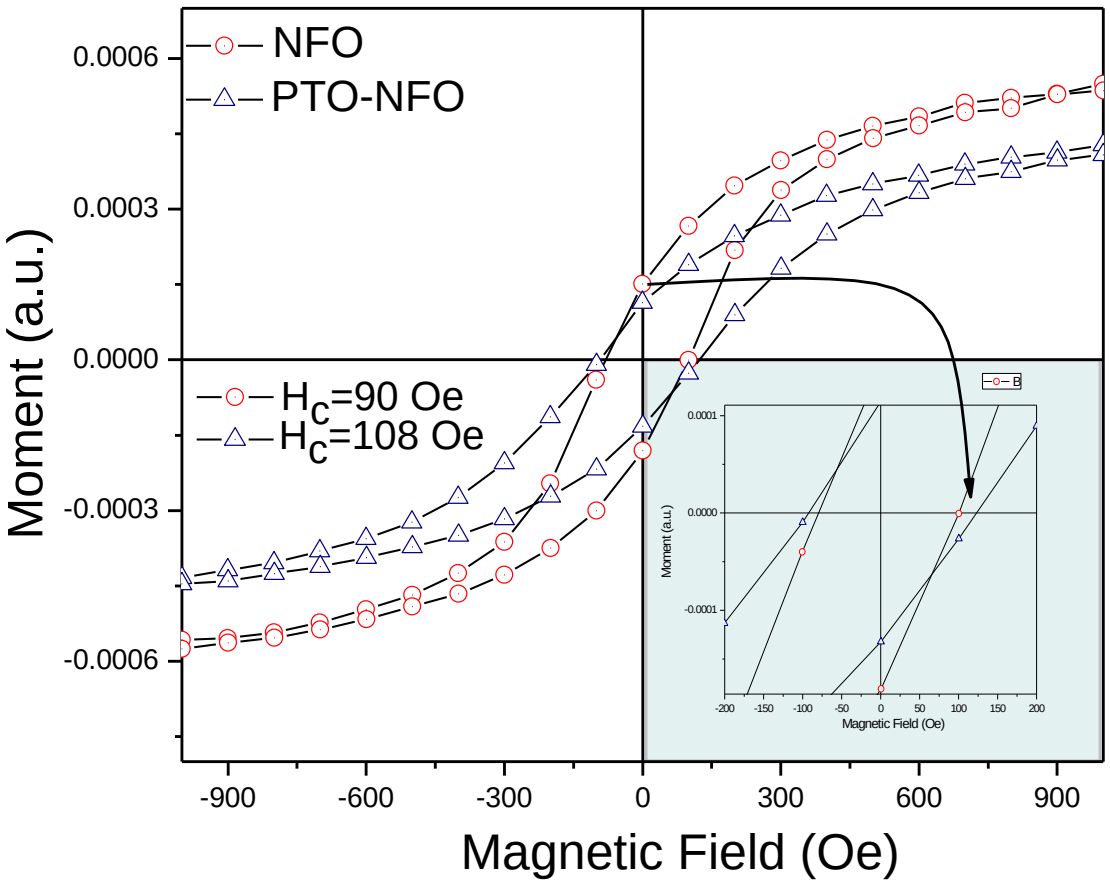

Figure 6.10. (a) Room temperature hysteresis loops of the pristine 200 nm-thick NFO film deposited on glass and the PTO-NFO bilayered nanocomposites.

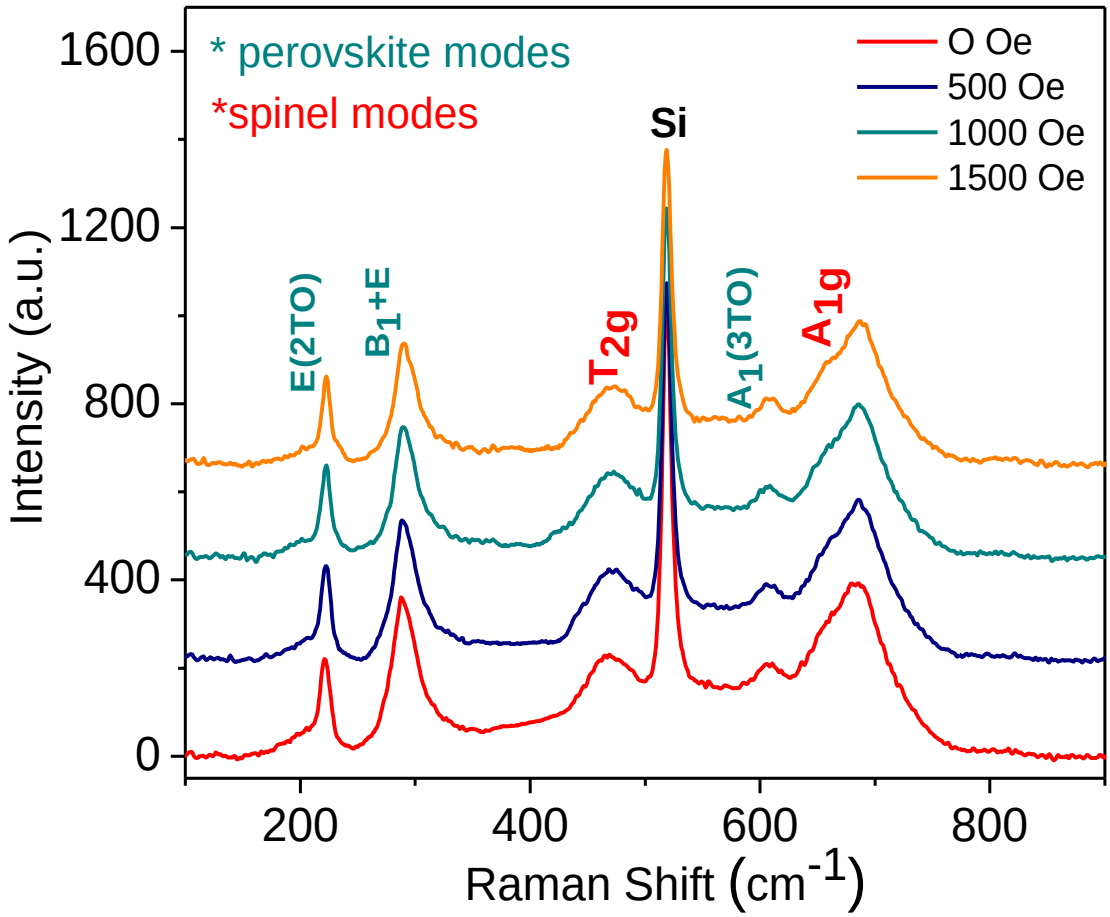

Figure.6.11. Raman spectra of the PTO-CFO bilayered structure in the absence (orange curve) and the presence of a magnetic field with different intensities.

Table 6.1. Values of the Raman shift of the perovskite and spinel layers in the PTO-CFO under a magnetic field

	Raman Bands					
	Ferrite Layer		Perovskite Layer			Si
H (Oe)	T_{2g}	A_{1g}	E(2TO)	B_1+E	A_1(3TO)	
0	465.9	683.2	220.8	292.4	604.4	519.5
500	467.3	685.3	221.8	292.2	606.7	519.7
1000	469.6	686.3	222.7	292.2	608.2	519.6
1500	471.3	688.5	223.3	292.1	609.7	519.3

the direction of the magnetic field. However, under a compression the magnetic layer will expand slightly in a direction parallel to the normal of the film generating a stress in the adjacent ferroelectric layer.

This stress, produced at the shared interfaces by the magnetoelastic effect will change the configuration of the ferroelectric domains in the perovskite phase, leading to a shift to higher frequencies of the E(2TO) and A_1(3TO) vibrational modes in the Raman spectrum. Although one can argue that the magnitude of the shift of the Raman modes is comparable to the instrumental resolution, the validity of the assumption that the shift in the Raman bands of the bilayered structure at H≠0 is associated to a stress-mediated magnetoelectric coupling was further confirmed by the position of the Raman more of the Si substrate, which remains virtually unchanged upon applying the magnetic field.

6.4. Conclusions

In summary, proof-of-concept experiments have demonstrated that it is possible to construct highly uniform polycrystalline $PbTiO_3$-$M_xFe_{3-x}O_4$ (M= Co, Ni) magnetoelectric (ME) bilayered nanocomposites, using the liquid-phase deposition process. This two-step procedure involves the sequential deposition of a PbTiO3 film, followed by the formation of a transition-metal ferrite layer at temperatures as low as 45°C. The resulting bilayered structures possess a granular morphology, are chemically pure, and are coupled through an elastic interaction, as evidenced by electron microscopy, X-ray diffraction, and magnetic field-assisted Raman spectroscopy. The general potential of the proposed route is multifold, because it allows the direct assembly of spinel and perovskite multicomponent metal oxide compositions into hierarchical multilayered structures via a simple chemical approach. At the same time, it allows for strict control over the number of perovskite/spinel layers, as well as their thickness and chemical composition. These hybrid nanostructures, in a film-on-substrate geometry, will open the door to more-detailed studies on their electrical and magnetic properties and stimulate the design of other combinations of spinel and perovskite phases in a planar geometry.

6.5. References

(1) Petrov, V. M.; Srinivasan, G.; Bichurin, M. I.; Gupta, A. *Physical Review B* **2007**, *75*.

(2) Lu, J.; Pan, D. A.; Bai, Y.; Su, Y. J.; Qiao, L. J. *Ieee Transactions on Magnetics* **2008**, *44*, 2127.

(3) Bichurin, M. I.; Petrov, V. M.; Petrov, R. V.; Kapralov, G. N.; Kiliba, Y. V.; Bukashev, F. I.; Smirnov, A. Y.; Tatarenko, A. S. *Ferroelectrics* **2002**, *280*, 377.

(4) Srinivasan, G.; Tatarenko, A. S.; Bichurin, M. I. *Electronics Letters* **2005**, *41*, 596.

(5) Dong, S. X.; Zhai, J. Y.; Xing, Z. P.; Li, J. F.; Viehland, D. *Applied Physics Letters* **2005**, *86*.

(6) Tatarenko, A. S.; Gheevarughese, V.; Srinivasan, G. *Electronics Letters* **2006**, *42*, 540.

(7) Tatarenko, A. S.; Srinivasana, G.; Bichurin, M. I. *Applied Physics Letters* **2006**, *88*.

(8) Fetisov, Y. K.; Srinivasan, G. *Applied Physics Letters* **2006**, *88*.

(9) Srinivasan, G.; Tatarenko, A. S.; Mathe, V.; Bichurin, M. I. *European Physical Journal B* **2009**, *71*, 371.

(10) Filippov, D. A.; Bichurin, M. I.; Petrov, V. M.; Laletin, V. M.; Srinivasan, G. *Physics of the Solid State* **2004**, *46*, 1674.

(11) Nan, C. W.; Bichurin, M. I.; Dong, S. X.; Viehland, D.; Srinivasan, G. *Journal of Applied Physics* **2008**, *103*.

(12) Chaudhuri, A. R.; Krupanidhi, S. B.; Mandal, P.; Sundaresan, A. *Journal of Applied Physics* **2009**, *106*.

(13) Dix, N.; Muralidharan, R.; Caicedo, J. M.; Hrabovsky, D.; Fina, I.; Fabrega, L.; Skumryev, V.; Varela, M.; Guyonnet, J.; Paruch, P.; Sanchez, F.; Fontcuberta, J. *J. Magn. Magn. Mater.* **2009**, *321*, 1790.

(14) Li, J. H.; Levin, I.; Slutsker, J.; Provenzano, V.; Schenck, P. K.; Ramesh, R.; Ouyang, J.; Roytburd, A. L. *Applied Physics Letters* **2005**, *87*.

(15) Zhu, J.; Zhou, L. X.; Huang, W.; Li, Y. Q.; Li, Y. R. *Journal of Crystal Growth* **2009**, *311*, 3300.

(16) Schlom, D. G.; Chen, L. Q.; Pan, X. Q.; Schmehl, A.; Zurbuchen, M. A. *Journal of the American Ceramic Society* **2008**, *91*, 2429.

(17) Bai, W.; Meng, X. J.; Yang, J.; Lin, T.; Zhang, Q. X.; Ma, J. H.; Sun, J. L.; Chu, J. H. *Journal of Physics D-Applied Physics* **2009**, *42*.

(18) Fina, I.; Dix, N.; Laukhin, V.; Fabrega, L.; Sanchez, F.; Fontcuberta, J. *J. Magn. Magn. Mater.* **2009**, *321*, 1795.

(19) Srinivasan, G.; Hayes, R.; Bichurin, M. I. *Solid State Communications* **2003**, *128*, 261.

(20) Huang, W.; Zhu, J.; Zeng, H. Z.; Wei, X. H.; Zhang, Y.; Li, Y. R.; Hao, J. H. *Scripta Materialia* **2008**, *58*, 1118.

(21) Luo, H. M.; Yang, H.; Bally, S. A.; Ugurlu, O.; Jain, M.; Hawley, M. E.; McCleskey, T. M.; Burrell, A. K.; Bauer, E.; Civale, L.; Holesinger, T. G.; Jia, Q. X. *Journal of the American Chemical Society* **2007**, *129*, 14132.

(22) Aoi, Y.; Kambayashi, H.; Kamijo, E.; Deki, S. *Journal of Materials Research* **2003**, *18*, 2832.

(23) Chou, J. S.; Lee, S. C. *Applied Physics Letters* **1994**, *64*, 1971.

(24) Cho, D. H.; Mizuhata, M.; Deki, S. *Journal of the Ceramic Society of Japan* **2007**, *115*, 608.

(25) Nakata, A.; Mizuhata, M.; Deki, S. *Electrochimica Acta* **2007**, *53*, 179.

(26) Deki, S.; Aoi, Y.; Okibe, J.; Yanagimoto, H.; Kajinami, A.; Mizuhata, M. *Journal of Materials Chemistry* **1997**, *7*, 1769.

(27) Lee, M. K.; Fan, C. H. *Journal of the Electrochemical Society* **2009**, *156*, D395.

(28) Lee, M. K.; Liao, H. C.; Tung, K. W.; Shih, C. M.; Shih, T. H. *Journal of Physics D-Applied Physics* **2002**, *35*, 61.

(29) Hsu, M.-C.; Sun, Y.-M.; Leu, I.-C.; Hon, M.-H. *Applied Surface Science* **2007**, *253*, 7639.

(30) Caruntu, G.; Bush, G. G.; O'Connor, C. J. *Journal of Materials Chemistry* **2004**, *14*, 2753.

(31) Caruntu, G.; Newell, A.; Caruntu, D.; O'Connor, C. J. *Journal of Alloys and Compounds* **2007**, *434*, 637.

(32) Meng, X. J.; Sun, J. L.; Yu, J.; Ye, H. J.; Guo, S. L.; Chu, J. H. *Applied Surface Science* **2001**, *171*, 68.

(33) He, H. C.; Ma, J.; Lin, Y. H.; Nan, C. W. *Journal of Physics D-Applied Physics* **2009**, *42*.

(34) Hsu, M. C.; Leu, I. C.; Sun, Y. M.; Hon, M. H. *Journal of Solid State Chemistry* **2006**, *179*, 1421.

(35) Vopsaroiu, M.; Blackburn, J.; Cain, M. G. *Journal of Physics D-Applied Physics* **2007**, *40*, 5027.

(36) Gao, Y.; Koumoto, K. *Crystal Growth & Design* **2005**, *5*, 1983.

(37) Werner, P. E.; Eriksson, L.; Westdahl, M. *Journal of Applied Crystallography* **1985**, *18*, 367.

(38) Kighelman, Z.; Damjanovic, D.; Cantoni, M.; Setter, N. *Journal of Applied Physics* **2002**, *91*, 1495.

(39) Kim, Y. K.; Kim, S. S.; Shin, H.; Baik, S. *Applied Physics Letters* **2004**, *84*, 5085.

(40) Suzuki, Y.; Hu, G.; van Dover, R. B.; Cava, R. J. *J. Magn. Magn. Mater.* **1999**, *191*, 1.

(41) Ung, D.; Tung, L. D.; Caruntu, G.; Delaportas, D.; Alexandrou, I.; Prior, I. A.; Thanh, N. T. K. *Crystengcomm* **2009**, *11*, 1309.

(42) Adireddy, S.; Lin, C. K.; Palshin, V.; Dong, Y. M.; Cole, R.; Caruntu, G. *Journal of Physical Chemistry C* **2009**, *113*, 20800.

(43) Robinson, I.; Volk, M.; Tung, L. D.; Caruntu, G.; Kay, N.; Thanh, N. T. K. *Journal of Physical Chemistry C* **2009**, *113*, 9497.

(44) Pignolet, A.; Schmid, P. E.; Wang, L.; Levy, F. *Journal of Physics D-Applied Physics* **1991**, *24*, 619.

(45) Taguchi, I.; Pignolet, A.; Wang, L.; Proctor, M.; Levy, F.; Schmid, P. E. *Journal of Applied Physics* **1993**, *73*, 394.

(46) Wang, Z. W.; Schiferl, D.; Zhao, Y. S.; O'Neill, H. S. C. *Journal of Physics and Chemistry of Solids* **2003**, *64*, 2517.

(47) Casula, M. F.; Floris, P.; Innocenti, C.; Lascialfari, A.; Marinone, M.; Corti, M.; Sperling, R. A.; Parak, W. J.; Sangregorio, C. *Chemistry of Materials* **2010**, *22*, 1739.

(48) Herranz, T.; Rojas, S.; Ojeda, M.; Pérez-Alonso, F. J.; Terreros, P.; Pirota, K.; Fierro, J. L. G. *Chemistry of Materials* **2006**, *18*, 2364.

(49) Li, Z.; Wang, Y.; Lin, Y. H.; Nan, C. *Physical Review B* **2009**, *79*.

(50) Sanjurjo, J. A.; Lopezcruz, E.; Burns, G. *Physical Review B* **1983**, *28*, 7260.

(51) Cheng, J. R.; He, L.; Yu, S. W.; Meng, Z. Y. *Applied Physics Letters* **2006**, *88*.

(52) Bhame, S. D.; Joy, P. A. *Journal of Physics D-Applied Physics* **2007**, *40*, 3263.

7. Probing the Local Strain-Mediated Magnetoelectric Coupling in Multiferroic Nanocomposites by Magnetic Field-Assisted Piezoresponse Force Microscopy

7.1. Introduction

Magnetoelectric (ME) multiferroics are materials which exhibit magnetic, ferroelectric and ferroelastic ordering simultaneously, and such unique feature make them the leading candidates for implementation in advanced technologies in computing[1], sensing[2] and data storage[3]. Of immediate technological interest are, however, ME composite systems because, unlike single phase multiferroic materials, they possess a ME response at room temperature[4-6] and a strong elastic coupling resulting from the high magnetostriction and large piezoelectric coefficients of the magnetic and ferroelectric phases, respectively. In a composite multiferroic the two constituent phases are artificially coupled via a mechanical strain and, therefore the magnetoelectric susceptibility is described as a product propriety: $\alpha = \frac{\partial E}{\partial H} = \frac{\partial z}{\partial H} \times \frac{\partial E}{\partial z}$ (7.1), where $\partial z / \partial H$ denotes the piezomagnetic deformation and $\partial E / \partial z$ is the piezoelectric generation of electrical charges[7]. In bulk and particulate strain-mediated magnetoelectric composites the modulation of the polarization with a magnetic field (the direct ME effect) is conventionally probed by measuring the dynamic change of the open-circuit voltage, capacitance or charge of the sample in the presence of an in-plane magnetic field[8-12] either in active[13-15] or passive mode[15-16]. Similarly, the converse ME effect can be determined experimentally by measuring the changes induced on the magnetic parameters of the material by the electric field, such as the domain dynamics, magnetization[17-22] and the coercive field. For multilayered structures the accurate measurement of the ME effect is oftentimes difficult due to the weak output signals resulting from the geometrical restriction along the c axis, the severe clamping effect exerted by the substrate (α~1μV·Oe for 100 nm-thick films) and the presence of parasitic effects, such as interfacial polarization leakage and the Maxwell-Wagner interfacial conductivity effect[23-27]. Moreover, the electro-magnetic induction and magnetoresistance of the magnetic phase, as well as thermal effects can contribute to the measured signal.[28-30] This will not only make difficult to distinguish the sample's response from measurement artifacts, but also it renders questionable the reproducibility of the experimental data. Recently, alternate methods, such as the measurement of the magnetization of the material as a function of the magnetic field before and after poling the electrostrictive phase[31-32], Kerr elipticity measurements[33], as well as the shift of the resonance frequency in the ferromagnetic resonance (FMR) spectrum in the presence of an

electric field[34-36] have been proposed for the study of the converse ME effect. As magnetoelectric composite materials are prime candidates for integration into microelectronic devices, it is important to characterize the magnetoelectric coupling at a local scale. Therefore, scanning probe microscopy techniques, such as electrostatic force microscopy (EFM) and magnetic force microscopy (MFM) have become increasingly important due to their non-invasive character, versatility and high spatial resolution.

Karpinsky and coworkers provided a qualitative estimation of the local magnetoelectric effect from MFM measurements before and after poling a $BaTiO_3$-$BaFe_{12}O_{19}$ composite sample with a moderate voltage (25V)[37]. The analysis of the topography magnetic contrast images and cross-section plots evidenced the existence of both a broadening effect of MFM peaks along with a shift of their maxima when the sample is subjected to the action of an electric field, indicating the existence of a stress-mediated ME coupling between the constituent phases. Using a similar method, Bai *et al.* furthermore calculated the value of ME coupling coefficient by assuming that in MFM mode the measured phase shift varies linearly with the magnetization of the sample.[38] Chung *et al.* reported on the microscopic probing and control of the magnetization in Ni-$PbTi_{0.48}Zr_{0.52}O_3$ (PZT) ME nanocomposites by performing MFM measurements in the presence of an electric field[39-40], whereas Xie and coworkers studied the ME effect in two phase $PbZr_{0.52}Ti_{0.48}O_3$ (PZT) and Terfenol nanocomposite disks by both magnetic force microscopy (MFM) and piezoresponse force microscopy (PFM) under an electric and magnetic field, respectively.[41] Recently, the same group reported on the estimation of the ME coupling between a magnetostrictive and ferroelectric phase in $CoFe_2O_4$-$PbZr_{0.52}Ti_{0.48}O_3$ core-shell nanofibers by measuring the piezoelectric deformation of the composite in the presence of the magnetic field[42]. However, the determined values of both the piezoelectric (d_{31}=485 pm/V) and the lateral magnetoelectric coupling coefficient (α_H = 29.5 V/cm·Oe) are unusually high compared to those reported in the literature for similar materials.[43,5,44,6].

In this paper we demonstrate that the strain-mediated ME coupling in nanocomposites can be evaluated at nanometer-length scale both qualitatively and quantitatively by measuring the local deformation of the electrostrictive layer when the sample is subjected to the action of an external magnetic field. The proposed experimental methodology enables the direct mapping of the ME coupling through domain imaging along with the quantitative estimation of the ME coupling coefficient from the amplitude *vs.* bias voltage hysteresis loops, a key prerequisite for understanding the physics of the magnetoelectric interactions and the role of interfaces in

nanocomposites, as well as the implementation of multiferroic materials in nanoscale functional devices.

7.2. Experimental

Three different series of perovskite-spinel magnetoelectric bilayered structures were selected for the study of the stress-mediated ME coupling by magnetic field-assisted piezoresponse force microscopy. The first two samples were made of an electrostrictive $PbTiO_3$ layer interfaced with a ferrite layer having the magnetic phase as the top layer of the ME nanostructure. Two types of magnetostrictive layers were used: a soft magnetic material with the nominal composition $Ni_{0.66}Fe_{2.34}O_4$ (NFO) and a hexagonal hard magnetic ferrite ($BaFe_{12}O_{19}$-BFO), respectively. Polycrystalline perovskite and ferrite films with average thicknesses of 200 nm were processed by liquid phase deposition (LPD) onto $LaNiO_3$-buffered (100) conductive Si substrate (Ω=0.05 ohm/m)) using an experimental procedure reported previously.[45] The third series of samples consisted of an epitaxial $BaTiO_3$ (BTO)-$CoFe_2O_4$ (CFO) bilayered ME nanostructure grown by pulse laser deposition (PLD) onto a (001) single crystalline $MgAl_2O_4$ substrate by a procedure similar to that proposed by Stern and coworkers.[46] Prior to the deposition of the ferroic layers, an epitaxial 100 nm-thick $Ni_{0.6}Al_{0.4}O_{1+\delta}$ (NAO) film was deposited by pulse laser deposition onto the $MgAl_2O_4$ (MAO) substrate. The NAO layer mediates the growth of the spinel phase onto the perovskite film and minimizes the formation of defects. In the next step 100 nm-thick $BaTiO_3$ and $CoFe_2O_4$ layers were successively grown onto the NAO-buffered MAO substrate by focusing a beam generated by a KrF excimer laser (λ=248 nm) onto sintered polycrystalline targets using an energy density of 3 J/cm^2. During the deposition, the temperature was maintained at 700 ^oC and the process was carried out under an O_2 pressure of 100 mTorr. At the end of the deposition process, films were cooled down to room temperature with a cooling rate of 5^o C/min.

The phase purity of the bilayered films was investigated by X-Ray diffraction using a Panalytical X'Pert System equipped with a curved graphite single-crystal monochromator (CuK_α radiation), whereas the surface morphology, chemical composition and microstructure of the films were investigated with a LEO model 1530VO FE-SEM system operating in low vacuum mode at an accelerating voltage of 200 kV equipped with an energy-dispersive spectroscopy (EDS) detector. The atomic force microscopy (AFM), voltage-induced polarization switching and piezoresponse force microscopy experiments were investigated with an Asylum Research

MFP-3D atomic force microscope working in contact mode. Magnetic field microscopy (MFM) experiments were performed by using a rare-earth alloy-coated silicon tip with coercivity greater than 5 kOe which can generate a uniform magnetic field perpendicular to the film plane. An Olympus AC240TM conductive microcantilever (spring constant k=2 N/m) made of a tetrahedral silicon tip coated with platinum and titanium was used to excite the sample with a small oscillating voltage $V_{tip}=V_{dc}+V_{ac}\cos(\omega t)$ (2) with the amplitude of 40 mV. The alternating current generated by the tip will polarize the ferroelectric layer, inducing its deformation due the converse piezoelectric effect.

Piezoresponse force microscopy experiments were performed in dual resonance tracking (DART) mode, which enables the efficient tracking of the resonance frequency of the cantilever, eliminating the cross-talk effects and enhances the sensitivity of the measurement. The photodetector signal amplitude generated by the elastic deformation of the piezoelectric layer was demodulated with two separated lock-in amplifiers and the values of the piezoelectric coefficient were obtained after calibrating the photodetector signal. Since the piezoresponse of the sample is described as the first harmonic component of the tip deflection $A=A_0+A_{1\omega}\cos(\omega t+\varphi)$ (3), the phase φ provides information about the orientation of the electrical dipoles, whereas the amplitude $A_{1\omega}$ describes the electromechanical proprieties of the material[47]. During the measurements, a *dc* magnetic field parallel to the film surface generated by a variable field module (VFM) from Asylum Research. The magnetic field was swept from 0 to 2000 Oe (with an error of ±1 Oe) by adjusting the distance between the poles of the variable field module. To ensure the generation of a uniform electric field during the magnetic field-assisted PFM measurements, samples were measured in capacitor geometries obtained by sputtering Au top electrodes with an area of 5 mm^2 and a thickness of 50 nm through a standard lithography process. The measurement of the piezoresponse signal was performed in different areas of the sample with a typical size of 5 x 5 μm^2 with each measurement repeated 5 times in order to reduce the experimental error and ensure a high reproducibility of the results. The characteristic amplitude at which the electrostrictive layer vibrates is proportional to the piezoelectric coefficient d_{ij}: $A=\delta d_{ij}V_{ac}$ (4), where δ is a proportionality factor which varies from 10 to 100 and accounts for the amplitude enhancement at the tip-sample resonance and V_{ac} is the testing voltage.

7.3. Results

As described previously, the X-Ray diffraction and inductive coupling plasma (ICP) spectroscopy data indicated that the polycrystalline oxide films composing the bilayered magnetoelectric nanostructures are single phase and their chemical composition is close to that obtained by EDX analysis.[45] In Figures 7.1 (a) and 7.1 (b) are shown the top-view FE-SEM images of the $PbTiO_3$ (PTO) and $Ni_{0.66}Fe_{2.34}O_4$ (NFO) layer forming the perovskite-spinel bilayered structure. The $PbTiO_3$ film is uniform being constructed by densely-packed quasi-spherical grains with an average size of 70-80 nm (Figure 7.1 (a)). Similarly, the nickel ferrite film contains rod-like nanoparticles with an average length of 200 nm and diameter of 15 nm which ensure an intimate contact between the perovskite and ferrite phases across the shared interfaces. The topological features of the PTO layer were also confirmed by vertical atomic force microscopy. As seen in Figure 7.2, the PFM phase contrast image of the bilayered structure reveals the existence of randomly distributed bright and dark areas all across the film surface (3 x 3 μm^2), corresponding to ferroelectric domains with the polarization oriented upwards and downwards, respectively. When a negative magnetic field (H= -600 Oe) was applied in the film plane, the bright areas nucleated and grew at the expense of the dark regions, whose dimensions diminished significantly (Figures 2 (a) and 2 (b)). Conversely, when the magnetic field was reversed and its magnitude was varied progressively from H= 0 to H= +600 Oe, the dark areas enlarged, whereas the size of the bright spots decreased (Figures 2 (c) and 2 (d)).

Such a behavior is similar to that reported by Xie and coworkers[41] and clearly indicates that the dielectric polarization of the bilayered structure can be reversed with a magnetic field as a result of a strain-mediated ME coupling between the perovskite and spinel layers of the ceramic nanocomposite. These results are in good agreement with the presented results in the chapter six by using Raman spectroscopy for a similar polycrystalline PTO-NFO sample which indicated that the optical phonon modes in the Raman scattering spectrum of the perovskite phase undergoes significant shifts when a magnetic field was applied in the film plane indicating the existence of an elastic coupling between the two ferroic layers of the nanocomposite.[45] The topography studies of the bilayered structure did not evidence significant changes during the PFM experiments indicating a minimum cross-talk between the topography of the sample and its piezoelectric response during the PFM scans. In general the quantification of the values of the local piezoelectric coefficient from PFM measurements is difficult in capacitor geometry with the tip as the top electrode due to inhomogeneities of the electric field generated by the tip, as

well as the poor contact between the tip and the sample's surface.[48] To avoid the experimental errors in the measurement of the phase and amplitude of the piezoelectric response the measurements were performed on thin film specimens sputtered with a 5 nm-thick Au layer. In Figures 7.3 (a) and 7.3 (b) are shown the vertical PFM phase hysteresis loops of the PTO-NFO bilayered heterostructure subjected to different magnetic fields. The curves are slightly asymmetric with respect to the zero bias line due to a negative offset and correspond to coercivity values for the local switching of 7.3, 9.7, 9.3, 7.1 and 7.3 V, respectively. The asymmetry of the phase hysteresis loops can originate from different factors, such as a small imprint[12,49-50], a different barrier potential between the electrode and the film[51], pinning of the domain walls by defects[50] or the presence of an internal electric field inside of the film.[52]

A closer inspection of the experimental data indicated that the shift of the hysteresis loops is reproducible but random, similar to that observed recently by Xie and coworkers in the case CFO-PZT core-shell nanofibers[42]. Interestingly, the phase loops reverse their orientation when the magnetic field increased from 600 to 900 Oe. As the phase of the piezoelectric signal is associated with the orientation of the dielectric polarization, the reversal of the orientation of the loops furthermore confirms the influence of the magnetic field on the dielectric polarization of the perovskite layer as a result of the mechanical stress produced in the adjacent ferrite layer at a critical value of the applied magnetic field. The value of the change in the phase signal is about 179^{o}, value which is consistent with the existence of 180^{o} ferroelectric domains in the polycrystalline PTO layer. This also indicates that the response of the sample is due to the electromechanical contribution and does not originate from long range electrostatic forces.[53]

The presence of the 180^{o} domain structures was further confirmed by the linearity of the amplitude loops of the piezoelectric signal (Figure 7.4), which exhibit a "butterfly"-type shape characteristic for a ferroelectric material. Interestingly, the piezoelectric response increased from 219 to 250, 288, 307, 385 and 454 pm and the linear portions of the amplitude loops become steeper by sweeping the magnetic field from 0 to 1500 Oe, which suggests that the piezoelectric coefficient is magnetic field dependent. To confirm this experimental observation and rule out any possible measurement artifacts, a series of measurements was carried out under the same experimental conditions by exciting the cantilever at frequencies far from its resonance value (270 kHz). In Figure 7.5, are presented the vertical PFM phase loops of the PTO-NFO bilayered nanostructure collected at 80, 120, 200 and 240 KHz, respectively. A closer look at the plots

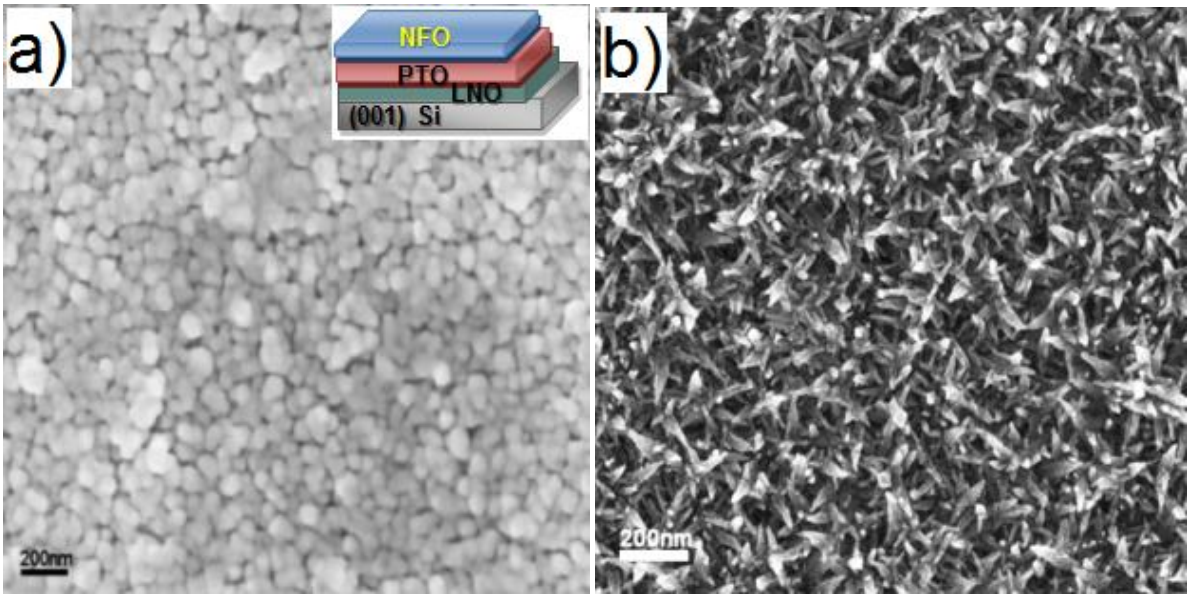

Figure 7.1. Top view field-emission scanning electron microscopy images of the images of the $PbTiO_3$ (Fig. 1a) and $Ni_{0.66}Fe_{2.34}O_4$ (Fig. 1b) layers of the ME thin film structure; AFM topography image of the $PbTiO_3$ layer (Fig. 1c) and schematic of the ME bilayered nanostructure deposited on a $LaNiO_3$-buferred (100) Si substrate

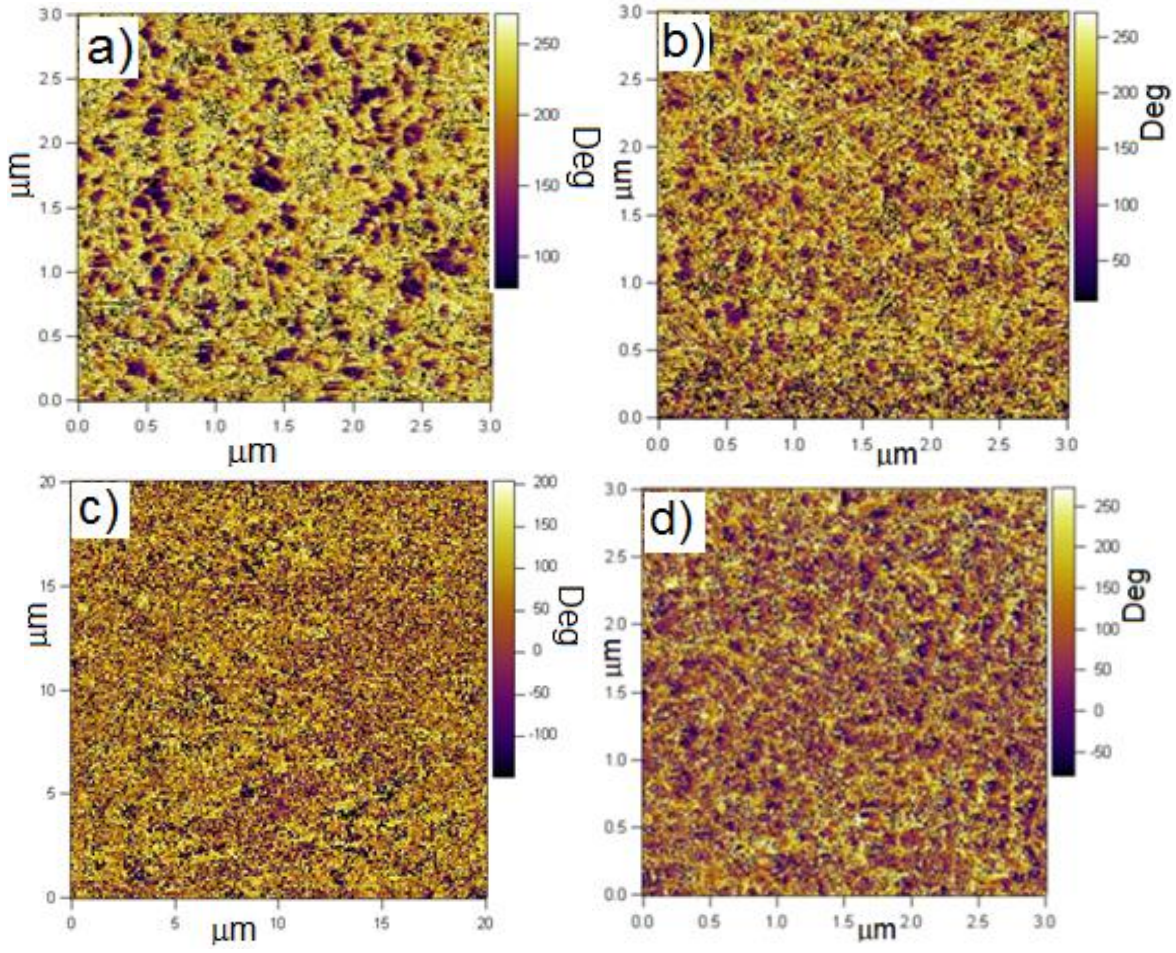

Figure 7.2. Out–of–plane PFM phase contrast images of the PTO-NFO bilayered composite under a magnetic field parallel to the plane of the film and different magnitudes H= -600 Oe (a), 0 Oe (b), +300 Oe (c) and +600 Oe (d), respectively

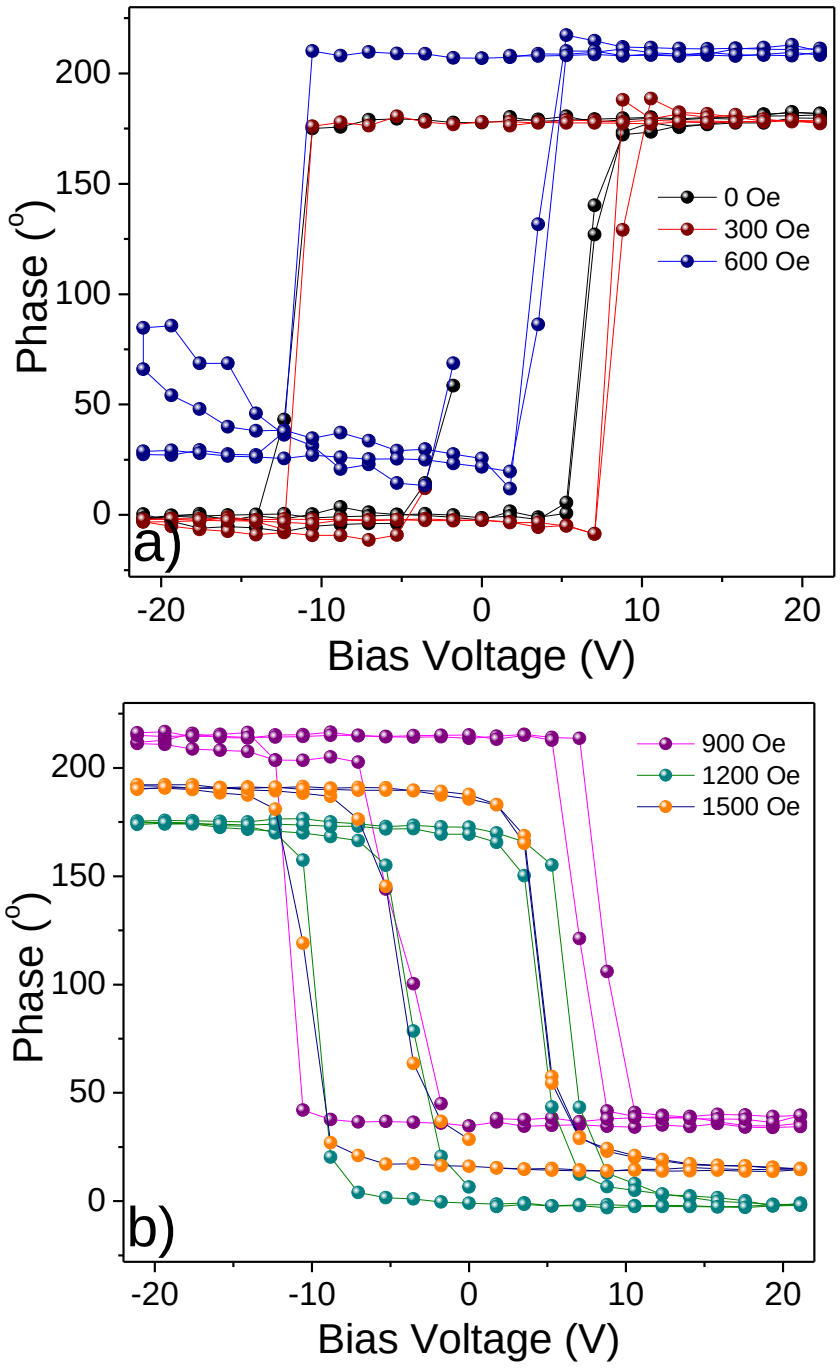

Figure 7.3. Phase (a) and amplitude (b) curves of the piezoresponse of the PTO-NFO bilayered structure under different magnetic fields

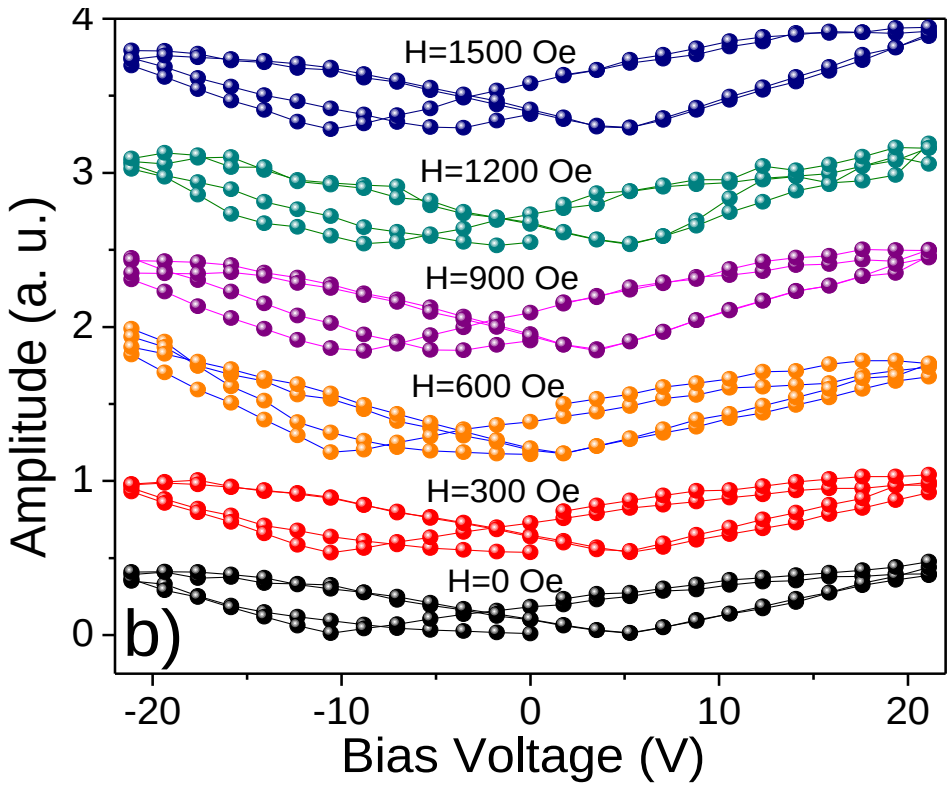

Figure.7.4. Amplitude PFM curves of the piezoresponse of the PTO-NFO bilayered structure collected in DART mode under different magnetic fields. The plots have been translated vertically to increase their visibility

evidenced several important trends in the aspect of the PFM amplitude data: (i) at low frequencies the noise level increases significantly but the piezoresponse of the multilayered nanocomposite still remains robust; (ii) at all frequencies the amplitude of the PFM signal increases with the magnetic field and the hysteresis loops present a vertical offset and (iii) the slope of the linear portions of the amplitude curves is positive and increases with the magnetic field.

Such a behavior is very similar to that observed when the PFM measurement was performed at frequencies near resonance and indicates that the collection of the experimental data in DART mode is highly reproducible and the piezoresponse signal of the sample does not interfere with measurement artifacts. To check whether the change in the slope of the amplitude loops is indeed reversible and originates from a stress-mediated coupling between the magnetic and electrostrictive layers of the nanocomposite, the piezoresponse of the sample was also measured in the negative range of values of the magnetic field. As seen in Figure 7.6, the values of the amplitude signal decreased from 857 to 775, 723, 700, 520 and 413 pm when the magnetic field varied from H= -1500, -1200, -900, -600 -300 and 0 Oe, respectively. It is noteworthy to mention that in a negative magnetic field the amplitude of the piezoresponse is almost two times higher than in positive field. Such a behavior closely matches the observation made recently by Xie *et al.*[41] and was ascribed to the fact that the strain induced in the magnetostrictive layer is invariant to the sign of the magnetic field since the magnetoelectric effect is quadratic in nature and generally produces a stronger ME effect in negative magnetic fields. The variation of the magnetostrictive strain with the applied magnetic field extracted from the room temperature hysteresis loops [54] is shown in Figure 7.7.

To further verify the role of the elastic coupling between the ferrite and perovskite phases on the piezoelectric deformation of the bilayered ceramic nanocomposites a control experiment consisting of collecting PFM scans in a magnetic field for of a $SrTiO_3$-Ni ferrite bilayered structure was performed. The experimental data shown in Figure 7.8 is very noisy and, more importantly, did not evidence detectable changes in the slope of the amplitude. This confirms once more that the magnetic field dependence of the piezoresponse of the nanocomposite is intrinsic and results solely from the electromechanical coupling between the magnetostrictive and piezoelectric layers in the nanocomposite. The linear fitting of the amplitude loops corresponding to the magnetic field-induced piezoelectric deformation of the samples yielded the following values of the effective longitudinal piezoelectric coefficient d_{33}:10.25±0.02,

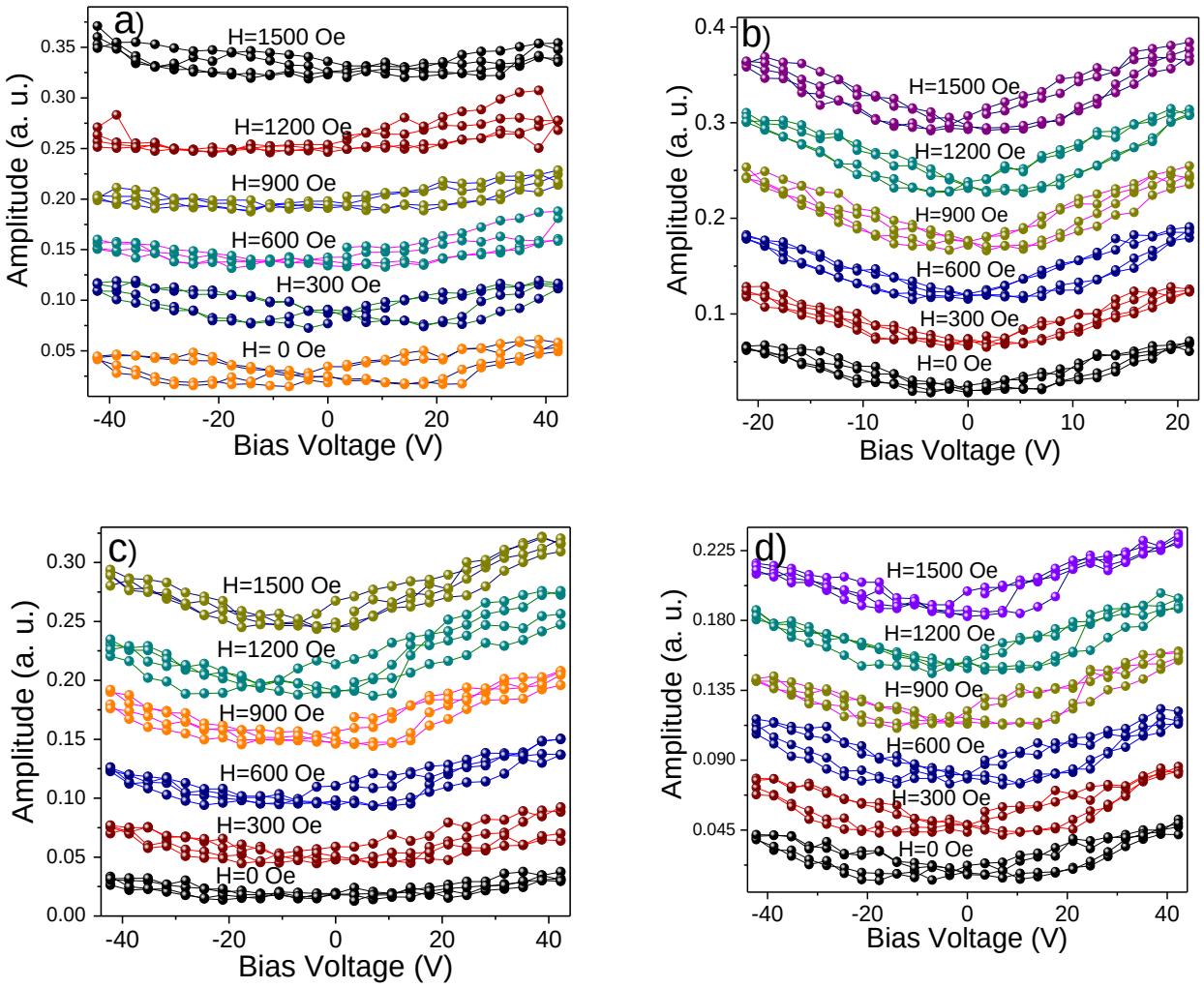

Figure 7.5. Magnetic field-dependent piezoresponse amplitude curves of the PTO-NFO bilayered structure measured in DART mode at different frequencies: 80 kHz (a), 120 kHz (b), 200 kHz (c) and 240 kHz (d), respectively

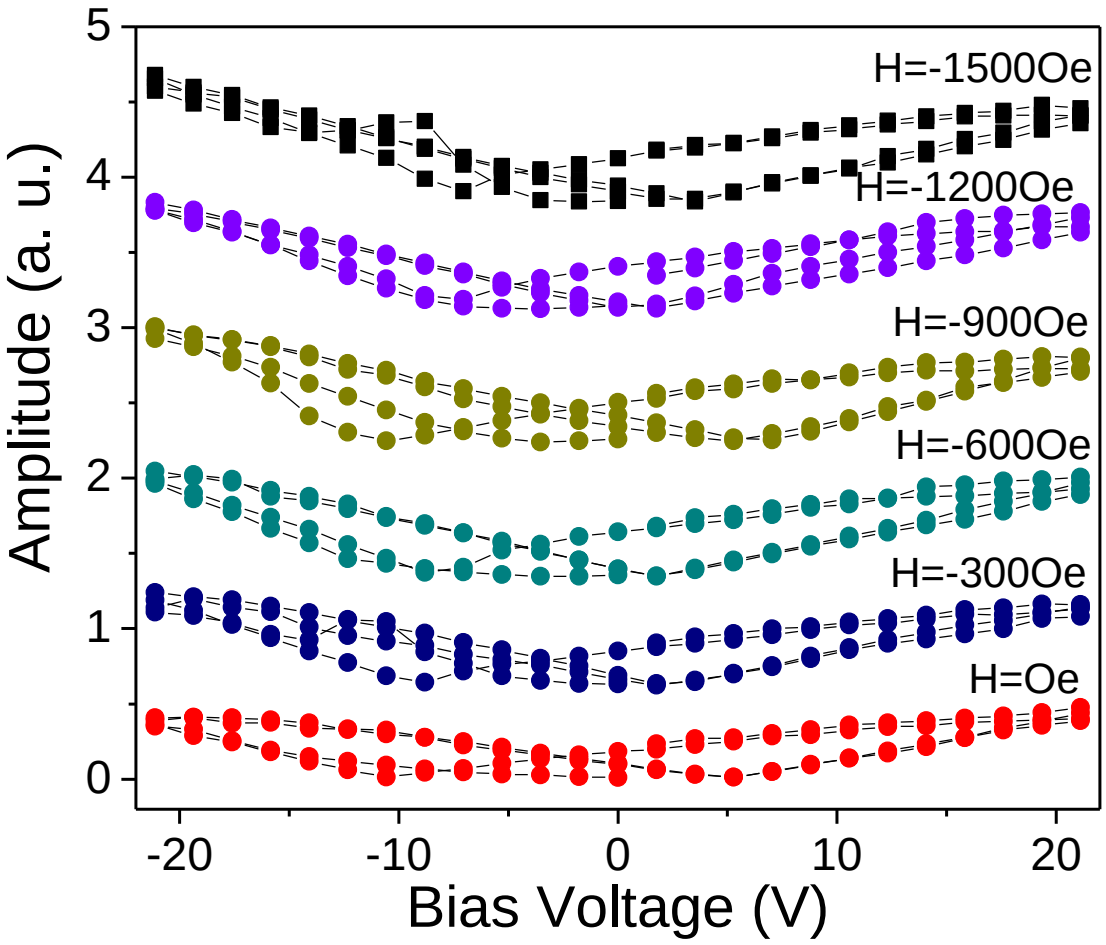

Figure 7.6. Magnetic field-dependent piezoresponse amplitude curves of the PTO-NFO bilayered structure measured by applying a negative magnetic field. The plots were translated vertically to increase their visibility

11.91±0.03, 13.56±0.02, 14.6±0.01, 17.97±0.08 and 21.7±0.09 pm/V for a magnetic field of 0, 300, 600, 900, 1200 and 1500 Oe. These values are smaller than the bulk (d_{33}≈160 pm/V)[55] value and do not vary noticeably at fields above H= 1200 Oe due to the complete saturation of the nickel ferrite layer.[45]

A second series of samples consisted of perovskite-spinel epitaxial heterostructures made of a 100 nm-thick $CoFe_2O_4$ (lattice parameter a=8.36 Å) film grown onto a $BaTiO_3$ layer with a similar thickness (lattice parameter a= 3.99 Å). In Figure 7.9 (a) is shown the θ-2θ X-Ray diffraction scan of the epitaxial $BaTiO_3$-$CoFe_2O_4$ (BTO-CFO) bilayered structure grown on a $Ni_{0.6}Al_{0.4}O$-buferred (001) $MgAl_2O_4$ (a= 8.084 Å) substrate. The XRD pattern features well defined peaks identified as the (004) reflection of the CFO layer (2θ≈ 43.1^o), the (002) reflection of the BTO film (2θ≈ 45.4^o) and the (002) peak of the $Ni_{0.6}Al_{0.4}O$ buffer layer (2θ≈ 45.4^o), respectively. Rocking curve measurements (Figure 7.10) revealed that both the BTO and CFO layers are crystalline and the BTO layer (average full-width-at-half maximum FWHM=0.286^o) has a better quality than the CFO layer (FWHM=0.405^o) respectively. Furthermore, the φ scans (not shown) indicated an epitaxial relationship $(001)_{CFO}||(001)_{BTO}||(001)_{NAO}$.

The inset of Figure 7.9 (a) displays the AFM topography image of the CFO top layer of the CFO-BTO epitaxial ME nanocomposite indicating that the film is smooth with a roughness of less than 1 nm and covers uniformly the substrate. As seen in Figures 7.9 (b) and (c), the magnetic domain structure of the BTO-CFO bilayered nanocomposites changes when the sample was electrically poled with a voltage of 10 V, indicating a strong coupling between the perovskite and spinel phases. Such a behavior was previously observed by Chung *et al*.[40] in the case of a PZT-Ni magnetoelectric bilayered structure and was ascribed to an incomplete reversal of the local longitudinal magnetization under the action of an electric field[31]. In Figure 7.11 are illustrated the phase *vs.* field curves of the BTO-CFO epitaxial bilayered nanostructure. Similar to the PTO-NFO bilayered composite, the phase curves are asymmetric and exhibit a hysteretic variation of the polarization with the electric field at room temperature.

It can be also noticed that the phase loops reverse their orientation at magnetic fields above 500 Oe and the values of the coercive voltage were 7.2, 7.7, 8.6, 4.3 and 9.4 V, respectively. The amplitude of the piezoelectric signal (Figure 7.12) was found to increase from 79.8, 102.9, 162.2, 238.5 and 264.1 pm when the magnetic field was increased from 0, 500, 1000, 1500 and 2000 Oe, respectively. A similar trend was observed for the slope of the linear

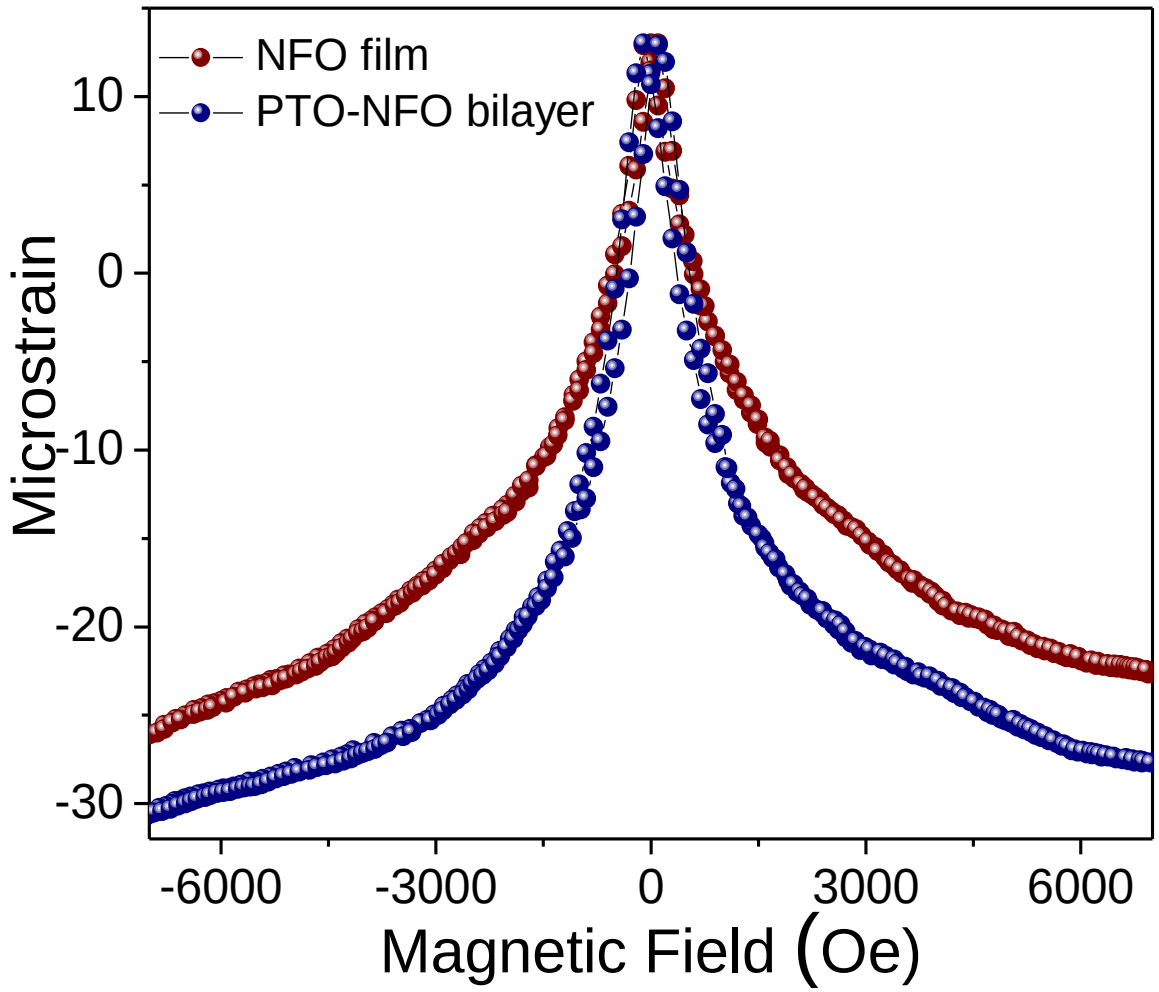

Figure 7.7. Magnetostriction of the NFO (red curve) and the NFO-PTO (blue curve) bilayered structure

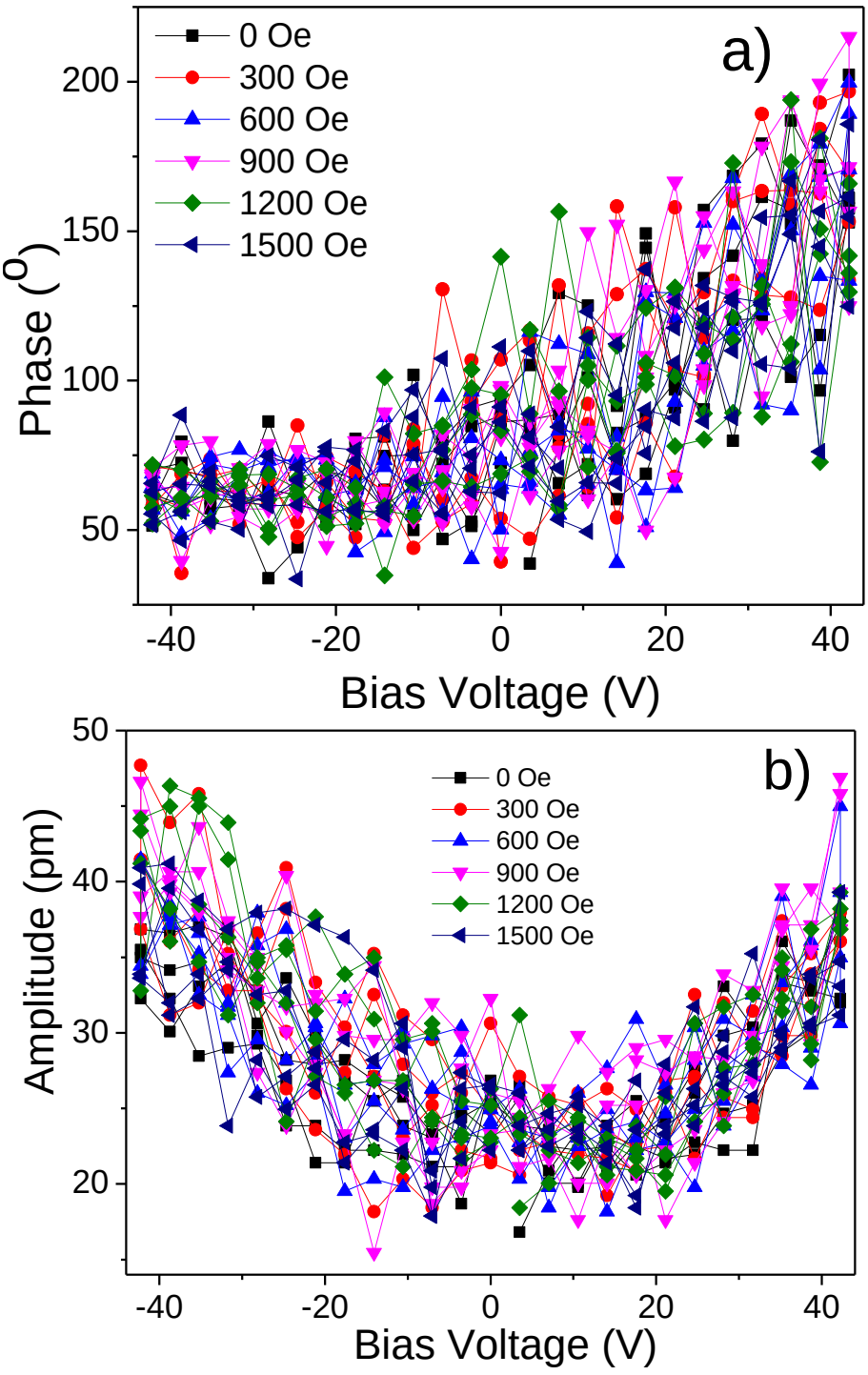

Figure 7.8. Phase and amplitude curves of the piezoelectric signal of for a PTO film deposited on a single crystalline (001) $SrTiO_3$ substrate

portion of the amplitude curves, suggesting that, similar as for the NFO-PTO polycrystalline bilayered nanostructure, the piezoelectric coefficient is magnetic field dependent. The corresponding piezoelectric coefficient d_{33} calculated from the linear fitting of the amplitude loops are smaller than to those obtained for the PTO-NFO nanocomposite film structure. Specifically, they were found to increase from 6.75±0.07 to 7.94±0.05, 9.24±0.02, 10.85±0.07 and 14.71±0.04 pm/V when the magnetic field was varied from 0 to 2000 Oe.

It is noteworthy to mention that based on the typical values of the saturation field of cobalt ferrite films (H≥ 6 KOe)[45,56-57], a further increase of the piezoelectric coefficient d_{33} with the magnetic field is expected since the $CoFe_2O_4$ layer of the bilayered nanocomposite is not completely saturated at 2 KOe, the maximum field attainable with the VFM module used in these experiments. Shown in Figure 7.13 (a), are the plots of the phase *vs*. the applied bias voltage for a third series of samples consisting of a polycrystalline PTO-$BaFe_{12}O_{19}$ bilayered nanocomposite. As in the case of other perovskite-ferrite bilayered structures, the phase curves indicate the existence of a switchable polarization in the $PbTiO_3$ layer; however, in this case no reversal of the orientation of the loops was observed experimentally. The phase loops present both a vertical and horizontal offset and undergo a significant change when the magnetic field varied from 0 to 2000 Oe due to the reorientation of ferroelectric domains. The saturation was reached at bias voltages typically below 12 V and the coercive bias for local switching was found to increase monotonically from 2.6 to 3.5, 6.9, 9.7 and 10.5 V when the magnetic field was varied from 0 to 2000 Oe. The piezoresponse amplitude curves presented in Figure 7.13 (b) show a substantial change of the displacement and slope when a magnetic was applied in the film plane. Unlike the spinel ferrite-containing bilayered nanostructures, the amplitude of the piezoelectric signal is much stronger and decreases from 845 pm to 604.5, 532, 471 and 433 pm when the magnetic field varied from 0, 500, 1000, 1500 and 2000 Oe, respectively.

The slope of the linear portions of the butterfly-loops follows a similar trend. The zero-field value of the longitudinal piezoelectric coefficient d_{33} calculated from the linear portion of the amplitude loops is 13.1±0.04 pm/V. This value is higher than the value measured in PTO-spinel ferrite bilayered nanostructures and was found to decrease monotonically from 13.01±0.04, 8.15±0.03, 6.45±0.06, 4.61±0.09 and 4.47±0.08 pm/V when the magnetic field varied from 0 to 500, 1000, 1500 and 2000 Oe, respectively.

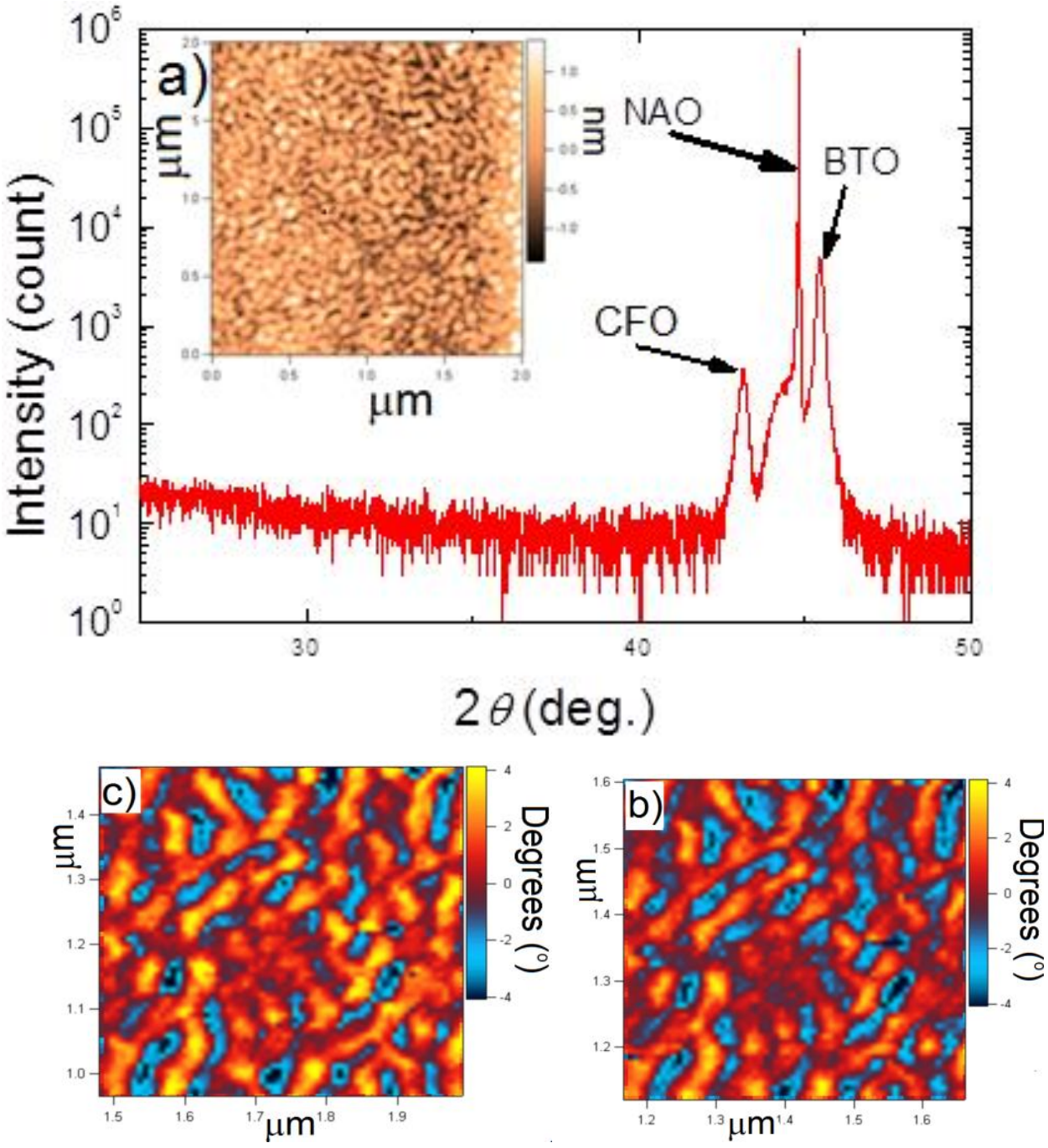

Figure.7.9. 2θ XRD scan of the BTO-CFO epitaxial bilayered nanostructure (a). Magnetic field microscopy images (MFM) of the sample before (b) and after electric poling with 10 V. The inset in Figure 5a represents a topography AFM image of the CFO layer of the magnetoelectric nanocomposite

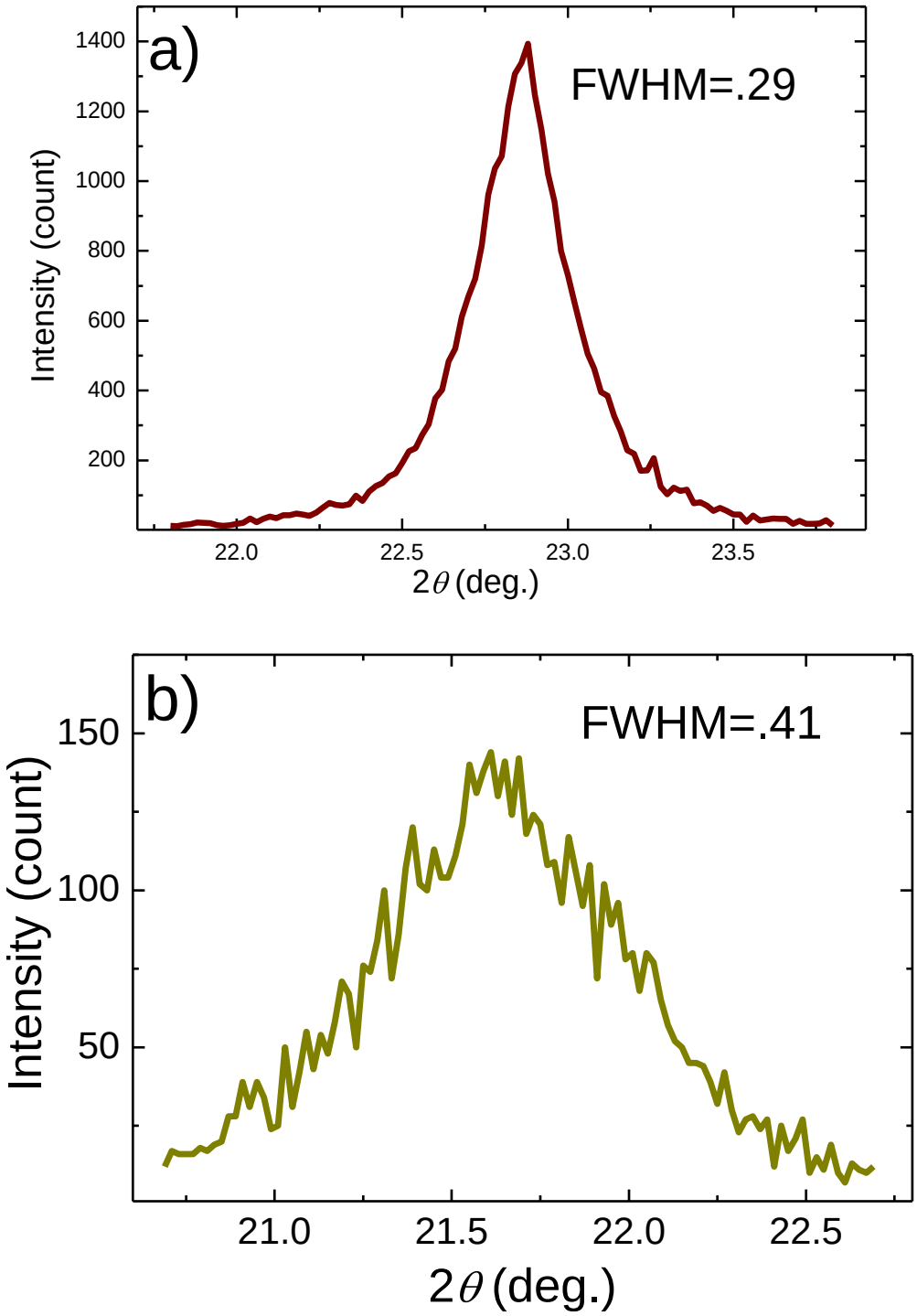

Figure 7.10. Rocking curves of the $BaTiO_3$ (a) and $CoFe_2O_4$ (b) layers of the epitaxial bilayered nanocomposite film

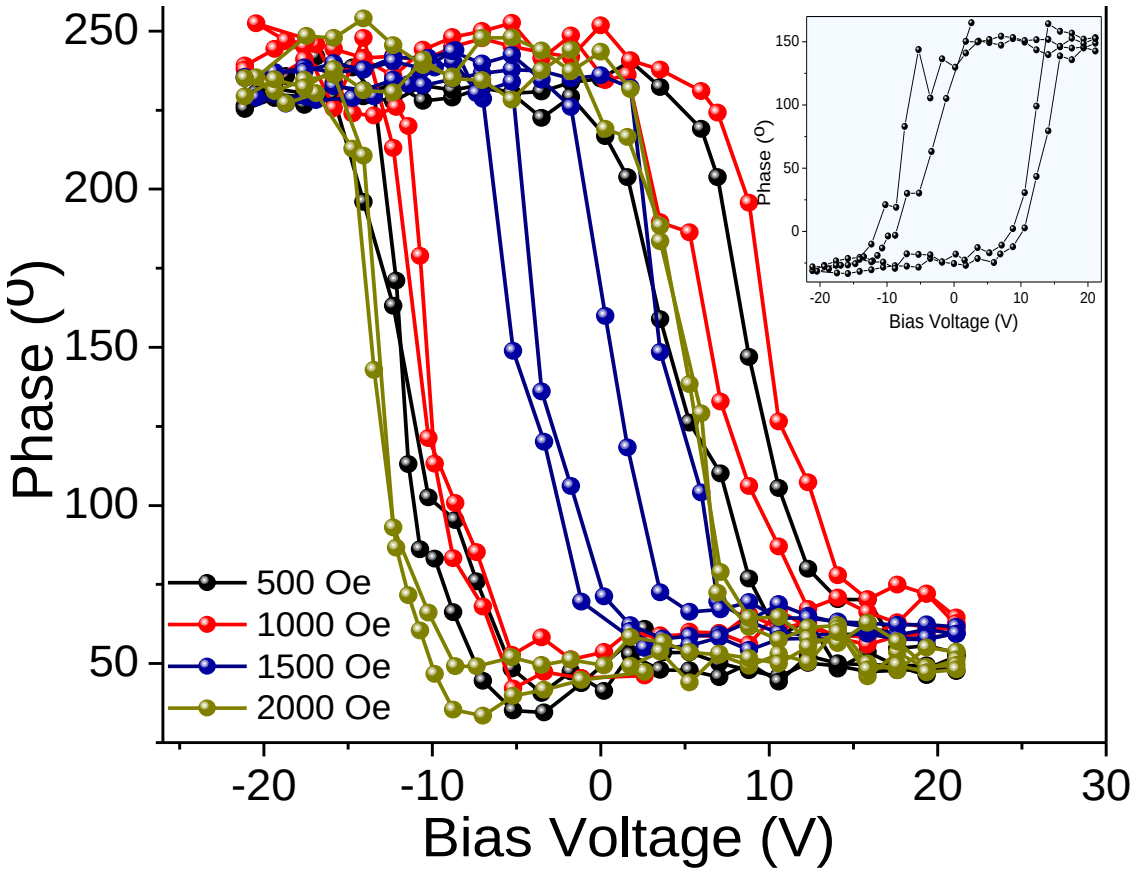

Figure.7.11. Phase of piezoresponse of the $BaTiO_3$-$CoFe_2O_4$ bilayered epitaxial nanostructure in different magnetic fields. The inset corresponds to the phase signal in the absence of the magnetic field

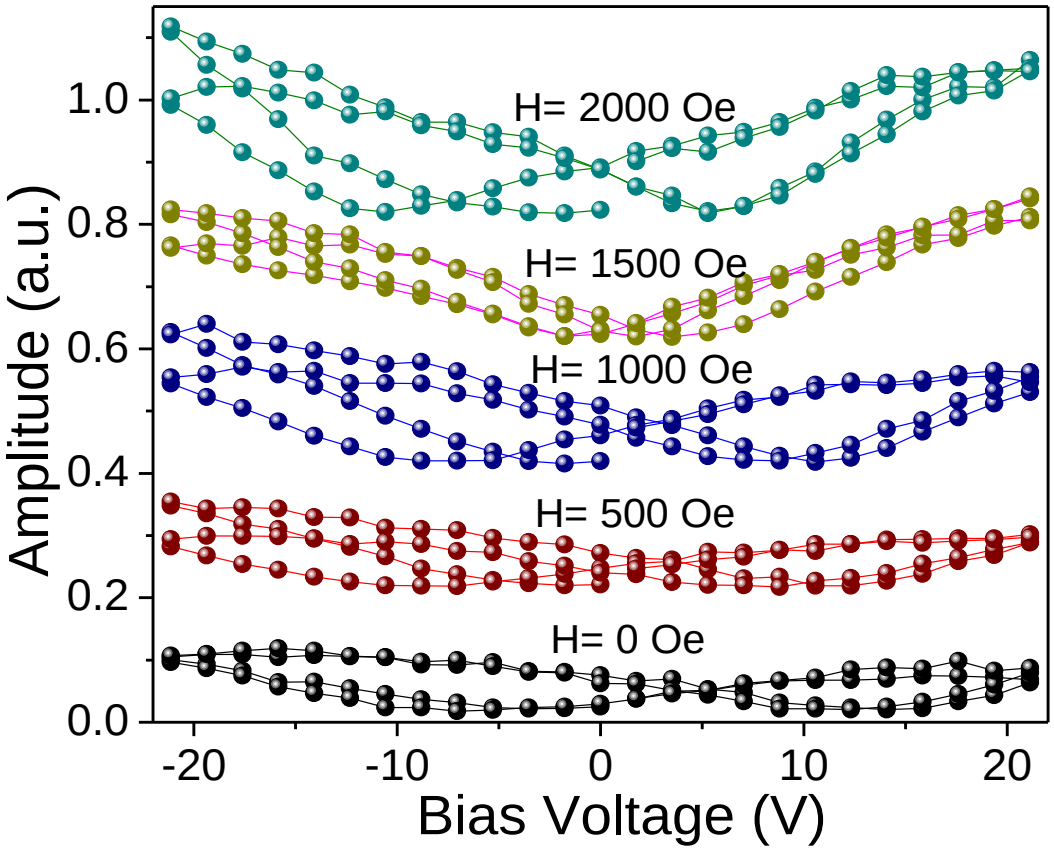

Figure.7.12. Phase of piezoresponse of the $BaTiO_3$-$CoFe_2O_4$ bilayered epitaxial nanostructure in different magnetic fields. Curves present a vertical offset to increase their visibility

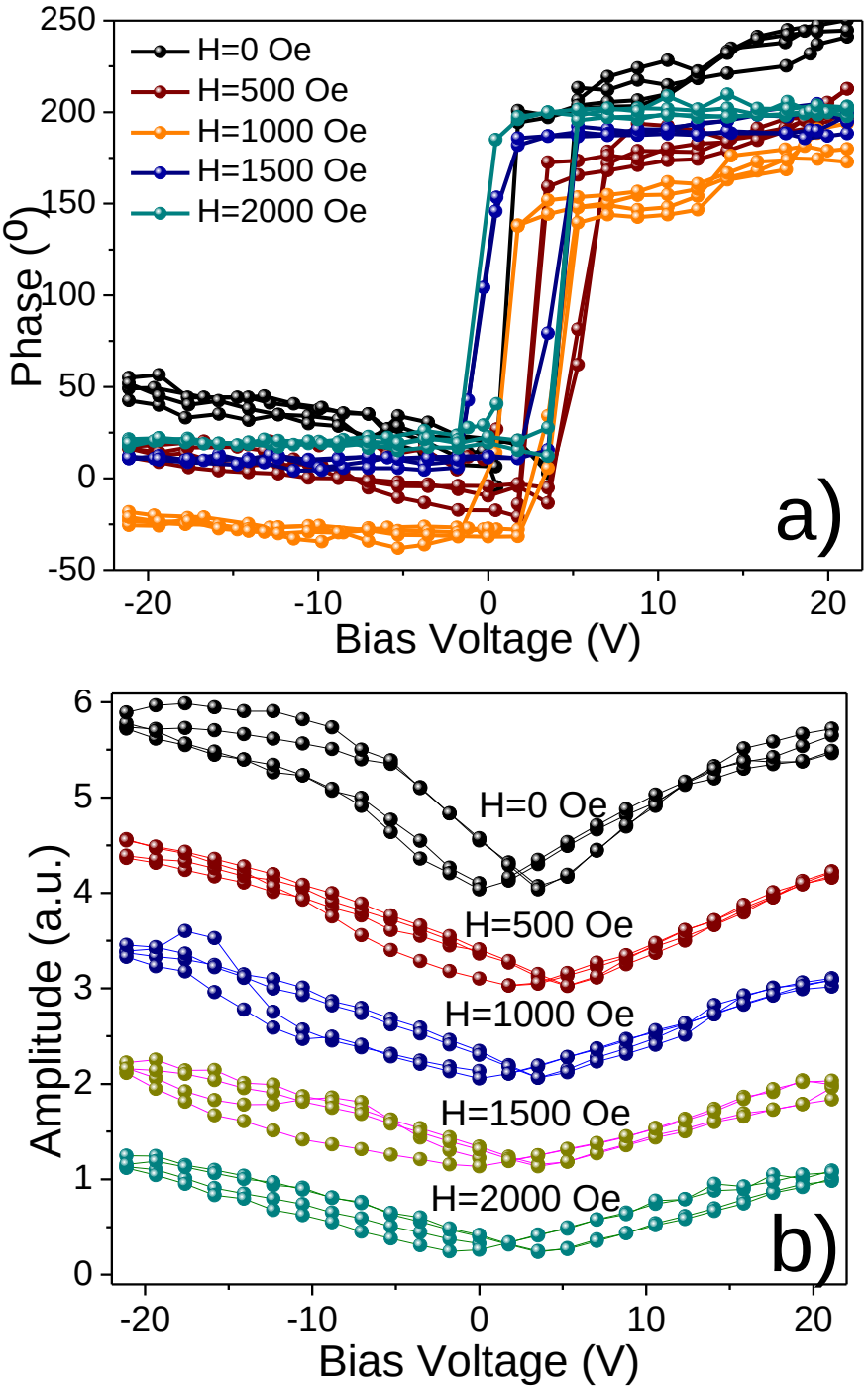

Figure.7.13. Phase (a) and amplitude (b) piezoresponse hysteresis loops of the PTO-Ba ferrite bilayered structure under a magnetic field

7.4. Discussion

Piezoresponse force microscopy is a reliable, non-destructive technique for the high-resolution characterization of the bias-induced deformation in ferroelectric materials. Although the PFM signal is generally weak, the sensitivity of the measurements can be considerably enhanced when the cantilever oscillations are driven in resonance mode[58-61,60]. High frequency PFM measurements generally lead to a substantial increase of both the signal-to-noise ratio and the mechanical amplification of the signal, thereby improving substantially the quality of the detected signal. An additional enhancement of the measurement can be achieved by increasing the stiffness of the cantilever; this improves the tip-surface interaction minimizing the non-local electrostatic contributions to the detected signal[62]. However, much care should be taken when measuring the piezoresponse signal near resonance since the contact frequency depends on both the dynamic response of the cantilever and/or the elastic modulus of the ferroelectric surface and this can lead to experimental artifacts. As an example, the non-uniform contact stiffness of the tip-surface contact during the measurement can induce fluctuations of the PFM amplitude. This can, in turn, lead to cross-talk between the topography and the piezoresponse signal of the sample rendering difficult the interpretation of the piezoelectric deformation of the sample's surface and eventually leading to unrealistic values of the piezoelectric and magnetoelectric coefficients.

To increase the reliability of the PFM measurements and, at the same time, eliminate possible artifacts associated with operating frequencies close to resonance, the PFM experiments were performed in dual *ac* resonance tracking (DART) mode. As such, DART experiments were carried out by driving the cantilever at two oscillating voltages below and above the resonance frequency (270 kHz) with a band width of 5 kHz. Under these experimental conditions the difference in the amplitude signals resulting from variations of the voltage frequencies can be used as an input to keep the piezoresponse amplitude constant and, therefore minimize the cross-talk effects. When a magnetic field is applied to a layered ME nanostructure, an elastic deformation is produced both in the plane of the film and in a direction perpendicular to the magnetostrictive layer as a result of the interactive coupling between the magnetic field and the magnetic moments of the individual domains in the material. This mechanical deformation leads to a strain which is subsequently transferred across the interface affecting the ferroelectric domains of the electrostrictive layer and inducing a sizeable change in its dielectric polarization. On the other hand, since the dielectric constant and polarization of the ferroelectric phase are

coupled with the piezoelectric coefficient, a magnetic field-induced change in the polar ordering of a ME material will modify the value of the piezoelectric coefficient and this can be detected by a change in slope of the variation of the amplitude PFM signal *vs.* the bias voltage.

In the experiments described above, the magnetic field-assisted PFM measurements were performed in perovskite-ferrite ME bilayered structures in which the magnetic phase forms the top layer. Although this geometry exploits the low resistivity of ferrites which serve as top electrodes, it is expected that the measured piezoresponse signal will contain an additional term associated with the transverse magnetostriction of the magnetic layer excluding those corresponding to the electrostatic, non-local contribution due to capacitive cantilever surface interactions[59,63-65] and the electromechanical contribution due to the converse piezoelectric effect.[66] Since the magnetostrictive deformations are several orders of magnitude smaller than the piezoelectric signal, and the transverse magnetostriction is nearly equal to one half of the longitudinal magnetostriction[54], the term associated to magnetostriction can be neglected in the quantitative estimation of the transversal piezoelectric coefficient.

The interpretation of the experimental results was performed in the frame of the theoretical model proposed by Vopsaroiu *et al.* based on the standard thermodynamic treatment of the electrical polarization in a ferroelectric material. These authors studied the magnetic field-induced coupling in a trilayered Permendur(CoFeV)/PZT/Permendur ME structure by piezoresponse force microscopy in the presence of two magnetic fields, one static and one dynamic, parallel to each other and parallel to the plane of the film[67]. The thermodynamic treatment of the ME coupling allowed for the quantitative estimation of the effective ME coefficient from the linear variation of the piezoelectric coefficient with the applied magnetic field:

$$d_{33}^{eff} = \frac{D_3}{\sigma_3} - \frac{\alpha_{33}}{\sigma_3} H_1 \qquad (7.2)$$

where α_{33} is the effective ME coupling coefficient, D_3 is the dielectric displacement, σ_3 is the mechanical stress, d_{33}^{eff} is the third rank tensor of the piezoelectric coefficient and H_1 is the magnetic field, respectively. The zero-field value of the effective longitudinal piezoelectric coefficient was d_{33}^{eff} = -28 pC/N. From Eq. (2) it can be inferred that d_{33}^{eff} increases linearly with H. For the trilayered Permendur(CoFeV)/PZT/Permendur this variation has a negative slope due

to the positive magnetostrictive coefficient of Permendur (λ=70 ppm[25]) associated with a positive stress σ_3. Based on Eq. (7.2), we propose that in ME materials in which the magnetic phase displays a negative magnetostriction coefficient, d_{33} will also vary linearly with the magnetic field, but in this case the corresponding slope is positive. Such a hypothesis was experimentally tested and proven in this work, since the fabricated nano-composite multiferroic samples contain each a ferrite material with negative or positive magnetostriction coefficient, respectively. This result has also been confirmed by experiments using a PTO-$Tb_{1-x}Dy_xFe$ (x=0.3) (Terfenol) sample, whereby the longitudinal piezoelectric coefficient d_{33} was found to decrease with increasing the magnetic field, similar to the case of the PTO-Ba ferrite bilayered structure.[68] These results are best emphasized in Figure 7.14, which shows the magnetic field dependence of the d_{33} coefficient for the polycrystalline layered ME nanocomposites.

A very interesting result of this work is the deduced positive magnetostriction of the Ba ferrite layer, as indicated by the decrease of the measured values of the d_{33} coefficient with the magnetic field in the case of the PTO-Ba ferrite layered nanocomposite (Figure 7.14 (b)). In general, ferrites have negative magnetostriction coefficients. However, in exact terms, the magnetostriction coefficient is a tensor and the signs of its tensor components are strongly dependent on the crystallographic direction along which they are measured. For example, the magnetostriction of bulk and single crystalline magnetite Fe_3O_4 is negative (λ_{100}= -19.4 ppm) along the (100) direction and becomes positive (λ_{111}= 86.4 ppm) along (111)[23]. Despite the increasing number of studies on the magnetic properties of hexagonal ferrites in the past few decades, little is known about the magnetostriction of $BaFe_{12}O_{19}$ in both bulk and nanostructured forms. Due to its intrinsic structural anisotropy, barium ferrite may show a positive magnetostriction along the c axis. Previous reports on the magnetoelastic properties of hexagonal ferrites suggested that the out of plane component of the magnetostriction in polycrystalline $BaFe_{12}O_{19}$ has a positive sign, whereas the in-plane component is negative.[24,69]

FE-SEM studies indicated that the barium ferrite film is textured in the plane of the film, being constructed by closely-packed rectangular grains. Thus, the contribution of the out-of-plane component will dominate the magnetostriction and, therefore the stress induced in the $BaFe_{12}O_{19}$ film under a magnetic field is a tensile stress. Consequently, the d_{33} coefficient will decrease with the magnetic field as a result of the mechanical deformation induced in the ferroelectric PTO layer, result which is fully consistent with Eq. (2) and the experimentally observed data. The direct ME coupling coefficient is conventionally defined as

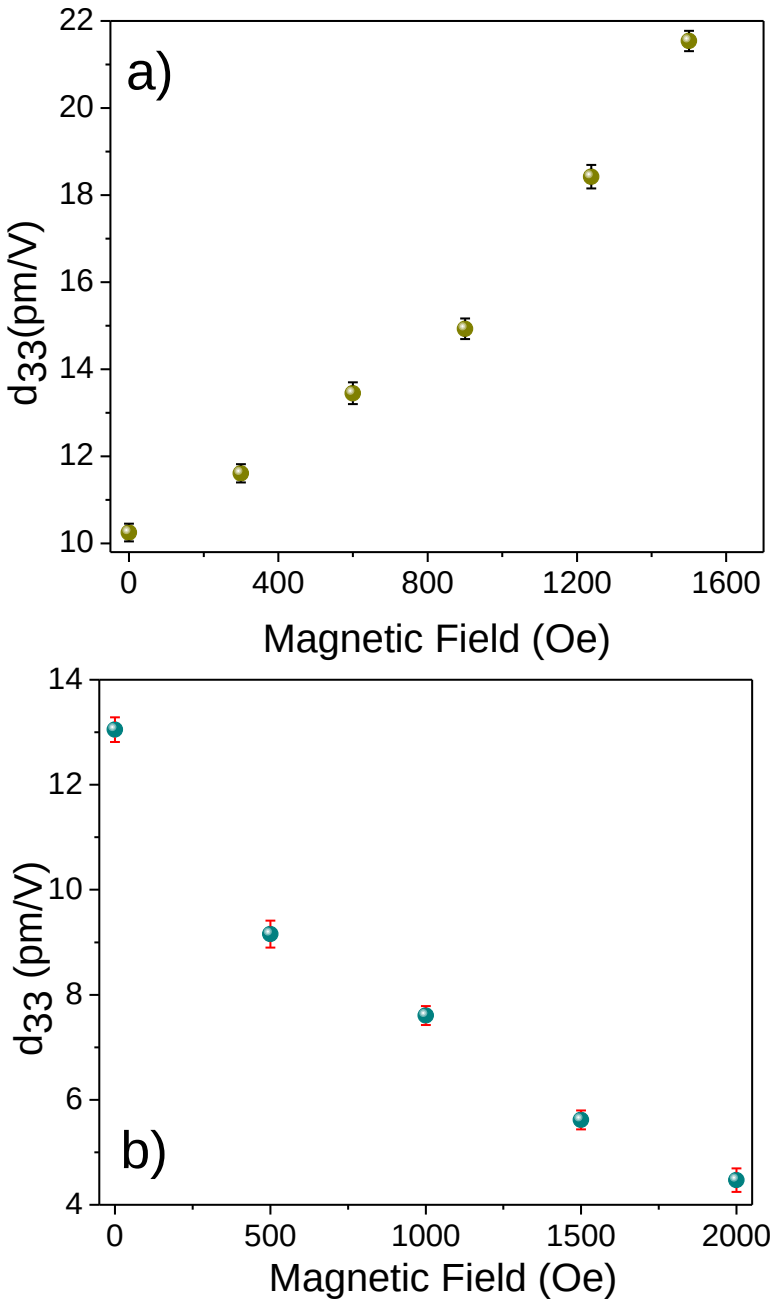

Figure.7.14. Magnetic field-dependence of the d_{33} coefficient for the PTO-NFO and PTO-Ba ferrite bilayered structures

$\alpha_{ME} = \frac{\partial E}{\partial H}$ (7.3), where E and H represent the electric and magnetic field, respectively. It is well known that the polarization in a dielectric material is proportional to the external electric field $P = \varepsilon_{33} E_3$ (7.4) where ε_{33} is the in-plane component of the dielectric permittivity tensor. On the other hand, it is acknowledged that in ferroelectrics with a centrosymmetric paraelectric phase, such as $PbTiO_3$, the piezoelectric effect may be considered as the electrostrictive effect biased by the spontaneous polarization[70]: $d_{33} = 2\varepsilon_{33} QP$ (7.5), where Q is the longitudinal electrostrictive coefficient. By combining Eqs. (7.3), (7.4) and (7.5) we obtain a relationship which allows the quantitative measurement of the direct ME coupling coefficient from the magnetic field dependence of the longitudinal piezoelectric coefficient:

$$\alpha_{ME} = \frac{1}{2\varepsilon_{33}^2 Q} \frac{\partial (d_{33})}{\partial H} \tag{7.6}$$

Using a value of the longitudinal electrostrictive coefficient[71] $Q_{33}=7.8.10^{-2}$ m^4/C^2 and an average value $\varepsilon \approx 360$ of the dielectric constant for $PbTiO_3$ thin films with a thickness comparable to that of the perovskite layers used in this work[72-73] and taking into account that the $LaNiO_3$ buffer layer generally increases the relative dielectric susceptibility coefficient by 25-30%[74] the ME coupling coefficients calculated from Eq. (7.6) were 284.3 mV/cm·Oe and 139.4 mV/cm·Oe for the $PbTiO_3$-$Ni_{0.66}Fe_{2.34}O_4$ and $PbTiO_3$-$BaFe_{12}O_{19}$ bilayered nanostructures, respectively.

In a similar fashion, by considering an average value of $\varepsilon \approx 750$ for the relative permittivity of the $BaTiO_3$ layer[75-76] and a value of $Q_{33}=0.11$ m^4/C^2 for the electrostrictive coefficient[77-79] for the epitaxial $BaTiO_3$-$CoFe_2O_4$ bilayered nanostructure the calculated value of the ME coupling coefficient was 562.1 mV/cm·Oe. These values indicate a very good ME coupling in the bilayered nanostructures studied in this work and are consistent with those reported in the literature for particulate perovskite ferrite ME nanocomposites.[80-82] It can be also noted that in the epitaxial nanostructure the elastic interaction between the ferroic layers is much stronger than that in polycrystalline samples, presumably due to the random orientation of the crystallites in the later ones. Interestingly, if we assume that for the small volumes of the samples in contact with the tip the generated electric field is homogeneous and consider the expression of the mechanical stress σ_3 in a piezoelectric material, which is defined as[70]:

$\sigma_3 = \frac{-E_3}{g_{33}}$ (7.10) and $g_{33} = \frac{d_{33}}{\varepsilon_{33}}$ (7.11), where g_{33} and d_{33} and piezoelectric coefficients and combine the equations (7.9) with (7.10) and (7.11) we obtain:

$$\alpha_{ME} == -\frac{\sigma}{\varepsilon_{33}} \frac{\partial(d_{33})}{\partial H} \tag{7.12}$$

which is identical to the expression proposed by Vopsaroiu *et al*.[67] This demonstrate that two equations are equivalent, and not only confirm that the variation of the piezoelectric coefficient is due to the existence of a magnetoelectric coupling between the two phases of the nanocomposite, but also validates the proposed model for the quantitative and qualitative measurement of the ME coupling coefficient from magnetic field-assisted PFM measurements.

7.5. Conclusions

In summary, the stress-mediated magnetoelectric coupling induced locally by a magnetic field in three different series of polycrystalline and epitaxial perovskite–ferrite heterostructures in a film-on-substrate geometry was investigated both qualitatively and quantitatively. The experimental protocol involves the measurement of the changes in the piezoresponse of the multiferroic sample when a static magnetic field is applied in the plane of the film. Due to the magnetostriction of the ferrite layer, the stress produced is transferred across the interface to the perovskite layer, thereby changing its piezoresponse which can be detected experimentally by a lock-in technique from the deflection of the AFM tip. From the magnetic field variation of the static piezoelectric coefficient a simple relationship for the quantitative estimation of the magnetoelectric coupling coefficient can be deduced. The obtained values were 284.3 mV cm^{-1} Oe^{-1} and 139.4 mV cm^{-1} Oe^{-1} for the polycrystalline $PbTiO_3$– $Ni_{0.66}Fe_{2.34}O_4$ and $PbTiO_3$–$BaFe_{12}O_{19}$ bilayered nanostructures and 562.1 mV cm^{-1} Oe^{-1} for the epitaxial $BaTiO_3$-$CoFe_2O_4$ film, respectively, indicating a strong ME coupling between the electrostrictive and magnetic layers at room temperature. The results obtained in the experiments described above indicate that this experimental protocol can be extended to other multiferroic structures with different chemical compositions, dimensionalities and connectivity schemes between the ferroelectric and magnetostrictive constituent phases.

7.6. References

(1) Bibes, M.; Barthelemy, A. *Nature Materials* **2008**, *7*, 425.

(2) Fiebig, M. *Journal of Physics D-Applied Physics* **2005**, *38*, R123.

(3) Scott, J. F. *Nature Materials* **2007**, *6*, 256.

(4) Ren, S. Q.; Weng, L. Q.; Song, S. H.; Li, F.; Wan, J. G.; Zeng, M. *JMatS* **2005**, *40*, 4375.

(5) Venkata Ramanaa, M.; Ramamanohar Reddy, N.; Sreenivasulu, G.; Siva kumar, K. V.; Murty, B. S.; Murthy, V. R. K. *CAP* **2009**, *9*, 1134.

(6) Wu, D. D.; Gong, W. H.; Deng, H. J.; Li, M. *Journal of Physics D-Applied Physics* **2007**, *40*, 5002.

(7) Nan, C.-W.; Bichurin, M. I.; Dong, S.; Viehland, D.; Srinivasan, G. *J. Appl. Phys.* **2008**, *103*, 031101.

(8) Dong, S.; Zhai, J.; Bai, F.; Li, J. F.; Viehland, D. *Appl. Phys. Lett.* **2005**, *87*.

(9) Filippov, D. A.; Bichurin, M. I.; Nan, C. W.; Liu, J. M. *J. Appl. Phys.* **2005**, *97*.

(10) Nan, C. W.; Liu, G.; Lin, Y. H.; Chen, H. D. *Phys. Rev. Lett.* **2005**, *94*.

(11) Laletin, V. M.; Paddubnaya, N.; Srinivasan, G.; De Vreugd, C. P.; Bichurin, M. I.; Petrov, V. M.; Filippov, D. A. *Appl. Phys. Lett.* **2005**, *87*.

(12) Gao, X. S.; Rodriguez, B. J.; Liu, L. F.; Birajdar, B.; Pantel, D.; Ziese, M.; Alexe, M.; Hesse, D. *Acs Nano*, *4*, 1099.

(13) Bai, F. M.; Zhang, H. W.; Li, J. F.; Viehland, D. *Journal of Physics D-Applied Physics* **2010**, *43*.

(14) Hibst, H. *Angewandte Chemie-International Edition in English* **1982**, *21*, 270.

(15) Rodriguez, B. J.; Eng, L. M.; Gruverman, A. *Appl. Phys. Lett.* **2010**, *97*.

(16) Wang, J.; Zhang, Y.; Ma, J.; Lin, Y. H.; Nan, C. W. *J. Appl. Phys.* **2008**, *104*.

(17) Chu, Y. H.; Martin, L. W.; Holcomb, M. B.; Ramesh, R. *Mater. Today* **2007**, *10*, 16.

(18) Zheng, H.; Wang, J.; Lofland, S. E.; Ma, Z.; Mohaddes-Ardabili, L.; Zhao, T.; Salamanca-Riba, L.; Shinde, S. R.; Ogale, S. B.; Bai, F.; Viehland, D.; Jia, Y.; Schlom, D. G.; Wuttig, M.; Roytburd, A.; Ramesh, R. *Sci* **2004**, *303*, 661.

(19) Thiele, C.; Dorr, K.; Bilani, O.; Rodel, J.; Schultz, L. *PhRvB* **2007**, *75*.

(20) Velev, J. P.; Duan, C.-G.; Burton, J. D.; Smogunov, A.; Niranjan, M. K.; Tosatti, E.; Jaswal, S. S.; Tsymbal, E. Y. *Nano Lett.* **2008**, *9*, 427.

(21) Catalan, G.; Noheda, B.; McAneney, J.; Sinnamon, L. J.; Gregg, J. M. *PhRvB* **2005**, *72*, 020102.

(22) Yang, J. J.; Zhao, Y. G.; Tian, H. F.; Luo, L. B.; Zhang, H. Y.; He, Y. J.; Luo, H. S. *Appl. Phys. Lett.* **2009**, *94*.

(23) Heaps, C. W. *PhRv* **1924**, *24*, 60.

(24) Turilli, G.; Licci, F.; Rinaldi, S.; Deriu, A. *J. Magn. Magn. Mater.* **1986**, *59*, 127.

(25) Filippov, D. A. *PhSS* **2005**, *47*, 1118.

(26) Gajek, M.; Bibes, M.; Fusil, S.; Bouzehouane, K.; Fontcuberta, J.; Barthelemy, A. E.; Fert, A. *Nature Materials* **2007**, *6*, 296.

(27) Aksenov, V. L.; Yu. Didyk, A.; Plakida, N. M. *physica status solidi (b)* **1984**, *124*, 45.

(28) Catalan, G. *Applied Physics Letters* **2006**, *88*.

(29) Vopsaroiu, M.; Cain, M. G.; Woolliams, P. D.; Weaver, P. M.; Stewart, M.; Wright, C. D.; Tran, Y. *J. Appl. Phys.* **2011**, *109*, 066101.

(30) Vopsaroiu, M.; Cain, M. G.; Woolliams, P. D.; Weaver, P. M.; Stewart, M.; Wright, C. D.; Tran, Y. *Journal of Applied Physics* **2011**, *109*.

(31) Zavaliche, F.; Zheng, H.; Mohaddes-Ardabili, L.; Yang, S. Y.; Zhan, Q.; Shafer, P.; Reilly, E.; Chopdekar, R.; Jia, Y.; Wright, P.; Schlom, D. G.; Suzuki, Y.; Ramesh, R. *Nano Lett.* **2005**, *5*, 1793.

(32) Eerenstein, W.; Wiora, M.; Prieto, J. L.; Scott, J. F.; Mathur, N. D. *Nature Materials* **2007**, *6*, 348.

(33) Mermin, N. D.; Wagner, H. *Phys. Rev. Lett.* **1966**, *17*, 1133.

(34) Liu, M.; Obi, O.; Lou, J.; Chen, Y. J.; Cai, Z. H.; Stoute, S.; Espanol, M.; Lew, M.; Situ, X.; Ziemer, K. S.; Harris, V. G.; Sun, N. X. *Adv. Funct. Mater.* **2009**, *19*, 1826.

(35) Srinivasan, G.; Fetisov, Y. K. *Fer* **2006**, *342*, 65.

(36) Srinivasan, G.; Hayes, R.; Bichurin, M. I. *Solid State Commun.* **2003**, *128*, 261.

(37) Karpinsky, D. V.; Pullar, R. C.; Fetisov, Y. K.; Kamentsev, K. E.; Kholkin, A. L. *J. Appl. Phys.* **2010**, *108*, 042012.

(38) Bai, F. M.; Zhang, H. W.; Li, J. F.; Viehland, D. *Journal of Physics D-Applied Physics* **2010**, *43*.

(39) Chung, T. K.; Keller, S.; Carman, G. P. *Appl. Phys. Lett.* **2009**, *94*.

(40) Chung, T. K.; Carman, G. P.; Mohanchandra, K. P. *Appl. Phys. Lett.* **2008**, *92*.

(41) Xie, S. H.; Liu, Y. M.; Liu, X. Y.; Zhou, Q. F.; Shung, K. K.; Zhou, Y. C.; Li, J. Y. *J. Appl. Phys.* **2010**, *108*.

(42) Xie, S.; Ma, F.; Liu, Y.; Li, J. *Nanoscale* **2011**.

(43) Patankar, K. K.; Dombale, P. D.; Mathe, V. L.; Patil, S. A.; Patil, R. N. *Materials Science and Engineering B-Solid State Materials for Advanced Technology* **2001**, *87*, 53.

(44) Srinivasan, G.; DeVreugd, C. P.; Flattery, C. S.; Laletsin, V. M.; Paddubnaya, N. *Appl. Phys. Lett.* **2004**, *85*, 2550.

(45) Yourdkhani, A.; Perez, A. K.; Lin, C. K.; Caruntu, G. *Chem. Mater.* **2010**, *22*, 6075.

(46) Stern, I. *Appl. Phys. Lett.* **2011**, *99*, 082908.

(47) Rodriguez, B. J.; Jesse, S.; Alexe, M.; Kalinin, S. V. *Adv. Mater.* **2008**, *20*, 109.

(48) Zavala, G.; Fendler, J. H.; TrolierMcKinstry, S. *J. Appl. Phys.* **1997**, *81*, 7480.

(49) Gruverman, A.; Rodriguez, B. J.; Nemanich, R. J.; Kingon, A. I. *J. Appl. Phys.* **2002**, *92*, 2734.

(50) Wang, Z.; Suryavanshi, A. P.; Yu, M.-F. *Appl. Phys. Lett.* **2006**, *89*, 082903.

(51) Damjanovic, D. *Rep. Prog. Phys.* **1998**, *61*, 1267.

(52) Shvartsman, V. V.; Pankrashkin, A. V.; Afanasjev, V. P.; Kaptelov, E. Y.; Pronin, I. P.; Kholkin, A. L. *Integrated Ferroelectrics: An International Journal* **2005**, *69*, 103

(53) Kalinin, S. V.; Bonnell, D. A. *J. Mater. Res.* **2002**, *17*, 936.

(54) Cullity, B. D.; Graham, C. D. *Introduction to magnetic materials*; Wiley, 2009.

(55) Pertsev, N. A.; Emelyanov, A. Y. *Appl. Phys. Lett.* **1997**, *71*, 3646.

(56) Jin, C. *J. Appl. Phys.* **2011**, *110*, 013917.

(57) Gao, X. S.; Bao, D. H.; Birajdar, B.; Habisreuther, T.; Mattheis, R.; Schubert, M. A.; Alexe, M.; Hesse, D. *Journal of Physics D-Applied Physics* **2009**, *42*.

(58) Likodimos, V.; Labardi, M.; Allegrini, M. *PhRvB* **2002**, *66*, 024104.

(59) Harnagea, C.; Alexe, M.; Hesse, D.; Pignolet, A. *Appl. Phys. Lett.* **2003**, *83*, 338.

(60) Seal, K.; Jesse, S.; Rodriguez, B. J.; Baddorf, A. P.; Kalinin, S. V. *High frequency piezoresponse force microscopy in the 1-10?MHz regime*; AIP, 2007; Vol. 91.

(61) Harnagea, C.; Pignolet, A.; Alexe, M.; Hesse, D. *ITUFF* **2006**, *53*, 2309.

(62) Jesse, S.; et al. *Nanotechnology* **2006**, *17*, 1615.

(63) Harnagea, C.; Pignolet, A.; Alexe, M.; Hesse, D. *InFer* **2004**, *60*, 101.

(64) Kalinin, S. V.; Bonnell, D. A. *PhRvB* **2001**, *63*.

(65) Hong, S.; Woo, J.; Shin, H.; Jeon, J. U.; Pak, Y. E.; Colla, E. L.; Setter, N.; Kim, E.; No, K. *J. Appl. Phys.* **2001**, *89*, 1377.

(66) Gruverman, A.; Kholkin, A. *Rep. Prog. Phys.* **2006**, *69*, 2443.

(67) Vopsaroiu, M.; Stewart, M.; Hegarty, T.; Muniz-Piniella, A.; McCartney, N.; Cain, M.; Srinivasan, G. *Measurement Science & Technology* **2008**, *19*.

(68) Yourdkhani, A. G., E. Zaldivar, L. Spinu, L. Caruntu, G. *ITM* **2011**, *47*, 4.

(69) Licci, F.; Rinaldi, S. *J. Appl. Phys.* **1981**, *52*, 2442.

(70) Damjanovic, D. *Rep. Prog. Phys.* **1998**, *61*, 1267.

(71) Haun, M. J.; Furman, E.; Jang, S. J.; McKinstry, H. A.; Cross, L. E. *J. Appl. Phys.* **1987**, *62*, 3331.

(72) Kim, B. H.; Moon, J. W.; Song, Y. D.; Mizutani, N.; Shinozaki, K. *J. Ceram. Soc. Jpn.* **2006**, *114*, 603.

(73) Dippel, A. C.; Schneller, T.; Waser, R. *InFer* **2008**, *98*, 3.

(74) Wang, G. S.; Remiens, D.; Soyer, C.; Dogheche, E.; Cattan, E. *J. Cryst. Growth* **2005**, *284*, 184.

(75) Lee, E. J. H.; Pontes, F. M.; Leite, E. R.; Longo, E.; Varela, J. A.; Araujo, E. B.; Eiras, J. A. *J. Mater. Sci. Lett.* **2000**, *19*, 1457.

(76) Hamano, T.; Towner, D. J.; Wessels, B. W. *Appl. Phys. Lett.* **2003**, *83*, 5274.

(77) Yamada, T. *J. Appl. Phys.* **1972**, *43*, 328.

(78) Wang, J. J.; Meng, F. Y.; Ma, X. Q.; Xu, M. X.; Chen, L. Q. *J. Appl. Phys.* **2010**, *108*, 034107.

(79) Hlinka, J.; Márton, P. *PhRvB* **2006**, *74*, 104104.

(80) Sreenivasulu, G.; Babu, V. H.; Markandeyulu, G.; Murty, B. S. *Appl. Phys. Lett.* **2009**, *94*.

(81) Islam, R. A.; Kim, H.; Priya, S.; Stephanou, H. *Appl. Phys. Lett.* **2006**, *89*.

(82) Islam, R. A.; Bedekar, V.; Poudyal, N.; Liu, J. P.; Priya, S. *J. Appl. Phys.* **2008**, *104*.

Vita

Amin Yourdkhani obtained his Bachelors of Science in Materials Engineering from University of Semnan at 2005. He accomplished his Masters of Science in Materials Science and Engineering at University of Tehran on 2008. Then, he joined to the PhD program in Chemistry Department at University of New Orleans with emphasis on Materials Science and Chemistry on 2009. He successfully finished his PhD thesis entitled “Synthesis and Characterization of Ferroic and Multiferroic Nanostructures by Liquid Phase Deposition” on October 2012.